

# **Structural modification of solids by ultra-short X-ray laser pulses**

Dissertation zur Erlangung des Doktorgrades  
der Fakultät für Physik  
der Universität Hamburg

**Shafagh Dastjani Farahani**

Tehran, Iran

Hamburg  
2017

Erklärung

Diese Dissertation wurde im Sinne von §13 Abs. 3 der Promotionsordnung vom 29. Jan 1998 von Prof. Dr. H. Chapman betreut.

Ehrenwörtliche Versicherung

Diese Dissertation wurde selbstständig, ohne unerlaubte Hilfe erarbeitet.

Hamburg, am 01.04.2017

Shafagh Dastjani Farahani

Gutachter/innen Disseration:

Prof. Dr. Henry Chapman

Prof. Dr. Michael Alexander Rübhausen

Gutachter/innen Disputation:

Prof. Dr. Henry Chapman

Prof. Dr. Arwen Pearson

Vorsitzende/r Prüfungskommission: Prof. Dr. Daniela Pfannkuche

Datum der Disputation: 21.09.2017

Vorsitzender des Fach-Promotionsausschusses PHYSIK: Prof. Dr. Wolfgang Hansen

Leiter des Fachbereichs PHYSIK: Prof. Dr. Michael Potthoff

Dekan der Fakultät MIN: Prof. Dr. Heinrich Graener





# Contents

<b>1</b>	<b>Die Zusammenfassung</b>	<b>9</b>
<b>2</b>	<b>Abstract</b>	<b>11</b>
<b>3</b>	<b>Introduction</b>	<b>13</b>
<b>4</b>	<b>Electromagnetic origin of radiation interaction with matter</b>	<b>17</b>
<b>5</b>	<b>Ultra-fast electrons and lattice dynamics</b>	<b>27</b>
5.1	A general picture . . . . .	27
5.2	X-ray FEL light, matter interaction . . . . .	30
5.3	Ablation . . . . .	33
5.4	Time scale of X-ray light-matter interaction . . . . .	35
5.5	Length scale of X-ray light, matter interaction . . . . .	36
5.6	Absorbed energy per volume . . . . .	38
<b>6</b>	<b>Low-Z materials</b>	<b>39</b>
6.1	Properties of amorphous carbon . . . . .	40
6.2	Amorphous carbon preparation . . . . .	42
6.3	CVD single crystal diamond . . . . .	42
<b>7</b>	<b>Experimental technique</b>	<b>45</b>
7.1	FLASH Beamlines and baseline instrumentation . . . . .	45
7.1.1	<i>BL2</i> . . . . .	46
7.1.2	<i>BL3</i> . . . . .	46
7.1.3	Gas monitor detector . . . . .	47
7.2	Dedicated set up for damage experiments . . . . .	48
7.2.1	Sample holder . . . . .	49
7.2.2	Detectors . . . . .	51
7.3	Alignment and experimental protocol . . . . .	53
7.3.1	Sample irradiation procedure . . . . .	55
7.4	Setup at other FEL sources . . . . .	57
7.4.1	Soft X-ray setup at SCSS . . . . .	57
7.4.2	LCLS Atomic, Molecular and Optical Science (AMO) . . . . .	58
7.5	Damage characterization . . . . .	61
7.5.1	Nomarski Microscope . . . . .	62
7.5.2	Atomic Force Microscopy . . . . .	64
7.5.3	Raman scattering . . . . .	67

7.5.4	White light interferometer . . . . .	68
7.5.5	Photoemission spectroscopy and Scanning Electron Microscopy . . . . .	69
<b>8</b>	<b>Damage Investigations</b>	<b>75</b>
8.1	Damage threshold . . . . .	76
8.2	Experimental Results . . . . .	82
8.2.1	Below and around carbon K-edge . . . . .	82
8.2.2	Above carbon K-edge . . . . .	84
8.2.3	Below carbon K-edge and at grazing angle . . . . .	85
8.2.4	Discussions . . . . .	93
8.3	Photoemission spectroscopy results . . . . .	98
8.4	Atomic Force Microscopy results . . . . .	100
8.5	Raman spectroscopy results . . . . .	109
<b>9</b>	<b>Simulations</b>	<b>119</b>
9.1	Hybrid code XTANT (Theoretical simulation) . . . . .	119
9.2	Heat diffusion simulation . . . . .	128
9.2.1	Discussions . . . . .	147
<b>10</b>	<b>Damage on gratings</b>	<b>151</b>
10.1	Grating's parameters . . . . .	153
10.2	Results of damage experiment on gratings . . . . .	153
<b>11</b>	<b>Discussions and summary</b>	<b>161</b>
11.1	Discussions . . . . .	161
11.2	Summary . . . . .	173
<b>12</b>	<b>Appendix A</b>	<b>177</b>
12.1	Damage threshold values summarized in Tables at different photon energies for a-C and CVD diamond . . . . .	177
12.2	Damage energy threshold and effective beam area at different photon energies on a-C and CVD diamond . . . . .	179
12.3	Damage energy threshold and effective beam area at different grazing angles on Nickel at 269 eV . . . . .	189
12.4	Damage energy threshold and effective beam area at different grazing angles on MoB4C at 269 eV . . . . .	195
12.5	Raman plots . . . . .	201
12.6	Heat diffusion plots . . . . .	205
	<b>List of Figures</b>	<b>209</b>
	<b>List of Tables</b>	<b>227</b>
	<b>Bibliography</b>	<b>229</b>
<b>13</b>	<b>Acknowledgement</b>	<b>241</b>

CONTENTS	7
----------	---

---

Curriculum vitae – Lebenslauf	243
-------------------------------	-----

List of Publications	247
----------------------	-----



## Chapter 1

# Die Zusammenfassung

Die Motivation für diese Doktorarbeit besteht darin, die strukturellen Änderungen von Festkörpern durch ultrakurze Röntgenstrahlungspulse zu bestimmen.

Diese Doktorarbeit fokussiert sich auf die Analyse von amorphen Kohlenstoff (a-C), das als potentielle Beschichtung für Spiegel, insbesondere der Weich-Röntgenstrahlbeamline des Europäischen Freie Elektronenlasers (European X-ray Free Electron Laser (XFEL)) in Hamburg in Frage kommt. Des weiteren soll chemische Gasphasenabscheidung (CVD) Diamant, das in Monochromatoren für Röntgenstrahlführung des XFELs eingesetzt wird, untersucht werden. Von Materialien mit einer hohen Kernladungszahl wurden Nickel (Ni) und MoB<sub>4</sub>C (Multilayer) bei einer Energie von 269 eV untersucht. Im Fokus stand dabei das Verhalten von a-C-beschichteten Spiegeln und den CVD-Diamant-Monochromatoren, die in den durchgeführten Experimenten das Hauptthema sind.

Freie-Elektronen Laser liefern fokussierte Pulse mit einer hohen spitzen-Brillanz, hoher Leistung und einer Pulsebreite in Femtosekundenbereich. Optische Elemente in diesen Anlagen sind von entscheidender Bedeutung, da sie den Strahl mit hoher Qualität weiterleiten sollen und zugleich die intensiven Strahlbedingungen standhalten müssen. Daher ist es wichtig, das Zusammenspiel der Röntgenstrahlungspulse des Freie-Elektronen Lasers mit den Spiegelbeschichtungen und den Einkristallen der Monochromatoren zu verstehen. Mit Hilfe dieses Projekts wird offensichtlich, dass auf einer fundamentalen Ebene verschiedene Mechanismen in einen Zerstörungsprozess auf unterschiedlichen Zeitskalen involviert sind. Innerhalb der ersten Femtosekunden (*fs*) ist der Photoionisation der Hauptmechanismus des Zerstörungsprozesses. Während dieser Zeit ändert sich die Materialdichte und das System neigt dazu einen energetisch stabilen Status zu erreichen (a-C/ CVD Diamant wandelt sich in Graphit um). Auf der Pikosekunden-Zeitskala werden sekundäre Prozesse initiiert. Unter diesen sind zu nennen: Auger-Effekt, Stoßionisation, Tunnelionisation, Leitungsdiffusion gefolgt von freien Ladungsträgern, die Z.B. mit dem Gitter interagieren, Elektron-Phononen Wechselwirkung, etc. Die Wärmediffusion beginnt nach einigen 100 *ps* und hält solange an bis das System nach einigen Mikrosekunden (7  $\mu$ s) wieder Raumtemperatur erreicht. Die Analyse des Zerstörungsprozesses kann in drei Hauptphasen unterteilt werden,

die auf den oben genannten Zeitskalen basieren.

Die Kombination von Wärmediffusion und sekundären Prozessen bewirkt eine nichtlineare Erhöhung der Grösse der Schadensflecken auf der logarithmischen Achse in Abhängigkeit von der Pulsenergie. Die Zerstörungsschwelle der Photoionisation (nicht thermisch) wird bestimmt durch Experimente, die an unterschiedlichen Freie-Elektronen Lasern bei unterschiedlichen Photonen-energien durchgeführt wurden. Durch Simulation der Wärmediffusion mit Hilfe von COMSOL (Software Paket basiert auf 'Advanced numerical methods'), kann die Schmelzenergieschwelle für jedes Material bei verschiedenen Photon-Energien bestimmt werden. Um einen tieferen Einblick in den Zerstörungsprozess in Rahmen dieses Projektes zu erhalten, wurden zusätzliche Untersuchungen, wie Rasterkraftmikroskopie (AFM), Raman-Spektroskopie, Photoemission-Spektroskopie und theoretische Simulationen mit dem Hybride XTANT Code durchgeführt.

## Chapter 2

# Abstract

The motivation behind this Ph.D. project is to determine the structural modification of solids by ultra-short X-ray laser pulses. This Ph.D. project focuses on determining the amorphous carbon (a-C) as a potential coating on the mirrors of the soft X-ray beamline of the European X-ray Free Electron Laser (XFEL) in Hamburg, in particular. Furthermore, chemical vapor deposition (CVD) diamond used in the monochromators for X-ray beamlines of European XFEL needs to be examined. Among high Z materials Nickel (Ni), MoB4C (multi-layer), are studied at 269 eV photon energy. The focus was on testing the behavior of a-C coated mirrors and the CVD diamond monochromators which are the main subject in the performed experiments.

XFEL deliver high peak brilliance, high power, femtosecond focused laser pulses. Optical elements in these facilities are of crucial importance as they should distribute the beam with high quality and survive the intense conditions. Hence, understanding the interplay between the X-ray FEL pulses with coatings on the mirrors as well as single crystal monochromators is important.

By means of this project it becomes evident that from the fundamental aspect, different mechanisms are involved in the damage process at different time scales. In the early femtosecond (*fs*) time zone, the photo-ionization is the main mechanism governing the damage process. During this time the material density changes. The system tends to reach its energetically stable potential state (a-C turns into graphite). In the picosecond (*ps*) time scale, secondary processes initiate. Among those, one can mention Auger, impact ionization, tunnel ionization, carrier diffusion followed by free carriers interaction with the lattice e.g. electron-phonon coupling, etc. The heat diffusion process starts to take place after some 100 *ps*, which continues until the system returns to room temperature after some  $\mu s$  (7  $\mu s$ ). The analysis of the damage process can be divided into three main phases; based on the different time zone named above.

The combination of heat diffusion and secondary processes cause a non-linear increase in the size of the damage spots on the logarithmic axis depending on the pulse energy.

The photo-ionization (non-thermal) damage threshold is determined from experiments performed at different FEL facilities on different photon energies. From heat diffusion simulation via COMSOL (software package based on advanced numerical methods), one can extract the melting energy threshold for

each material at different photon energies. To gain a deeper knowledge on the damage process within the scope of this project, several investigations such as Atomic Force Microscopy (AFM), Raman spectroscopy, photoemission spectroscopy, and theoretical simulation via Hybrid XTANT code were conducted based on the subjected samples.



## Chapter 3

# Introduction

The 4<sup>th</sup> generation of X-ray light sources, Free Electron Lasers (FEL), deliver high-intensity ultra-short (sub-100 fs) pulses with photon energy ranging from UV-VUV (FELBE located in Dresden [1], FERMI@Elettra is a single-pass FEL user-facility located in Trieste, Italy [2] and FLASH facility located in Hamburg [3]) to hard X-rays. The Linac Coherent Light Source at the Stanford Linear Accelerator Center (LCLS) [4], SACLA-XFEL in Japan (located in Hyogo Prefecture) and the European XFEL (starting in the first half of 2017) in Hamburg produce radiation with wavelengths from nanometers to sub-angstroms, and the pulse energy ranges in milli-Joules. The photon beam transport system in these facilities is of great importance [5], [6]. This system (see Fig 3.1) has the function of transporting the X-ray FEL beam, produced by undulators, to scientific stations and instruments. Beam transport is carried out with design and installation of several optical elements such as mirrors and gratings, etc. The background radiation is filtered out in some parts of the spectrum via a

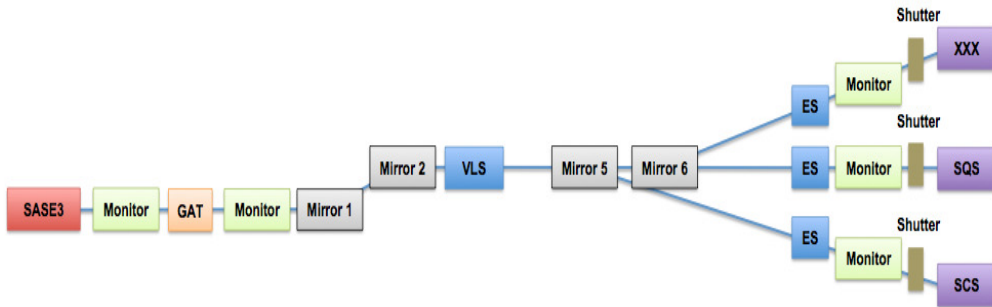


Fig. 3.1.: An example of beamline components like mirror configuration at SASE 3 beamline at European XFEL [7].

monochromator. (Monochromators are used to select specific regions of the X-ray spectrum for the experiments.) When X-ray pulse trains pass by and illuminate the optical elements, these should withstand the high power load (e.g. high fluence, heat load, etc.). They should also preserve the wave front and timing properties [7] of the beam. In fact, as some experiments rely on the

coherence and high quality of the wave front of the beam, any degradation of the optical components even on the nano scale will affect the performance of these experiments.

The high reflectivity of X-ray mirrors is another significant issue in FELs. Mirrors are used at very shallow grazing angles (lower than the critical angle). Since beam coherence should be conserved during the beam transport, understanding how degradation or deformation of the optical coating leads to changes in the beam quality is important. These components should, therefore, be manufactured with certain specific characteristic parameters to let the FEL run for a sustained duration under reliable conditions.

For example, the effects of ionizing radiation on the coatings (e.g. amorphous carbon (a-C) coatings in this case) in soft X-ray regime, and the energy thresholds for surface damage/modifications had to be studied. The length of mirrors at European-XFEL are around 1 m long. They will be installed at a grazing angle, as they work in X-ray regime with total external reflection. There is a compensation (relation) between the length of the mirrors and the angle at which they operate. This means using lower angles would necessitate manufacturing longer mirrors; a difficult task for industry (to produce long smooth coherent surfaces). These facts limit the production.

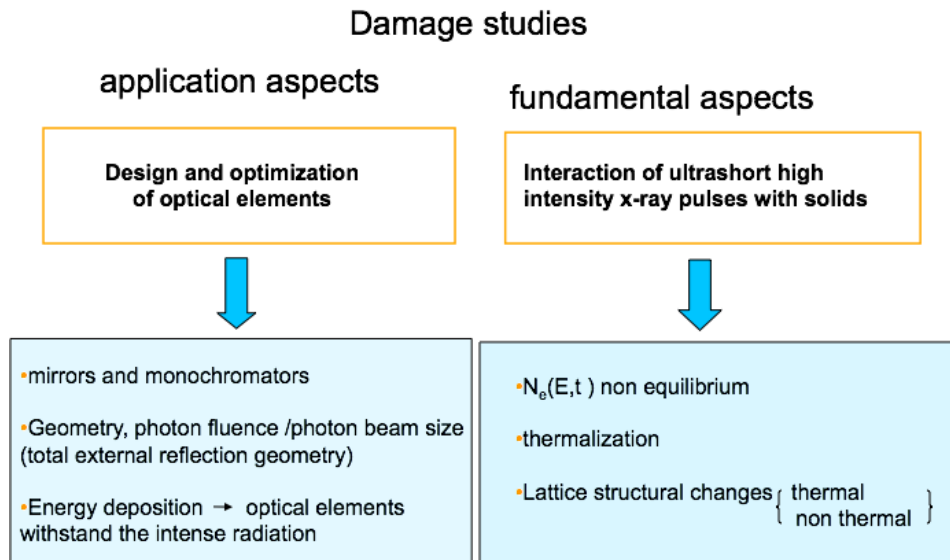


Fig. 3.2.: Damage studies.

This Ph.D. project focuses on the coating of the mirrors and the optics of monochromators. Low  $Z$  material like carbon coatings and high  $Z$  material like Ni, MoB4C, which are used to reflect and focus the beam, as well as CVD diamond (used in monochromators) are studied at different photon energies.

The two aspects studied here are the application aspect and the fundamental aspect (see Fig 3.2). The application aspect is focused on the damage process and the amount of absorbed energy and fluence threshold for each photon energy

at different incidence angles (grazing angles are the main focus in practical use). In the fundamental aspect, the focus is on the process of damage on matter caused by FEL beam in femtosecond (*fs*) time scale. The *fs* is the time scale during which the semiclassical wave packet circulates the proton in an atom (Hydrogen atom), its corresponding wavelength being around 300 *nm*.

FEL beam pulses with a pulse duration in the *fs* timescale allow studying the interaction of X-rays with a matter with a very high time-resolution. This is important e.g. for the understanding of the vibration of chemical bondings or the creation of plasmas.

After the system is being exposed to FEL pulse, the electronic system of the material gets highly excited. During and after the first 100 *fs*, the excited electrons decay back to low energy thermalized states. Where the electrons and lattice coupling is dominated by transferring kinetic and potential energy to the atoms of the lattice. At this point, the atoms experience a modified potential energy surface and relax into the new phase. The purely solid to solid transition occurs extremely fast (100 *fs*). The thermal process is assigned as a direct increase in the kinetic energy (temperature) of atoms in the lattice, and the non-thermal melting process is addressed as changes in the interatomic potential which is caused due to the changes in the potential energy of the system [8].

Whether these interactions are thermal or non-thermal, and the possible phases that the material undergoes from the moment of the beam illuminating the sample's surface to the moment that the sample cools, are important to understanding the processes taking place. Any ablation, spallation or melting and the physical reasons connected to such processes are, to some extent, addressed by this project.



## Chapter 4

# Electromagnetic origin of radiation interaction with matter

Light is a primary tool for perceiving the world and communicating within it. Its interaction with matter helped to structure the universe. Its transmission of spatial and temporal information provides a window to the universe, from cosmological to atomic scales. Light wave-particle nature, revealed in quantum mechanics, isn't exclusive to it but is shared by all of the primary constituents of nature (electrons are another example of this duality). In classical electromagnetism, light can be described by coupled electric and magnetic fields in form of waves propagating in the medium. Maxwell's equations are the four fundamental equations describing the propagation of light in medium [9], [10] (see Equations 4.1-4.4).

$$\nabla \cdot E = 4\pi\rho \quad (4.1)$$

$$\nabla \cdot B = 0 \quad (4.2)$$

$$\nabla \times E = -\frac{1}{c} \frac{\partial B}{\partial t} \quad (4.3)$$

$$\nabla \times B = \frac{1}{c} \frac{\partial E}{\partial t} + \frac{4\pi}{c} J \quad (4.4)$$

The speed of light (as a wave propagating) in each medium depends on the properties of that medium, which is described using its phase and group velocity (see Eq 4.12).

In quantum mechanics, light is described as discrete packets of energy, called photons.

Regarding maxwell equations (see Equations 4.1-4.4), one can obtain a simple electromagnetic wave equation, described by the Equation 4.5

$$\nabla^2 E - \mu_0\epsilon_0\ddot{E} = 0 \quad (4.5)$$

which can be simplified (time independent part of wave equation considering separation of variable methods) to a Helmholtz equation (plane wave equation) given by

$$\nabla^2 E + k^2 E = 0 \quad (4.6)$$

Knowing that Magnetic and electric field are in phase and perpendicular to each other, the solution to this equation is a plane wave of the following form (Gaussian wave Equation)

$$E(\vec{r}, t) = \vec{E}_0 e^{i(k \cdot r - \omega t)} \quad (4.7)$$

Hence, the intensity of the Gaussian beam propagating inside the medium would be as follows

$$I \propto | (E_0 e^{i(k \cdot r - \omega t)}) |^2 \quad (4.8)$$

$$I \propto | E_0 |^2 e^{-\alpha \cdot r} \quad (4.9)$$

The  $\alpha$  is the absorption coefficient, where

$$\alpha = 1/\sigma_p \quad (4.10)$$

and  $\sigma_p$  is the penetration depth.

The wave vector  $k$  and the angular frequency  $\omega$  obey the following relations

$$k = \frac{2\pi}{\lambda}, \frac{\omega}{k} = \sqrt{\frac{1}{\epsilon_0 \mu_0}} \quad (4.11)$$

$$v_{ph} = \frac{\omega}{k}, v_{gr} = \frac{\partial \omega}{\partial k} \quad (4.12)$$

The phase velocity  $v_{ph}$  describes the speed of wave crest and the group velocity  $v_{gr}$ , the speed of the center of mass of a wave packet with middle frequency  $w$ . In vacuum the phase and group velocity are the same and equal to the speed of light (see Eq 4.13).  $\epsilon_0$  and  $\mu_0$  are called dielectric constant and permeability of vacuum, respectively.

$$c = \frac{1}{\sqrt{\mu_0 \epsilon_0}} \quad (4.13)$$

Understanding principles of the interaction of electromagnetic waves with matter is a useful aid in developing methods of understanding the structure of matter and its different chemical, mechanical, electrical and thermal properties.

Chemical bonding (ionic, metallic, valence, van der Waals and hydrogen bonding) ascribes a potential which creates the interactions holding the atoms in molecules or crystal together. There are several theories, including Bloch theory, Tight-Binding model, etc., which describe the periodic potential in which atoms (ions) are located and electrons move. Each atomic orbital corresponds to a particular energy level of the electron [11], [12]. The time independent Schrödinger equation (see Eq 4.14) explains the energy levels and bond structure in a matter.

$$E\Psi = \frac{-\hbar}{2m}\nabla^2\Psi + V^2\Psi \quad (4.14)$$

The electromagnetic force between electrons and protons is responsible for building up atoms which requires an external source of energy for the electron to escape its atom. The closer an electron is to the nucleus, the greater the attractive force. Electrons bound near the center of the potential well (core electrons) therefore, need more energy to escape from the atom than those at higher shells (valence electrons). Valence electrons are those occupying the outermost shell or highest energy level of an atom and are responsible for building up atomic bondings [11], [9]. In contrast, the core electrons do not participate in bindings in that sense.

Electrons in solid insulators can be considered confined to each atom. One can treat them as a harmonic oscillator, where each can be described with

$$m(\ddot{r} + \gamma\dot{r} + \omega_0^2 r) = eE(r(x, y, z), t) \quad (4.15)$$

where the solution to this equation would be

$$\vec{r} = \frac{e\vec{E}(r(x, y, z), t)}{m((\omega_0^2 - \omega^2) + i\gamma\omega)} \quad (4.16)$$

Exposed by the electromagnetic wave, the atoms/molecules in matter get polarized (because of the electromagnetic force acting on them (see Eq 4.17)). The electromagnetic wave acts on a charge particle via force  $F$  given by

$$\vec{F} = q(\vec{E} + \frac{v}{c} \times \vec{B}) \quad (4.17)$$

As  $v \leq c$ , the electric field is the dominant factor in this equation.

The electric displacement is defined as

$$\vec{D} = \epsilon_0\vec{E} + \vec{P} \quad (4.18)$$

Proceeding with that equation (Eq 4.18) the wave equation (see Eq 4.5) turns to

$$\nabla^2 E - \mu_0\epsilon_0\ddot{E} = \mu_0\ddot{P} \quad (4.19)$$

which states that each dipole, where its second derivative varying with time, is a source of electromagnetic wave propagating in a medium. Where  $\vec{E}(t) = \vec{E}e^{i\omega t}$ ,  $\vec{r}(t) = \vec{r}e^{i\omega t}$  and  $\vec{P} = e\vec{r}(t) = \vec{p}e^{i\omega t}$ .

The dipole moment of the charge (as the electromagnetic wave acts on it) changes with (involving results of Eq 4.15 for  $\vec{r}$ )

$$\vec{P} = e\vec{r} = \frac{e^2}{m}(\omega_0^2 - \omega^2 - i\gamma\omega)^{-1}\vec{E} \quad (4.20)$$

If one assumes a linear relationship between  $P$  (polarization) and  $E$  (electric field) such as

$$\frac{\vec{P}}{\epsilon_0} = \chi\vec{E} \quad (4.21)$$

Then

$$\chi = \frac{e^2 N}{\epsilon_0 m (\omega_0^2 - \omega^2 - i\gamma\omega)} \quad (4.22)$$

with  $\chi$  called the susceptibility ( $\epsilon = 4\pi\chi + 1$ ) respectively, or in the form of

$$\vec{D} = \epsilon_0(1 + 4\pi\chi)\vec{E} = \epsilon_0\epsilon\vec{E} \quad (4.23)$$

Where both  $\epsilon$  and  $\chi$  depend on  $(\omega, \mathbf{k})$ .

Suppose there are  $N$  molecules inside the medium and each molecule has  $Z$  electrons with a binding frequency of  $\omega_i$  and damping constant  $\gamma_i$ , where  $\sum f_i = Z$ . The dielectric constant gets the following form

$$\epsilon(\omega) = 1 + \frac{4\pi N e^2}{m} \sum (f_i (\omega_i^2 - \omega^2 - i\gamma_i\omega)^{-1}) \quad (4.24)$$

where the damping constant is usually small compared to the binding or resonant frequency  $\omega_i$ . The  $\epsilon_\omega$  for most frequencies is real and  $\omega_i^2 - \omega^2$  is positive for  $\omega \leq \omega_i$  and negative for  $\omega \geq \omega_i$ . Below the smallest  $\omega_i$ , at low frequencies the  $\epsilon(\omega)$  is greater than unity. An interesting behavior is seen when the  $\epsilon(\omega)$  is negative. It occurs on passing the smallest values of  $\epsilon(\omega)$  and reaching high frequencies as in the case of X-rays (see Figs 4.1). This means in that region, the phase velocity (velocity of wave crest) is faster than the speed of light.

In the neighborhood of any  $\omega_i$  one sees an extreme behavior (see Figs 4.1). The absorption is at maximum and the phase speed is very low. The resonance frequencies are defined as frequencies at which the radiation will be absorbed to the maximum, and the imaginary part is large.

For a better understanding one can describe the wave vector of the propagating wave by

$$k^2 = (1 + \chi(\omega))\omega^2/c^2 \quad (4.25)$$

Where the refractive index is introduced as  $n^2 = (1 + \chi(\omega))$ . Since  $\chi(\omega)$  [9] is a complex number, the refractive index can be presented in its real and imaginary components

$$n = 1 - \delta(\omega) + i\beta(\omega) \quad (4.26)$$

The real part  $1 - \delta(\omega)$  (see Figs 4.1 and 4.3) describes the phase velocity and  $\beta(\omega)$  is related to the absorption of radiation through the medium.

With Beer Lambert Law (is relevant mainly for linear optic [14]), it is possible to calculate the changes in the intensity of the EM radiation as it enters and propagates inside the medium. Starting with the Equation 4.7 and substituting  $k$  with the

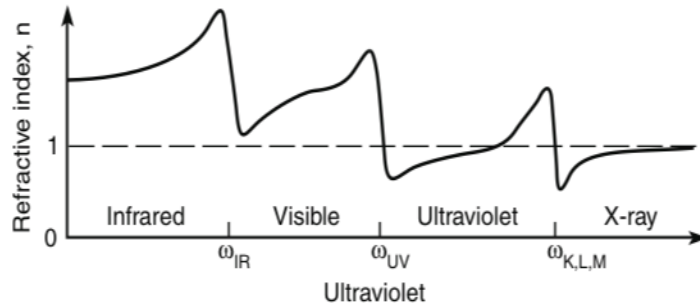
$$k = n\omega/c \quad (4.27)$$

where  $n$  is described in the Equation 4.26 it appears that

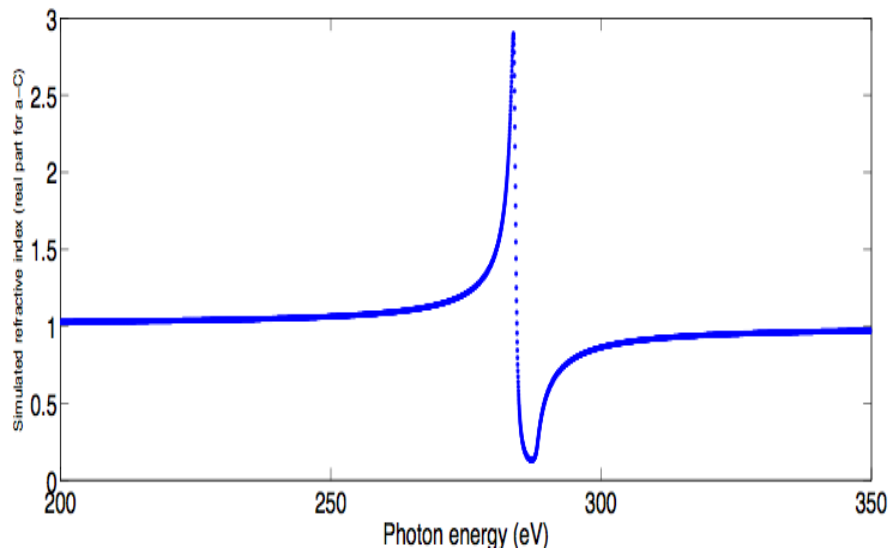
$$I(z) = I_0 e^{(-4\pi\beta(\omega)/\lambda)r} \quad (4.28)$$

Here  $\lambda$  is the wavelength of radiation,  $r$  the distance the radiation will travel to and  $\beta$  the absorption parameter in refractive index. The distance





(a)



(b)

Fig. 4.1.: (a): The refractive index  $1 - \delta$  as a function of frequency. In case of X-rays the refractive index for all materials is less than 1 which means the total external refraction would take place in case of X-rays which is not the case in other regime with frequencies below X-rays. The edges are the resonance frequencies at which the radiation will be absorbed [13]. (b): This plot represents the simulated refractive index (see Equation 4.24) for X-ray on a-C.

up to which the radiation decays is called the attenuation length (where the intensity becomes  $1/e$  of its initial value, the  $\alpha$  in the Equation 4.9 is exactly  $1/L_{att}$  which is named the absorption coefficient) and can be determined by

$$L_{att} = \lambda/(4\pi\beta(\omega)) \quad (4.29)$$

This quantity depends on both the wavelength of the incident radiation and the medium, in the latter case the imaginary part of the refractive index (see Fig 4.3) being the key factor. In general, the attenuation depth varies from  $nm$  to  $\mu m$ . Calculations show that X-ray attenuates deep inside the medium depth (at high photon energies up to few  $\mu m$  and at very low photon energies up to few  $nm$  [15], [8]). If the medium is transparent to a sort of radiation, it denotes that there are no available energy levels matching the radiation wavelength in the matter and energy can not get absorbed. In the case of strong electric field, in non-linear medium, the induced polarization can be expressed by the Taylor expression

$$P = \epsilon_0(\chi_1 E + \chi_2 E^2 + \chi_3 E^3 \dots) \quad (4.30)$$

$\chi_2, \chi_3$ , etc. described in nonlinear optics, are high-order terms which can be obtained in this condition. The high-order-of-magnitude waves from these terms are named as 2nd, 3rd harmonic waves, with a frequency of twice or triple the incident waves. Electric displacement would therefore not have the simple form as in Equation 4.18. Hence, the refractive index would have a more complicated form.

The reflectivity of a material depends on its reflective index and the incidence angle of the incoming beam. In the X-ray beam transport system, the aim is to maximize the reflected intensity. It is desired, to avoid normal incidence geometry, which increases the absorption percentage of the beam. The goal is to maximize reflection at the surface of the coating material at a grazing incidence angle. The candidate material in the case of this project was amorphous carbon.

According to Snell law (see Equation 4.31), it is possible to calculate the most appropriate geometry, at which the reflectivity, for a given material, is maximized. The angle of incidence beyond which, rays of light passing through a denser medium to the surface of a less dense medium and are no longer refracted but totally reflected is named as the critical angle. The total reflection occurs at an angle larger than a particular critical angle (with respect to the normal to the surface).

One obtains the critical angle through following steps

$$n' \sin(\phi') = n \sin(\phi) \quad (4.31)$$

$(\phi)$  is the incident angle of the EM radiation,  $n = 1$  (in vacuum), as mentioned in Fig 4.1 in the X-ray regime  $n'$  is smaller than 1,  $n' = (1 - \delta)$  and  $\beta$  (see Fig 4.3) can be neglected in this regime. Equation 4.31 turns into

$$\sin(\phi') = \sin(\phi)/1 - \delta \quad (4.32)$$

In the case of critical angle

$$\phi' \Rightarrow \pi/2 \quad (4.33)$$

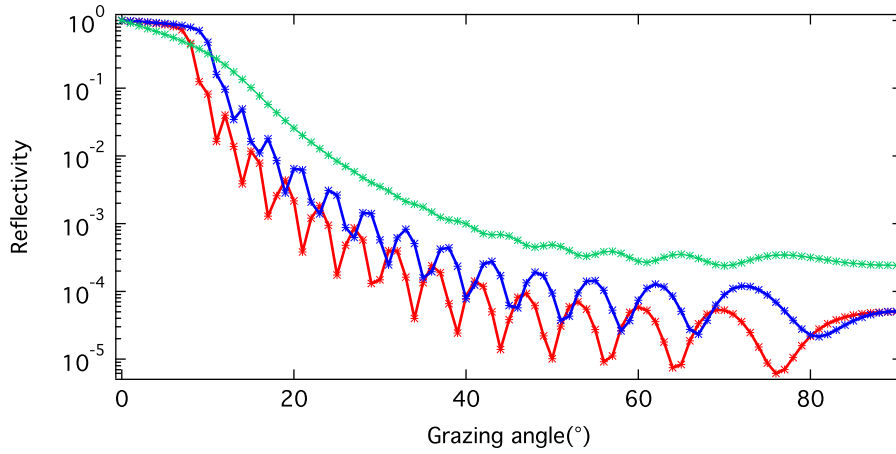
$$1 = \sin(\phi)/1 - \delta \quad (4.34)$$

and substitution of  $\theta = 90 - \phi$  and considering the Taylor expansion of  $\cos(\theta)$  results in

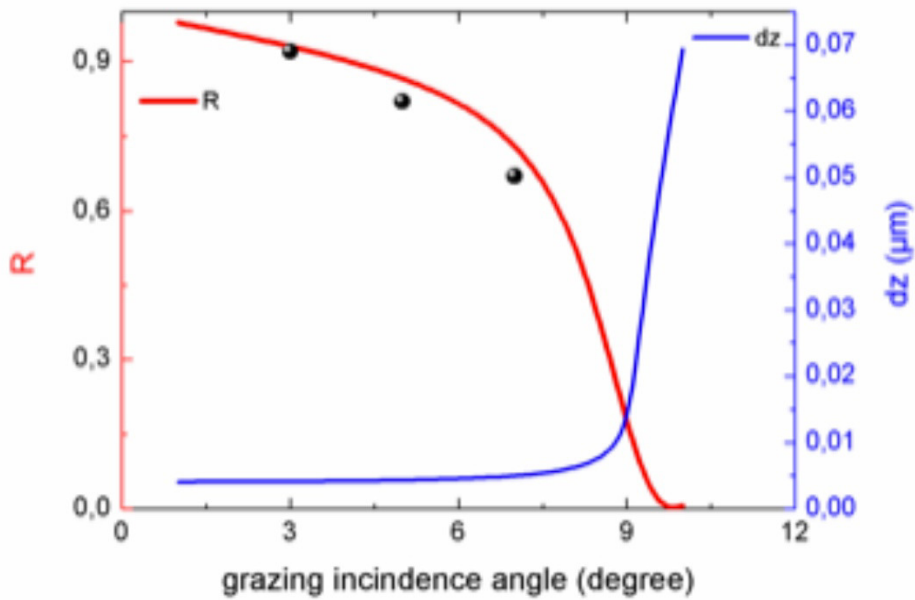
$$\theta_c = \sqrt{2\delta} \quad (4.35)$$

The  $\theta_c$  is called critical angle. The critical angle depends on the  $\delta$  (different for each material). Hence, the type of material plays an important role in designing the optical elements. Attenuation length as shown in the Equation 4.29 changes depending on the absorption coefficient. Fig 4.4 represents changes of the Attenuation length for different materials as well as the reflectivity of each of these materials at different photon energies (for this project plotted for energies between 200–800 eV). At different grazing angles, the reflectivity and attenuation length change and for each specific material at a specific photon energy the critical angle changes as well. This is shown in Fig 4.2, where the experimental data and theoretically calculated data via CXRO are compared. It is observed that there is a good agreement between the experiment and calculated data.

For grazing angles smaller than the critical angle  $\theta_c$  [13] (with respect to the surface), the X-rays will be reflected back in to the vacuum and the reflectivity as seen in Fig 4.2 is one or very close to one and above the critical angle this term significantly reduces.

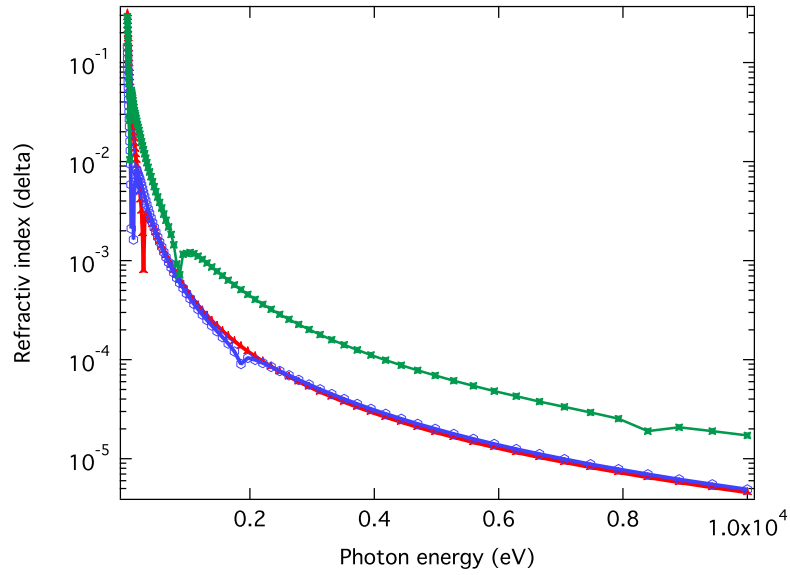


(a) Reflectivity as a function of incidence angle showing that at very low grazing angles the reflectivity is at the maximum of its range. This is plotted in blue for an amorphous carbon coated layer with  $SiO_2$  substrate at  $177eV$  photon energy and in red for CVD diamond. The green line show the reflectivity of Ni. The data is taken from CXRO data [15].

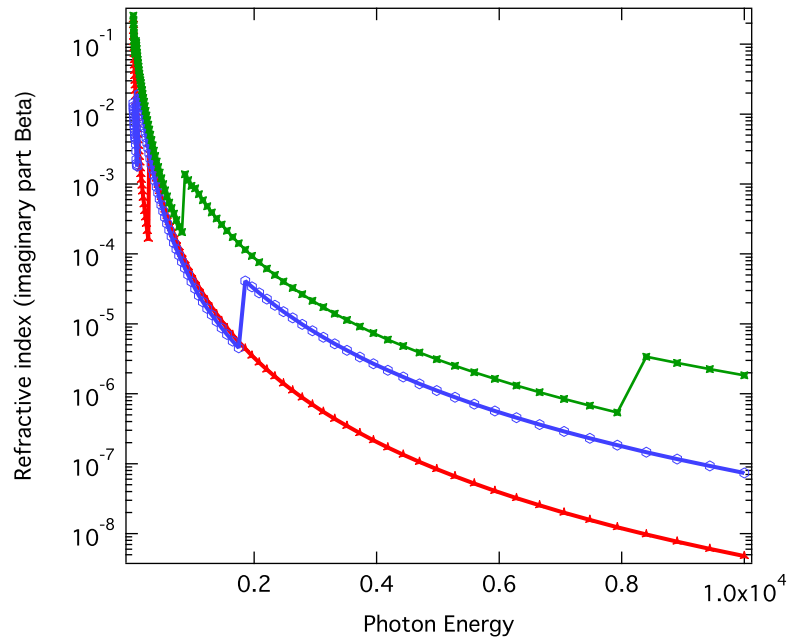


(b) Reflectivity and attenuation depth is plotted as a function of incidence angle, at very low grazing angles the reflectivity is at maximum of its range. This is plotted in red for an amorphous carbon coated layer with  $SiO_2$  substrate at  $177eV$  photon energy. Attenuation depth is plotted in blue. The solid lines are taken from CXRO data [15] and the black circles are the experimental results published in [16].

Fig. 4.2.

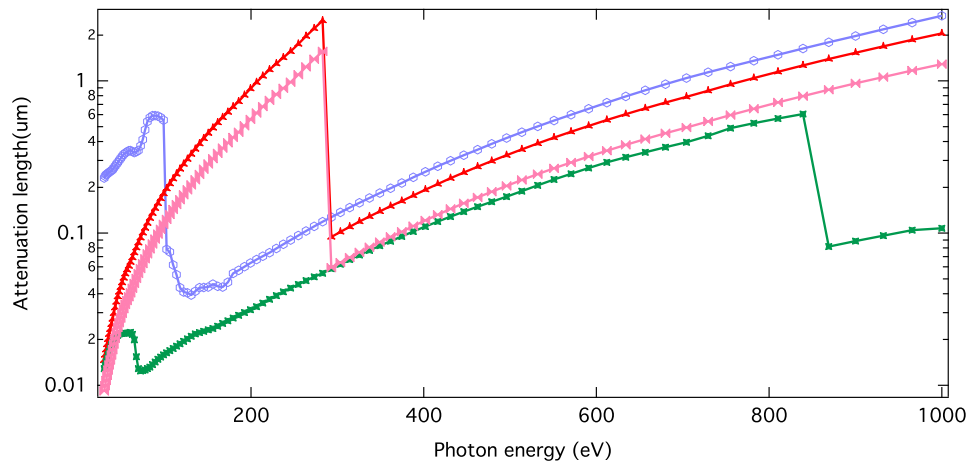


(a)

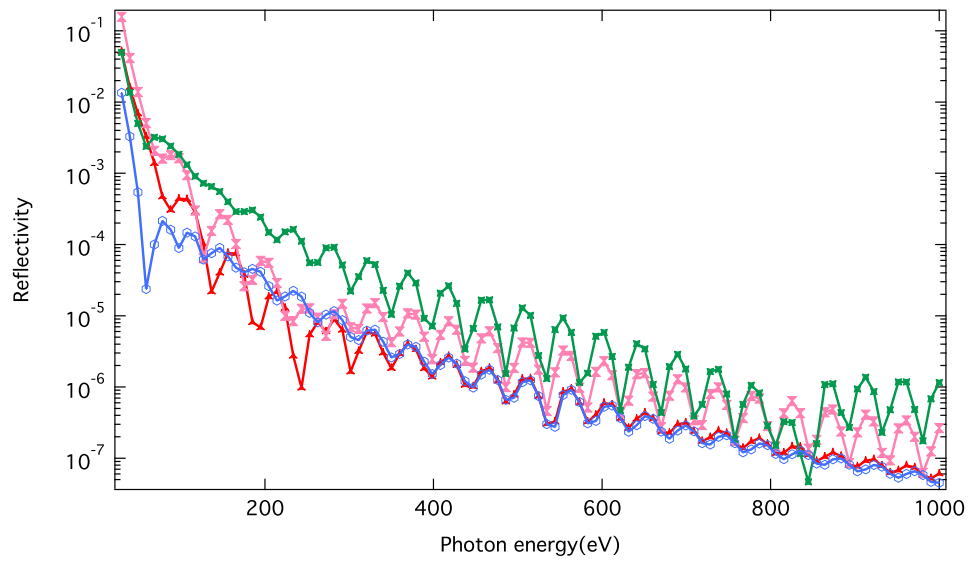


(b)

Fig. 4.3.: A comparison of the real ( $1-\delta$ ) (a) and imaginary part (b) of the refractive index of X-ray radiation inside a wide energy range for a-C (red), Si (violet) and Ni (green) is shown in this plot. Raw data has been taken from [15]. Ni has density  $8.9 \text{ gr/cm}^3$  and Si  $2.33 \text{ gr/cm}^3$  and a-C has the density of  $2.2 \text{ gr/cm}^3$ . Plots show that at very low energy basically the absorption and phase velocity of the X-ray light is high and going towards higher photon energies both of these parameters decrease.



(a)



(b)

Fig. 4.4.: (a): Attenuation length at different photon energies are compared for different materials. a-C (red), CVD (pink), Si (violet) and Ni (green). (b): Reflectivity of a-C (red), CVD (pink), Si (Violet), Ni (green) vs photon energies are compared here.

## Chapter 5

# Ultra-fast electrons and lattice dynamics

### 5.1 A general picture

The X-ray FEL beam interacts directly with the electronic system of the material (see Figs 5.1 and 5.2). It excites the atoms, moving electrons from initial ground state to the unoccupied levels, resulting in the creation of electron-hole pairs. The time-dependent intensity of the laser pulse has an effect on the degree of damage. Since the laser pulses are FEL pulses with  $fs$  time scale, the excitation process occurs very quickly. As a consequence, the non-equilibrium distribution of electrons gets thermalized through electron-electron collisions. Hence, the system returns to a Fermi-like equilibrium state in a short time. This thermalization results in a single chemical potential. As the laser intensity is very high, a vast number of electrons and hole pairs are created. At the same time, this means that the recombination time becomes short and ions also get displaced to large distances compared to a low-intensity laser pulse. Displacements of ions (in large distances) on the other hand means that the electronic band structure gets modified and valence and conduction bands can cross each other (in the case of insulators or semiconductors). During this time, the lattice undergoes some modifications such as bonds breaking, and the material gets restructured. This results in the possibility of the material undergoing crystal phase changes, melting, ablation, etc. Besides, the laser pulse causes heat diffusion in the sample as well, a process which takes a long time ( $ps$ – $ns$ ) compared to the non-thermal structural changes of the matter. As the heat diffuses inside the sample, it can cause a more significant amount of damage in the sample. There are two processes, the heat that gets diffused into the original material through conduction, and the heat which passes through from the center of damaged area towards the rest of the sample. After some hundreds of  $\mu s$  the sample cools down to the room temperature.

If a semiconductor gets excited with an ultrashort laser pulse, it undergoes several stages of relaxation before returning to the equilibrium state. These can be categorized under

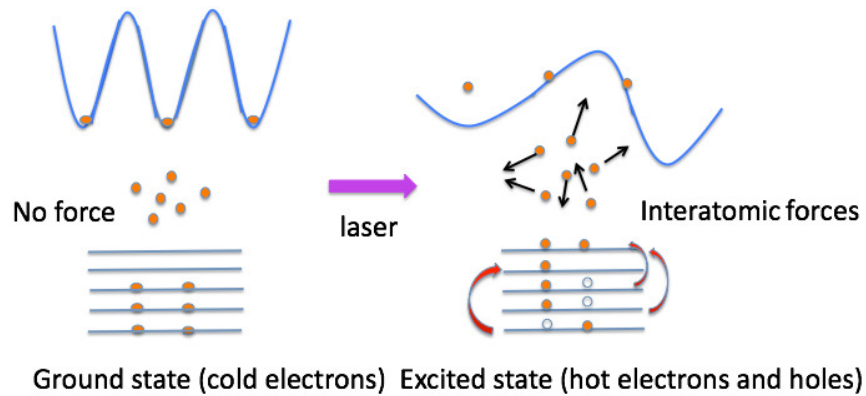


Fig. 5.1.: Very simple schematic of the matter and laser beam interaction [17]. The left side shows the system in its ground state; the electrons cold state. The potential landscape shows minima at the crystal lattice sites. Therefore, no external forces are acting on them except tight binding Coulomb potential induced by the lattice. On the right side, the laser light has affected the system and transported it to an excited state. Hot electrons and holes are created here. The potential landscape undergoes qualitative and quantitative changes, resulting in disappearance or shifting of the minima. This happens in very short time scale (shorter than reaction time); as a result, forces act on the carriers/atoms and move them.

- Carrier excitation
- Thermalization
- Carrier removal
- Thermal and structural effects



- Carrier excitation

If the photon energy is larger than the band gap, single photon absorption process dominates in exciting the valence electrons to the conduction band. If the semiconductor has an indirect band gap such as Silicon (*Si*), the absorbed optical photon can still excite the valence electron, but here the assistance of a phonon would be necessary (for the momentum conservation). As the coherence between the electromagnetic field of the radiation and the excitation disappears (due to scattering), and bonds break, the carriers become free. The free carriers can be absorbed into the conduction band. This results in an increase of energy in the free carriers plasma. In the case of carriers with energies higher than the bandgap, it is possible to generate more free carriers through the impact ionization.

The photo-absorption process could be linear or nonlinear. This is simply influenced by the duration of the pulse. In the case of long pulses, the linear photo-absorption process takes place. Where the photon gets absorbed and the photo-absorption happens as a result of the Beer-Lambert-law. Whereas in the case of femtosecond optical laser pulses of the same fluence intensity, the absorption follows a nonlinear process. Main active processes in the case of the *fs* laser pulses are impact ionization, tunnel ionization and multiphoton ionization [18], [19], [20], [21], [22], [23], [24], [25], [26], [27], [28].

- Thermalization

Carrier-carrier scattering or carrier-phonon scattering takes place as soon as the free carriers are generated. Carrier-carrier scattering doesn't change the total energy in the excited carrier system, but rather causes dephasing which can take place within a 10 *fs* timescale. Whereas approaching the Fermi-Dirac distribution would take 100s of *fs*. In contrast, carriers lose or absorb energy and momentum by scattering with phonons [29]. Through this interaction energy of carriers can decrease due to spontaneous phonon emission. Since phonons can carry very little energy, it may take several picoseconds to achieve thermal equilibrium between lattice and carriers [30].

- Carrier removal

Before the thermal equilibrium is reached a state exists where carriers and lattice are in equilibrium at a defined temperature, but the density of free carriers is more than at in thermal equilibrium. At this stage, the excess free carriers disappear via electron-hole recombinations or escape from the excited region and defects. In the case of recombination, one of two processes will occur; either the excess energy will be emitted in the shape of a photon (Luminescence), or it will have enough energy to kick an electron out from an upper shell in the conduction band (Auger

process). Excess energy will be spent on the removal of carriers from the surface when defects or surface recombinations occur. The increase of free carriers density will lower the band gap.

- Thermal and structural effects

At this stage, the lattice and free carriers are at the same temperature, and the excess free carriers are removed from the material. Reaching this thermal equilibrium state may take some picoseconds, but the excess carriers removal takes place over a longer time. If the lattice temperature goes above the melting or boiling point, the material can become melted or vaporize away. This happens over longer timescales, more than few tens of picoseconds. In the case of evaporation or melting, the temperature drops down via resolidification. This, however, doesn't mean that the material turns back to the original structure or phase [29]. In the event of no phase transition, the temperature drops down to ambient temperature in microseconds.

## 5.2 X-ray FEL light, matter interaction

X-ray photons, exposing the matter, either get absorbed or scattered away. It is possible that X-ray photons get elastically or inelastically scattered instead of being absorbed. The elastically scattered photons have no energy change. This process is called Rayleigh scattering, which happens when the particle has smaller dimensions than the radiation wavelength, and the scatterer has enormous mass (infinite). This is when photons scatter off the bound electrons. The nucleus is heavy enough to act as the required large mass. In the case of free electrons, the elastic scattering can only occur if photons have low energy to let quasi-elastic scattering happen.

The inelastic scattering of photons off a free electron (charge particle) is called Compton scattering. In this process, the incoming photon interacts with the charged particle and get scattered with a different wavelength and with the angle of  $\theta$ . Hence, an electron with an energy difference of scattered and initial photon energy gets scattered away.

Studies show that in damage process with *fs* FEL pulses, the photo-ionization has a maximum cross section compared to the scattering processes like Compton scattering, which play a minor role in the damage process [31], [32], [33], [34], [35].

Photo-ionization is the leading process in the interaction of *fs* laser pulses with matter both in the case of the optical laser (depending on the photon energy, the incoming energetic photon has enough energy to kick an electron out of the bond system) or in the case of the X-ray FEL. X-ray photons have high enough energy to ionize the atoms and kick electrons out of the bound state. The X-ray photons, also, can attenuate deep (up to few  $\mu m$ ) inside the matter.

High energy (around or above core level energy state) X-ray photons interact with inner shell electrons of atoms. This could result in the ejection of a core level electron, which can be refilled with an electron from an upper-level shell and the emission of another photon called fluorescence photon or another electron from the atom, which is called the Auger electron. This process takes place during the pulse. The ejected Auger electron (in the case of low  $Z$  materials, this is the dominant process) or fluorescence photon will have a defined amount of energy and will interact with surrounding atoms inside the material through different processes. In other words, the Auger electron, as an example, causes further electronic excitations, e.g., electron excitation from the valence band into the conduction band, even from deep shell electronic state or through impact ionization. They also could get elastically scattered away or even skip out of the medium from the surface (see Fig: 5.2). On the other hand, they might just excite an atom. In this case, the atom would get back to the normal inert state by emitting a photon or phonon, depending on the energy of the whole system. All these processes can get categorized as secondary processes. The energy of the emitted photoelectrons depends on the photon energy of the initial photon (of the incoming beam) and also the binding energy in the atomic system (see Equation 5.1). The number of photons, which are interacting with the matter (a higher or lower flux of photons) in each pulse, the energy of each photon and the binding energy of the electrons have a significant impact on changing the interaction intensity and the damage level.

$$K_E = h\nu - \phi - B_E \quad (5.1)$$

If the free electron absorbs high enough energy from a photon to ionize another electron from an atom, there will be two free electrons available in the system. These two can absorb energy from incoming photons (as free carriers) and undergo the same cycle. This process continues and produces a high rate of free carriers in what is called avalanche ionization.

Optical laser avalanche ionization is mainly an active process for the laser intensities below  $10^{12} \text{ W/cm}^2$ . Avalanche ionization, in the sense of cascades via electron impact ionization, is the dominant channel for free-electron production for the case of X-rays [36].

The impact ionization occurs on the femtosecond time scale. In contrast, the elastic scattering of photons as an example takes place over a longer time scale (typically in picosecond time scale). In the case of Carbon for the impact ionization as an example, the minimum amount of energy need is around the indirect bandgap ( $E_e > 4.8 \text{ eV}$ ) [36]. Another effect which can occur is the inverse-Bremsstrahlung, in which the free electron in the presence of an ion interacts with the X-ray photon without ionizing another electron from the system. One can say that the electron absorbs energy from the beam during the collision with an ion. This collision result in an electron-positron pair production [37], [30], [36]. Inverse-Bremsstrahlung is a complicated process, more pronounced in lower X-ray energies and lower electron temperatures. For X-ray, direct photo-absorption by free electrons (or inverse-Bremsstrahlung) is negligible, as the deep-shell photo-ionization is the dominated processes in this

case.

If  $N$  photons strike a bound electron (each with an energy of  $h\nu$ ), it seems that the electron is facing a photon with  $Nh\nu$  energy and  $\lambda/N$  wavelength, in multiphoton ionization. If the energy is high enough the electron will become free and the atom ionized. The intensity at which multiphoton ionization mainly takes place is  $10^{13} \text{ W/cm}^2$  [38]. Photons should have a minimum amount of energy to be able to ionize the valence electrons to the conduction band.

Tunnel ionization (a process in which electrons in an atom (or a molecule) pass through the potential barrier and escape from the atom/molecule) mainly takes place when the intensity is higher than  $10^{15} \text{ W/cm}^2$ . The multiphoton ionization and tunnel ionization are sometimes called strong electron field ionization. It is important to mention that the peak brightness in case of FEL is of the order of  $10^{14} \text{ W/cm}^2$  in general norm [38]. The temporal number of free electrons, ionized by the direct photo-ionization (photo-absorption), electron impact ionization and Auger-like processes, increases during the *fs* FEL pulse very fast. The impact ionization collision time can be estimated around  $10^{-16} \text{ s}$ . In comparison to visible light, the impact ionization is the first dominant process, and the Auger-like process is the second dominant processes in the free secondary electron production process [36] (see Fig 9.7).

Bloembergen, Perry, and Du and co-workers conducted several studies on laser-induced damage of alkali halides, fused silica, and some other dielectric materials by using nanosecond and picosecond laser pulses [40], [38], [25], [41]. Investigations and studies show in the case of femtosecond laser pulses; several different processes are involved in the damage process. Among these are Coulomb explosion [42], thermal melting [42], [43], plasma formation [43] and material cracking caused by thermoelastic stress [44], [45](see Fig 5.2). While the underlying physics may be totally different, all cases have a critical energy density (where free electron density saturates), at which damage occurs. At this stage, the reflectivity is at maximum state (see Eq 5.2).

The state at which matter is in the form of a mixture of positive ions and negatively charged particles is called plasma. Since the invention of laser, creation of plasma in matter has been studied [46], [47], [48], [49]. It is believed that when the ionization is completed, the free electron density is comparable to the ion density of about  $10^{23} \text{ cm}^{-3}$  [50]. The critical density (see Eq 5.2) is the free-electron density when the plasma oscillation frequency equals the laser frequency

$$n_{cr} = \frac{\pi m_e c^2}{e^2 \lambda^2} \quad (5.2)$$

Where  $m_e$  is the electron mass,  $c$  speed of light,  $e$  the electron charge and  $\lambda$  the laser wavelength. The importance of critical density in the interaction of electromagnetic waves with plasmas becomes apparent when considering the dielectric function of the plasma. This is given by

$$\epsilon_w = 1 - \frac{\omega_{pe}^2}{\omega(\omega + iv_m)} \quad (5.3)$$

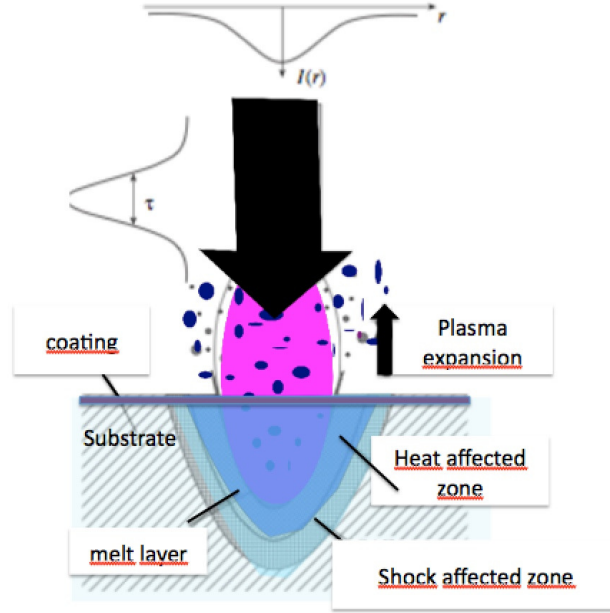


Fig. 5.2.: Very simple schematic of the matter and X-ray FEL beam interaction [39]. The incoming beam has its temporal and spatial dimensions depicted in the picture with the Gaussian profiles on the top and the side. The material is undergone photo-ionization processes. Some free carriers escaped from the surface, and hot plasma of free carriers is created inside the material at the beam affected zone. The heat affected zone shows the region where the heat gets diffused into and the shock affected zone describe the area where the high pressure starts to induce shock waves. There is a thin layer right behind the heat-affected zone, which is showing the melted layer.

Where  $\omega_{pe}$  ( $rad/s$ ) is defined by  $4\pi N_e e^2 / m^2$  and  $\frac{N_e}{N_{cr}} = \frac{\omega_{pe}^2}{\omega^2}$ . The difference between Equation 5.3 and 4.24 lies within the fact that in the case of a plasma there are no bound electrons in the system. Studying the Equation 5.3 also shows that if the frequency goes higher than the plasma frequency there would be no absorption and the material becomes transparent to that radiation.

Dielectric function of plasma determines both the refractive index and absorption of electromagnetic waves within the plasma [51], [52], [53]. Hence, changes in the dielectric function lead to changes in material properties (reflection and absorption, or, e.g., dielectric to metallic state).

### 5.3 Ablation

The concept of material removal in laser interactions depends on several factors such as material properties, laser intensity, pulse duration, wavelength, and the number of pulses. When the material is transformed into an absorbing plasma, it shows metallic properties. The laser plasma interaction causes a phase change of the bulk material. Without existing free electrons, the process of ablation does not take place [54].

There exist two ablation mechanisms (regimes), distinguished by their pulse durations. In the case of long pulses (longer than 100 *ps*), the ablation proceeds in equilibrium conditions. The damage fluence threshold, in this case, increases with pulse duration. The interaction of the pulse with matter is different depending on the type of matter. In the case of metals, ablation occurs at very low intensities, whereas in the case of dielectrics this process is very weak at low intensities. All possible processes like the electron-to-ion energy transfer, the electron heat conduction, and therefore the hydrodynamic or expansion, appear to take place over a longer time scale (equilibrium conditions) compared to the case of *fs* pulses.

In the case of *fs* pulses, the laser matter interaction appears to take place with the matter with constant density.

Since energy transition from the electron to the lattice with regard to sub-picosecond pulses (*fs* or faster) takes place on a time scale of 1 – 10 *ps* (which is longer than the pulse duration itself), therefore the ablation proceeds in non-equilibrium conditions and the conventional hydrodynamics motion does not occur during the femtosecond interaction time. One can say the electrons cool down without transferring energy to the lattice. Because the electron heating rate is much greater than the rate of energy transfer to the lattice. Hence, in latter case the ablation doesn't depend on the pulse duration [52], [53], [51], [55], [56], [57].

The laser ablation is sometimes mentioned as laser induced breakdown [38]. Among several existing theories [52], [53], one states that multiphoton ionization supplies seed electrons, while avalanche ionization is still responsible for the ablation. For pulses shorter than 100 *fs* the ionization process is governed by the multiphoton ionization. Some theories [52], [53], [58], [59], [60], [61] based on analytic models and Boltzmann equations (distribution), given by  $n_c = n_e e^{(e\phi/K_B T_e)}$  with  $T_e$  as electron temperature and  $n_c$  as electron density (while ignoring ion motion) and experimental measurements, confirm that multiphoton ionization dominates free electron generation at intensities on the order of  $10^{14}$  *W/cm<sup>2</sup>*. After the critical density is created, Bremsstrahlung and resonance absorption play a significant role in absorbing energy.

If the intensity is much higher than the threshold fluence, then it is possible that the vaporization process occurs. Where the electron-phonon collisions increase the local temperature above the vaporization point.

Another parameter which plays a role in ablation in the case of the ultrafast pulses is the Coulomb explosion at intensities near the ablation threshold fluence in dielectrics [14], [62]. Since electron-to-ion energy exchange time, as well as the heat conduction time, is much longer than the pulse duration, the ions remain cold during that process. Hence, excited electrons escape from the surface of the bulk materials and form a strong electric field that pulls out the ions from within the impact area.

In high-density plasmas, the electron-ion (e-i) interaction leads to ionization, excitation, and reduction of the electron temperature. However, elastic collisions can also lead to absorption, where a photon is absorbed by a free electron which is excited to a more energetic continuum state in the Coulomb field of an ion. This "absorption through collisions" is often referred to as inverse

Bremsstrahlung [49], [63], [64], [65], [66], [67], [68], [69], [70].

In general, one can say that energy transfer from electron to ions occurs in  $ps$  time scale. Hence, it's mainly deposited in a small layer in electron-photon interaction process. Therefore, during the pulse, heat conduction and hydrodynamic motions are negligible and thermal damage (micro cracks or shock affected zone) and the heat affected zone are also reduced regarding short  $fs$  pulses [71].

## 5.4 Time scale of X-ray light-matter interaction

The pulse duration declares how long the energy is deposited into the matter. The deposited energy gets absorbed mainly through photo-ionization.

The photo-ionization cross-section as a function of energy for different materials is found in literature [15]. The ionized electrons and ions, as well as phonons, distribute the deposited energy inside the matter. This type of interaction occurs in  $1 - 10 ps$  and is categorized as thermal conduction. X-ray photon absorption decreases the number of bound electrons, therefore the number of free electrons increases, the system heats up, and the absorption capabilities of the matter decrease. With increasing X-ray intensity, ionization of bound electrons increases and the material becomes more and more transparent to the X-ray absorption.

The whole X-ray absorption process including the photo-ionization and secondary processes such as Auger electron ejection etc. happens in the very short time scale up to  $100 fs$ . Phonons are also a result of the interaction of the emitted electrons with atoms inside the material. The recombination of electrons and ions is among all the processes which take place during the interaction process [72]. After a sufficient time in  $ps$  regime, the number of electrons and ions and the temperature of the system is high enough to have a hot plasma consisting of electrons and ions. The system gets into a state that tries to reduce the heat and return to a thermodynamic stable state. Part of the hot plasma gets depleted from the matter and part distributed inside the bulk. At this point, craters appear, which usually have a size bigger than the beam size. This is because of the secondary processes and the heat transfer inside a volume within the bulk.

Basically, for short pulses (sub- $100 fs$ ), the ionization processes are much more efficient during the pulse than the recombination processes such as Auger-like recombination of the valence-band hole or fluorescence. In contrast, if the pulse is very long, there is enough time for all those processes to happen, even the recombination process possibly taking place during the pulse. The excited matter transforms into a thermodynamic equilibrium state of materials. A consequence of X-ray interaction with matter is an increase in temperature, pressure and ionization, all inducing stress and stress gradients in the material.

To stabilize the system, these can all lead to a phase transition in the material. Among different types of phase transitions, one can mention Solid-liquid, liquid-gas, solid-gas as well as solid to plasma transition.

## 5.5 Length scale of X-ray light, matter interaction

In optical *fs* laser, the depth to which radiation would drill was estimated to be very close to skin depth. Since the incident electric field decreases exponentially, the skin depth increases logarithmically with fluence [53]

$$d_{eV} = \frac{l_s}{2} \ln \frac{F}{F_{th}} \quad (5.4)$$

with  $l_s = \frac{c}{\omega k}$  ( $k$  taken as the imaginary part of refractive index) represented as skin depth (field penetration depth),  $F_{th}$  fluence threshold and  $d_{eV}$  as the crater depth. Another part of the studies shows that the heat wave propagates inside the matter to a depth less than the skin depth during the pulse. This comes from the energy transfer between the electrons to ions in solid which occurs with a frequency almost matching the plasma frequency of electrons [53], [60]. The characteristic heat conduction time is given by

$$t_{th} = \frac{l_s^2}{D} \quad (5.5)$$

Where  $D$  is thermal diffusivity. Gamaly [50], [52], [53] demonstrated (in the case of thermal melting) electrons have no time to transfer the energy to the ions during the laser pulse  $\tau_{ei} > t_p$ . The target density remains constant during the laser pulse. Since the heat conductivity time is also much longer than the pulse duration, its not possible for electrons to transfer the heat out of the skin layer (except X-ray excited electrons which are fast). With the help of conventional thermal diffusion, one can get

$$t_{th} \approx \frac{l_e^2}{\kappa} \quad (5.6)$$

$$\kappa = \frac{l_e v_e}{3} \quad (5.7)$$

where  $\kappa$  is the coefficient of thermal diffusion and  $l_e$  and  $v_e$  are the electron mean free path and velocity, respectively. X-rays interact with matter in  $\mu m$  scale in normal incidence geometry. Therefore the interaction takes place in a large volume compared to other types of radiation. Worthy of note is the incidence angle which, alongside the optical properties of the material itself, plays a role in attenuation length. For instance, the attenuation length versus the photon energy in the case of amorphous carbon is depicted in Fig 5.3. The sudden drop is due to the ionization threshold of this element. The attenuation depth is not the only important factor, but also the path that electrons travel after they are ejected via the X-ray photons inside that material. The direction where those electrons travel depends on the electric field of the incoming radiation (on the polarization of the radiation). In the total external reflection geometry and XUV radiation case (where  $\sigma$  (see section 5.1) is positive, and  $\beta$  is nonzero for all materials), the electric field decays in exponential dependence on depth. As a result, the energy absorbed by the coating is deposited on the layer, a few nanometers below the surface, characterized by the absorption depth  $d_z$



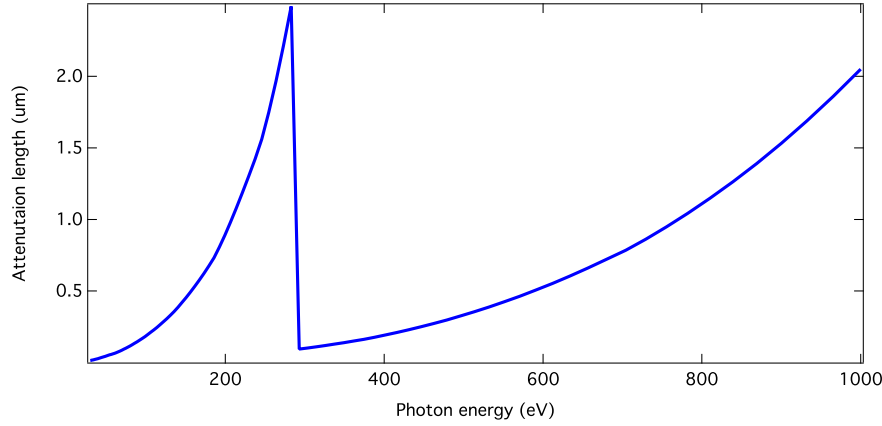


Fig. 5.3.: Attenuation length of X-ray radiation with different energies inside a thin layer of amorphous carbon with 2.2 ratio of  $SP^3/SP^2$  [15]. The drop is at the cutting edge at 284 eV.

$$d_z = (\lambda/16\pi\beta) \sqrt{(\sin^2\theta - 2 * \sigma + \sqrt{(\sin^2\theta - 2 * \sigma)^2 + 4 * \beta^2})} \quad (5.8)$$

Near the normal incidence this becomes

$$d_z \rightarrow \lambda/16\pi\beta \quad (5.9)$$

since the

$$\sqrt{(\sin^2\theta - 2 * \sigma + \sqrt{(\sin^2\theta - 2 * \sigma)^2 + 4 * \beta^2})} \sim 1 \quad (5.10)$$

Nevertheless, this formula does not take into account the electron transport [73], [74]. A simple way to consider electron transport effects is to sum the squares of the electron stopping power (energy range relation for electrons) [75]  $d_e$  and the absorption depth. Hence,  $d$  which is the interaction depth, is given by

$$d = \sqrt{d_z^2 + d_e^2} \quad (5.11)$$

The stopping power considers the interaction of the emitted electron with other electrons/atoms inside the material. If these electrons are highly energetic (short de Broglie wavelength) they interact with (single) atoms elastically which means that their direction of motion changes. If the emitted electrons do not have high energy and are slow, they interact inelastically with atoms (valence electron). Hence, they lose energy. The core level electrons do not take part in these interactions unless the incoming electron's energy is above the  $K$ -edge energy level (as an example higher than 284 eV in the case of carbon).

Under X-ray irradiation, the solid material tries to expand, but it is limited by the surrounding material. Therefore its expansion effort turns into stress

which is transported through the matter. The mechanical response is faster than the heat conduction inside the medium [76], [77], [62].

## 5.6 Absorbed energy per volume

The absorbed dose, sometimes also known as the physical dose, corresponds to the amount of energy absorbed per unit mass, from the deposited energy in the material at the time of exposure. Assuming that all the energy is absorbed within the volume limited by the attenuation length, dose is calculated with the Equation 5.12

$$D = F * (1 - R) / d * n_a e \quad (5.12)$$

The fluence (F) is defined in *SI* units by  $W/m^2$ . In damage studies, the fluence unit is usually defined by  $J/cm^2$ . The  $e$  is the electric charge ( $1.602 * 10^{-19}C$ ) and  $n_a$  the atomic density ( $1.10 * 10^{23} atom/cm^3$  in the case of a-C).  $R$  represents the reflectivity and penetration (absorption) depth as explained in last section is taken equal to the interaction (attenuation) depth  $d = d_z$  (This formula does not take into account the electron transport).

The amount of absorbed energy with respect to the beam footprint area decreases with a decrease in the incidence angle (from normal to lower than the critical angle). This happens because the cross section area of the beam irradiating the material increases when decreasing the incidence angle.

However, the dose is also affected by changes in reflectivity. Looking at reflectivity shows that, it decreases with decreasing angle from normal to grazing angles, which is an opposite effect compared to the absorption depth see Fig 4.2.

## Chapter 6

# Low-Z materials

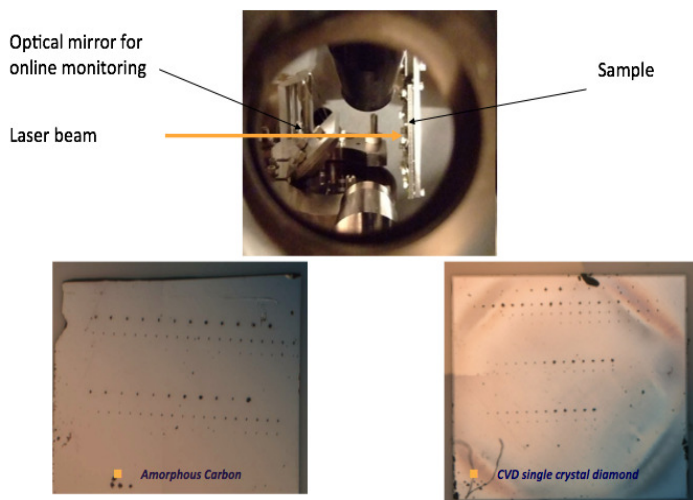


Fig. 6.1.: Maps of CVD diamond and amorphous carbon samples exposed with single shots at LCLS.

FEL, compared to a synchrotron in which just the average peak power is high, delivers a photon beam with high peak power and high brilliance. Hence, it's a challenge to design and construct the optical system for this type of facility. The challenge is to design the optical system in such a way as to preserve the beam quality (high peak power and brilliance) till the end station (experimental station) at the beamline.

The optical system at FEL is responsible for transport, focus, and dispersion of the radiation with as high precision as possible. Optical coatings on mirrors as well as monochromators are part of this optical system. Choosing a suitable coating has a huge impact on the beam transport process at these facilities. Light elements (low Z materials) show high reflectivity and low absorption over a wide wavelength range, which makes them preferred the candidate to be used for optical elements such as a coating on mirrors.

Carbon is among the low Z materials, and its absorption edge lies around 284 eV. Due to its high reflectivity, minimum absorption and high melting point, it is considered a possible coating material on XFEL optical mirrors.

The pioneer FEL, FLASH based in Hamburg, has also used carbon as a coating on its beamline mirrors. CVD Diamond has a high melting temperature, high breakdown electric field, a large band gap of  $5.5\text{ eV}$  and high chemical stability [78] and is considered to be a suitable candidate to be used as a single crystal monochromator's component. Among metals, Nickel is the only possible candidate examined during this Ph.D. project. Among multilayers, MoB<sub>4</sub>C has been considered as a possible coating and tested in the scope of this project.

The focus was on testing the behavior of a-C coated mirrors and the CVD diamond monochromators which are the main subject in the performed experiments and this chapter.

The study is divided in damage studies below and around carbon K-edge, higher than carbon K-edge energy regime, and at grazing and normal incidence angles

## 6.1 Properties of amorphous carbon

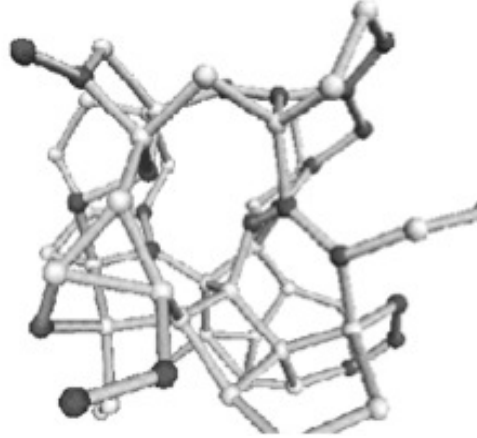


Fig. 6.2.: Snapshot of the 64 atom ta-C network. The heavy lines show the network of bonds; the 22 dark spheres depict threefold coordinated atoms ( $sp^2$  hybridized) and the 42 light spheres show the fourfold coordinated atoms ( $sp^3$  hybridized). The simulations were performed by N. Marks, (Dept of Applied Physics, University of Sydney) at the Max Planck Institute, Stuttgart [79].

Amorphous carbon (see Fig 6.2) is an allotrope of carbon, made up of a mixture of tetrahedral  $sp^3$  (Diamond-like) and trigonal  $sp^2$  (graphite-like) carbon in various ratios and very small ratio of  $sp^1$  (see Fig 6.3, 6.4). Diamond-like carbon has high  $sp^3$  content. Physical properties of a-C (such as mechanical and radiation hardness, biocompatibility, and chemical inertness) make it of high relevance in numerous domains ranging from X-ray optics to microelectronics [80], [81]. It can also be found as Hydrogenated amorphous carbon (a-C: H) or Tetrahedral amorphous carbon (T: a-C) which is diamond-like and doesn't have a crystal structure [82]. Melting threshold of carbon at  $3800\text{ K}$  is about  $0.98\text{ eV/atom}$  (estimated with simple formula  $E_{melting}=3K_B T_{melting}$ ).

Several different processes like annealing, irradiation by ions, electron and

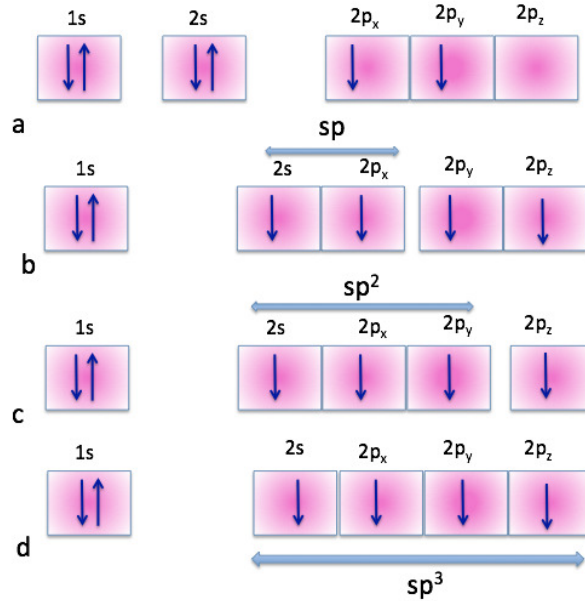


Fig. 6.3.: Electron configuration of carbon in ground state(a), excited hybridized state  $SP^1$ (b),  $Sp^2$ (c),  $Sp^3$  (d).

optical laser pulses could initiate the phase transition in a-C [83], [84], [85]. Studies show that the a-C structure in all those processes has been modified and formed a more ordered structure configuration (graphite), in other words, it has undergone a transition from an amorphous structure to a crystal structure [86], [87], [88]. The other interesting part of the process is the time scale of these phase transitions, in other words, if the process is a thermal or non-thermal or a plasma formation transition takes place or not. Depending on the type of experimental condition thermal or non-thermal processes might take place. In the case of the FEL process with short, intense pulses of  $fs$  time scale, the damage is categorized to be non-thermal (it takes place in very first 100 of  $fs$  of the illumination in the case of graphitization, and for Si this lies within the first 300-500  $fs$ ) through photo-ionization and thermal processes take place

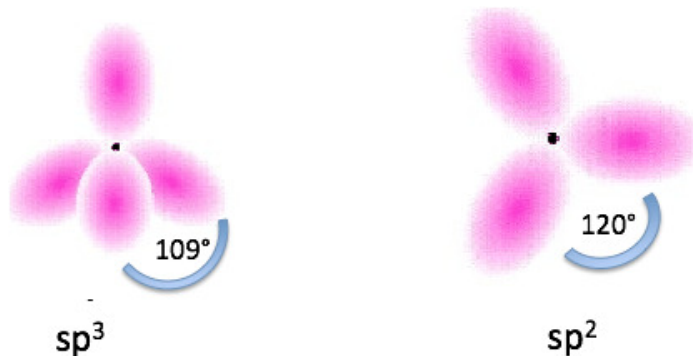


Fig. 6.4.: Orbital configuration of carbon  $Sp^3$ (mainly in Diamond),  $Sp^2$ (mainly in Graphite).

after some 100s of *ps* (see following chapters and discussion 8, 9).

## 6.2 Amorphous carbon preparation

Single layers of a-C were deposited on a planar well-polished silicon substrate in an ultra-high vacuum chamber at Helmholtz-Zentrum Geesthacht Centre for Materials and Coastal Research (HZG) via dc magnetron sputtering (chamber was designed at HZG). The thickness of the samples was usually kept constant to enable comparison of the results in a coherent way and also because the experiments were mainly focused on short wavelength induced damage on thin layers.

The sample thickness (depending on the wavelength at which the experiment was planned) was about 40–45 *nm* to 1.4  $\mu\text{m}$ . To compare the effect of radiation on bulk and thin layers of the a-C, coatings with different thickness were used. As an example one can mention the experiment at 177 *eV* at FLASH (see reference [16]).

Two magnetron sources, placed in the deposition chamber have a diameter of 7.6 *cm*. During the sputtering (coating) process, the substrate was rotating (to produce a uniform coating), and it was water cooled. The sputtering gas was the argon with high purity of 99.99999% *nm/s*. Sputtering pressure was of the order of 0.05–0.5 *Pa* and the base pressure was less than  $10^{-8}$  *Pa*. The deposition time varied between 0.02 and 0.2 *nm/s*, a computer driven shutter was responsible for controlling the deposition time. The manufactured films were analyzed via X-ray reflectometer. The reflectometry curves were simulated via D.L.Windt IMD program and compared with the results from the reflectometry experiments. The thickness and density of the films were also determined, e.g., the roughness of the 44 *nm* thin film was measured to be 0.5 *nm* [89]. For example, the roughness measurement performed via AFM on two different prepared coatings with 40 *nm* and 900 *nm* are presented in Fig 6.5. The 900 *nm* sample had an RMS roughness of 1.28 *nm*, the peak to valley value was 35.24 *nm* and maximum peak height has been determined to be 50.6 *nm* and the 40 *nm* sample's roughness was 0.4 *nm* RMS, the peak to valley value for this sample is 72.14 *nm* and maximum peak height was 80.5 *nm*. The bonding ratios of the films were characterized doing Raman spectroscopy. The ratio of  $Sp^3/Sp^2 = 0.2$  [90] and density of 2.2  $\text{g}/\text{cm}^3$  [91], [89] were determined.

## 6.3 CVD single crystal diamond

Diamond has a face-centered crystal structure (see Fig 6.6) and is a metastable allotrope of carbon. Compared to graphite, diamond has a less stable structure but it has a very strong covalent bonding of  $sp^3$  type (see Fig 6.3, 6.4). Diamond has the highest hardness and thermal conductivity of any bulk material.

Single crystal diamond samples used for the European XFEL damage experiments were provided by the ElementSix company. These crystals are manufactured through chemical vapor deposition (CVD) synthetics. They are produced

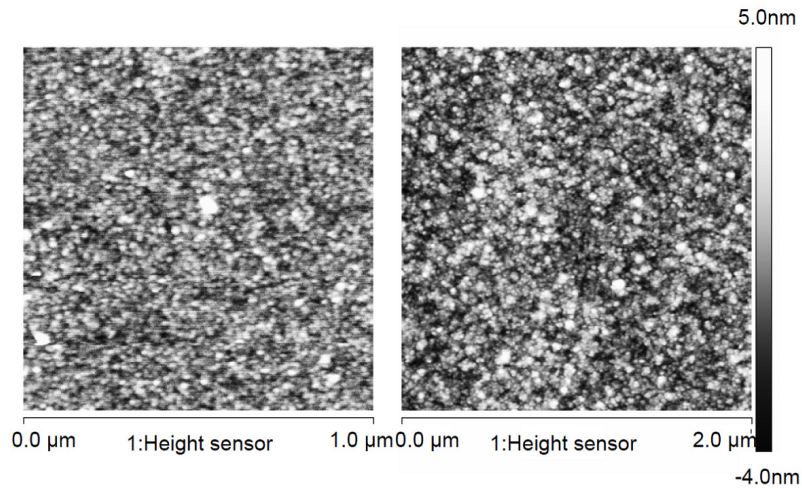


Fig. 6.5.: Measured surface roughness with AFM on (a) 40 *nm* thick aC coating and on (b) 900 *nm* aC coating on Si substrate. The 900 *nm* sample has an rms roughness of 1.28 *nm*, the peak to valley value is 35.24 *nm* and maximum peak height is 50.6 *nm* and the 40 *nm* samples roughness is 0.4 *nm* rms, the peak to valley value for this sample is 72.14 *nm* and maximum peak height is 80.5 *nm* [16].

in high purity and are transparent in the UV-THz regime. They have high thermal conductivity and low absorption coefficient, hence suitable for optical applications. The CVD type employed in our experiments is 4.5 x 4.5 *mm*, 0.5 *mm* thick plates with,  $\langle 110 \rangle$  edges. They have low nitrogen content and are polished with precise laser cut edges [93].

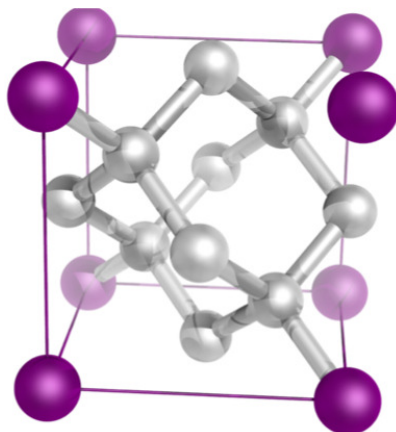


Fig. 6.6.: Sketch of diamond crystal [92].





## Chapter 7

# Experimental technique

X-ray FELs are the source of short pulses, high-peak-power, and high-brilliance photon beams. This fact makes it challenging to construct the optical system for such facilities. These properties can render an optical element useless in a fraction of a second. Besides, it is possible to face new damage mechanisms that degrade optical components in the X-ray beamlines in comparison to storage rings/synchrotrons (at synchrotrons high average power load is the possible source of damage to optical elements). The characteristic properties of FEL facilities around the world differ from each other with regards to the wavelength range, peak brilliance and pulse parameters at which they operate. Therefore, the study of the damage mechanism at those different facilities is helpful to gain a vast knowledge of this process.

In this chapter, different characteristic parameters of various FEL facilities are briefly described. Special attention is dedicated to FLASH, where most of the experiments of this work were performed at. The experimental set up which was developed at FLASH for the most recent experiment with 4.6 *nm* wavelength (the wavelength varied between 4.7 *nm* and 4.5 *nm*. This probably was due to the two upstream carbon coated mirrors present in the beamline. Carbon mirrors are very sensitive around the carbon K-edge (at 4.37 *nm*). These mirrors absorb the radiation inside the water window and are therefore unsuitable for use at these wavelengths.) is described in more details in this chapter. Later in the chapter, the experiment's parameters at other facilities (at those experiments were performed) will be given.

### 7.1 FLASH Beamlines and baseline instrumentation

FLASH source runs at a maximum repetition rate of 10 *Hz* with 800 pulses in 800  $\mu s$  long bunch trains [5], [94]. The beam can be distributed to the direct or the monochromator branch. The branches leading to beamline 1 (*BL1*), *BL2* and *BL3* utilizes the direct FEL beam. The three end-stations offer different focusing schemes leading to more or less intensely collimated FEL beams. The beam is distributed to the different *BLs* by switching one or two plane mirrors. An attenuation system based on gas absorption and a set of four gas monitors are used for the beam intensity and beam position determination before it gets

branched into different *BLs*. A variable line spacing spectrograph available at each *BL* could monitor the beam spectrum parallel to user experiments.

To provide high degrees of reflectivity, avoid the risk of damage due to the high peak powers and minimize deformation of the mirrors at long bunch trains, very shallow incidence angles of  $2^\circ$  and  $3^\circ$  were chosen [5]. Damage experiments (for this work) at FLASH were done at two of the existing beamlines: *BL2* (see section 7.1.1) and *BL3* (see section 7.1.2). Each is equipped with ellipsoidal mirror with the focal point at  $2\text{ m}$  focal distance.

The fast shutter available at the beamlines behind the ellipsoid mirror makes it possible to work with single pulses.

Each of the experimental stations can be combined with a synchronized femtosecond optical laser system in a laser hutch and a THz source generated by an additional undulator through which the FLASH electron beam is passed. Both can be combined with FEL pulses for femtosecond time-resolved pump-and-probe experiments with a time resolution of  $100\text{ fs}$  [5].

### 7.1.1 *BL2*

*BL2* [5] is equipped with ellipsoidal mirrors which generate focal sizes of  $\sim 20 - 30\ \mu\text{m}$  (FWHM). High-density carbon coated mirrors ( $0.5\text{ m}$  long) have a low surface roughness, less than  $5\ \text{\AA}$  over the full mirror length. The almost constant high reflectivity of these coatings was the reason for choosing them [5]. At *BL2* there are 3 carbon coated mirrors available with grazing incidence angles of  $2^\circ$  and  $3^\circ$ . At the experiment time (in 2008/2009) the transmission of the beam-line was calculated via reflectivity calculations considering each of the 3 plane amorphous carbon (a-C) coated mirrors in the beamline using the CXRO website [15]. During the experiment, samples were mainly placed in focus position. The focus spot size (smallest) was found to be  $5\ \mu\text{m}$  corresponding to the maximum achievable fluence of  $50\text{ J/cm}^2$ .

### 7.1.2 *BL3*

*BL3* beam-line [5], which was used for our experiment in May 2011, is equipped with 2 plane nickel mirrors and 3 plane a-C coated mirrors (1 focusing mirror with a  $2\text{ m}$  focal point and 2 reflecting mirrors). The mirrors work under the grazing angles of  $2^\circ$  and  $3^\circ$  respectively. To obtain a Gaussian-like beam shape, circular apertures of various diameters ( $1, 3, 5$  and  $10\text{ mm}$ ) were placed upstream to the focusing mirror and the gas monitor detector.

The focused beam FWHM is typically on the order of  $20\ \mu\text{m}$ , the unfocussed beam size  $5\text{--}10\text{ mm}$  (depending on wavelength). Users can install their own optics if needed. A back-reflecting multilayer mirror on this beamline makes it possible to vary the beam from a non-focused beam with  $\sim 10\text{ mm}$  to  $\sim 2\ \mu\text{m}$  radius (we didn't use the multilayer mirror in our experiment). Hence, it is possible to study a broad range of scientific fields (e.g. plasma physics, cluster science or materials research) [95], [96]. In the experiment close to the carbon K-edge, the pulse duration was on the order of  $125 \pm 25\text{ fs}$ , where the electron bunch was  $300\text{ pC}$ . The wavelength during this experiment had an absolute

uncertainty of 0.1  $nm$  for the beam wavelength of 4.6  $nm$  and the bandwidth shot-to-shot fluctuation was found to be negligible (see ref [94], [97]). The average energy per pulse was typically in the range of 10–90  $\mu J$  with peak values up to 170  $\mu J$ . The maximum repetition rate was 10  $Hz$  and the 800  $\mu s$  long bunch train contained 800 pulses.

### 7.1.3 Gas monitor detector

One of the common elements in all the beamlines is the gas monitor detector, known as GMD, which allows one to measure the pulse energy. The GMD used in our experiments was developed at FLASH. It was optimized for the current and future X-ray free electron laser facilities for shot-to-shot measurements. It has an online determination of the beam position and a temporal resolution better than 100  $ns$ . The relative standard uncertainty of the photon pulse energy was measured to be better than 10 % (dominated by the inherent statistical shot-to-shot fluctuations of an SASE-FEL like FLASH). The photon beam position was measured to be below 20  $\mu m$ . All these mentioned above were achieved at a quality checking test of this device [98]. An upgraded version of the device for the hard X-ray regime, X-GMD, was presented with a signal amplification up to  $10^6$  by means of an open electron multiplier for ion detection, which was tested at LCLS. There are four GMDs available at FLASH beamline construction, which are also used to determine the beam position for each pulse. Two of these are placed at the end of the accelerator tunnel and two others are in use at the beginning of the experimental hall. Between these two sets, a 15  $m$  long gas attenuator reduces the FEL intensity by many orders of magnitude without changing the accelerator parameters

Since the GMD detector (at FLASH) is located before the optical elements of the beamline, one should consider the beamline transmission after the optical element, in order to get the correct pulse energy values. The GMD is based on photo-ionization of a low-density noble gas or  $N_2$ , creating ions and electrons which are detected by a Faraday cup [98], [99] (see Fig 7.1).

$$N = N_{ph}n\sigma l \quad (7.1)$$

Where  $N$  is the number of electrons or ions and  $N_{ph}$  is the number of photons. The  $n$  represents the target density,  $\sigma$  the photo-ionization cross-section and  $l$  is the length of interaction volume.

Typically the ion signal, calibrated at a synchrotron storage ring with an uncertainty of 4%, was averaged over 25  $s$ .

The electron signal was used to get (measure) individual pulse energies. The electron signal was calibrated by comparing its average to the average ion signal. Hence, the relative pulse fluctuations are dominated by the inherent statistical fluctuations of the FEL pulse intensities during the calibration and less than 1% for pulses of more than  $10^{10}$  photons.

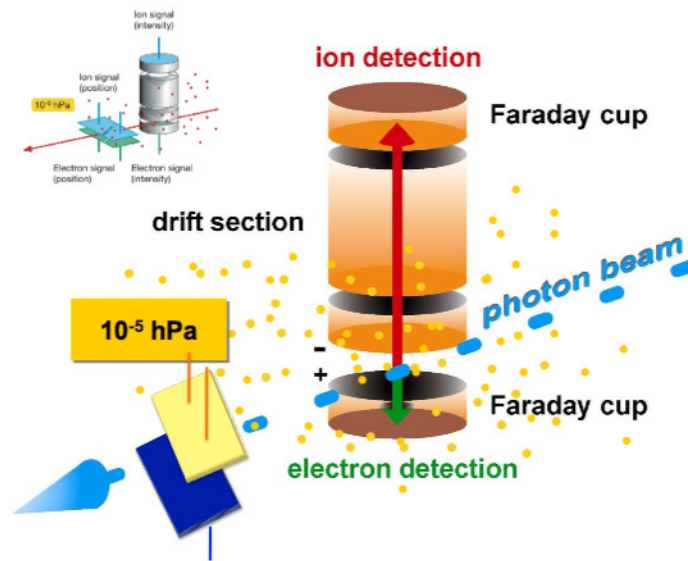


Fig. 7.1.: Schematic view of developed GMD at FLASH [85]. A Faraday cup counts the electrons and ions that are produced as the FEL pulse passes through the ionization chamber containing nitrogen or rare gases at very low pressure. After the faraday cup there are the two split electrodes to determine the horizontal position of the beam.

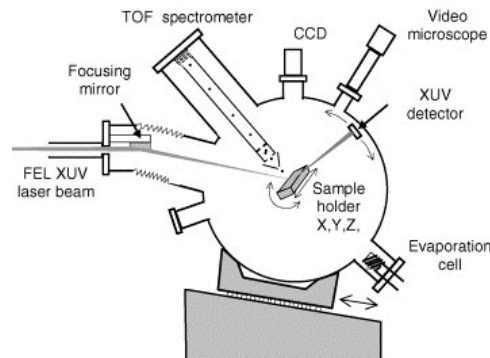
## 7.2 Dedicated set up for damage experiments

A spherical ultra high vacuum experimental chamber, specifically dedicated to the damage experiments, was built in 2005 [94]. This chamber is known as Free-Electron Laser Interaction with Solids (FELIS) and has been upgraded several times and recently modified for the experiment in 2011 at FLASH at a wavelength close to carbon K-edge (see Figs 7.2, 7.4).

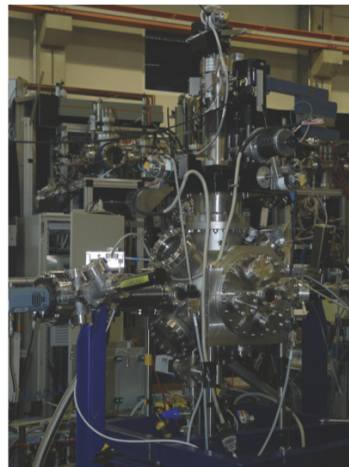
There are several ports and windows available on it, which permit the attachment of devices like the sample holder which is attached to the motorized manipulator, various number of detectors, optical elements, vacuum pumps or viewport, etc.

The vacuum level in the chamber is adjusted via different vacuum pumps. A turbo pump reduces the vacuum down to  $10^{-7}$  mbar and by means of an ion pump, the minimum achieved pressure is  $10^{-9}$  mbar [97].

The experimental chamber as a whole body (including the sample holders manipulator and detectors), is mounted on an adjustable stand. The stand allows precise alignment of the primary experimental axis with respect to the incident FEL beam. The best irradiation position was where the focus is the best and the beam has its best spot size in the focus. By moving the chamber position via the stand in the beam direction, one can change the spot size of the beam (beam fluence).



(a)



(b)

Fig. 7.2.: (a): Draft of the FELIS experimental chamber at FLASH in Hamburg in 2005 [94], [100]. (b): The FELIS experimental chamber modified for the damage experiment in 2011 at FLASH in Hamburg

### 7.2.1 Sample holder

The sample holder (see Fig 7.3) is made of stainless steel with holes to fix the samples to it. Its dimensions are  $150 \times 60 \text{ mm}^2$  and thickness of  $5 \text{ mm}$ . In order to get a higher flatness, the sample holder was mechanically polished and attached to the sample manipulator. The center of the sample holder is at the approximately center of the experimental chamber [97].

The sample holder is attached to a motorized manipulator. This manipulator gives the degree of freedom to move the sample holder in X, Y, Z directions and allows rotations around the vertical axis perpendicular to the incoming beam direction. This configuration makes it possible to run angularly resolved measurements. The translation in the different directions is used to move the point at which the sample will be irradiated. The translation ranges are  $5 \text{ cm}$  and  $10 \text{ cm}$  in the directions perpendicular and parallel to the rotation axis, respectively. The Z-axis of the manipulator is aligned parallel to the primary experimental axis, which is defined by the center of two flanges (so called entrance and exit flanges for the FEL beam depicted in Figs 7.4, 7.5).

The samples were fixed onto the sample holder and were almost all the

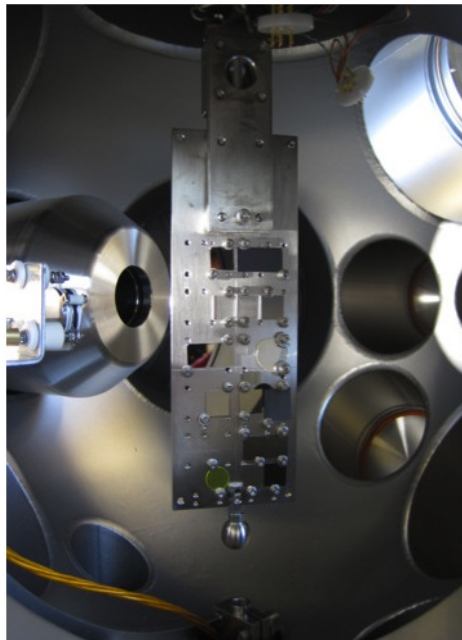


Fig. 7.3.: View of the inside of the chamber from the sample holder with mounted samples on it.

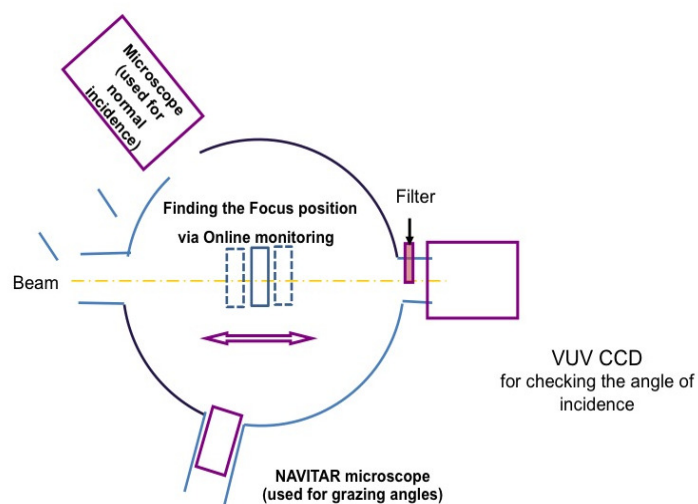


Fig. 7.4.: Schematic view of the inside of the chamber, illustrating the sample positioning.

same size. Typically  $10 \times 10 \text{ mm}^2$  or  $10 \times 20 \text{ mm}^2$ , up to a few mm thick (see Fig 7.3, 7.7).

### 7.2.2 Detectors

Several different in-situ diagnostics elements and detectors are mounted on the experimental chamber through flanges. These are: Multi channel plate (MCP), CCD camera, diodes, video microscopes, time-of-flight detector of emitted charged particles, optical spectrometer, pump-and-probe set-up and XUV radiation detectors (see Fig 7.5). All detectors and view ports are mounted on vacuum flanges (16 flanges are available in total) and are directed to the interaction point in the center of the experimental chamber. Due to a modular construction, the choice of the detectors can be adjusted to the specific experimental requirements. It is also possible to get a pump and probe set up installed to do time resolved microscopy.

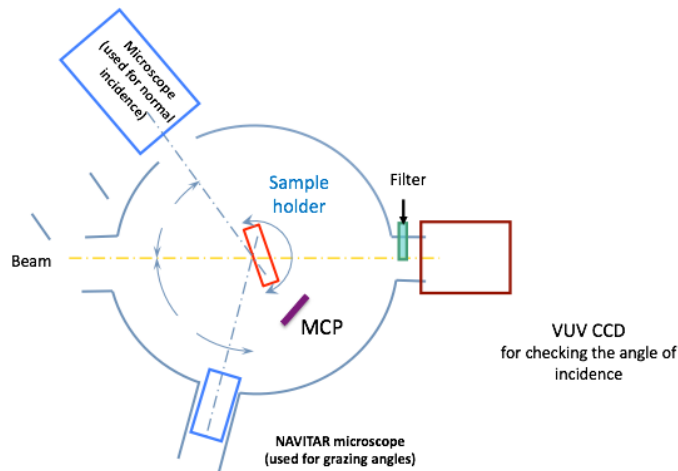


Fig. 7.5.: Schematic view of the inside the chamber with the sample rotation axis.

#### MCP detector

The intensity of the scattered light has been measured by a Chevron-type Multi Channel Plate (MCP) detector, which was installed inside the chamber. The effective area of the MCP is  $1 \text{ cm}^2$  and there was no aperture installed in-front of it. Since MCP has been mounted on a rotational arm, it could rotate with the sample. Hence, it was possible to perform the angular resolved measurements (see Fig 7.5). A  $1 \text{ GHz}$  oscilloscope without any amplification, was used to measure the electrical signal of the MCP. In order to optimize the signal of the oscilloscope the MCP's bias voltage was adjusted to approximately  $1400 \text{ V}$ .

The detector was tested with use of the unfocused beam by correlating the pulse energy measured by the GMD with the amplitude of the MCP signal (see Fig 7.6). MCP and GMD signals roughly correlate. The limited correlation is

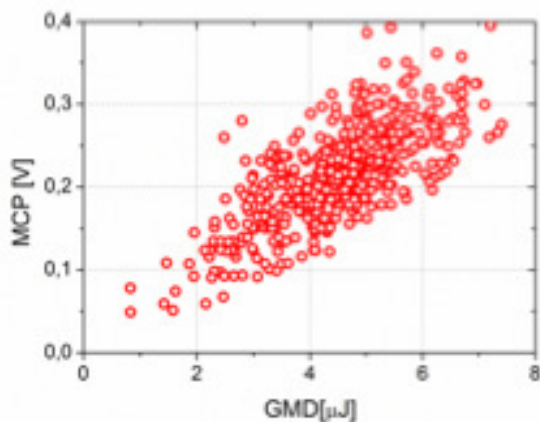


Fig. 7.6.: Correlation of the pulse energy measured by the GMD with the amplitude of the MCP signal when sample was exposed to 500 pulses attenuated below the multi shot damage threshold of Si sample [97].

most probably caused by the pointing instability of the FLASH beam which results in irradiation of slightly different places from shot to shot [97].

### XUV CCD camera

The XUV CCD camera was used to monitor the position of direct or reflected beam. It was mounted at the beams exit flange at the back side of the experimental chamber. To avoid saturation (or in extreme cases damage), thin foils in front of the detectors were used as attenuator. Furthermore, the photocurrent was measured during irradiations as the ionizing FEL radiation leads to the emission of electrons from the samples (Fig 7.4, 7.5).

### Optical spectrometer and time of flight detector

An optical spectrometer and time of flight detector (TOF) were used to observe the fluorescence and plasma emission. Electrons, ions and charged clusters of atoms emitted from the irradiated samples were detected and analyzed with respect to their masses and energies with the TOF. It is possible to measure the energy spectra of particles (ions and electrons) with the energy ranging from a few  $eV$  up to few  $KeV$ . Detailed information on the design of the TOF can be found in the ref [94]. The ionizing radiation, like XUV photons, can lead to the emission of electrons from the samples. An oscilloscope was directly connected to the sample holder via a wire and measured the photocurrent.

### Video microscopes

In order to position the samples with respect to the beam and surface monitoring, the two long video microscopes were involved. The focus beam diameter on the sample was of the order of  $5 \mu m$ . Hence, a high resolution-imaging device



for microscopic imaging ( $1 - 2\mu m$ ) was necessary. The inlet flanges were used to minimize the working distance.

### 7.3 Alignment and experimental protocol

Starting the experiment needs precisely aligned experimental elements and components. These steps can be summarized as follows: Alignment of experimental chamber, determination of the samples' coordinates, finding the focus position and the calibration of the grazing angle.

Alignment of the chamber axis means that the center of the chamber should approximately be at the focus position. This procedure is done in two steps: pre-alignment, using optical laser light and final alignment. In our case, a He-Ne laser beam which is collinear with the FEL beam served this task. During this process, the motors of the manipulator were kept in the middle of their travel ranges. At this point, the two online microscopes were used. In this way, the height and the horizontal position of the chamber were aligned. Here the position of laser light on the sample holder was observed while the chamber was transported on the stand. If the spot position was always seen unchanged and static, that point was the best alignment position.

Further, the offset angles for the rotational motor on both sides of the sample holder were calibrated (the read-out of the motors position while the He-Ne laser beam was under normal incidence angle to the holder's surface). Similar alignment procedures were repeated using the FEL beam and plasma emission from metals or fluorescence from a Ce: YAG crystal.

The samples were mounted on the sample holder in the clean room. Each sample was given a defined coordinate system with a horizontal and vertical axis (see Fig 7.7), lying in the plane of the sample's surface. This made it possible to have a map, on which one can picture the movement of the FEL beam on the surface of the sample. The sample holder was then, mounted on the manipulator. The manipulator's angular and height accuracy are respectively better than  $0.1^\circ$  and  $100\ \mu m$ .

The focus of the beam on each sample was examined by studying the imprint of the beam on a PMMA sample (see Fig 7.8). At different positions with respect to the chamber, imprints were made and observed by means of online microscopes. The focus shape changes due to astigmatism at different positions. The best focus position was where the imprints were most circular in shape.

As the samples have all a certain thickness, this could effect the best focus position. Hence, their thickness was measured and taken into account while positioning them. An optical microscope with accuracy better than  $50\ \mu m$  was used for this purpose, where the depth of focus was measured.

In order to control the angle of the incident beam on the sample, the offset angle to rotate the motors had to be found. The angles normal to the sample's surface and the normal to the samples holder are collinear and the offset angles for a rotational motor were the same.

Finding the correct grazing angle is done via the following steps. In order to measure the direct beam position, a charge coupled device (*CCD*) was mounted

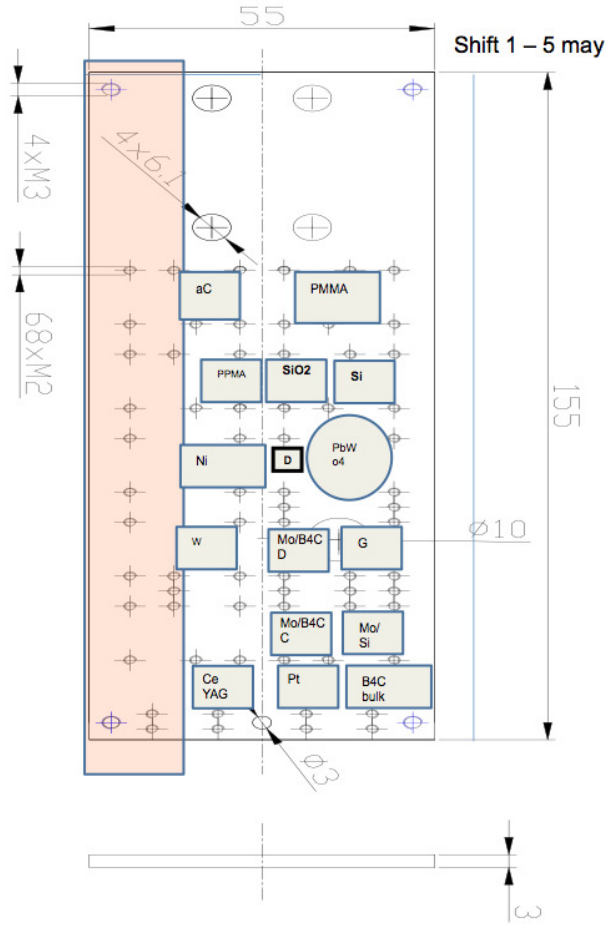


Fig. 7.7.: Schematic view of the sample's position on the sample holder, they were given an x and y position regarding their position on the sample holder.

behind the sample holder. By inserting the sample in the beam it was possible to measure the position of the reflected beam on the *CCD*. The distance between the sample and the *CCD* measured as "a" and the horizontal distance between the straight and the reflected beam was noted as "b" (see Fig 7.9). The grazing angle can be calculated by

$$(b/a) = \tan(2\alpha) \quad (7.2)$$

The next step was to compare the angle with the rotational motors position and the offset angle for the given sample was calculated with an accuracy better than  $0.1^\circ$ . Here, the flatness of the samples is an important factor, which had to be considered. For selected samples, we measured the offset angles at different positions. It was found out, that in almost all cases the samples flatness (variations of the offset angles) was better than  $0.1^\circ$  (with one exception of  $0.3^\circ$ ).

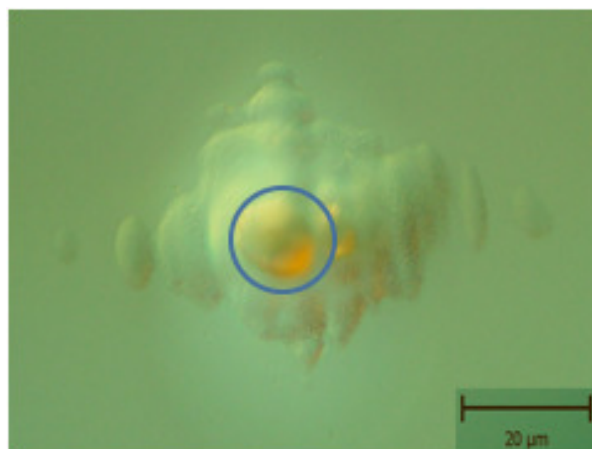


Fig. 7.8.: PMMA 5  $\mu\text{m}$  was shot at 13.5 nm at FLASH (11-08-2008) to find the beam size and focus point, the highlighted area is taken to be the beam area and it was measured to be 101.4  $\mu\text{m}^2$ .

### 7.3.1 Sample irradiation procedure

After positioning the samples under the focus of the beam at the proper angle, the irradiation was initiated. This means that through the specific filters or just by tuning the gas attenuator the pulse energy was tuned and the fast shutter was used to expose the samples to single shots (or multiple shots). Here the steps are defined by the user. The coordinates at which the shots should be made and motors should move to are given to the motors beforehand. The exposure time could also be changed. During FLASH experiments the pulse duration mainly is about 30 fs but in the previous experiment performed in the frame of this work in 2011, it was upgraded to 125 fs. In order to make sure

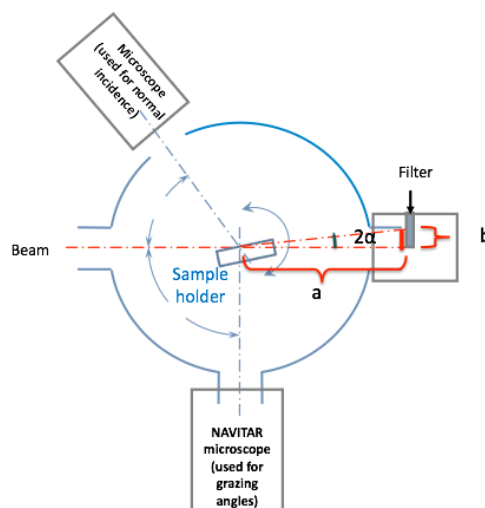


Fig. 7.9.: Schematic view of the inside of the chamber showing the angle determination

everything works properly before starting to irradiate the sample with single shots, whether at the beginning of the line or at one of the corners of the sample (at edge), several shots (multi shots) were done as marker (see Figs 7.10, 7.11).

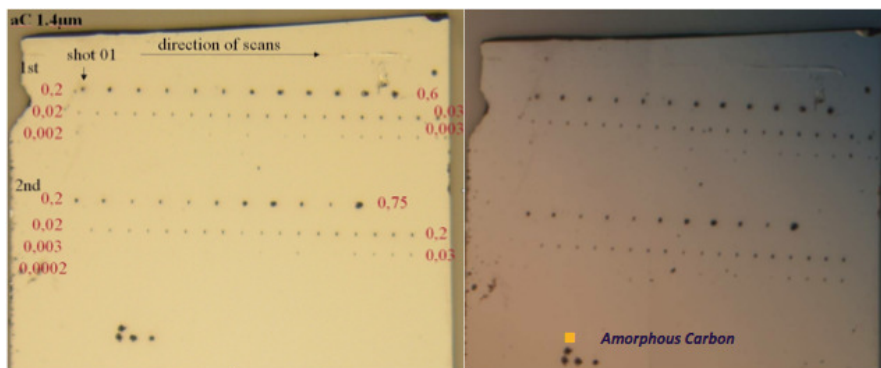


Fig. 7.10.: Maps of amorphous carbon sample with  $1.4 \mu m$  thickness, exposed to single shots at LCLS 2009 with  $830 eV$ . On the left side, one can see the picture taken from the sample after the shots. The numbers (names) of the lines are marked and the shot direction as well. The right pic is the image of the sample itself after the shots are made. The pictures are taken via Nomarski microscope.



Fig. 7.11.: Marker on the map of amorphous carbon sample with  $890 nm$  thickness, exposed to single shots at FLASH 2008 with  $177 eV$ . Scale size on the bottom right side is  $20 \mu m$ .

It's important to know which damage spot has been made by which amount of pulse energy. Hence, simultaneously, a map of shots in written format was prepared by hand while doing the shots, where the number of lines and the beginning of each line is recorded in writing. It's also important to have specific signs, giving hints where shots start and where do they end. Besides the number of shots in each line, the time at which experiment starts and ends on each sample should be documented. The online microscopes allow monitoring the appearance of damage and adapting the pulse energy. The image of one of the damaged samples is depicted in Fig 7.10.

wavelength ( <i>nm</i> )	pulse energy ( $\mu J$ )	pulse length/ <i>fs</i>	line band- width	max repetition rate ( <i>Hz</i> )	beam di- vergence ( <i>mrad</i> )
51	10	100	1%	60	0.2
60	30	100	1%	60	0.2

Table 7.1.: Characteristic parameters at SCSS in Japan 2010. [101]

After the experiment was finished the samples were taken out, transported to assembly lab for postmortem studies. The irradiated samples were then examined using the optical microscope with differential interference contrast - DIC (with Nomarski prism) to confirm whether the pulse energy range went beyond the damage threshold level for each sample or not. This will be explained in the section 7.5.1.

In multi shot irradiation mode, the samples were exposed to many FEL pulses at the same position. In general, the irradiation procedures are similar to the ones of the single shot exposures. It is important to reduce the pulse energy well below (more than one order of magnitude) the surface modifications threshold energy for single shot exposures and to minimize the energy fluctuations. Otherwise, due to stochastic nature of the radiation, a single pulse with high energy could exceed this limit and would result in different final structural changes of the sample. Another important requirement is that of beam stability. Two apertures at a large distance were used to define the optimal direction of the beam resulting in minimization of the spot position variations in the sample. The irradiated spots were investigated after the beam time with similar techniques as in the case of single shot exposures [97].

## 7.4 Setup at other FEL sources

In addition to the experiments performed at FLASH, several experiments were performed at other FEL sources. In this section, these setups will be briefly described.

### 7.4.1 Soft X-ray setup at SCSS

The experiments at wavelengths of 51 and 60 *nm* (24, 20 *eV*) were performed at the SCSS (Spring8 Compact SASE Source) light source. These experiments were single shot experiments in which the maximum pulse energy went up to 10  $\mu J$  for 51 *nm* and up to 30  $\mu J$  for 60 *nm* wavelength. The characteristic parameters are given in Table 7.1. The beam size was measured using two different methods: scanning a pinhole and ablation analysis. An image showing the setup used for this purpose is shown in Fig 7.12. The position of the GMD and gas attenuator are shown in Fig 7.13 and the beamline design in Figure 7.14. The fluence was varied using an argon gas attenuator and solid thin Tin (Sn) filter. The pulse energy was measured with GMD. The postmortem analysis were done ex-situ. The chamber used in this experiment is depicted in Fig 7.14.

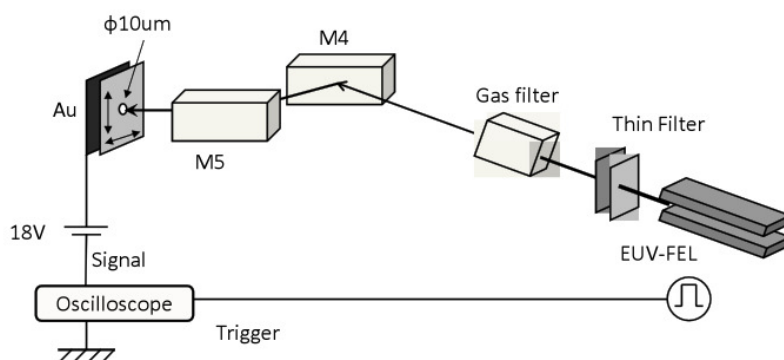


Fig. 7.12.: Scanning pinhole structure designed for the SCSS in Japan in 2010 [101].

#### 7.4.2 LCLS Atomic, Molecular and Optical Science (AMO)

This soft X-ray beamline at LCLS provides intense ultra-short soft X-ray pulses, generated by the free electron laser. AMO is designed to minimize losses and deliver the maximum possible X-ray intensity to the interaction region. In order to maintain the high peak brightness of the LCLS X-ray pulse, a minimal set of optics is used to deliver the beam to the target in the AMO instrument. Figure 7.15 gives an overview of the design of the beamline and its parts. There

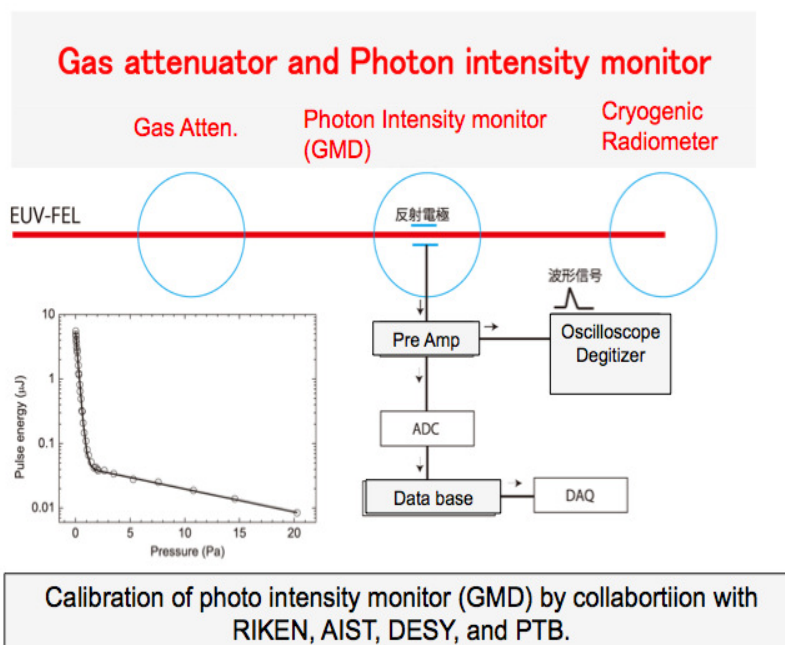
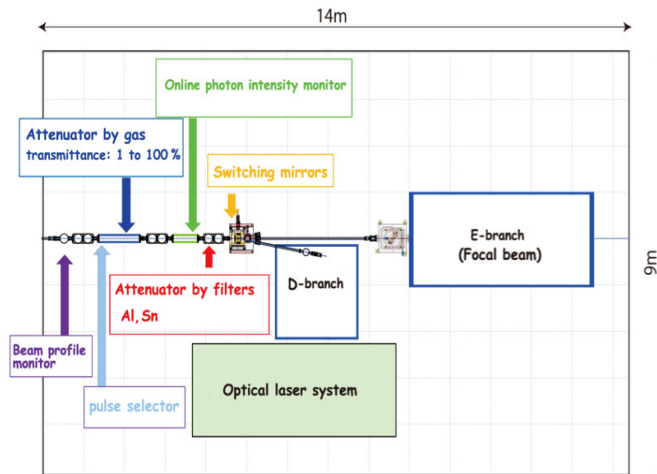


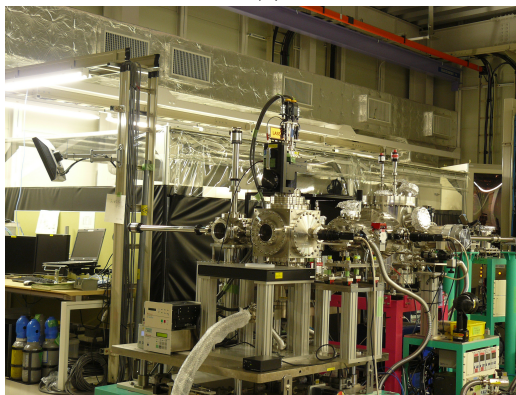
Fig. 7.13.: Gas attenuator and Photon intensity monitor at SCSS in Japan in 2010 [102], [103], [101].



(a)



(b)



(c)

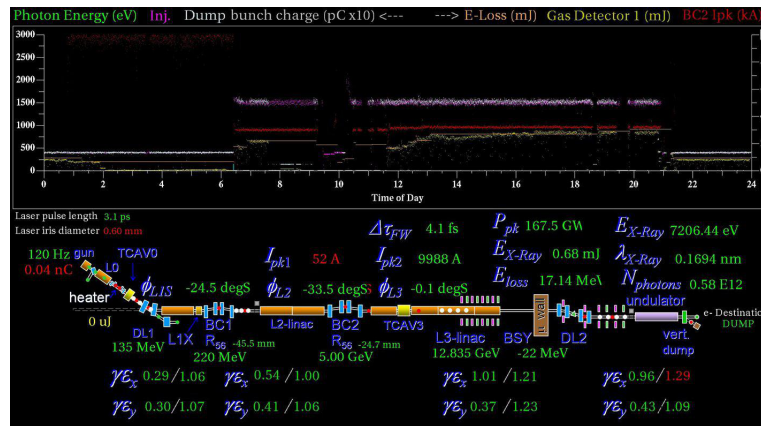
Fig. 7.14.: (a): Design of the experimental beamline at SCSS in Japan [101]. (b): The experimental beamline and chamber. (c): The experimental chamber.

were 5 B4C coated mirrors (3 flat and 2 curved, KB focusing mirrors) installed. The angle of incidence was  $14.5 \text{ mrad}$ . In addition to the three soft X-ray offset mirrors (SOMS) that deliver the beam to the soft X-ray branches, two planar-elliptically bent Kirkpatrick-Baez mirrors are used to focus the beam to approximately  $1 \mu\text{m}$  in the first interaction region within the high-field physics chamber. The mirrors can be bent to various radii, allowing the focus to be moved along the beam or the size of the beam in the interaction region could be varied as desired for the experiment. At the more downstream interaction region in either the CAMP chamber or the Diagnostics chamber, foci's of  $\sim 3\text{--}5 \mu\text{m}$  can be achieved [104].

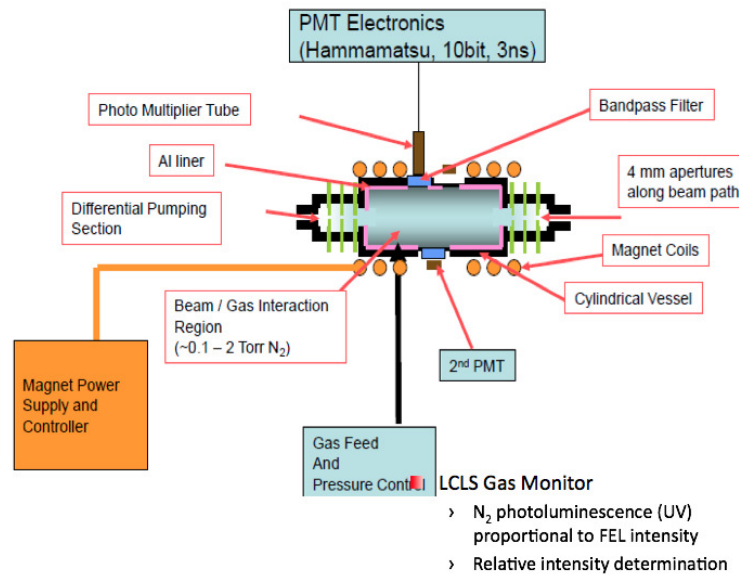
In the case of this work, the damage experiment performed at this beamline ran at the first commissioning time. At this time the FLASH Gas monitor detector based on ionization of rare gasses was used (see Fig 7.15).

A Faraday cup was installed right behind the focusing mirror [105], which was used to detect the photoelectrons and photo-ions. The other purpose of the experiment was to compare the FLASH designed Gas monitor and the alternative gas monitor based on photoluminescence (see Figs 7.15, 7.1) in nitrogen designed by Livermore IOF. Hence, after the comparison, the photoluminescence detector was used for reading the pulse energies here. The attenuators are far upstream in the beamline design.





(a)



(b)

Fig. 7.15.: (a): The structure of the AMO beam-line at LCLS [104]. (b): The Gas Monitor at AMO beam-line at LCLS based on the photoluminescence process [106].

## 7.5 Damage characterization

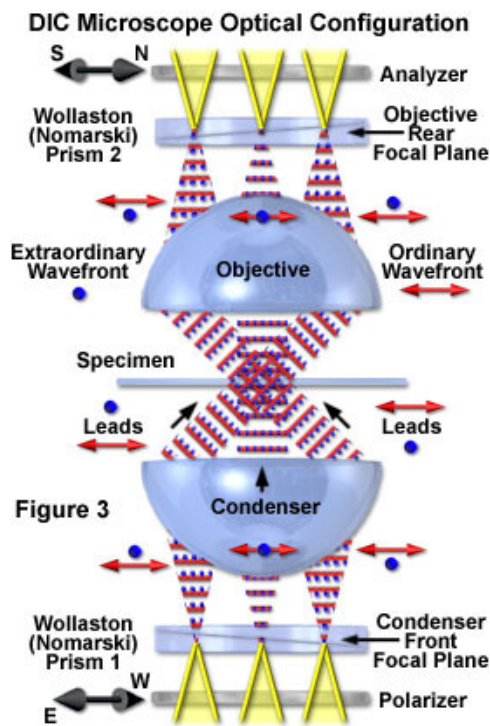
After experiments, several ex-situ nondestructive postmortem studies on the samples were performed. The effects of irradiation were investigated using different types of analysis techniques. One of the great challenges of these analyses is to perform measurements on micron-sized structures (the typical diameter of the damaged spots). Two main types of techniques can be distinguished:

- surface analyses providing information on the shape/morphology of the irradiated spots
- structural analyses providing information on phase transitions or structural changes

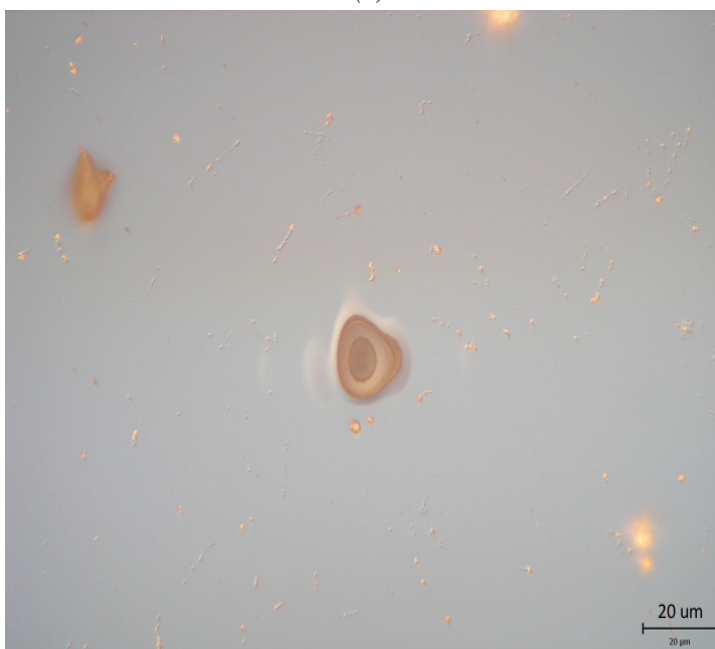
### 7.5.1 Nomarski Microscope

Differential interference contrast microscopy (DIC), also known as Nomarski Interference Contrast (NIC) or Nomarski microscope, works on the principle of interferometry to gain information about the optical path length of the sample, to see otherwise invisible features. The phase contrast first was developed by Frits Zernike in the 1930s. The basic differential interference contrast (DIC) system, first devised by Francis Smith in 1955, is a modified polarized light microscope with two Wollaston prisms added, one to the front focal plane of the condenser and a second at the rear focal plane of the objective. Several years later, Georges Nomarski, a Polish-born French physicist, modified the standard Wollaston prism configuration to enable the exceedingly thin optical components to be physically located away from the aperture conjugate planes [107].

The wave pairs (see Fig 7.16) employed in differential interference contrast are generated by the action of a birefringent beamsplitter (either a Wollaston or Nomarski compound prism) on a plane-polarized wavefront of coherent light originating from a tungsten filament and focused into the front focal plane of the microscope condenser (where the beamsplitter is positioned). When a pair of coherent light rays produced by the beamsplitter encounters a phase gradient, due to the refractive index and/or thickness variations, each ray will become deformed and experience a slightly different optical path difference when traversing through the specimen. Upon emerging from the specimen, the rays will be unequal in phase. The difference in the optical path is translated by the DIC microscope into a change in amplitude in the final image observed through the eyepieces. However, from simply examining the image, it is impossible to determine whether the phase gradient in the specimen occurs because of differences in refractive index or thickness (or both). This uncertainty is due to the fact that optical path difference is derived from the product of refractive index and thickness. Hence, lacking independent information about either quantity is the origin of the fact that the difference cannot be ascertained. An image of a damaged spot on a-C took via Nomarski microscope is depicted in Fig 7.16, clearly the different colors and color tones show the damage spots and their sizes and changes from the undamaged part.



(a)



(b)

Fig. 7.16.: (a): Idealized schematic diagram of the major components and light pathways through a typical DIC microscope optical train [107]. (b): A DIC microscope image taken from a damage spot on a-C (890 nm thick on Si substrate) sample. The sample was exposed to a single pulse with 4.83  $\mu\text{J}$  energy at FLASH. The experiment was performed at 91 eV photon energy. The scale is 20  $\mu\text{m}$ .

## 7.5.2 Atomic Force Microscopy

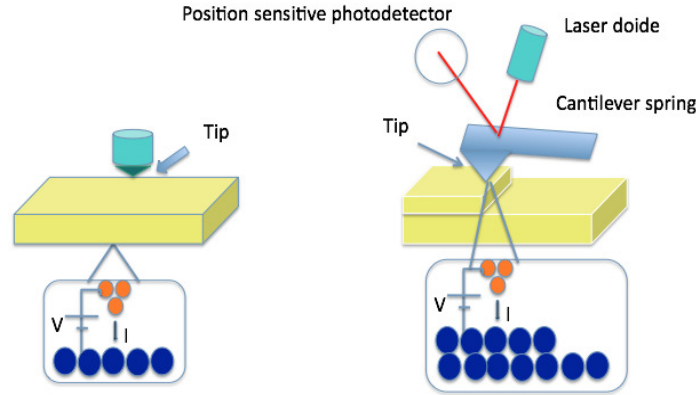
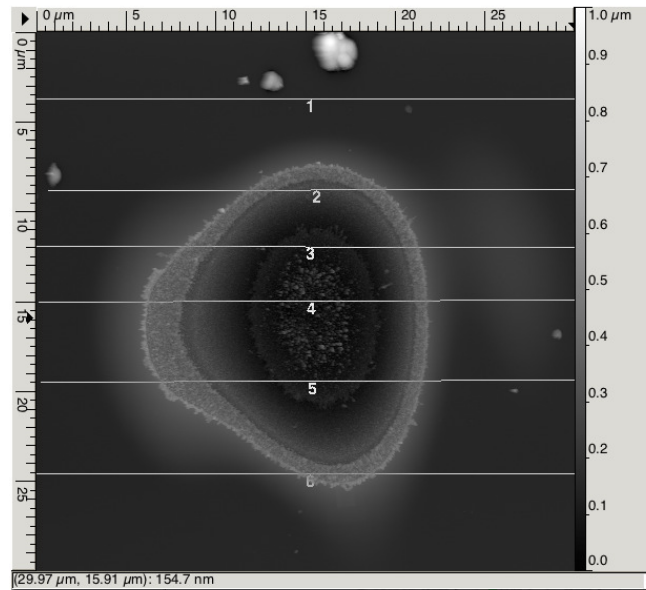


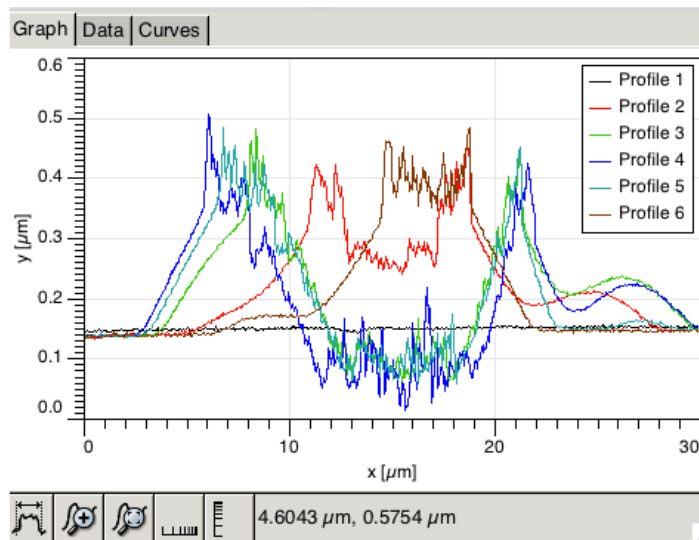
Fig. 7.17.: Simple schematic of Atomic Force Microscopy spectroscopy.

The Atomic Force Microscope (AFM)(depicted in Fig 7.17) is a tool with which one is able to have a closer look at the area of damage with a resolution less than  $0.1 \text{ nm}$ , showing the material extrusion [108]. Most AFMs use a laser beam deflection system nowadays, introduced by Meyer and Amer, where a laser is reflected from the back of the reflective AFM lever and onto a position-sensitive detector. The Atomic force microscope relies on the forces between the tip and sample, knowing these forces is important for proper imaging. The force is not measured directly but calculated by measuring the deflection of the lever and knowing the stiffness of the cantilever. Hooks law gives  $F = -kz$ , where  $F$  is the force,  $k$  is the stiffness of the lever, and  $z$  is the distance the lever is bent. AFM measurements providing a 2D depth map of the low fluence irradiations show the formation of a bubble-like damage or craters. Finding of the changes of the roughness can provide us information on the effect of electronic dynamics inside the matter and providing information on the reflectivity changes. The AFM measurements were done at different institutes.

The facilities belong to Physics department of University of Hamburg (Laser Institute and Experimental institute) and CFEL institute at DESY in Hamburg. Measurements were done in scanning mode at CFEL. An example of this type of measurement is depicted in Figure 7.18. AFM images of a damaged spot on a-C at SCSS with  $4.8 \mu\text{J}$  pulse energy are depicted in Figs 7.19, the photon energy was at  $24 \text{ eV}$ . The White Light Microscopic (WLM) image of this spot is depicted in the section 7.5.4 to give an idea and comparison of the two techniques.

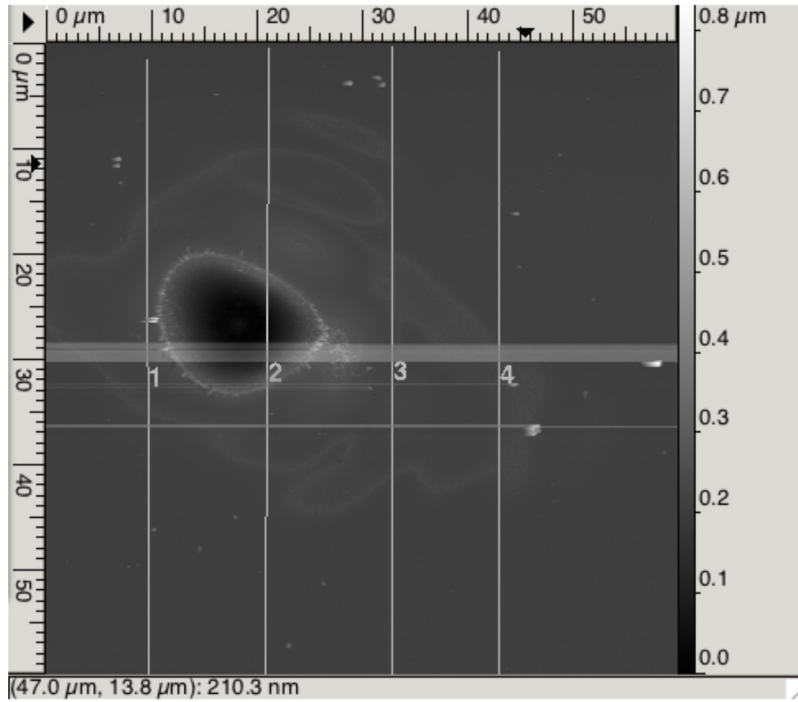


(a) AFM profile image of a-C sample damaged at FLASH at 91 eV photon energy, with 2.97 uJ pulse energy. The coating was 890nm thick. The profile lines are numerated.

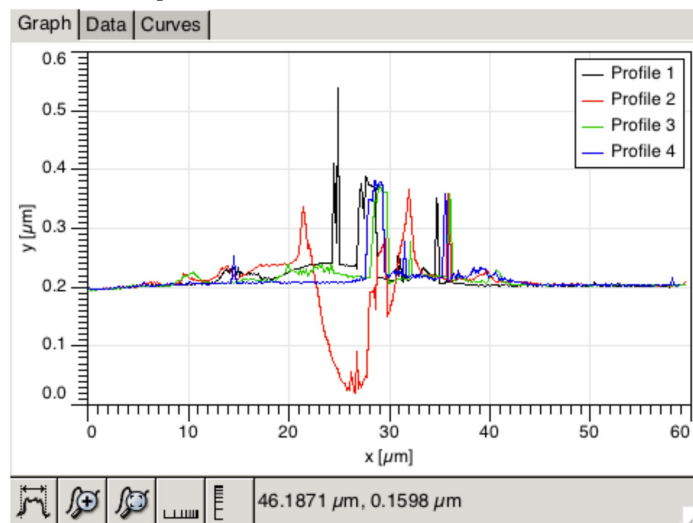


(b) AFM measured profiles depicted here.

Fig. 7.18.



(a) An AFM image of the damage spot on a-C (50 nm thick on Si substrate) sample. The sample was exposed to a single pulse with 4.8  $\mu\text{J}$  energy at SCSS Japan. The experiment was performed at 24 eV photon energy. Lines present where the profiles are measured.



(b) Its measured Profile.

Fig. 7.19.

### 7.5.3 Raman scattering

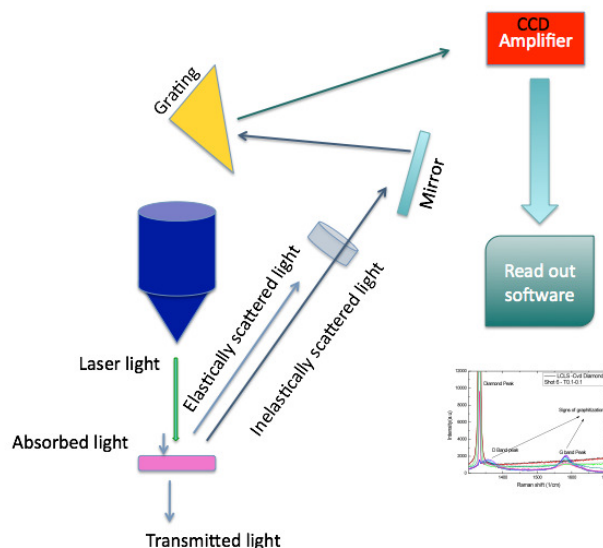


Fig. 7.20.: Simple schematic of Micro-Raman spectroscope.

Raman scattering is named after Indian physicist C. V. Raman who discovered it in 1928. The technique is used to study changes in chemical bonding (see Fig 7.20). The incident photon excites one of the electrons into a virtual state. If the molecule gets excited from the ground state into a virtual energy state, then relaxes into a vibrational excited state, this will generate the Stokes Raman scattering. If the molecule is already in a vibrational excited state before scattering and it ends in the ground state afterward. The detected wavelength would have a shorter wavelength, which is called the anti-Stokes scattering. Raman scattering can be described as the inelastic scattering of photons by phonons due to the change of polarization caused by the phonon mode. Changes in molecular polarizability or deformation of the electron cloud with respect to the vibrational coordinates will result in observing the Raman effect. The Raman intensity is defined by changes in amount of polarizability and the Raman shift by the vibrational level. The analysis were performed with a micro-Raman spectrometer (Renishaw Ramascope, model 1000 ) coupled to an optical microscope focusing the  $\lambda = 514.5 \text{ nm}$  laser beam to a  $2 \mu\text{m}$  spot diameter. At  $514.5 \text{ nm}$  the  $sp^2$  [109] have a much higher scattering rate compared to  $sp^3$  bonds [110]. Measurements were performed on several samples from each experiment at FLASH, LCLS, etc. A Raman spectrum of the amorphous carbon sample, which was damaged via a single shot with the pulse energy of  $6.50 \mu\text{J}$  at FLASH with a photon energy of  $177 \text{ eV}$  is depicted in Fig 7.21. The G and D peak lie at around  $1560$  and  $1360 \text{ 1/cm}$  respectively (for visible excitation).

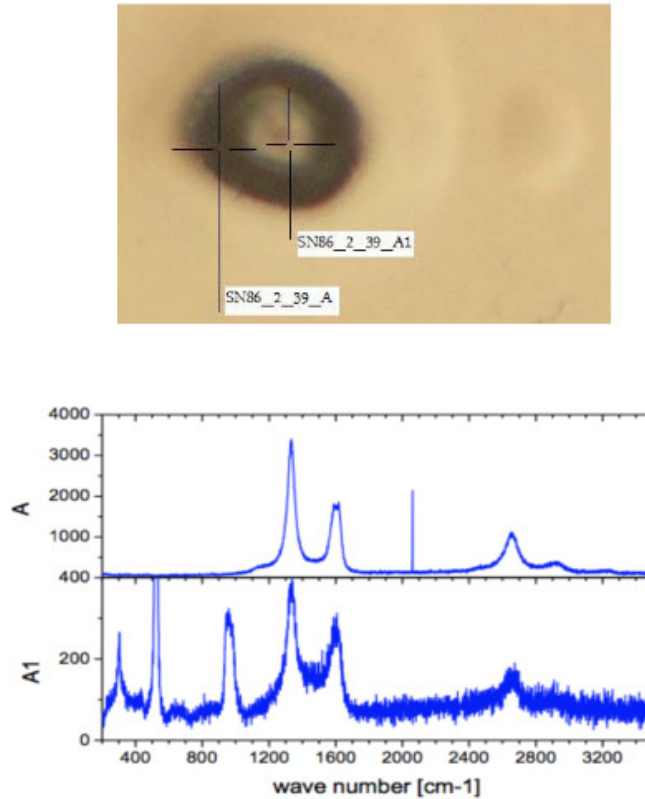


Fig. 7.21.: Top: Raman spectrum taken on the point marked as "A" on the amorphous carbon coated sample (890 nm thick on Si substrate) exposed to the 177 eV beam with single shot of 4.8  $\mu\text{J}$  at FLASH. Marked points show the coordinates on which Raman data were taken. Bottom: Raman profile spectra showing the position and width of D, G, G' and T peaks (see section 8.5).

#### 7.5.4 White light interferometer

This topography measurement is based on a technique called white light interferometry that scans the surface height of the test object. To achieve this, a beam splitter divides the beam coming from a white light source into two parts. The reference beam is reflected from a reference plane while the measurement beam is incident on the test object. When changing the distance between the sample and the interferometer, optical interference occurs at every point of the surface where the optical path length is exactly the same for the reference and the measurement beam. During the vertical scan, the interference patterns are captured by the video camera while the software computes the topography from this data. The white light interferometer used at European XFEL Lab



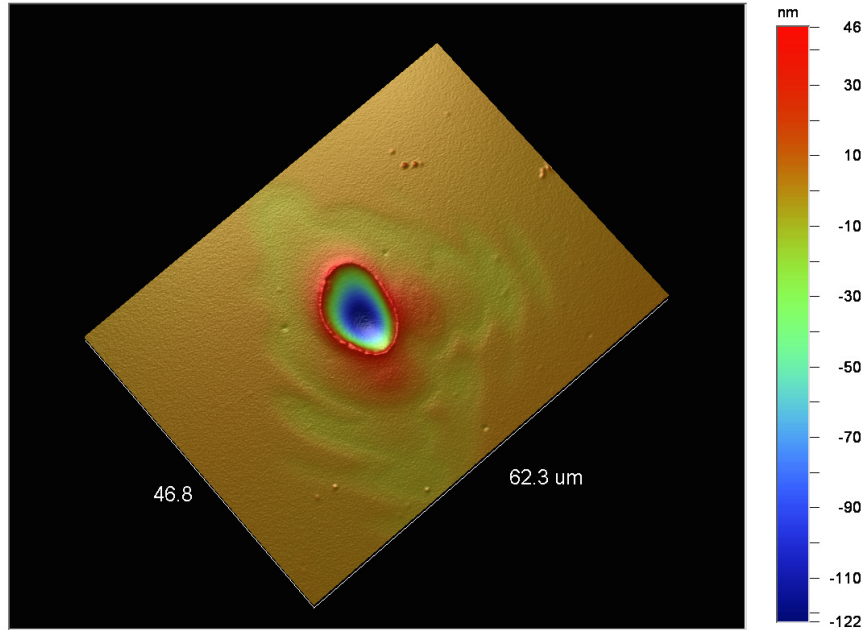


Fig. 7.22.: White Light Interferometer image of the a-C damaged at SCSS. The single shot with  $4.8 \mu J$  with photon beam energy of  $24 eV$ .

is from OPTICAL PROFILING SYSTEM, WYKO and the model is NT9100. Figure 7.22 is an image of one of the damage spots on an a-C sample which was damaged at SCSS under  $4.8 \mu J$  pulse energy with photon energy of  $24 eV$  at normal incidence. The specific parameter of the WHL used in this project are given in Table 7.2.

Vertical Resolution (nm)	Field of view (with the 50x and 1x FOV lens) mm x mm	Field of view (with the 2.5x and 1x FOV lens) mm x mm	Working distance (with the 50x) mm	Working distance (with the 2.5x) mm	Optical resolution (with the 50x) $\mu m$	Optical resolution (with the 2.5x) $\mu m$
0.1	0.13x0.10	2.53x1.90	3.4	3.5	0.49	3.82

Table 7.2.: Characteristic parameters at SCSS in Japan 2010 [101]

### 7.5.5 Photoemission spectroscopy and Scanning Electron Microscopy

In different electron microscopy techniques, (e.g scanning electron microscopy (SEM) and transmission electron microscopy (TEM)), the energy loss of electrons after being (inelastically) scattered, will be registered. In SEM as an example, an electron beam is used to probe the sample surface. The signal result from interactions of the electron beam with atoms at or near the sur-

face of the sample via secondary electrons is registered via a detector. In the most common or standard detection mode, (secondary electron imaging), the SEM (see Fig 7.23) can produce very high-resolution images of a sample surface, revealing details less than 1 nm in size. At the same time, these methods are ei-

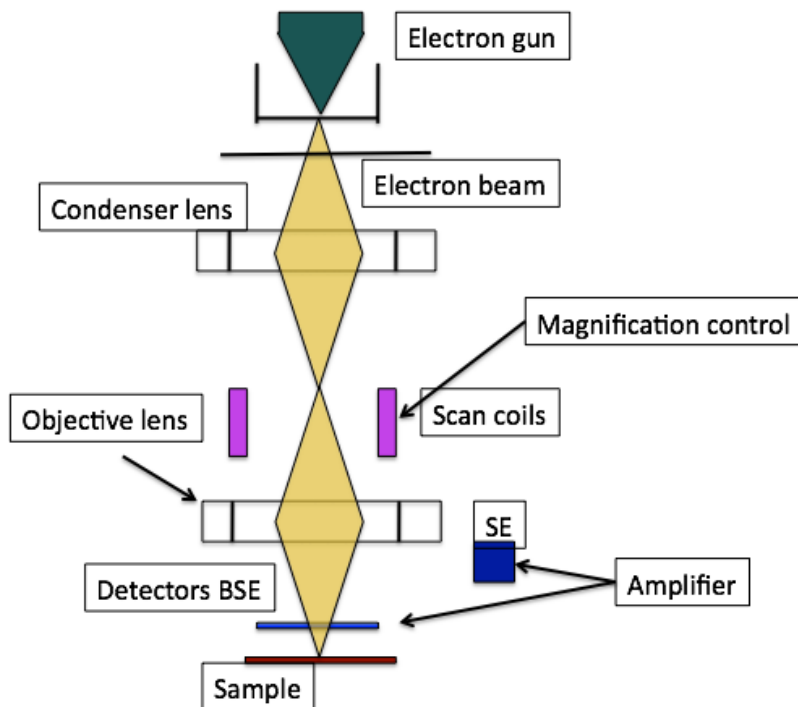


Fig. 7.23.: Simple image of an Scanning Electron Microscope (SEM).

ther limited in energy resolution, surface sensitivity or are destructive. Besides Raman and AFM spectroscopy, the Photo Emission Spectroscopy (detecting photo electrons emitted from the top few layers of the specimen) is an alternative method. Photoemission spectroscopy (PES) as a well-established technique can be used to characterize a-C [80], [111], [112] and its  $sp^3$  and  $sp^2$  content. This method is explained in section 8.3. The experiment was performed at the Elettra synchrotron facility.

SEM uses the electron beam and excites the atoms of the sample. The back scattered, secondary electrons (SE), characteristic X-rays, light (Cathode-Luminescence) (CL) are among all the possible products of this interaction. But usually its possible to detect one of these products, e.g the secondary electrons (SE) can be detected (with one device). Ejected secondary electrons have low energy, get accelerated towards an electrically biased grid and further towards a phosphor or scintillator positively biased to about +2000 V. After this process, these electrons have significantly high energy cause the scintillator to emit flashes of light. The amplified electrical signal output by the photomultiplier is then displayed as a two-dimensional intensity distribution that can be viewed and photographed. One can compare the Nomarski Microscope, AFM and SEM image of the same spot (see Figs 7.24 and 7.25). In order to use the

SEM, the sample should get cut into small pieces, this can damage the whole sample (since samples are thin). The AFM or the white light interferometer are less destructive methods in order to get a clear vision of the surface topology.

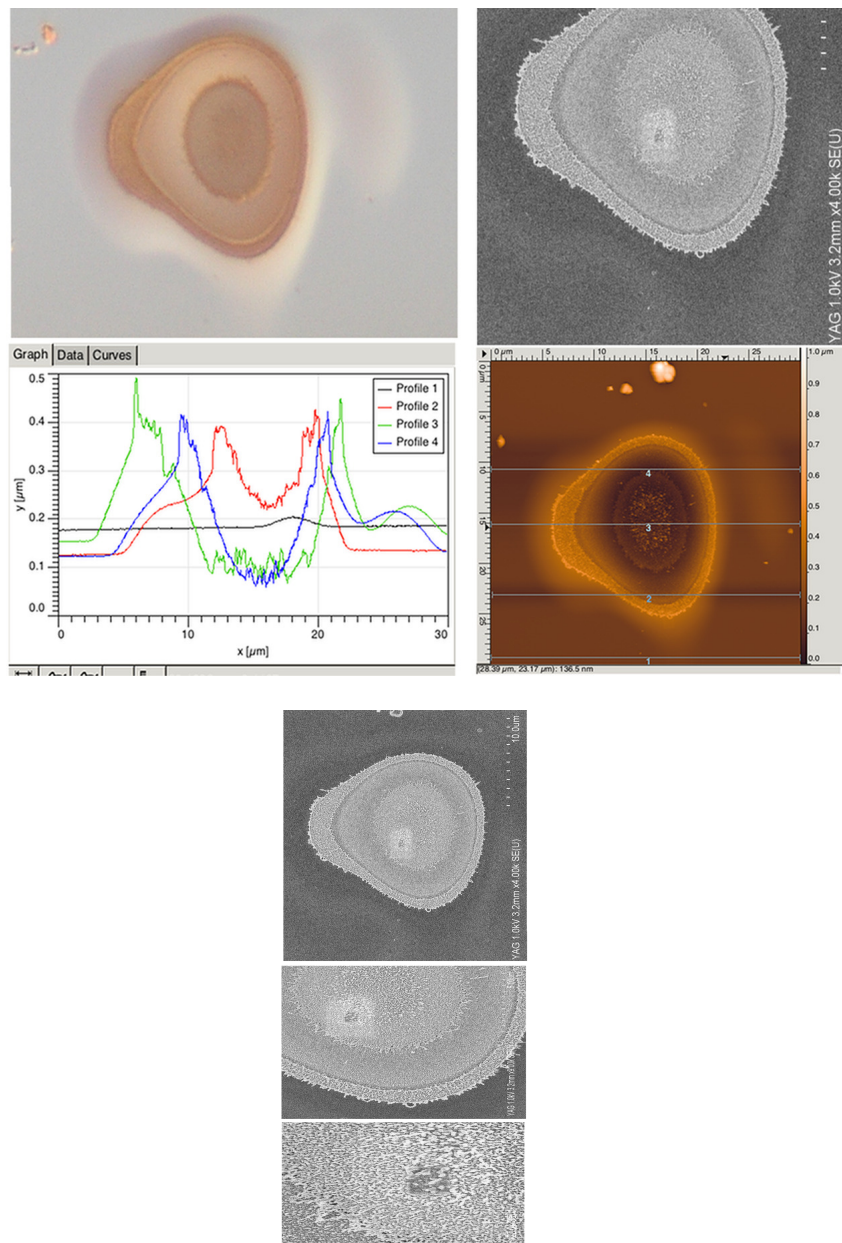


Fig. 7.24.: SEM, AFM, Nomarski microscope images taken at the damaged spot on amorphous carbon sample ( $890\text{ nm}$  thick on Si substrate) exposed to the  $91\text{ eV}$  beam with single shot pulse energy of  $4.83\ \mu\text{J}$  at FLASH. The three SEM images step by step zoom inside the damaged spot and show more details. From the top, the first image has  $10\ \mu\text{m}$  scale and the second taken with  $5\ \mu\text{m}$  and the third with  $2\ \mu\text{m}$ . The rough surface is completely obvious that smooth surface of a-C has turned into a rough graphite surface. There is a swollen observable area around the damaged spot which might have been created due to shock waves as the pressure goes high inside the hot plasma of free carriers. Since the material can't expand easily towards the rest of the volume, it causes a shock wave to reduce the pressure inside the damaged region. This also causes the material not to be easily removed from the surface [113]. The other reason might be due to beamline aperture which causes some other parts be illuminated by the beam at the time of exposure. This defect could be also created at the boundary between Si and a-C. From the heat diffusion simulation in chapter 9 it can be seen that material (a-C and Si) has reached melting temperature at this pulse energy which causes the larger damage area and explains the deformations observed on the surface.

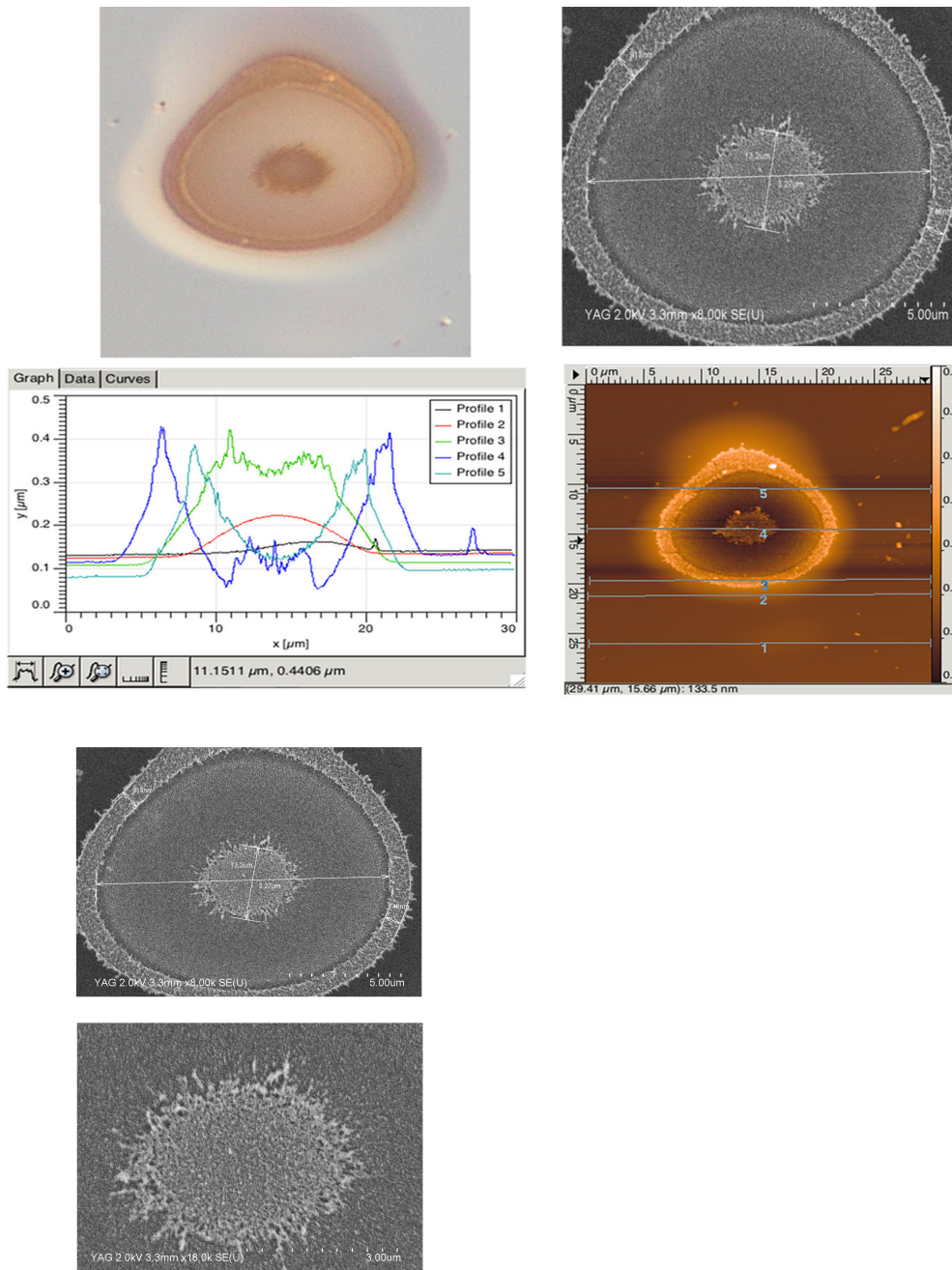


Fig. 7.25.: Nomarski microscope, AFM and SEM images taken of the damage spot on amorphous carbon sample (890 nm thick on Si substrate) exposed to the 91 eV beam with single shot pulse energy of 2.97 μJ at FLASH. From the heat diffusion simulation in chapter 9 it can be seen that material (a-C and Si) was melted at this pulse energy.



## Chapter 8

# Damage Investigations

Damage experiments under the scope of this project were performed at different Free Electron Laser (FEL) facilities around the world. The specific wavelength desired for further investigations of the damage process was among the criteria of why a specific FEL facility was chosen over another.

Most of the experiments were performed at FLASH [114]. Each of those was focused on a different wavelength. The experiments were performed using normal and grazing angles (smaller than the critical angle) defined for each wavelength. The performed experiments are listed here.

1. 20 eV at normal incidence angle at SCSS in Hyogo Prefecture (Japan) on CVD diamond and a-C samples
2. 24 eV at normal incidence angle at SCSS in Japan on CVD diamond and a-C samples
3. 91 eV at normal/grazing incidence angle at FLASH in Hamburg on CVD diamond and a-C samples
4. 177 eV at normal/grazing incidence angle at FLASH in Hamburg on CVD diamond and a-C samples
5. 269 eV at normal/grazing incidence angle at FLASH in Hamburg/Germany on CVD diamond and a-C samples as well as on Ni and MoB4C
6. 830 eV at normal incidence angle at LCLS in California/USA on CVD diamond and a-C samples

Table 8.1 represents parameters such as pulse duration at each experiment. The damage investigation procedure is divided into "Surface analysis" and "Structural analysis". The surface analysis provides information on the morphology of damaged spots. The Structural analysis provides information on structural changes of the material under irradiation.

The surface analysis includes determining the size of damaged areas (this is about  $\mu m^2$  in dimension), 'Nomarski microscopy' was the best tool for making this type of measurement (see section 7.5.1). Example images of damage spots

Photon energy (eV)	angle (°)	Pulse duration fs
890	90	100
269	90	125
177	90	30
91	90	30
24	90	100
20	90	100

Table 8.1.: Damage experiment parameter on CVD diamond/a-C at different photon energy levels.

on both single CVD diamond crystal and amorphous carbon are depicted in Figs 8.1, 8.2, 8.4. These images are the initial snapshots in determining the damage threshold, explained in further detail in the next section. The White light interferometer, AFM and Scanning Electron Microscopy (SEM) (all explained in section 7.5) are other surface analysis methods which are used to obtain information on the morphological level. Micro-Raman spectroscopy [80] and SPEM [115] make it possible to gain information on the changes of the local atomic order and electronic properties of the damaged spots respectively. It is also possible to apply Scanning Transmission Electron Microscopy (STEM) as an additional method for structural analysis. This destructive method is applied when all other measurements are performed on the sample. To characterize the long-range order (crystalizing order) of the matter, X-ray diffraction would provide the necessary information [100], [116].

## 8.1 Damage threshold

Damage threshold energy is defined as the minimum amount of energy deposited in the matter, by which the first sign of damage can be detected (this includes changes of the reflectivity or roughness that when compared to the sample's initial state are considered as damage). This is measured postmortem in the frame of this work.

The procedure for damage threshold retrieval starts with taking images from each damage spot on each sample. The microscope used in the frame of this work had a resolution between 500 nm and 1  $\mu$ m and was bought from Lesia company. Recognizing the damage spots is often not straightforward. Observation of any changes in color or removal or expansion of the material is key to recognizing the damaged area. At very high fluence, the substrate might be affected by the beam (melted, ablated, etc.). This can be seen in Fig 8.2. In this case, the sample coating was not thick enough in comparison to the beam penetration depth. The beam has reached the substrate at high fluence, where it melted the substrate and caused a larger beam imprint area on the spot.

After preparing the images, the next step is to measure the area of each damage spot and document them with regards to their position. This is a com-



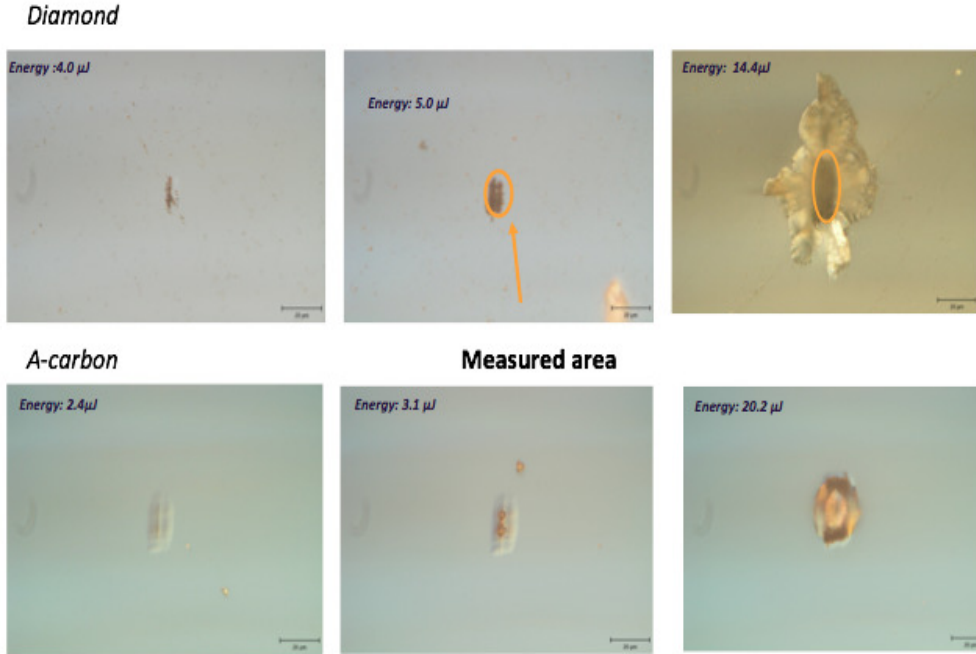


Fig. 8.1.: Damage spots on CVD diamond and amorphous carbon samples. These are exposed to single shots at LCLS with 830 eV photon energy. From left to right the pulse energy increases and one can see that the damage is more intense. These images are taken existu, via Nomarski microscope. With increasing the pulse energy, the shock waves appear in CVD diamond. Through heat diffusion part of sample get melted (including the Si substrate) in the case of a-C (amorphous carbon). The scale is 20  $\mu\text{m}$  in all these pictures.

plicated task, in some cases what is observed under the Nomarski microscope is not necessarily the initial beam footprint with its specific shape. It is possible to observe different phases or shades on one damage spot. The fluence of radiation causing the damage is a means to discern the response of the matter to the radiation. Hence, the inaccurate definition of beam footprint can lead to wrong interpretations of the data. For measuring the areas a software package called Gimp was used. Gimp is a graphical tool with maximum possible accuracy to measure the area of each damaged spot.

It should be taken into account that the area of each damage spot (see Fig 8.4) represents a cross section area of the beam with a specific fluence at the sample. This area changes with the pulse energies used to make each damage shot. In the case of a real Gaussian beam, the  $1/e$  of the full width at the Half Maximum of the beam intensity profile is proportional to the beam area (see Fig 8.3). This means that in the case of the Gaussian beam, at  $1/e$  of the FWHM, the beam has an area which is proportional to  $r^2$ , where  $r$  is the radius of the beam (Liu's method [117]). If we consider a Gaussian beam described by spatial and temporal dimensions, where  $r$  is the beam radius and  $c$  and  $f$  are the beam spatial and temporal radius, at  $1/e$  of the beam, the intensity contour (beam waist) respectively will be in the following form

$$I = I_0 e^{-r^2/c^2} e^{-t^2/f^2} \quad (8.1)$$

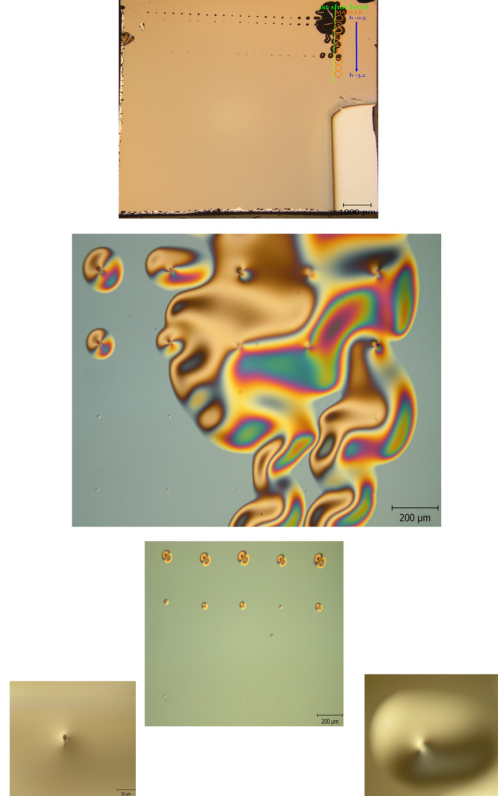


Fig. 8.2.: The schematic view of the damaged spot on the amorphous carbon sample in the experiment at FLASH May 2011 with 269 eV. The sample thickness was small ( $1.4 \mu m$ ) for this photon energy and the beam has penetrated into the substrate, and one of the following effects may be responsible for what one observes on the surface. It may be that the coating is peeled from the substrate, from the AFM image taken one could estimate about  $0.5 nm$  to be the height of the swollen surface. The second possibility for this effect is that the substrate was melted at higher fluence and pushed the coating to the top, towards the outside. It is possible that the coating had a defect at that region of the sample (attenuation length at 269 eV is approximately  $2.2 \mu m$ ).

taking the spatial part into account will give

$$E(r) = E_0 e^{-r^2/2c^2} \quad (8.2)$$

Then the radius of the beam on the plane perpendicular to the beam propagation can be taken out by

$$\ln(E) - \ln(E_0) = -r^2/2c^2 \quad (8.3)$$

$$r = c\sqrt{2\ln 2} \quad (8.4)$$

$$2r = 2c\sqrt{2\ln 2} \quad (8.5)$$

The next step is determining the corresponding pulse energy with which each damage spot has been created. Each damaged spot has been created by a certain amount of energy in a single shot (or multi shots in a multi shot damage

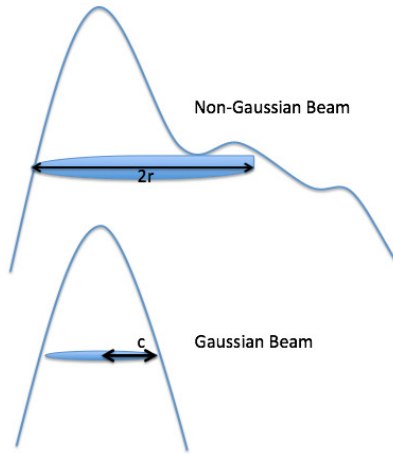


Fig. 8.3.: Comparison between beam profile in the case of a Gaussian (lui's method) and Non-Gaussian beam (F-scan method)

experiment). Hence, the corresponding pulse energy causing the damaged spots should be found from GMD data set by comparing the bunch ID number and other necessary parameters. For this purpose, there is a small algorithm written in MATLAB, which helps to find the corresponding energy values for each damage shot on each sample.

The pulse energy of each single shot is then plotted versus the corresponding damage area of each shot (see Fig 8.5). The energy threshold is determined by fitting the experimental points (red dotted line in graph). For this purpose the given logarithm-based fitting function in equation 8.6 was used.

$$S = a + b * \ln(E) \quad (8.6)$$

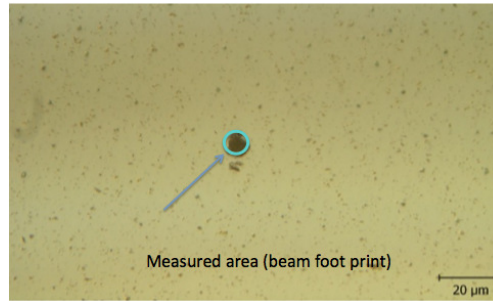


Fig. 8.4.: View of the damage spot on the CVD Diamond sample at the experiment at FLASH may 2011 with 269 eV.

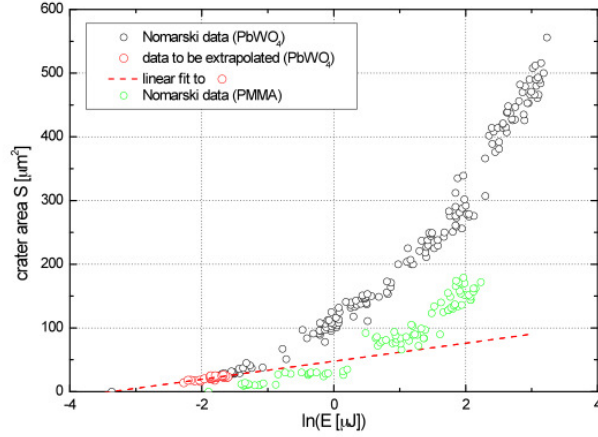
where  $S$  represents the area of each damage spot and  $E$  the corresponding pulse energy as described in refs [117], [118]. The  $a$  and  $b$  are taken as area dependent parameters ( $area * \ln(E)$  at any point). The fit contends exclusively with the  $\ln$  of a number (which is the  $\ln$  of energy/energy threshold) and not on a unit. At  $E = E_0$  this area would turn to be 0.

The energy threshold is found by extrapolating the low-energy linear part (with the help of the linear fit) of the Liu's plot to zero crater area (see Fig 8.5). Due to the fluctuations of the data points, the energy threshold is determined within a certain degree of accuracy. The statistical uncertainty method on the fit parameters is used to determine the error bars of the energy threshold.

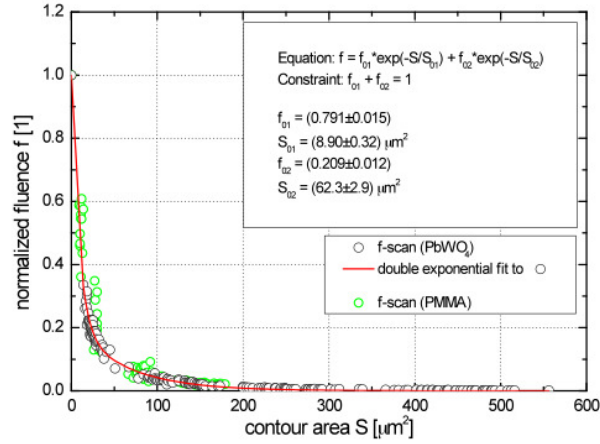
To determine the size of the beam, the F-scan method is constructed. In that method, the ratio of the energy of each pulse to the damage energy threshold (the ratio of fluence for each pulse energy to the fluence threshold) is plotted versus the beam imprint area of each damage spot. This is represented in Fig 8.5. This is a one-dimensional representation of a two-dimensional beam profile which is normalized to the unity and can be fitted by the sum of two exponential functions. Which can also be used in the case of non-Gaussian beam shape (when the beam profile consists of a Gaussian-like central peak surrounded by a broadened pedestal or wings (see Fig 8.3)). The integral under the fitted curve represents the effective area of the beam.

The ratio of the energy threshold to the effective beam footprint area ( $F_{th} = E_{th}/S_{eff}$ ) is the damage fluence threshold. By this definition, fluence threshold describes the necessary amount of energy ( $\mu J$ ) to be absorbed per unit area ((beam size)  $1/cm^2$ ) to cause the damage.

The method reported in references [120], [118], [121] assumes that the  $PbWO_4$  ablation threshold remains constant and independent of the impinging peak fluence and of any energy transport processes such as diffusion [80], [122]. It is based on single-shot ablation imprints in lead tungsten ( $PbWO_4$ ). This is a good reference for checking the accuracy of the beam size calculated via the F-scan method. To characterize the focused beam, we have used (e.g., at FLASH May 2011) this method. The beam size can be measured via the beam imprint size on the  $PMMA$  (or  $PbWO_4$ ) sample. The  $PMMA$  sample was 5  $\mu m$  thick. It was spin coated on a silicon slab, which was used for determination of the size of the focused beam. The pertinent information lies within the amount of absorbed energy per atom at the threshold. In order to obtain the threshold dose, it is assumed that all the energy is absorbed in a volume, limited in depth by the value of  $dz$  (absorption depth). Nevertheless, in the conduction band, the electrons ionized by the X-ray photons can diffuse into a volume larger than the effectively irradiated one. The mean free path of these electrons can be evaluated by using simple assumptions and considering the data of the stopping power of electrons [75]. Taking the electron stopping power into account would result in new values of dose and attenuation lengths especially at grazing incidence angles. In any case the dose threshold values were determined by the formula (dose) defined in chapter 5 in section 5.6 via Equation 5.12. It should be mentioned that in all these experiments the pulse duration was within the femtosecond ( $fs$ ) regime. The maximum pulse duration at latest experiment at FLASH in 2011 was around 125  $fs$ .



(a)



(b)

Fig. 8.5.: (a): The damage spots on PMMA (green dots measured via Nomarski microscope) and PbWO<sub>4</sub> (black dots measured via Nomarski microscope) to measure the beam size at FLASH May 2011 with 269 eV. The red dots are the extrapolated data points and the red dotted line is the linear fit function defined in reference [117]. (b): An F-scan derived from PbWO<sub>4</sub> and PMMA ablation imprints. The PbWO<sub>4</sub> data were fitted by a sum of two exponential functions applicable as a model for a Gaussian beam surrounded by an extended background. Determined parameters are :  $f_{01} = 0.79 \pm 0.015$  ,  $S_{01} = 8.90 \pm 0.32$  ,  $f_{02} = 0.209 \pm 0.012$  and  $S_{02} = 62.3 \pm 2.9$ . These are samples examined at FLASH in May 2011 with 269 eV photon energy [119].

## 8.2 Experimental Results

The experiments performed in the context of this project can be divided into two main groups; below and above the carbon K–edge. The results of the experiments below carbon K–edge at normal incidence are outlined here first. Afterward the results of the experiments above the K–edge are presented. Next, the results of experiments at grazing incidence angles with three different photon energies are reported. Some of the results are presented here and the rest in Appendix A.

### 8.2.1 Below and around carbon K–edge

The lowest photon energies with which the damage experiment was performed were 20 and 24  $eV$  at the SCSS facility. This was followed by energies at 91 and 177  $eV$ , which have been performed at FLASH. The most recent experiment in the frame of this project was performed at FLASH at 269  $eV$  (4.6  $nm$  wavelength), where due to some effect (two upstream carbon coated mirrors at beamline) the wavelength value could not be fixed, and it was fluctuating. This caused an uncertainty factor of  $\pm 0.1 nm$  of the wavelength for that experiment. This error bar corresponds to the uncertainty of the absolute value of the wavelength and not to the pulse-to-pulse jittering (fluctuations), which has been measured and found to be negligible (around  $1e^{-3} nm$ ). The pulse duration was estimated to be  $125 \pm 5 fs$  and the electron bunch during the experiment was evaluated to be 300  $pC$ .

To extract the damage fluence threshold as described in section 8.1, the energy threshold, and beam imprint areas are determined. These are depicted below (e.g. Figure 8.6). The first graph shows the dataset used to determine the energy threshold. Where the  $x$  axis is plotted in logarithmic scale, representing the pulse energy of each damage spot and the  $y$  axis representing the beam imprint area of each damage shot and is in linear scale. The second graph illustrates the beam effective area (so called F-scan method (sometimes mentioned as Q-factor method) [118]).

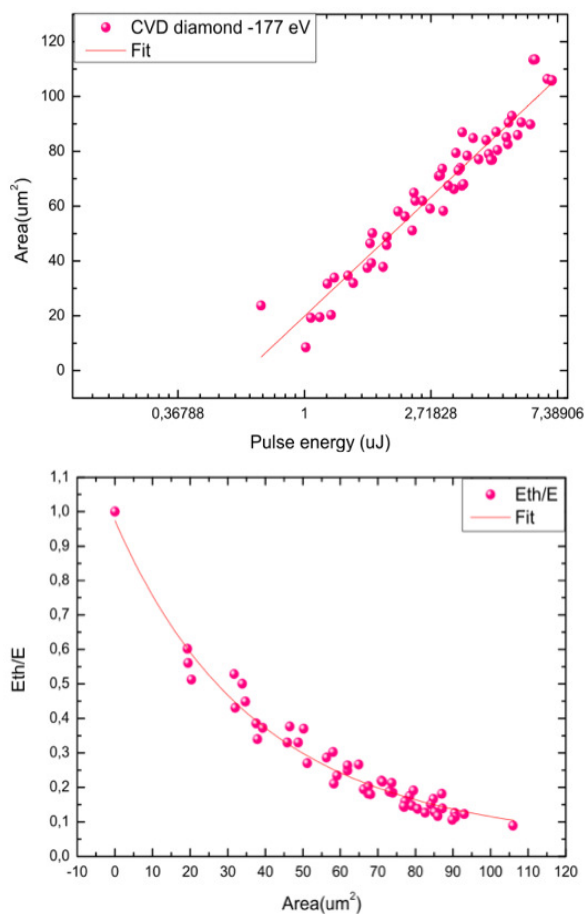


Fig. 8.6.: CVD diamond sample exposed to the 177 eV beam with single shots at FLASH at normal incidence angle. Top panel shows the plotted pulse energy ( $\ln(E)$ ) vs the damage footprint area. Bottom panel represents the F-scan method, where the footprint areas are plotted vs the corresponding normalized pulse energies for each shot. The Integral of the area underneath the curve (fit line) gives the effective area of the beam. This method is explained in Section 8.1.

### 8.2.2 Above carbon K-edge

The highest photon energy in the frame of this project, at which the damage experiment was performed, is  $830\text{ eV}$ . That experiment took place at LCLS. As an example, Figure 8.7 represents the threshold energy and beam effective area determination on a-C at this photon energy.

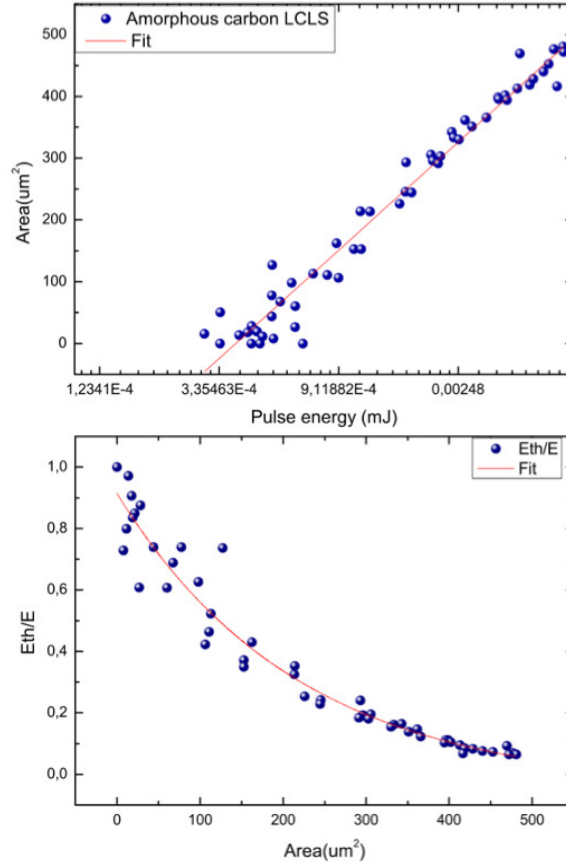


Fig. 8.7.: Amorphous carbon exposed to the  $830\text{ eV}$  beam with single shots at LCLS. The Top panel shows the pulse energy in logarithmic scale vs the measured footprint area. The fit gives the energy threshold. The Bottom panel represents the plotted areas vs normalized pulse energies (for each shot) with the energy threshold evaluated in the top plot. The integral of the curve under the fit gives the effective beam area (see Section 8.1).

In all these experiments the samples had almost uniform quality. The a-C samples were prepared by GKSS group and were made of  $50\text{-}60\text{ nm}$  a-C coating on a  $\text{Si } 60\text{ }\mu\text{m}$  substrate. The CVD samples were all ordered by ELEMENT SIX Company.



### 8.2.3 Below carbon K-edge and at grazing angle

It is critical in the design of any (safe) beamline to know the maximum fluence that can impinge on the optical elements for a given photon energy without damaging them. Since X-ray mirrors work under total external reflection geometry (at the grazing angle which is smaller than the critical angle  $\theta_c$  (see Equation 4.35)), the energy deposits in the very few first  $nm$  layers of the coating, which can be characterized by the absorption depth  $d_z$  (see Equations 5.8 and 5.11).

As a high flux of radiation is desired in any beamline, the reflectivity of these mirrors (their coatings) at those certain photon energies and grazing angles is one of the critical parameters which should be considered while choosing the optical coatings.

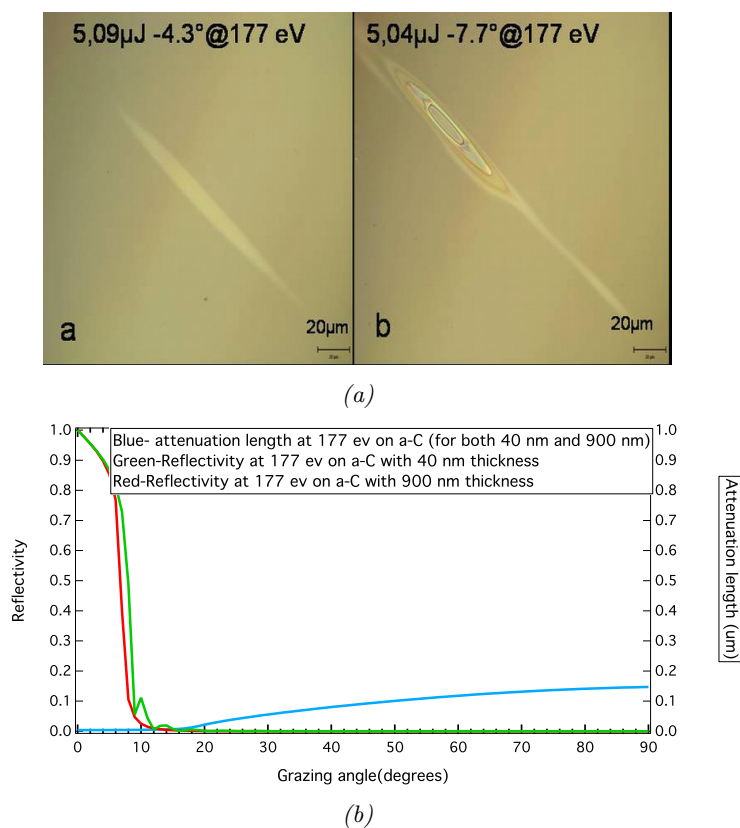


Fig. 8.8.: (a): Damage on amorphous carbon at grazing angles of  $4.3^\circ$  and  $7.7^\circ$  at  $177eV$  at FLASH. (b): Comparing changes of the attenuation length and reflectivity on the thin (40  $nm$ ) and bulk (900  $nm$ ) a-C sample at 177  $eV$  on a-C. The attenuation length doesn't change but the reflectivity slightly changes and on a thicker sample the drop happens at a slightly lower angle.

The attenuation depth, the area of the damaged spot and the reflectivity of the material, all change with tuning the grazing angle (see Fig 8.8). The amount of the absorbed dose in the material also depends on the grazing angle. In the case of a-C, most of the X-ray photons get reflected away at low photon energies. Increasing the photon energy results in reduction of reflectivity and

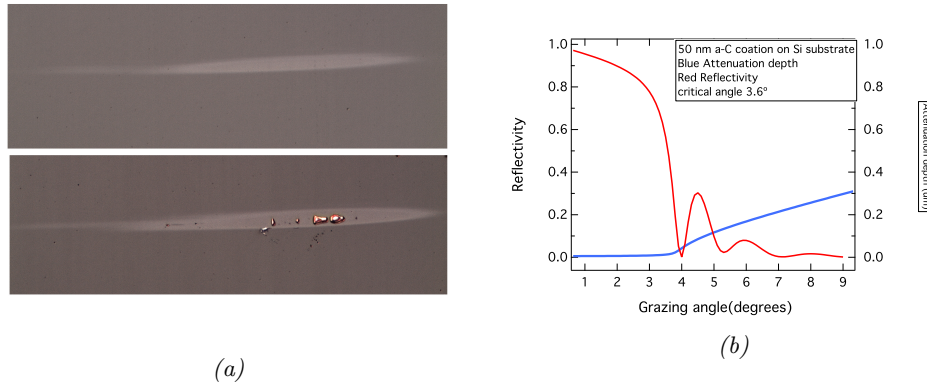


Fig. 8.9.: (a): Damage shots at the grazing incidence angle of  $7^\circ$  at  $269 \text{ eV}$  on a-C with a thickness of  $50 \text{ nm}$ . The above panel shows the damaged spot at  $14.4 \mu\text{J}$  and the lower panel shows the damaged spot at  $20.08 \mu\text{J}$ . (b): Reflectivity and attenuation depth plotted as a function of grazing angle. The changes are shown here around critical angle ( $3.6^\circ$ ) at  $269 \text{ eV}$  for a  $50 \text{ nm}$  thick a-C layer on a Si substrate. At very low grazing angle the reflectivity is at the maximum of its range, this is plotted in red. Attenuation depth is plotted in blue. The solid lines are taken from CXRO data set [15].

more absorption of X-ray photons in the matter (see Figs 4.3, 4.4). The sample quality can influence the amount of the absorbed dose and the corresponding damage.

Potential differences in the damage process, making it interesting to perform the experiment on thick ( $900 \text{ nm}$ ) and thin ( $40 - 60 \text{ nm}$ ) coating layers (a-C) at the same grazing angles and compare the results. Because the coating of mirrors at beamlines are very thin and on the order of  $40 - 60 \text{ nm}$  testing the grazing angle experiment at a thin layer of a-C is worthwhile.

In this work energy thresholds for  $4.31^\circ$  and  $7.71^\circ$  grazing incidence angles (below and above critical angle) on thin ( $40 \text{ nm}$ ) and thick ( $900 \text{ nm}$ ) layers of amorphous carbon at  $177 \text{ eV}$  (depicted in Fig 8.8) and for  $7^\circ$  at  $269 \text{ eV}$  were determined (depicted in Figs 8.9). The critical angle in the case of  $177 \text{ eV}$  photon energy is  $7.6^\circ$ . The corresponding angle for  $269 \text{ eV}$  is  $3.6^\circ$ . The results are presented in Figures 8.10 and the corresponding Tables 8.2 and 8.3. Attenuation depth and reflectivity around the critical angle at  $177 \text{ eV}$  are plotted in Fig 8.8. Figure 8.9 shows these properties at  $269 \text{ eV}$ . The measured effective areas at  $177 \text{ eV}$  in the case of  $4.31^\circ$  and  $7.71^\circ$  were  $351.30 \mu\text{m}^2$  and  $455.25 \mu\text{m}^2$  respectively. In the case of the experiment at  $269 \text{ eV}$  the effective beam area was  $424.02 \mu\text{m}^2$ . The ratio of the energy threshold and effective area of the damaged spot (the fluence ( $F_{th} = E_{th}/A_{eff}$ )) were calculated and are presented in Table 8.2 and 8.3.

Measured fluence threshold in case of  $40 \text{ nm}$  shows a higher value than the bulk sample. This indicates a different damage mechanism in bulk and thin layer samples.

In previous studies with the optical laser, on the a-C sample with  $60 \text{ nm}$  thickness at the grazing angle of  $7.71^\circ$  mechanical damage was detected [123]. The mechanical damage occurs over a longer time scale compared to the phase transition. This can be observed as delamination fractures. Hence, it was also worth checking this effect in the case of damage experiment with X-ray FEL

single pulses. After doing so, under the Nomarski microscope, no sign of mechanical damage was detected, ablation, however, was observed (see Figs 8.8). The ablation can be recognized by observing the removal of the coating material as well as melting of the substrate [16].

An interesting observation is the changes of fluence threshold at the same grazing angle for the thin and thick sample. The Fluence threshold (dose threshold as well) in the case of the thin layer is higher than of a bulk sample. One explanation could be the sample quality. The fact that the deposition time for a bulk sample is longer than for a thin layer suggests that this can cause more defect and changes of surface roughness and density. Defects or high roughness increase the damage possibilities. The roughness of both samples measured via AFM shows that roughness of the bulk sample is higher (see Fig: 6.5). Also as a result of irradiation, free carriers can escape from the surface of the sample and carry away some energy with them as leaving the sample. This means the higher the grazing angle, the greater the number of the scattered away electrons from the surface of the sample will be. In the case of the thin coating layer, this effect could increase the fluence threshold more than in the case of the bulk sample. Another fact is that free carriers can get scattered within a larger volume inside a bulk sample, which increases the secondary ionization possibilities inside the coating. The volume which gets involved in the damage process is not limited to the attenuation depth (see Chapter 5) but also depends on the mean free path of these carriers, electron range (see Chapter 9) as well as on the depth to which the heat can get diffused to. In a thin sample, heat can be transferred towards the substrate, much faster than in the bulk sample. At the experiment with 269 eV photon energy, the attenuation depth (see Fig 8.9 and Tables 8.3 and 8.2) was higher than the thickness of a-C coating. It means the substrate was affected by the pulse and this event had influenced the damage threshold (coating thickness should have been larger).

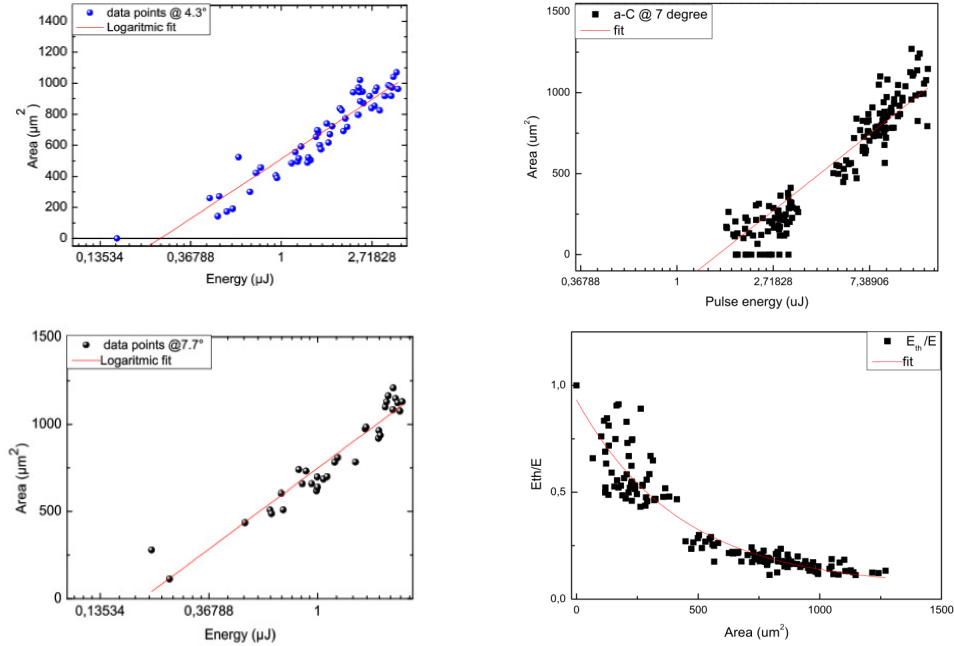


Fig. 8.10.: Top panel: Damage area versus the pulse energy of the grazing angle of  $4.31^\circ$  for  $40\text{ nm}$  thick sample and at the grazing angle of  $7.71^\circ$ . The energy threshold of damage is found with the logarithmic fit. Bottom panel: Damage on amorphous carbon at grazing angle of  $7^\circ$  at  $269\text{ eV}$  at FLASH on the left side and on the right side is the effective area obtained using the F-scan method (integral underneath the fit gives the effective damage area).

During the experiment at  $269\text{ eV}$  at FLASH, some of the high  $Z$  materials were also investigated. Among those are Nickel (Ni) and MoB4C to be mentioned. Ni has been already used as coating at some beamlines, e.g. at FLASH *BL3* [5]. The extracted results on Ni and MoB4C at different grazing angles are presented in the Appendix 12.3 and 12.6 (see Table: 12.5, 12.6). The main purpose is to compare the damage threshold of high  $Z$  materials with low  $Z$  materials at different photon energies. Single layer mirrors usually have very small reflectivity near normal incidence. As mentioned, the maximum reflectivity of the single-layer X-ray mirrors could be achieved at very small grazing angles (see Fig 4.4). Around normal incidence, the reflectivity of these mirrors are very small, and the imaged field is usually very small. Multilayer mirrors, on the other hand, give the opportunity of high reflectivity around normal incidence angles [124]. At grazing angles, they provide 10 times higher reflectivity compared to single layer mirrors. All these properties make the multilayer mirrors very useful especially at soft X-ray regime to be implemented at beam deflectors, spectral filters, collimators or focusing elements. Different multilayer based on their optical constants were suggested and tested. Boron-based multilayers are among those, which performed especially well above the Boron (B) K-absorption edge at  $6.63\text{ nm}$ . [125], [126], [127], [128].

MoB4C multilayer was chosen as a candidate coating based on the published optical constants [127] and its thermal stability [129], [130], [131] which was manufactured via sputtering. The MoB4C multilayer examined at  $4.6\text{ nm}$  wavelength is constructed with 160 bilayers with the  $\lambda = 3.4\text{ nm}$ . Comparing

the thickness of Mo layer to the B4C results in 0.33. The multilayers are finished with the B4C. In the FLASH experiment at 4.6 *nm* wavelength, they were exposed to the beam under normal and grazing angles, and in each case one sample was annealed for about an hour at 500°C, to compare the stability of the multilayer under this circumstance. Around carbon edge, the B4C in comparison to Ni has lower reflectivity, but at higher energies, up to 3 keV (interesting for XFEL in Hamburg), this value changes and Ni has lower reflectivity. That is why it is interesting to compare the damage threshold and to investigate the possibility of using it (Ni) as a coating on mirrors. Two stripes, one out of Ni and one out of B4C would be a great combination for coating on one mirror but due to cost reason it was decided to use B4C for mirrors with 20 *mm* wide, reflecting area at XFEL beamline; which was more of practical use [132] [125], [133], [134]. Next important factor is the answer to the question of if this coating could be good enough for vast energy range in comparison to low Z material or multilayers like B4C. The energy threshold results and effective areas are plotted in Appendix 12.3- 12.5. Further studies on Ni at different photon energies could be considered for future experiments.

Table 8.2.: Results of the damage experiment on amorphous carbon material at different photon energies at different grazing angles, comparing thin layer and bulk sample. The values in case of the bulk sample are from the experiment performed at FLASH in 2009 [73] and the results of grazing experiment at 7 degrees grazing angle on a-C at 269 eV in 2011 at FLASH. The attenuation length is taken from Henke's tables on CXRO website.

Photon energy (eV)	angle(°)	Reflectivity	attenuation length (nm)	Fluence threshold (for 40 nm) ( $mJ/cm^2$ )	Fluence threshold (for 900nm) ( $mJ/cm^2$ )	Dose (eV/atom) (for 40 nm)	Dose (eV/atom) (for 900 nm)
177	4.3	0.89	4.78	$74 \pm 22$	$52 \pm 30$	$0.95 \pm 0.3$	$0.61 \pm 0.4$
177	7.7	0.59	14.6	$43.7 \pm 13$	$19 \pm 13$	$0.69 \pm 0.2$	$0.33 \pm 0.3$
269	7	0.055	210.0	$350.00 \pm 2$	—	$0.915 \pm 0.02$	—

Table 8.3.: Results of the damage experiment on amorphous carbon material at different photon energies and different grazing angles, comparing thin layer and bulk sample. The values in case of the bulk sample are from the experiment performed at FLASH in 2009 with photon energy of 177 eV [73] and the results of grazing experiment at 7 degrees grazing angle on a-C at 269 eV in 2011 at FLASH. The attenuation length is calculated with the electron stopping power in each case.

Photon energy (eV)	angle(°)	Reflectivity	attenuation and stopping power (nm)	Fluence threshold (for 40 nm) ( $mJ/cm^2$ )	Fluence threshold (for 900nm) ( $mJ/cm^2$ )	Dose ( $eV/atom$ ) (for 40 nm)	Dose ( $eV/atom$ ) (for 900 nm)
177	4.3	0.89	9.27	74 ± 22	52 ± 30	0.49 ± 0.3	0.35 ± 0.2
177	7.7	0.59	16.64	43.7 ± 13	19 ± 13	0.61 ± 0.2	0.26 ± 0.1
269	7	0.055	214.31	350.00 ± 2	—	0.913 ± 0.02	—





### 8.2.4 Discussions

As mentioned at the beginning of the Chapter 8 damage experiments in the scope of this project were performed at different Free Electron Laser facilities around the world under different conditions.

Tables 12.1 to 12.4 (in Appendix) summarize the obtained damage threshold values on energy, effective beam area, fluence and absorbed the amount of dose per atom in the CVD diamond and amorphous carbon (a-C) samples under the normal incidence angle with different photon energies. These values are compared in plotted figures in Figs 8.11, 8.12 and 8.13. In Tables 12.2, 12.4, the stopping power of electrons at each photon energy for each material (CVD diamond and a-C) is considered in those calculation.

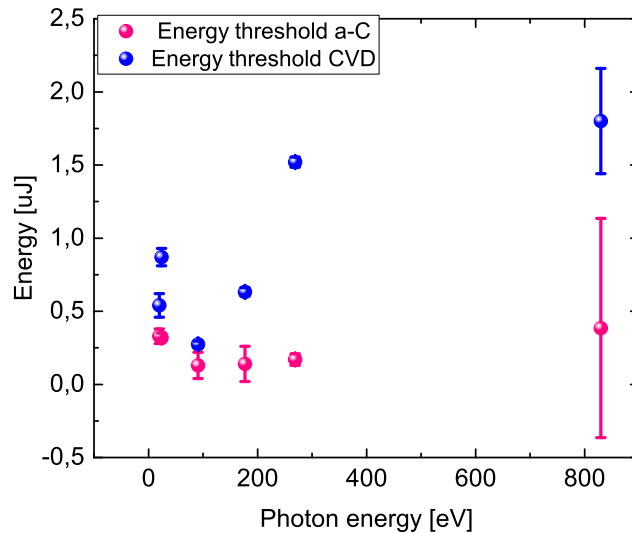


Fig. 8.11.: Comparing the damage energy threshold at different photon energy on CVD diamond and amorphous carbon.

Comparing the trend in the absorbed dose (see Fig 8.13) at the damage threshold in the case of a-C and CVD diamond shows that both materials absorb almost the same constant amount of energy per atom at the damage threshold in the case of experiment with 91, 177 and 830 eV except for the photon energies of 269, 20 and 24 eV. The damage threshold is also below the melting threshold values (see Fig 9.29) in all these cases.

Calculating the absorbed amount of dose around 20 and 24 eV with the introduced method in section 5.6 results in extremely high values. At 20 and 24 eV photon energies, it was hard to distinguish the damage spots under Nomarski microscope because they were mostly not detectable at this magnification. The extreme behavior is due to the different damage mechanism at those photon energies. At very low photon energies the reflectivity is high and the attenuation depth is pretty small. Hence, the energy is being absorbed by a thin layer on the surface. Through the photon ionization process and all the secondary processes,

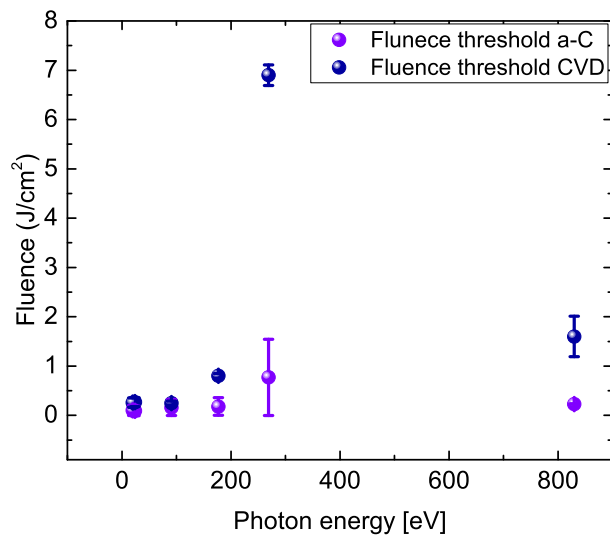


Fig. 8.12.: Comparing the damage Fluence threshold at different photon energy on CVD diamond/a-C.

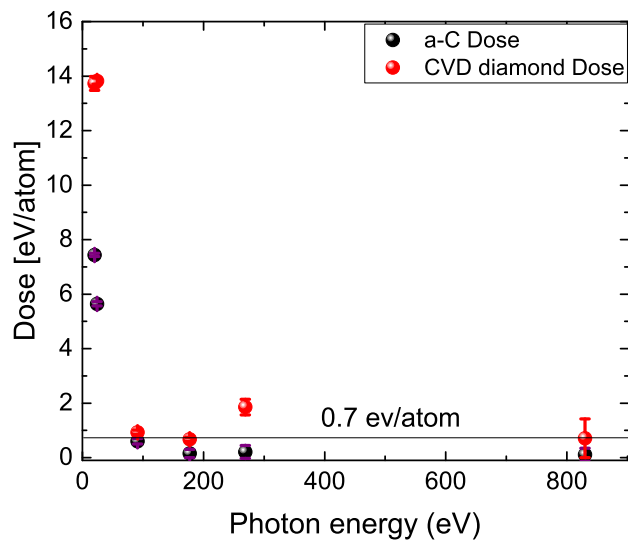


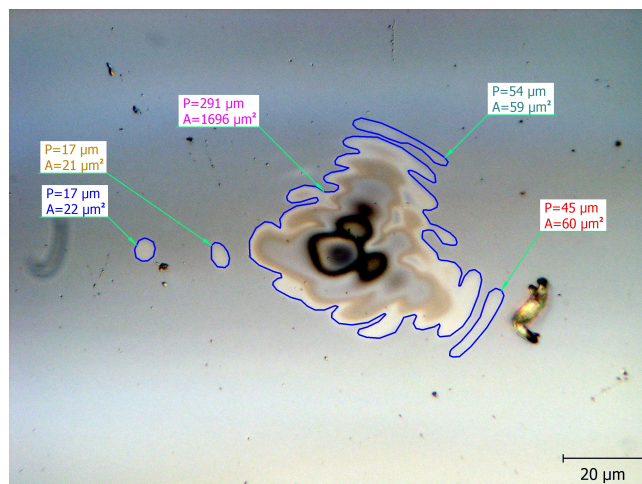
Fig. 8.13.: Comparing the damage dose threshold at different photon energies on CVD diamond and amorphous carbon. The line at  $0.7 \text{ eV}$  represents the calculated damage dose threshold theoretically via Hybrid XTANT model mentioned in chapter 9 [135].

the density of free carriers is raised to very high levels with a large number of free electrons being produced. This can cause a screen effect, which means that very soon no more photons will be absorbed, and most of the beam will be reflected. The material behaves like metal in that state. Free carriers can get scattered and escape away from the surface very fast. Which cause the material gets damaged at higher absorbed dose. Coulomb explosion is another phenomenon that might take place during the damage process. Here, the repulsion force between the same charges causes an explosion, resulting in a small plasma cloud of energetic ions with a higher velocity than the thermal diffusion. The created plasma can still absorb energy from the beam. Hence, the pressure inside this cloud increases. The plasma expands and by its expansion creates a so called shock wave. This is because the rest of the matter is at its initial state and as the plasma get expanded, it forces the rest of matter outwards with its pressure and causes shock waves. This could be imaged as sonic sound. This effect is more evident on the CVD sample at 830 eV (see Fig 8.1). At photon energies of 20 eV or 24 eV shock waves are not seen (see Fig 8.14). Instead, the fringes due to the beam pattern are visible. Nomarski images of the damaged spots (at those photon energies) show the beam interference pattern on the sample which is readily detectable. This is due to the beam focus and the focus apertures in the beamline. This effect can be seen on Fig 8.14 as an example for both a-C and CVD sample.

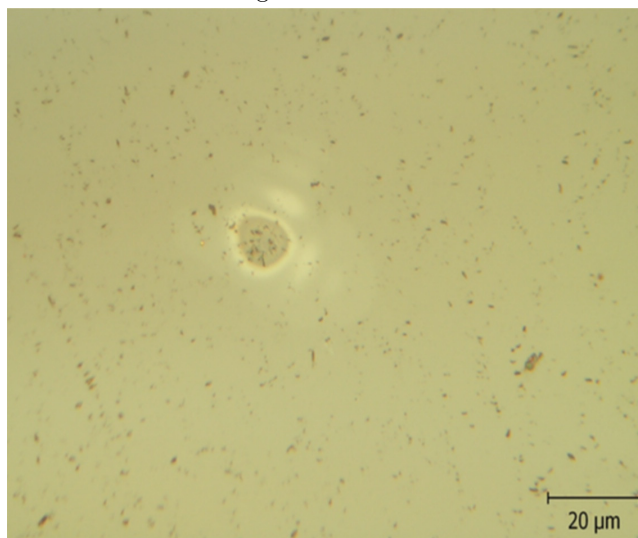
Heat diffusion also plays an important part here (at 20 and 24 eV photon energies). Due to the short attenuation depth, the sample stays hot in a longer time scale on the surface compared to the case at higher photon energies. This increases the vibration of atoms in the system and the pressure in the damaged volume. Looking at Fig 9.17 shows that a-C (heat simulation section for 20–24 eV) gets heated up to its melting temperature at pulse energies around  $1\mu J$ , whereas Si does not reach its melting temperature. In contrast at higher photon energies around this pulse energy both Si and a-C gets heated up to their melting temperatures. These facts suggest that one should consider the free carriers escape, cascade, scattering, heat diffusion and possibly shockwaves, to some extent into account while calculating the threshold dose values for low photon energies (20 eV or less).

The process of damage starts with photo-ionization which lasts over 100's of fs. Free carriers cause secondary processes (e.g. impact ionization, Auger process, etc. named in chapter 5). Due to photo-ionization and secondary processes, the ionic bonds break in a very short time. The system tries to bring itself to an energetically stable state. Stability is achieved when the diamond crystal turns to a more stable structure (graphite), and the same result happens to the a-C. Due to the phase transition the density of the material changes and if the matter doesn't evaporate (without mass lost), the volume (of the damaged spot) changes. To ensure that the phase transition took place, the photoemission spectroscopy has been done on the samples. The results and details of the experiment are presented in section 8.3. Already at 100s of ps the heat diffusion starts to happen. The carrier diffusion and heat diffusion distribute the free carriers and heat in the sample, which depending on their energies can cause further damage. These two processes overlap at least up

to some  $ns$ . After that time, the heat diffusion and other processes like shock waves take over the damage process. These last up to some  $\mu s$  (almost  $7 \mu s$ ). Defects in samples or several experimental factors cause uncertainty in the measurements (as mentioned in 7.1.3). Fluctuating data points result in obtaining threshold values within a certain accuracy. This causes statistical uncertainty within the derived parameters.



(a) The damage spot at  $20 eV$  photon energy on amorphous carbon with  $16.4 \mu J$ . The diffraction pattern of the beam is observable on this image. This shot was created under tight focus.



(b) The damage CVD sample with  $17.2 \mu J$  pulse energy, at  $20 eV$ .

Fig. 8.14.

Observing the results of the experiment with  $269 eV$  photon energy, the absorbed dose is high for CVD diamond. A large amount of absorbed dose on CVD at  $269 eV$  is due to carbon K-edge, which lies very close to this photon energy. The attenuation length below the K-edge is high compared to the photon energies after K-edge. Hence, the beam can penetrate deep into the sample in both cases of CVD and a-C. At  $269 eV$  due to the photo-ionization

process, lots of electrons above the K-shell are ejected out of atoms in the CVD crystal structure. The 2S-shell is being ionized first, and the ejected electrons have 160 eV rest energy that still can ionize the upper shell electrons. Auger process and other secondary process are running at the same time. These all create enormously high numbers of free carriers. Besides the fact that some of the free electrons can escape away from the surface. The free carriers can cause screening effect (metallic behavior of the electrically insulating solid material). This could also lead to a high absorbed dose at this photon energy. Through  $F$ -scan method calculation, the obtained beam imprint radius is much larger than the beam radius given as a parameter at the time of the experiment. That's why in the calculation of absorbed dose, the beam size is taken as given from the facility (FLASH) at the time of the experiment.

At 269 eV photon energy the a-C sample was partly swollen, and it seemed that the substrate was molten underneath the coating, or the coating was peeled off. Unfortunately, at this experiment, the a-C coating thickness was made shorter than the attenuation length of radiation. Hence, the substrate was also irradiated by the pulse, and part of the dose was absorbed into the substrate (Si). At higher pulse energies Si has been molten. This is also obvious in heat simulation calculations in chapter 9 (see Fig 9.17).

Considering the sample was only made out of Si, the absorbed dose has been calculated. The attenuation depth and reflectivity for Si wafer (substrate) at 269 eV are 0.20  $\mu\text{m}$  and  $7.2 * 10^{-6}$  respectively. The damage absorbed dose for Si was found to be 0.15 eV/atom. The threshold energy was taken the same as evaluated (0.17  $\mu\text{J}$ ).

The melting threshold for Si was estimated to be 0.4 eV, by using the following formula (see Eq 8.7)

$$C_v = 3 * K_B * T_{melting} \quad (8.7)$$

As mentioned before, the melting threshold dose was 1 eV (calculated in section 6.1 with the above-given formula) for Carbon. Hence, the sample reaches high temperatures close to melting temperature, at higher pulse energies, sooner at the substrate (in this case) compared to a-C. This causes an extra induced pressure which forces the coating outwards. The free carriers also have high energy and possibility to move around from a-C to Si or vice versa, and this causes secondary effects or ionization of further atoms on their path. Another effect is due to the shock waves, which increases the pressure inside the volume. This could happen in between the Si and a-C layer as well [113].

### 8.3 Photoemission spectroscopy results

Photoemission Spectroscopy (PEM) is a well-established surface analysis method to study the electronic structure of matter. PEM examines the sample with a specific wavelength of photon beam (beam of UV or XUV light), and one gains information on the binding energies of the electrons (which also depends on their vibrational state and rotational level) through emitted photoelectrons. SPEM as an imaging technique allows the same type of analysis in a space-resolved way. For solids, photoelectrons can only escape from a depth on the order of nanometers (that is the surface layer). The binding energies of the measured electrons are characteristic of the chemical structure and molecular bonding of the material. With this technique, one can gain information on changes in the bindings of the material. Hence, if the material is modified via damage process, SPEM measurement determines the changes.

The SPEM experiment was performed at the ESCA microscopy beamline at the Elettra synchrotron facility. The complete description of the beamline is given in ref [136]. In this experiment, the monochromatized X-ray photon beam with 649 eV was focused on zone plate optic. As a result, a circular spot with a diameter of about 150 nm was determined, which scanned over the sample. A hemispherical sector spectrometer collected the photo-emitted electrons, which were measured by a multi-channel (48-channel) detector. The data acquisition for each pixel was performed in a spectra-imaging mode.

Figure 8.15 shows the a-C 1s core level photoemission spectrum resulting from an average over  $10 \times 10$  pixels for two different regions correspondingly depicted. Black curve: Non-irradiated sample. Gray curve: Center of the irradiated sample corresponding to 1.4 J/cm<sup>2</sup>.

The SPEM spectra of the a-C show two energy regions. The first is (282.9 eV to 284.7 eV) where the signal is mainly due to  $sp^2$  bonds and the second (284.9 eV to 286.7 eV) corresponds to  $sp^3$  bonds. Determining peak positions, their intensities and width are a way to extract information on the chemical changes inside the sample [80] [137], [111]. In the irradiated area, the  $sp^2$  component is higher, whereas the  $sp^3$  is reduced compared to the original material, indicating the conversion of the  $sp^3$  to the  $sp^2$  bonds, e.g., graphitization of the sample, similar to what has been observed from an annealed a-C sample. [137]. Since the two components of the C 1s peak overlap, the SPEM images give only a qualitative indication and not an absolute measurement of the hybrid contents.

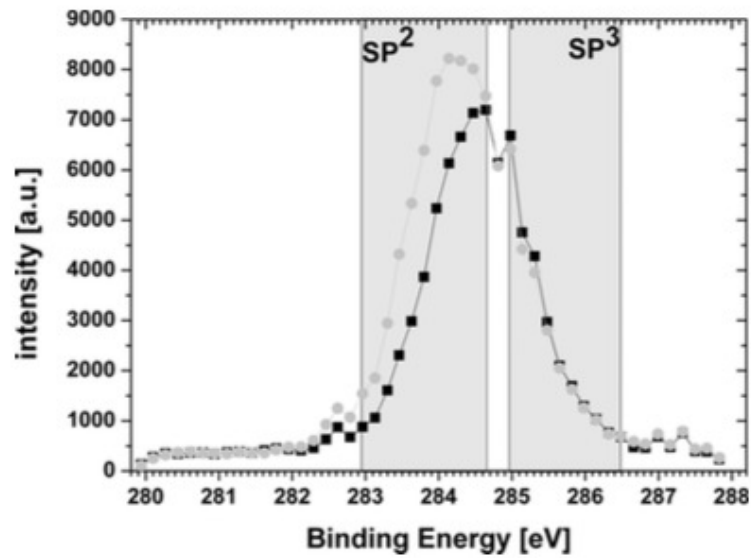


Fig. 8.15.: a-C Photoemission spectra from SPEM measurements obtained from averaging over two 10 X 10 pixel areas. Black curve: Non-irradiated sample. Gray curve: Center of the irradiated sample corresponding to  $1.4 J/cm^2$  with 830 eV photon energy [80].

## 8.4 Atomic Force Microscopy results

Atomic Force Microscopy (AFM) measurements provided information on the depth or the height of each damage spot, surface roughness, as well as the map of local fluence value which relates the height to the fluence value on each spot (see Fig 8.16).

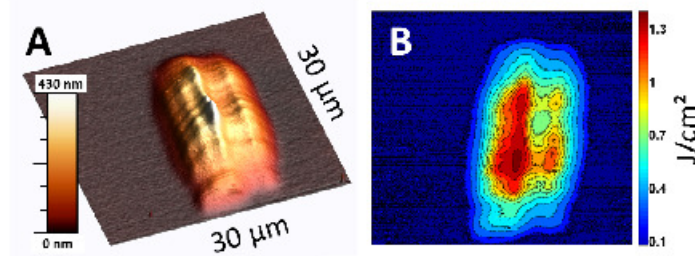


Fig. 8.16.: A: AFM topography of an irradiated area on a-C sample with a  $2.5 \mu\text{J}$  FEL pulse with  $830 \text{ eV}$  photon energy. B: Fluence map deduced from the AFM measurement. The color scale is in  $\text{J}/\text{cm}^2$  [80]. The material is expanded in volume.

Examining the damage spots via AFM reveals two different features: craters and swollen regions. Possible reasons for the observed swollen regions (mostly on a-C sample) are phase transition to graphite, melting and shock waves that push the material away towards the surface from the center of the damage spot (see Figs 8.16 – 8.20). Crater shape damage spots are detectable on a-C samples as well as on the CVD diamond (see Figs 8.19, 8.24). In comparison more craters can be observed in the case of CVD diamond, (see Fig 8.21 – 8.22) where the roughness at the spot has changed to higher values.

Since different features appear after the interaction of the beam with the sample, the depth up to which the damage is created inside the sample is not always measurable utilizing AFM spectroscopy.

With the help of a macro, it was possible to read out the AFM image of each measured spot in pixels. This was used to estimate the volume of each spot in  $\mu\text{m}^3$ . After all, the image was 3D mapped enabling reading of the volume of that spot. Some of these 3D images are depicted in the following Figures 8.17, 8.19 and 8.21. The calculated volume is then used to estimate if any mass is lost during the damage process. For this purpose one obtains the calculated volume of each damage spot via AFM data, knowing the density of the matter at the spot (which is the density of the graphite) and can discern the mass of the measured volume.

Also one calculates the amount of mass which might have been melted away during the damage process. This is calculated via  $Q = mC_v\delta T$ . Where  $Q$  is the energy of the pulse and  $C_v$ ,  $\text{J}/\text{grK}$  is the specific heat estimated with  $3N_A K/\text{mol}$  and  $T$  the melting temperature. We know the area of the incoming beam in each case, alongside the attenuation depth of each photon energy for each experiment, as well as the density of a-C or CVD. It is possible to calculate the expected volume the beam could travel into and have caused damage



and phase transition on the sample (a-C or CVD). In this way, one can also calculate the corresponding mass of the material which could be influenced by the beam. Comparing these three obtained masses makes clear whether part of the mass of material is lost. This comparison showed that a negligible amount of mass disappeared during the damage process. The amount of mass melted or evaporated away is very low at low pulse energies. This increases in the case of high pulse energies, which is in agreement with the simulation result of heat diffusion which can be found in chapter 9.

At high pulse energies the heat diffusion can heat up the substrate or the a-C to melting temperature, and this increases the pressure inside the damage and pushes the coating towards the surface or ablates the material. In the case of CVD, this increased pressure also induces shock waves as seen in the case of the experiment at 830 eV (see last Fig on the right for CVD diamond in Fig 8.1 [113]).

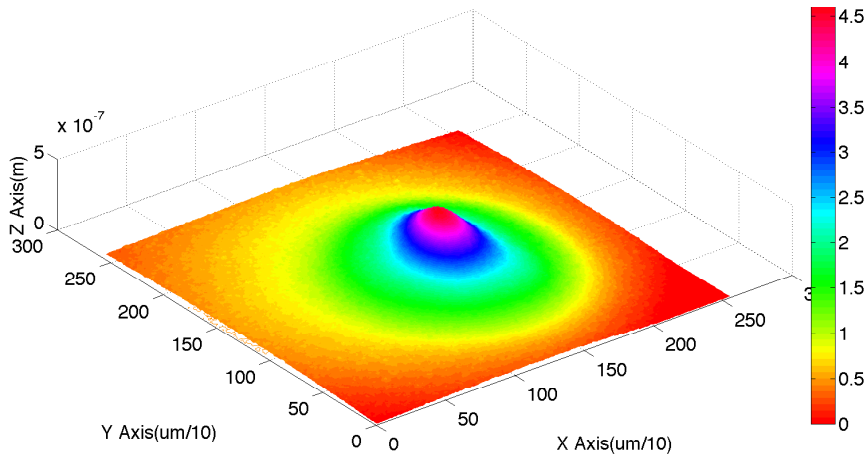
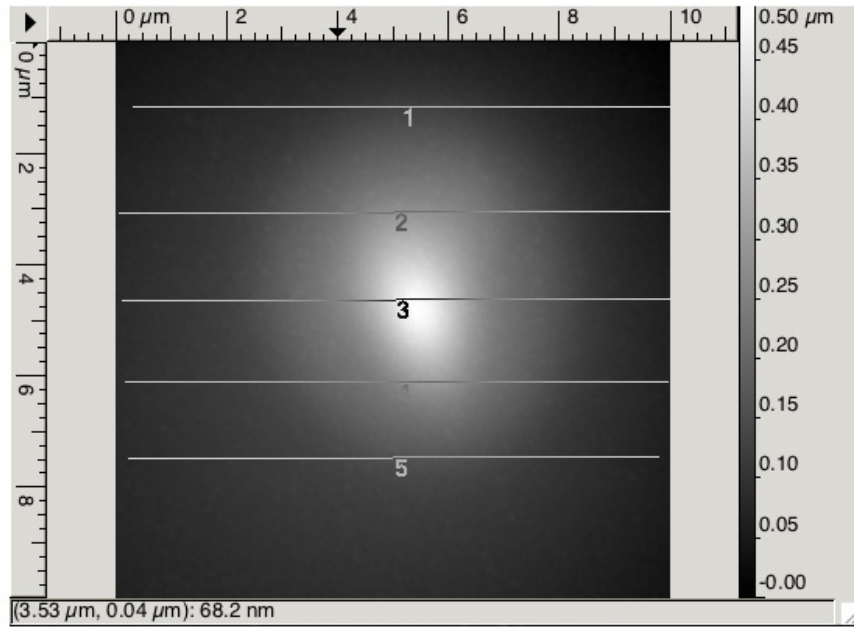


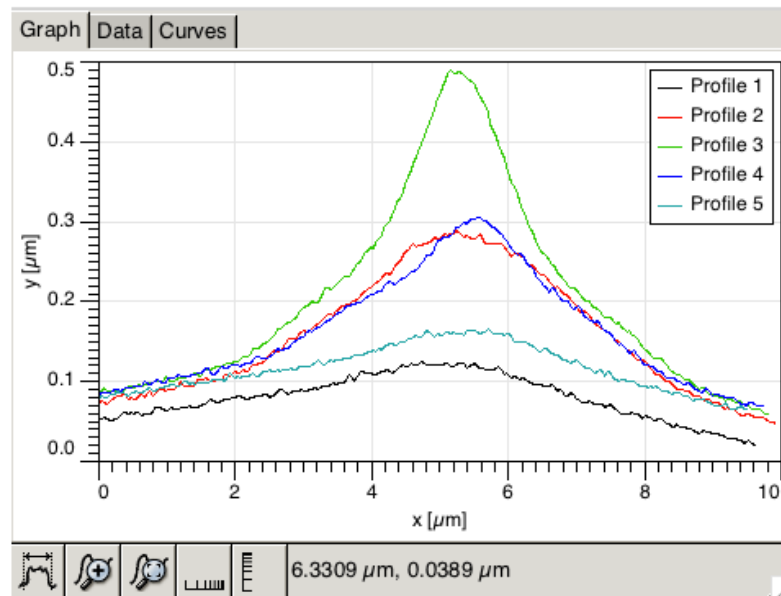
Fig. 8.17.: AFM topography volume profile of an irradiated area on a-C with a  $0.56 \mu J$  FEL pulse at 269eV at FLASH. Volume of the spot is calculated via the AFM image with the self derived MATLAB Code. The color scale is in  $J/cm^2$  [80].

Figure 7.21 in the previous chapter shows the Raman spectrum taken on the same spot as in Figure 8.20a which shows a clear growth of Graphite peaks inside the damaged spot and changes of phase of the a-C is observable. This could indicate the fact that the phase transition is mainly taking place without mass loss in the damage process.

It is possible to estimate the depth into which the damage inside the material is done, even if we do not have the possibility to measure this event directly via AFM microscopy in some cases. The estimation is done via following steps: First from the AFM profile, one can read the area of the damaged spot as well as its height. Damage spots show a cone shape form. Which allows one to calculate the volume of the measured profile with the volume of a cone (see Formula 8.9). Taking the density of graphite at the damaged spot and comparing it with the density of the original material (a-C or CVD diamond) allows for a simple calculation. Where the ratio of the densities is vice versa equal to the ratio of the volumes (see Formula 8.8). This comes from the fact



(a) AFM topography depth profile of an irradiated area on a-C with a  $0.56 \mu\text{J}$  FEL pulse at 269eV at FLASH. Lines represent the profiles taken.



(b) AFM topography depth profile.

Fig. 8.18.

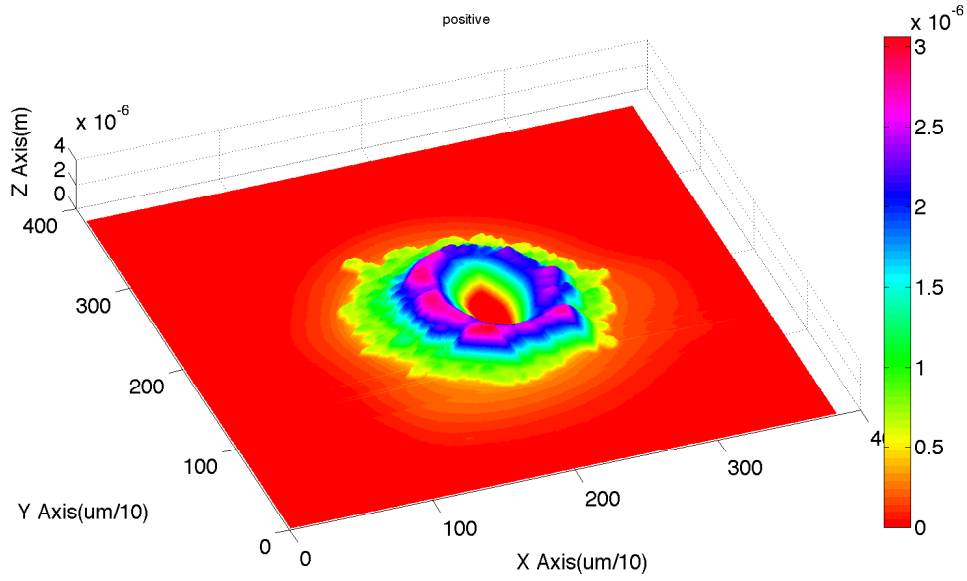


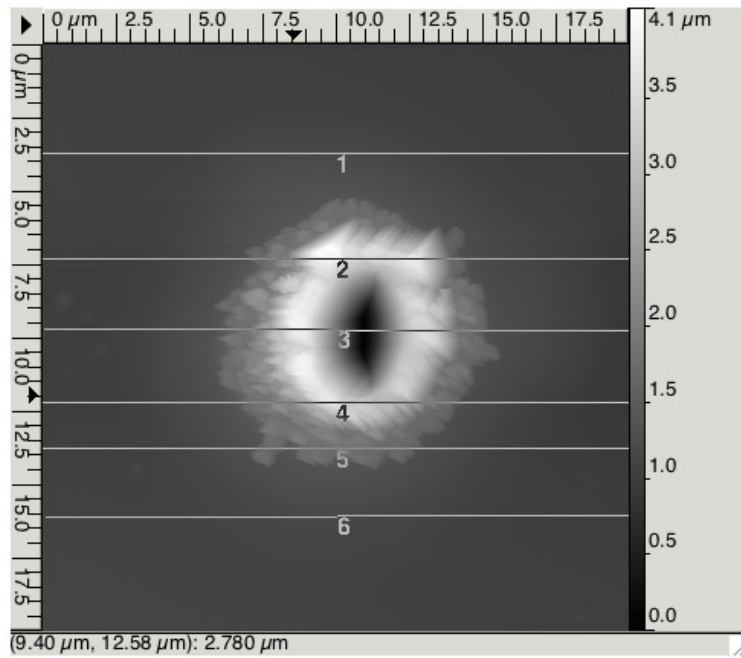
Fig. 8.19.: AFM topography volume profile of an irradiated area on a-C with a  $4,8 \mu J$  FEL pulse at  $177eV$  at FLASH. Volume of the spot is calculated via the AFM image with the self derived MATLAB Code. The color scale is in  $J/cm^2$ .

that we have estimated that no mass disappears during the damage process. Hence, it is possible to determine the depth to which the damage is done inside the sample. This depth is usually deeper than the attenuation depth. This can be observed in the following Figures 8.23, 8.20.

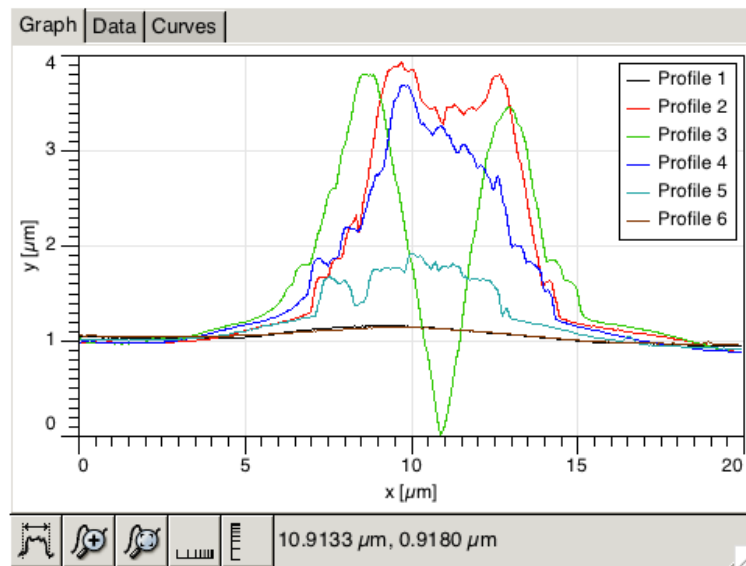
$$\frac{\rho_{graphite}}{\rho_{a-C}} = \frac{V_{a-C}}{V_{graphite}} \quad (8.8)$$

$$Cone_{volume} = \frac{\pi r^2 h}{3} \quad (8.9)$$

From these calculations, it can be seen that the estimated damage depth is in average, deeper than the attenuation depth, (which is usually taken into account in the dose damage threshold calculations). This might happen due to electron cascade after ionization and the heat diffusion process that causes deeper penetration depth inside the material.



(a) AFM topography depth profile of an irradiated area on a-C with a 4, 8  $\mu\text{J}$  FEL pulse at 177eV. Lines represent the taken profiles in (b).



(b) AFM topography depth profile.

Fig. 8.20.

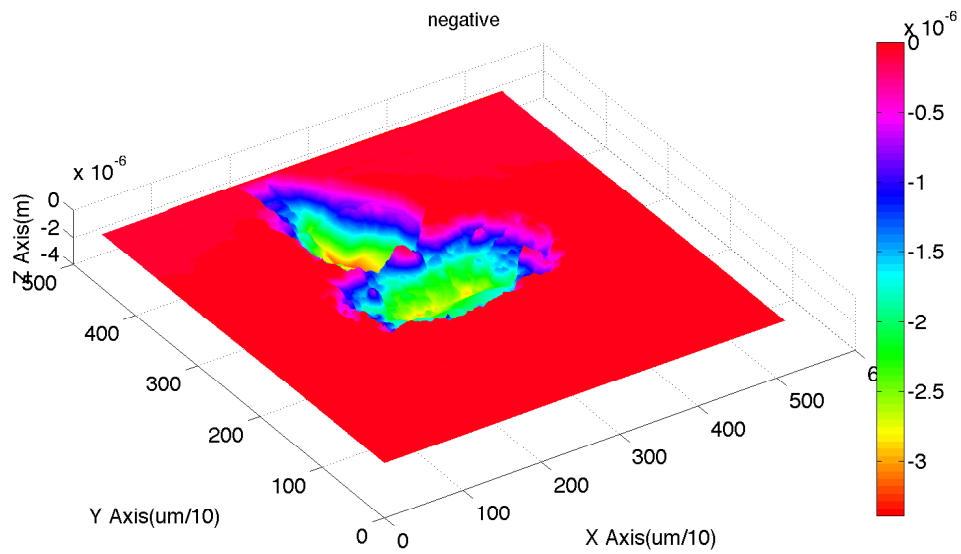
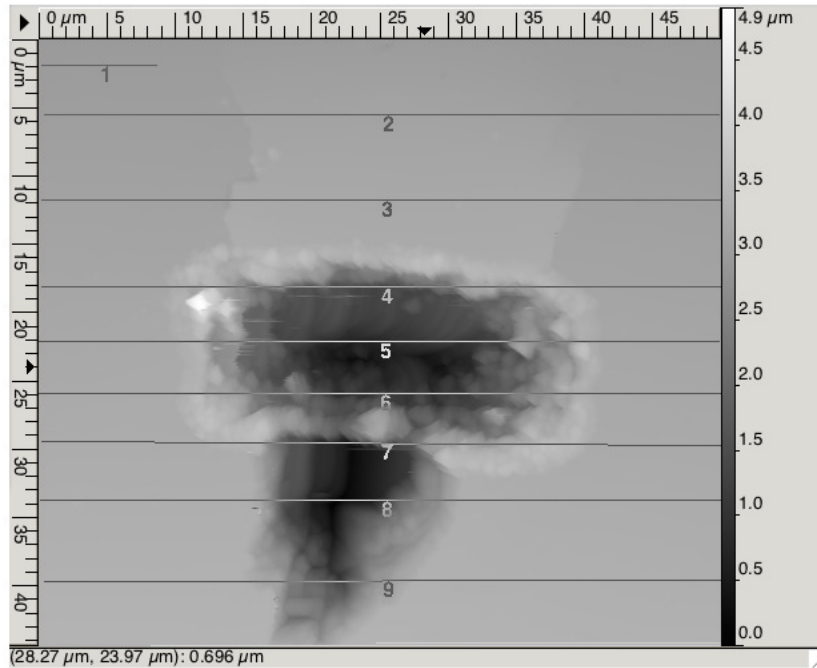
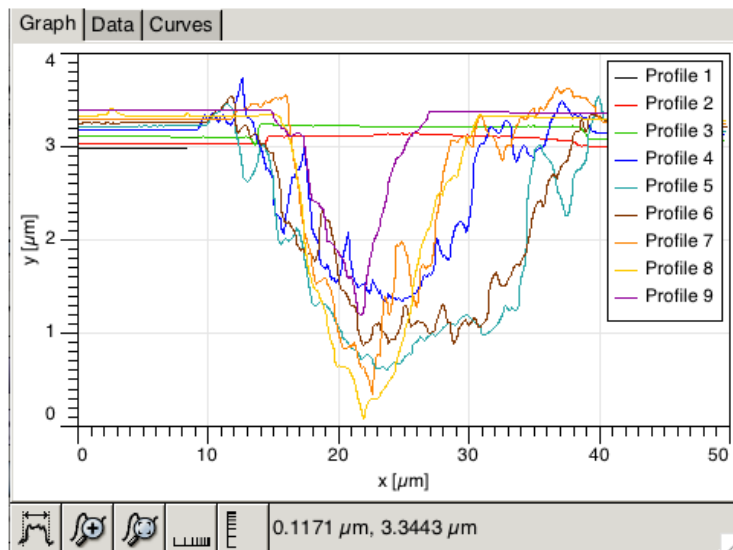


Fig. 8.21.: AFM topography volume profile of an irradiated area on CVD diamond sample damaged at LCLS at  $830\text{ eV}$  photon energy, with  $0.49\text{ mJ}$  pulse energy. Volume of the spot is calculated via the AFM image with the self derived MATLAB Code. The color scale is in  $J/cm^2$ .



(a) CVD diamond sample damaged at LCLS at 830 eV photon energy, with 0.49 mJ pulse energy. The AFM reveals: pressure induced graphitization, probably the result in a shock wave. This process can be triggered only for  $P > 100$  GPa. Lines show the taken profiles in (b).



(b) The AFM profile of (a) showing the depth and the shape of the damage spot.

Fig. 8.22.

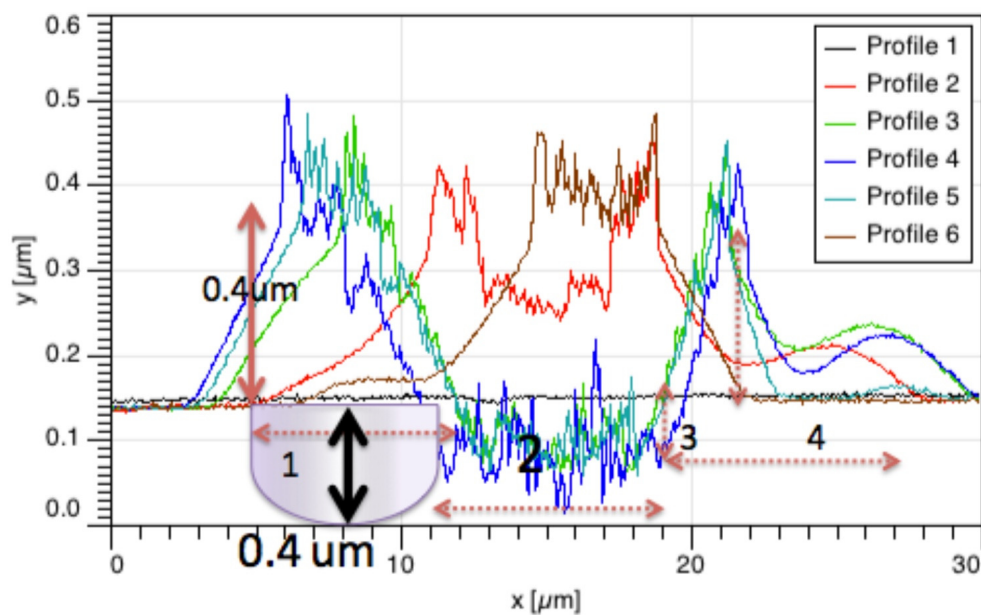
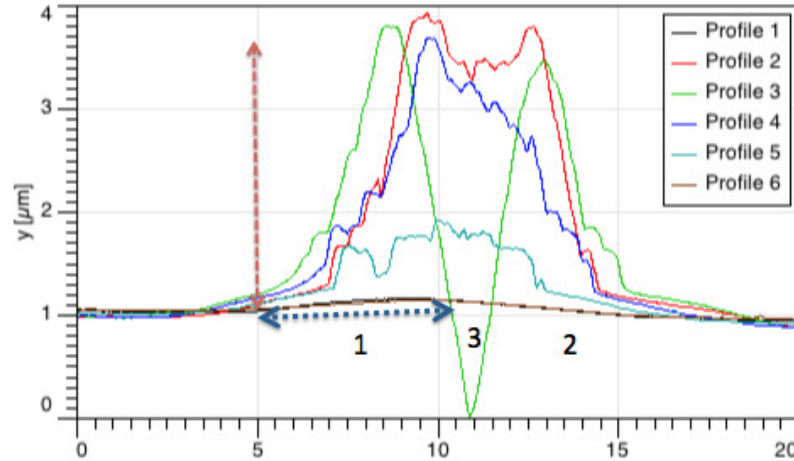
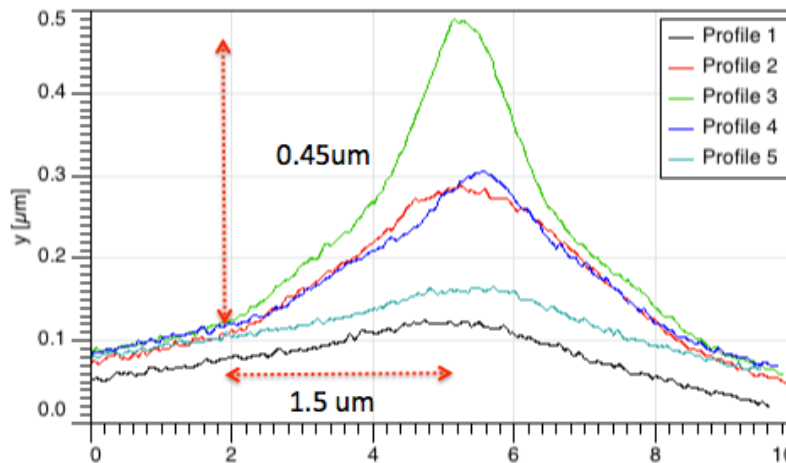


Fig. 8.23.: Amorphous carbon damaged with  $2.97 \mu J$  pulse energy and photon beam energy of  $91 eV$  at FLASH. The height and length are measured and through the Equation 8.8 the depth to which the damage could have been created is calculated. In region one the depth is calculated to be  $0.4 \mu m$ , region 2 it is  $0.1 \mu m$ , region 3 it is  $0.35 \mu m$  and region 4 it is  $0.61 \mu m$ . The attenuation depth at this photon energy is  $0.15 \mu m$ . In all these regions the depth to which damage might be reached is deeper than the attenuation depth. This is evidence that taking the attenuation depth for calculating the dose is not necessary the most accurate.



(a) Amorphous carbon damaged with  $4.8 \mu\text{J}$  and photon beam energy of  $177 \text{ eV}$  at FLASH. In the region one the depth is calculated to be  $6.07 \mu\text{m}$ , region 2 it is  $5.78 \mu\text{m}$ , region 3 it is  $1 \mu\text{m}$ . The attenuation depth at this photon energy is  $0.66 \mu\text{m}$ .



(b) Amorphous carbon damaged with  $0.56 \mu\text{J}$  and photon beam energy of  $269 \text{ eV}$  at FLASH. The depth is calculated to be  $0.77 \mu\text{m}$ . The attenuation depth at this photon energy is  $1.4 \mu\text{m}$ . In this case the thickness of the coating was much smaller than the attenuation depth ( $50 \text{ nm}$ ). That's why the substrate Si, was melted and due to the pressure the bubble shape region is detectable.

Fig. 8.24.



## 8.5 Raman spectroscopy results

In Raman spectra taken from carbon the two main characteristic peaks are the G and D peak lying at 1560 and 1360 ( $1/cm$ ) respectively (see Figs 8.25 and 8.29, as well as Figures in the Appendix 12.26, 12.27, 12.28, 12.29). In UV regime there is a so-called T peak observable around 1060 ( $1/cm$ ), but except the UV regime the Raman spectra from carbon is mainly driven by the  $sp^2$  bonds, which are due to the excitation of  $\pi$  bonds in the visible regime (because a  $\pi$  orbital usually interacts with  $\pi$  states of more than one atom to form a conjugated system such as benzene, then one can no longer define unique bond orbitals). Each bond is made of adjacent bonds, giving rise to longer-range forces and long-range polarizabilities [109], [110].

The visible regime resonates  $sp^2$  states the most. Hence, even if the  $sp^3$  content of the sample, in the case of amorphous carbon, is high, the excitation and Raman spectra are due to the  $sp^2$  bonds. The  $sp^3$  bond causes a C-C bonding vibration, only made of  $\sigma$  bondings. These are much easier detected under UV excitations. Under these circumstances, the total energy, charge density, or polarizability for each bond can then be expressed as simply the sum of independent, short-range terms. Figure 8.26 shows (with a simple sketch) the changes of the structures from a-C to graphite and Figure 8.28 shows the graphite structure with a certain distance between the parallel planes and their bindings. In the case of diamond or samples containing a significant fraction of diamond bonds, the spectra are dominated by the  $sp^3$  bonds, which results in a peak around 1332 ( $1/cm$ ) (see Figs 8.27, 8.30 and Table 8.7).

The G peak appears due to the bond stretching of all pairs of  $sp^2$  states in both rings and chains. The D peak is due to the breathing modes of the  $sp^2$  bonds in the rings. There is another observable peak in a defect graphite structure, called D' and appears around 1620 ( $1/cm$ ).

Raman spectra taken from Graphene and bulk graphite (see Fig 8.31 and Table 8.8) with visible light show the two most prominent peaks are the G peak around 1560 ( $1/cm$ ) and the so-called G' peak which is the second order of D peak and lies around 2700 ( $1/cm$ ) [138], [141], [142]. The peak's positions and names are summarized in Table 8.4.

The Raman spectrum is considered to depend on different stages

- clustering of the  $sp^2$  phase
- bond disorder
- presence of  $sp^2$  rings or chains
- the  $sp^2/sp^3$  ratio

Referring to the research of Tuinstra and Koenig ( $T_K$ ) [143] (regarding disorder in graphite), the ratio of the intensity of D peak to G peak varies inversely with the  $L_a$  (see Equation 8.10). This holds just for the case of low-level defects in the graphite.

In the case of high degree of disorder, the G peak position moves from 1560 to 1600 ( $1/cm$ ). The three dimensional ordering fades away and with that the

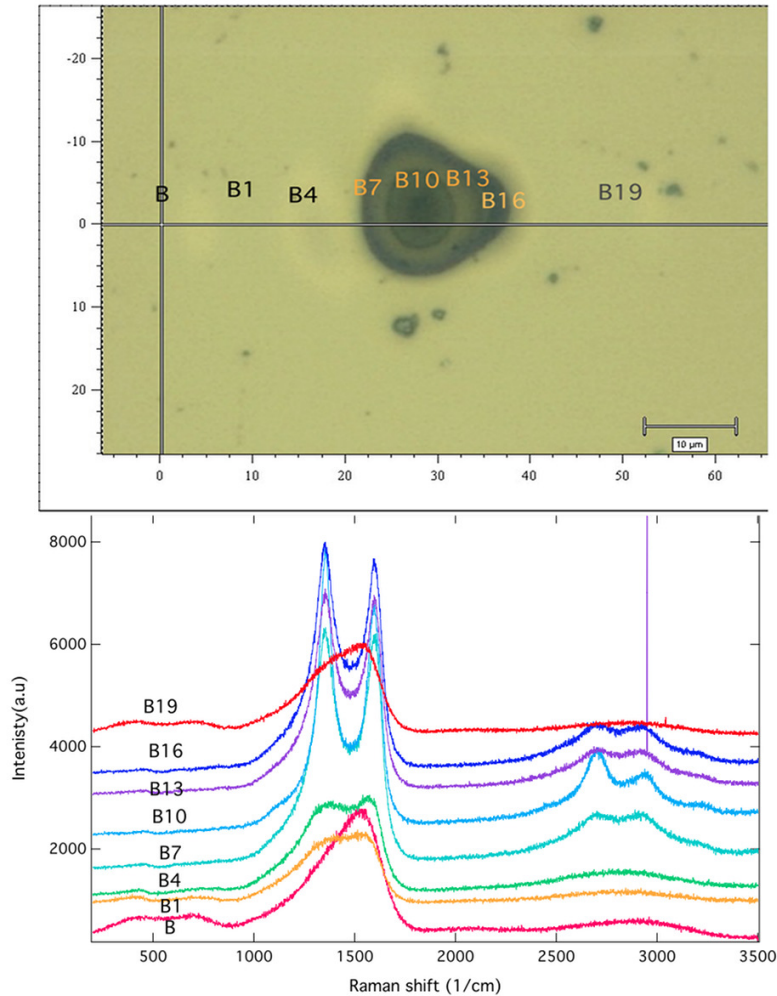


Fig. 8.25.: Amorphous carbon damage spot with  $4.83 \mu\text{J}$  and photon beam energy of  $91 \text{ eV}$  single shots at FLASH. The  $\mu$ -Raman analysis evidence the ordering of the a-C structure to nanocrystallites of graphite, in good agreement with the 3 step model of Ferrari et al [138], [109], [110], [139]. Looking at the heat simulation in chapter 9 shows that at this pulse energy a-C and Si both have reached melting temperature. This figure also shows that beam fringes are observable at this point. This could be due to the apertures in beamline and the beam focus which was causing interference patterns on the sample. This fact that graphitization is observable outside of the main dark spot of the damage is clearly showing that a larger area of the sample at the damaged spot compared to the beam radius at this experiment was effected, and phase transformed. The rest of Profiles which are not shown here are presented in the Appendix. The profiles are enumerated from B-B20 (see Fig 8.29 and in Appendix 12.5).

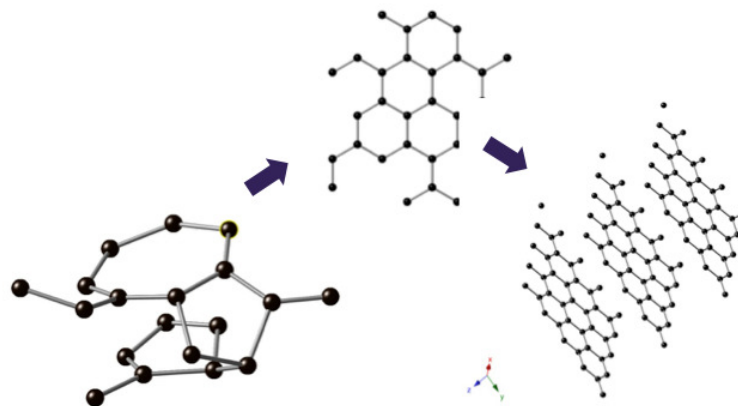


Fig. 8.26.: structural changes from amorphous to graphite.

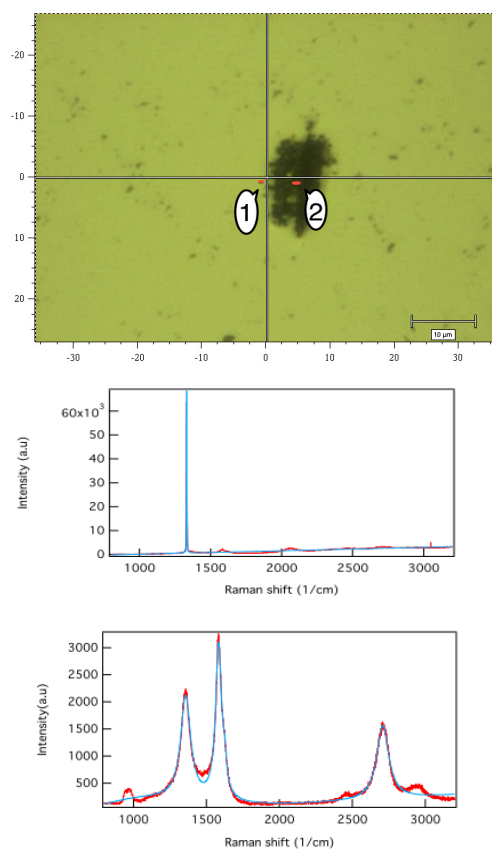


Fig. 8.27.: Raman spectrum of CVD diamond sample damaged at LCLS with  $830\text{eV}$  photon energy and  $5.11\ \mu\text{J}$  pulse energy. Raman spectra were taken from two different spots on the sample, marked as 1 and 2. The red line shows the Raman spectrum taken on the spot and the blue line shows the fit. Spectrum on point 1 is plotted first and underneath is the spectrum on point 2, which is on the damaged spot directly. Point 1 lies at the edge where no graphitization is observed and it shows a CVD diamond characteristic peak.

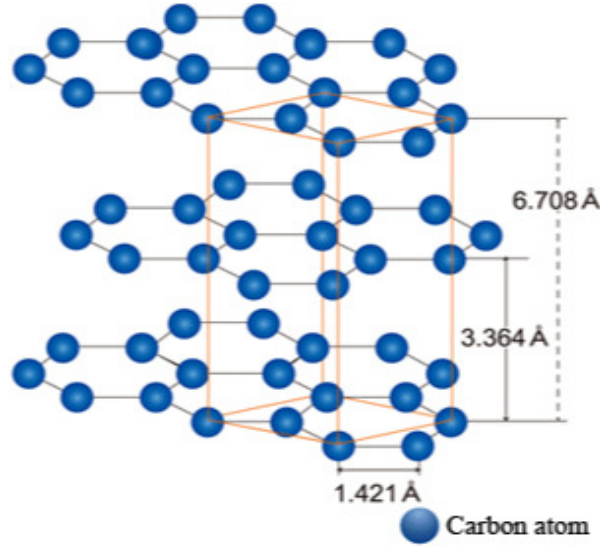


Fig. 8.28.: Sketch of Graphite structure [140].

doublet in D peak and in its second order peak disappear. The ratio of D to G peak intensity changes to the  $L_a^2$  (see Equation 8.11 [144], [145], [143]). Through the calculations, the size of graphitized region is on the order of  $nm$ . Looking at Figure 8.28 shows the distance between the nearest neighbor atoms in the graphite sheets. From the Raman spectra taken on a-C (depicted in Fig 8.25), on spot B7 the length of these sheets is calculated via the ratio of  $I_D/I_G$ , this was about  $3.4 nm$  when considering the low order graphite structure and considering the  $L_a^2$  formula the sheets would be  $6.9 nm$  long. These calculations were performed considering the following Equations (see Equations 8.10, 8.11):

$$I(D)/I(G) = C(\lambda)/L_a, C(515) \sim 44\text{\AA} \quad (8.10)$$

$$I(D)/I(G) = C'(\lambda)L_a^2, C'(515) \sim 0.0055 \quad (8.11)$$

If one assumes the planes are not parallel to the surface but perpendicular, the above-calculated length would be the depth to which the phase transition occurs. Hence, comparing the depth calculated from the AFM data in section 8.4 can give us an idea of the direction of the planes.

From AFM estimation on the a-C, the calculated depth was  $0.4 \mu m$  and  $0.6 \mu m$ , whereas the planes are calculated to be  $6.9 nm$  long. This does not match, which gives an indication that the planes are probably oriented or tend to orient parallel to the surface rather than perpendicular.

Increasing the disorder causes the clusters to shrink and rings to diminish in number, that results in an increase in distortion until they open up. Since with the loss of  $sp^2$  rings the intensity of D peak reduces, and the  $T_K$  relation is no longer valid.

For small ' $L_a$ ', the D mode strength is proportional to the probability of finding a sixfold ring in the cluster, i.e. to the cluster area. Thus, in amorphous carbon the development of a D peak indicates ordering, that is exactly the opposite to the case of graphite [146], [147], [148].

Bond	peak position (1/cm)	name
$sp^2$	1360	D
$sp^2$	1560	G
$sp^2$	1620	D'
$sp^2$	2700	G'
$sp^3$	1332	-

Table 8.4.: Bonds and their pick position on a Raman spectra

With a small fit function developed in Igor the spectra were fitted for evaluation. A combination out of the most widely used Voigt (see Equation 8.12) for the G peak (due to its asymmetric line shape) and a Lorentzian 8.13 function (for the D peak) has been used to fit these spectra [139], [149], [150], [151], [152], [153], [109], [110].

$$I_{voigt} = \frac{a_0 \cdot a_3}{\pi \cdot \sqrt{\pi} \cdot a_2} \int_{-\infty}^{\infty} \frac{e^{-(t^2)}}{(a_3 + (1 + (((x - a_1)/a_2) - t)^2))} dt \quad (8.12)$$

$$I_{Lor} = \frac{a_0}{\pi \cdot a_2 (1 + (x - a_1/a_2)^2)} \quad (8.13)$$

$a_0$  is peak intensity,  $a_1$  is peak position,  $a_2$  is assumed as the full width at half maximum FWHM, and the shape in the Voigt function is represented by  $a_3$ . The combination of the two named functions is the fit function used for these analyses.

sample-Spot Nr	$sp^3$ peak position (1/cm)	G peak position (1/cm)	$sp^3/sp^2$ area	$sp^3/sp^2$ height	$sp^3/sp^2$ FWHM
a-C-B	1334	1532.9	1.14	0.61	1.24

Table 8.5.: Result of the Raman experiment on a-C sample damaged with the photon beam of 91 eV and with pulse energy of 4.83  $\mu J$ . In the case of spot B the D peak is not detectable, instead the  $sp^3$  peak. The amorphous carbon has combination of  $sp^3, sp^2$  and  $sp^1$  bonds. In the case of the samples for this project the ratio initially was  $sp^3/sp^2=0.2$ .

Raman spectra taken on a-C and the information gained from those are represented in Tables 8.5 and 8.6. It is observable that, the  $sp^3$  peak appears around 1332 (1/cm), depending on the deformation of the bond it might shifted to other values. The G peak should theoretically appear around 1560 (1/cm) and the D peak around 1360 (1/cm) as mentioned before, they represent the  $sp^2$  bonds. In Table 8.6, the G peak position gets shifted from 1560 (1/cm) to 1593 (1/cm). This fact helps to gain information on the degree of Graphitization.

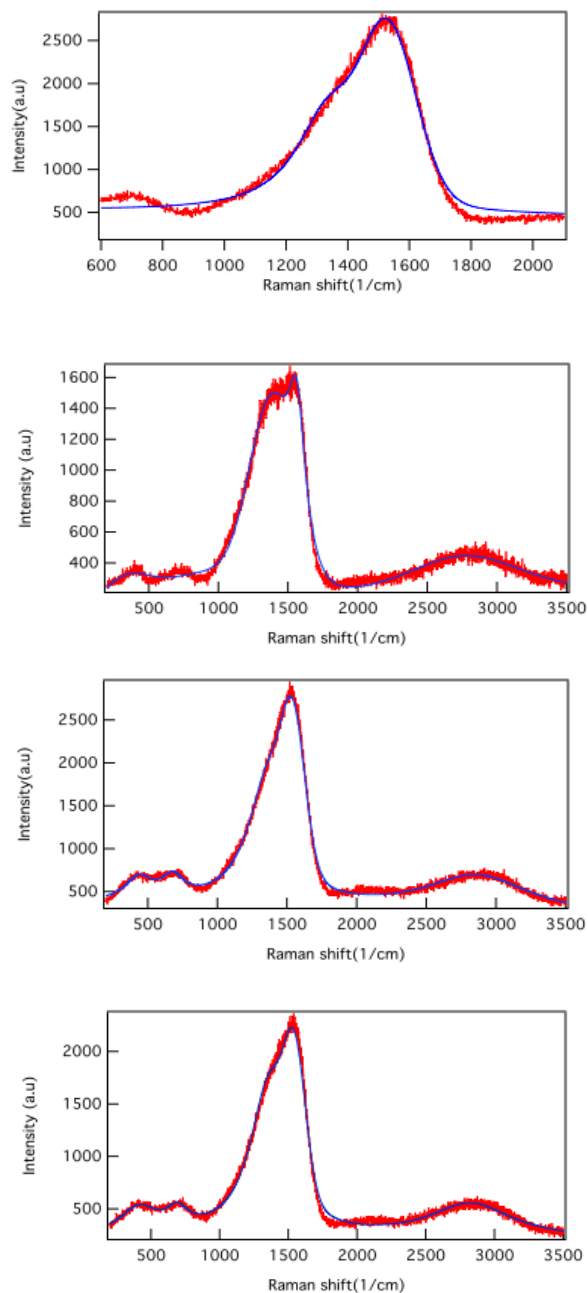


Fig. 8.29.: a-C exposed to the 91 eV beam with single shots at FLASH with  $4.83 \mu J$  pulse energy. The positions on which spectrum has been taken are marked in Fig 8.25 respectively from top to bottom (B-B3). The rest of spectra on the pointed spots are depicted in the appendix A.

sample-Spot Nr	D peak position ( $1/cm$ )	G peak position ( $1/cm$ )	D peak area /G peak area	D peak height/ G peak height	D peak FWHM/ G peak FWHM
a-C-B-1	1377.5	1564.5	2.55	1.43	2.62
a-C-B-2	1359.1	1543.5	2.24	0.88	1.73
a-C-B-3	1356.2	1545.9	2.84	1.11	1.76
a-C-B-4	1354	1566.3	4.57	1.46	2.10
a-C-B-5	1352.3	1561.7	4.87	1.49	2.20
a-C-B-6	1364.9	1589.2	4.10	1.26	2.20
a-C-B-7	1359.6	1591.9	2.86	1.16	1.76
a-C-B-8	1360.5	1592.4	2.82	1.14	1.79
a-C-B-9	1357.4	1592.6	2.08	1.16	1.45
a-C-B-10	1356.2	1592.9	1.64	1.23	1.18
a-C-B-11	1356.6	1592.9	1.79	1.18	1.31
a-C-B-12	1357.4	1592.4	2.01	1.16	1.41
a-C-B-13	1357.4	1591.6	2.96	1.13	1.75
a-C-B-14	1359.3	1592.1	2.83	1.15	1.80
a-C-B-15	1357	1593	2.49	1.17	1.65
a-C-B-16	1357.5	1591.8	2.81	1.21	1.68
a-C-B-17	1351.6	1562.3	4.49	1.48	2.05
a-C-B-18	1356.5	1543.5	2.21	0.8	1.78
a-C-B-19	1364.4	1548.7	4.10	1.31	2.11

Table 8.6.: Result of the Raman experiment on a-C sample damaged with the photon beam of 91 eV and with pulse energy of 4.83  $\mu J$ . The amorphous carbon has combination of  $sp^3$ ,  $sp^2$  and  $sp^1$  bonds. Initially the ratio of  $sp^3/sp^2$  was 0.2.

The G' peak around 2700 ( $1/cm$ ) is also observable, depending on the position on which Raman spectra has been taken (on the damage spot or outside) and on the degree of graphitization (see Figs 8.29- 12.29 (one set of images are depicted here and the rest in Appendix B)). In Table 8.6 clearly it's obvious that the G peak gets wider and grows higher when traveling from out side towards the middle of the damage spot. Of course it doesn't reach a pure Graphite peak width or height but changes are clearly observable.

A large area around the damage shot (outside of the damaged spot) on the a-C sample shows some signs of varying low degree graphitization. In the case of CVD diamond, right after the black damaged part, there is sole evidence of CVD diamond peak and no sign of D and G peaks (see Fig 8.27 red line is the spectrum and blue is the fit). The table 8.7 includes information on the peak position, peak width, and height of the CVD diamond sample damaged at LCLS (830 eV) with pulse energy of 5.11  $\mu J$ . Outside of the damaged spot, there is just one peak present that represents the CVD diamond structure. On the damaged spot, both G and D peaks are developed, indicating the phase transition of diamond to graphite.

Comparing the Raman spectra on CVD diamond taken at different photon energies but with a fix pulse energy, evident that the graphitization process

sample	D peak position (1/cm)	G peak position (1/cm)	D peak area /G peak area	D peak height/G peak height	D peak FWHM/G peak FWHM	$sp^3$ position
CVD diamond-on the 1	—	—	—	—	—	1331.7
CVD diamond-on the 2	1357.6	1583.9	1.07	$3.11e^{-5}$	1.62	—

Table 8.7.: Result of the Raman experiment on CVD diamond at LCLS with 830 eV photon energy and the pulse energy of 5.11  $\mu J$  sample.

had occurred in all these cases. The pulse energy with which the damage was created is around 5  $\mu J$  (Fig 8.30). Noteworthy is the change in the degree of graphitization. This could occur due to experimental conditions as well as differences in the photon energy of the incoming beam.

These spectra indicate an increase in the degree of graphitization moving from low to high (20-830 eV) photon energies. This means the higher the photon energies, the higher energized ionized electrons and free carriers. Hence, they create more free carriers and, therefore, secondary processes are sustained for longer and are also stronger. The higher photon energies also mean that the attenuation depth and the affected volume is larger. That means that those high energetic electrons get distributed over a larger volume.

A Raman spectrum of a pure graphite sample depicted in Fig 8.31 with the Table 8.8 provides information on the position of each D and G peak, their intensities, FWHM alongside peak areas.

sample	D peak position (1/cm)	G peak position (1/cm)	D peak area /G peak area	D peak height/G peak height	D peak FWHM/G peak FWHM
Graphite	1351.7	1577.9	0.34	2.48	2.53

Table 8.8.: Result of the Raman experiment on the Graphite sample.



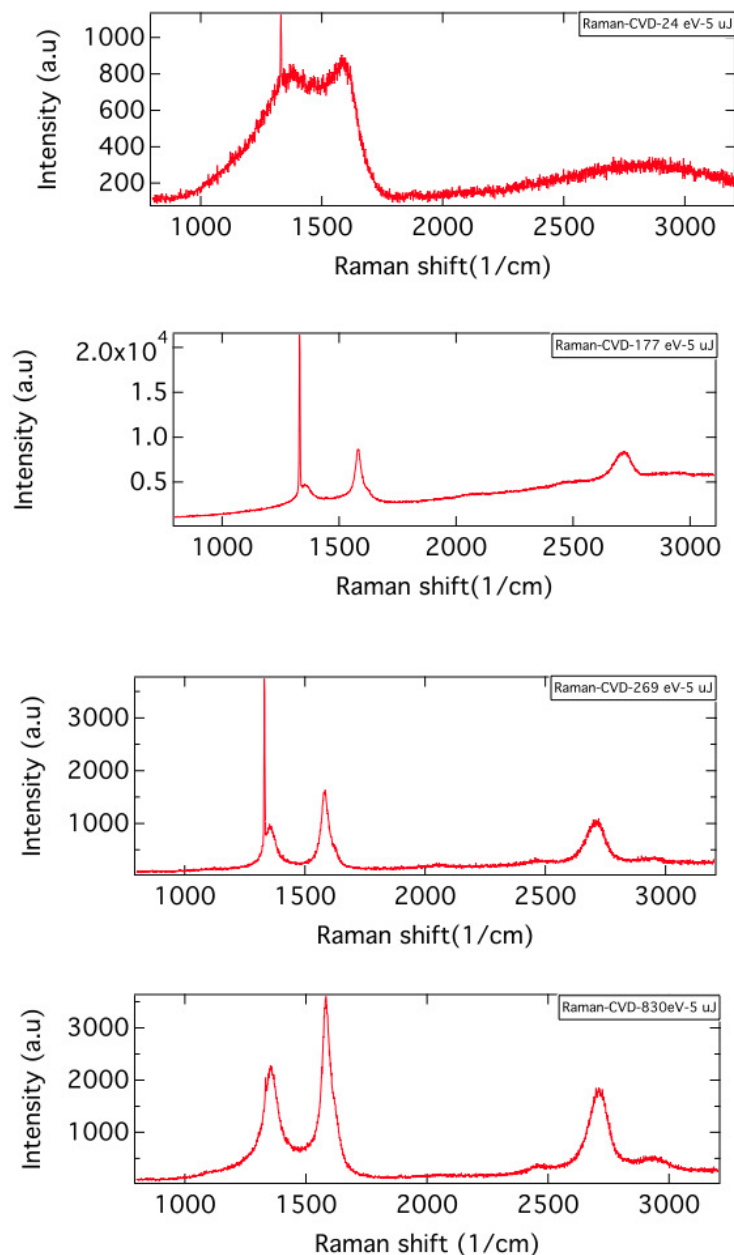


Fig. 8.30.: Raman spectrum on CVD sample at different photon energies with the same pulse energy ( $5 \mu J$ ) are compared. Graphitization process has been seen in all of these experiments and the degree of this process changes. Depending on the photon energy and experimental conditions these differences in peak width, position etc. have happened. Samples have had the same quality in all of these experiments.

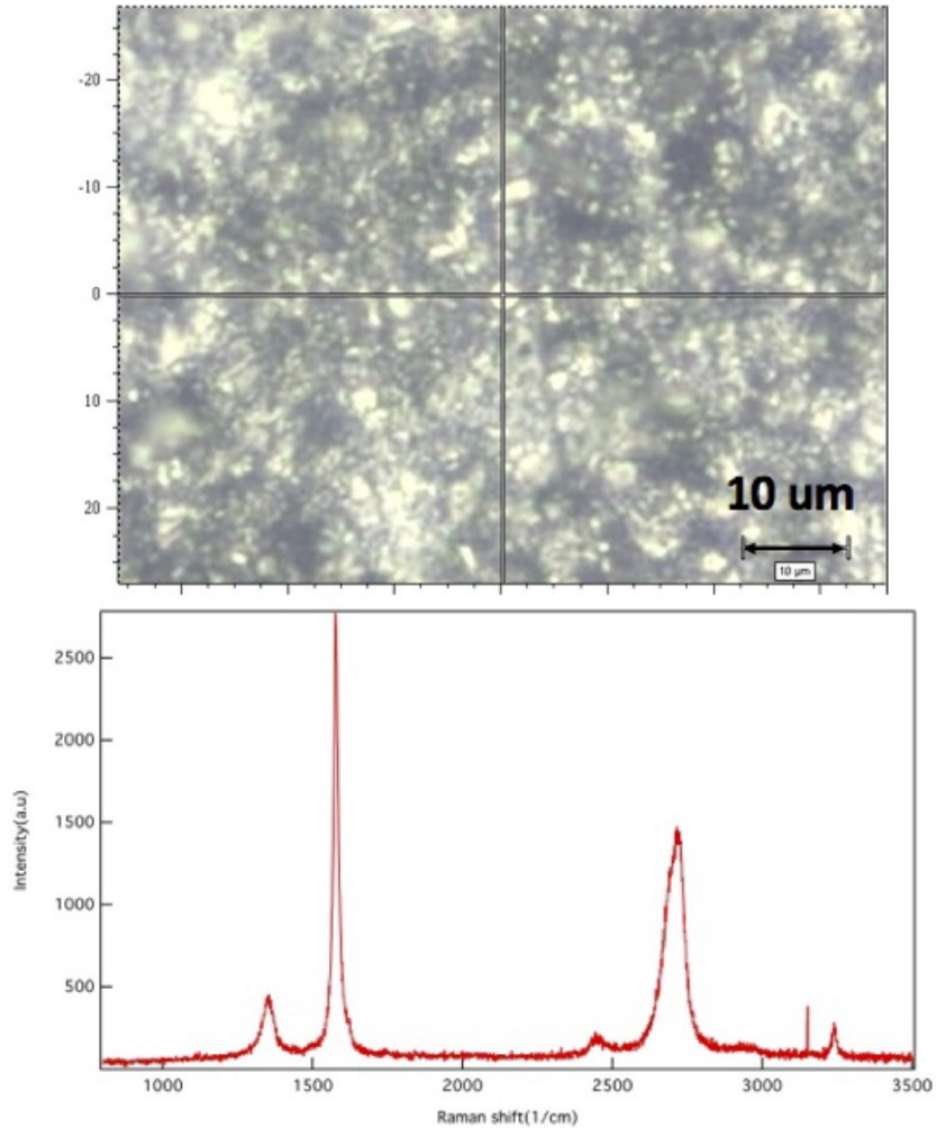


Fig. 8.31.: Raman spectrum of pure Graphite sample to compare with the damaged a-C and CVD diamond samples. Raman spectra were taken from the white spots and black spots on both the samples. The results were the same.

## Chapter 9

# Simulations

In the following two sections, the results of theoretical simulation via Hybrid XTANT model and the heat diffusion process (simulated via COMSOL) are presented. With the help of Hybrid model, it is possible to follow the changes of the electronic states and its potential energy states, from the time that the FEL pulse irradiates the sample until some 100's of *fs* after the irradiation. This section focuses on the ionization processes and consequences as bond breaking, secondary processes, etc. Heat diffusion, on the other hand, starts to take part in the damage process after some 100's of *ps* after the irradiation and last up to some  $\mu s$  until sample gets back to the room temperature. Heat diffusion helps to estimate if the sample could reach melting temperature during the damage process and how far it could affect the size of imprints. After some 100's of *ps* one can not separate these processes from each other. There is an overlap between them, where each process is active but with different intensity compared to the other.

### 9.1 Hybrid code XTANT (Theoretical simulation)

Under femtosecond irradiation as mentioned in chapter 5, semiconductors undergo several sequences of processes. The photo-ionization process, which happens within *fs* is followed by secondary processes like decay of Auger electrons or fluorescence photons. These decays lead to the production of further atomic excitation, bond breaking, and free carriers production e.g. via exciting electrons from the valence band into the conduction band. Elastic or inelastic scattering of electrons or photons (for example through impact ionization) takes place within *fs*, while the scattering of electrons on atoms or phonons leads to significant energy losses and occurs over significant longer time periods, typically in the order of *ps* [154], [155].

This inter-particle interaction leads to changes of the inter-particle potential energy. The electronic state of the system in covalently bonded material influences the (inter) atomic bindings. Hence, any changes e.g. the number of anti-bonding states will result in an ultra-fast rearrangement of atoms. This is because the system tries to balance and minimize the potential energy of the electronic system. This happens in the form of phase transition, where in the

case of diamond,  $sp^3$  bonds change into  $sp^2$  bonds and the material turns into graphite. A phase transition process can take place in a few hundred  $fs$ . The photo-ionization process is the leading process here. Besides, there is a great possibility that graphitization occurs due to the heat generated through free carriers. Calculations show that around  $T_m = 1360 K$  diamond can undergo graphitization. This temperature is calculated with Lindemann's formula (see equation 9.1) and so-called intra-cell graphitization [156].

$$T_m = \frac{x_m^2}{9\hbar^2} MK\theta^2 r_s^2 \quad (9.1)$$

The theoretical simulation attempts modeling the phase transition through  $fs$  FEL pulses and is undertaken by a group of theoretical physicists. The group comprising Dr. H. Jeschke, Dr. N. Medvedev and Dr. B. Ziaja at Frankfurt University and CFEL in DESY in Hamburg developed a Hybrid model, which traces non-equilibrium kinetics of electrons under ultrashort laser irradiation and follows the rearrangement of atoms.

The model is based on the following combined codes (Monte Carlo, Tracing the temperature of valence and low energy conduction band electrons, Molecular Dynamics, Tight Binding model) described in great detail in the following references [17], [157], [158], [135], [30], [159], [36], [160], [161]. These models are briefly explained here:

- Monte Carlo (MC): treating the non-equilibrium kinetics of high energy electrons after photo-absorption. Here, the photo-absorption and secondary electron cascading have been modeled in a simulation box. The photon pulse temporal profile is taken to have a Gaussian shape with e.g.  $10fs$  FWHM. The penetration details are taken from photo-absorption length corresponding to the specific photon energy. Photo-absorption can occur in valence band or K-shell depending on the energy of the photon. In the case of valence band photo-absorption in this model, an energy level among all the valence band levels has been chosen randomly (obtained from tight-binding formalism). In this model, it is assumed that each photon excites just one electron. The excited electron undergoes several secondary scattering processes. The inelastic mean free path of these electrons, which depends on their energy, has been calculated using the complex dielectric function. The inelastic electron scattering cross section is therefore calculated with the help of the complex dielectric function within the first Born approximation. The mean free path of electrons for diamond and graphite is then calculated and compared in this model. This shows that mean free paths are similar to each other for both graphite and diamond. Due to the difference in the band gap of graphite and diamond, a shift to a lower energy is present in the case of graphite. The band gap of diamond is around  $5.5 eV$  whereas this vanishes for graphite because it is a semimetal.
- Tracing the temperature of valence and low energy conduction band electrons, which are in thermal equilibrium:  
The low energy electrons are assumed to be in partial equilibrium. The

number of electrons which get excited to high energy states or fall back into low energy states is followed here. This distribution function for valence band and the low energy conduction band is calculated via Fermi function. This is carried out because the electron distribution function changes due to the changes in the electronic states. This is defined in the MC step algorithm.

- Molecular Dynamics (MD), focuses on picturing the atomic motion of all atoms individually in the simulation box:  
The classical motion of all atoms are described by spatial coordinates and velocities, and the collective potential energy surface is described quantum mechanically. Two cases analyzed here are under two different conditions, one with a constant volume of the simulation box and the other with constant pressure (see Fig 9.2). The potential energy surface is defined by the transient electron distribution function, the position of all atoms in the supercell and by the transient band structure updated with the tight binding method at each time step. For constant volume simulation, the MD model employs Parrinello-Rahman method [162].
- Tight Binding model for tracing the transient electron band structure and collective interatomic forces:  
In this part of the model, the electronic energy levels are calculated at each time step. This is used to determine the potential energy surface. The interatomic forces are being calculated here. The atomic Hamiltonian considered here is two-fold: The attractive part depending on the electron configuration and the repulsive part which illustrate the repulsion of atomic cores.

A simple schematic is depicted in Fig 9.1 which shows how these models are combined and the structure of the simulation is built.

With this model, they have tried to reproduce the experimental parameters at different photon energies and for different fluences. Some of simulated results in the case of 830 eV are depicted below (these data sets are not published yet) in Figs 9.4a, 9.4b, 9.4c, 9.4d. From the previous calculations it was expected that at constant pressure the value of 1 eV/atom absorbed dose is above the damage threshold. The damage threshold in the case of diamond in previous works was reported to be 0.69 eV/atom for constant pressure. With the help of this Hybrid model, the damage threshold for constant volume was calculated as well and found to be 0.74 eV/atom (see ref [158], [159], [36]). A simple sign for recognizing the phase transition is the sudden strong drop in the atomic potential energy. This can be seen in Figs 9.4a for fluence energy of 1.87 J/cm<sup>2</sup> at 830 eV photon energy. These graphs show that the total energy is constant except for the deposition time. In this period the energy is transferred from the pulse to the high energy electrons. Hence, the total energy of atoms is lower than the total energy of electrons and atoms. After some time this changes and some part of the energy gets transferred to the potential energy, in other words to the low energy domain. Hence, both the total energy of atoms and electrons (blue) and total energy of atoms (green) curves meet (see Fig 9.4c). Around 90

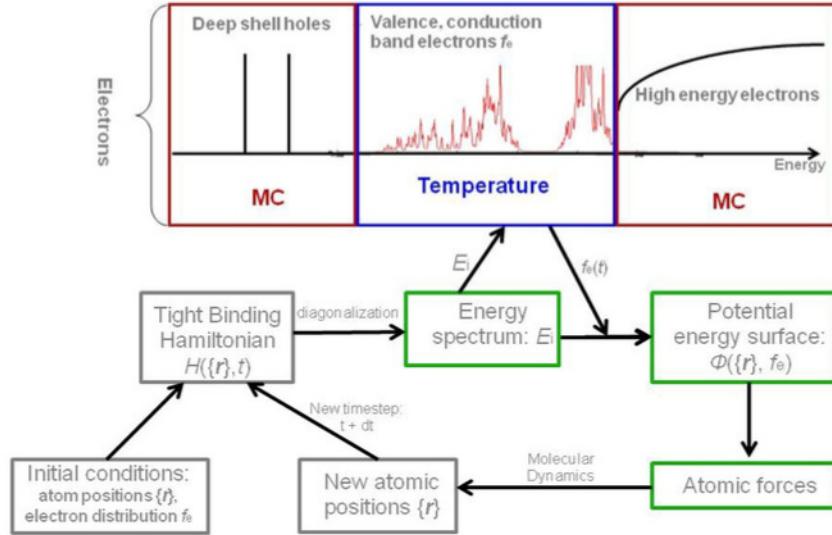


Fig. 9.1.: Schematic picture of the algorithm of the developed combined model consisting of the interconnected modules responsible for different calculations: MC, Temperature equation for electrons, tight binding model and MD [158].

$f_s$  the potential energy undergoes strong decrease. That is because of the phase transition of diamond to graphite which has happened at this point. At  $92 \text{ eV}$  the potential energy has been calculated for both cases of constant pressure and constant volume (see Fig 9.2). Here one can observe that phase transition in the case of constant pressure takes place in a shorter time of  $90 \text{ fs}$  compared to the constant volume where phase transition occurs after  $200 \text{ fs}$  post irradiation. This is because the system in a fixed volume can not relax as a whole. Thus, phase transition takes a longer time. Which actually might be closer to what happens in real case (there has been no experiment so far studying this to test its proof). The pressure has high fluctuation compared to the volume when the phase transition occurs.

Other evidence indicating the phase transition can be found in changes of the band gap. Figure 9.4d (for fluence of  $1.87 \text{ J/cm}^2$ ) clearly display that around  $90 \text{ fs}$  the band gap disappears from  $5.5 \text{ eV}$  to almost  $0 \text{ eV}$ . Due to some fluctuations because of numerical reasons it could be reasonable to consider this drop to  $1 \text{ eV}$ .

It is also obvious that the chemical potential has dropped as the band gap disappears but again get back to its initial value after the phase transition. As a consequence of changes in the potential energy of the system, electrons' and atoms' temperature changes after the irradiation. This is observable in the following Fig 9.4b for fluence of  $1.87 \text{ J/cm}^2$ . The electrons' temperature rises first, and after the phase transition, it decreases. There is an increase in the temperature of atoms after the phase transition. This is where heat diffusion in the system plays a role and carries the heat into the rest of the system towards the substrate and along the surface (see section 9.2). The phase transition turns diamond into graphite. This means that material changes from an electrical

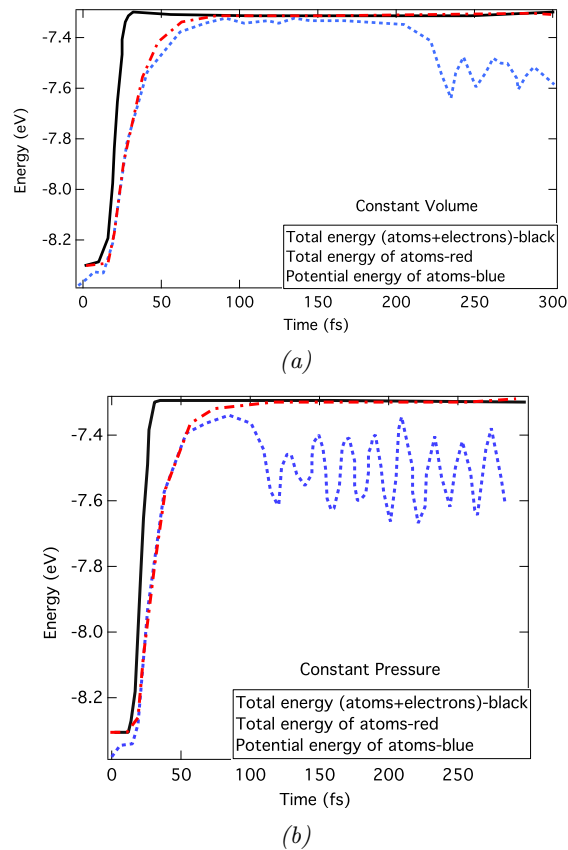


Fig. 9.2.: (a): Diamond irradiated at  $92 \text{ eV}$  photon energy with  $10 \text{ fs}$  laser pulse. The absorbed energy was  $1 \text{ eV/atom}$ . The total energy of the system (electrons and atoms) is plotted in black and total energy of atoms is depicted in red dash line, the blue dashed line shows the potential energy of the system [158]. (b): The same simulation under the constant pressure.

insulator to semimetal, and in this case, there is no band gap; and also the conduction band should be occupied like the case in metals. This is depicted (for the case of irradiation with fluence of  $1.87 \text{ J/cm}^2$  at  $830 \text{ eV}$ ) in Fig 9.4a.

In this model, one can also calculate the number of high energy electrons and all deep shell holes involved in the phase transition after the exposure time. This is depicted in Fig 9.4b for fluence of  $1.87 \text{ J/cm}^2$  at  $830 \text{ eV}$ .

In previous work of Dr. N. Medvedev fluence threshold for CVD diamond [158] was theoretically calculated and comparing that data set with the experimental data from this Ph.D. project, shows an agreement between these two sets of information (see Fig 9.3). Dr. N. Medvedev also calculated [163] changes of the band gap, electron occupancy in conduction band as well as distance to the nearest neighbor at different photon energies for CVD diamond (see Fig 9.5). In all these calculations the density of electrons in conduction band increases after the pulse (at some photon energies also already during the pulse). The band gap decreases as well as the distance to the nearest neighboring atom.

The absorbed dose is simulated to be around  $0.7 \text{ eV/atom}$ , which stays the same for all the considered photon energies. Looking at the experimental values,

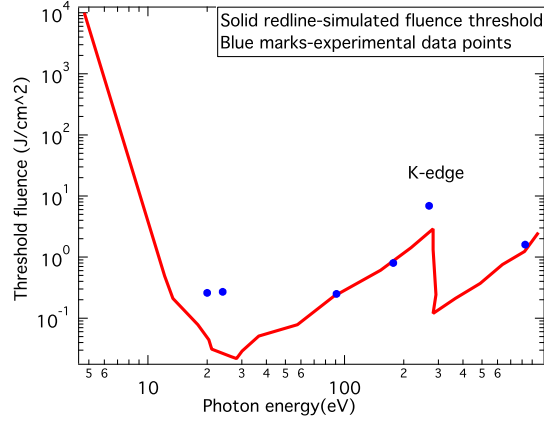


Fig. 9.3.: Simulated fluence energy threshold for the graphitization of diamond as a function of photon energy during and after the pulse at different photon energies on CVD diamond sample vs experimental values. Data is simulated with a Hybrid code XTANT developed by Dr.N.Medvedev [158].

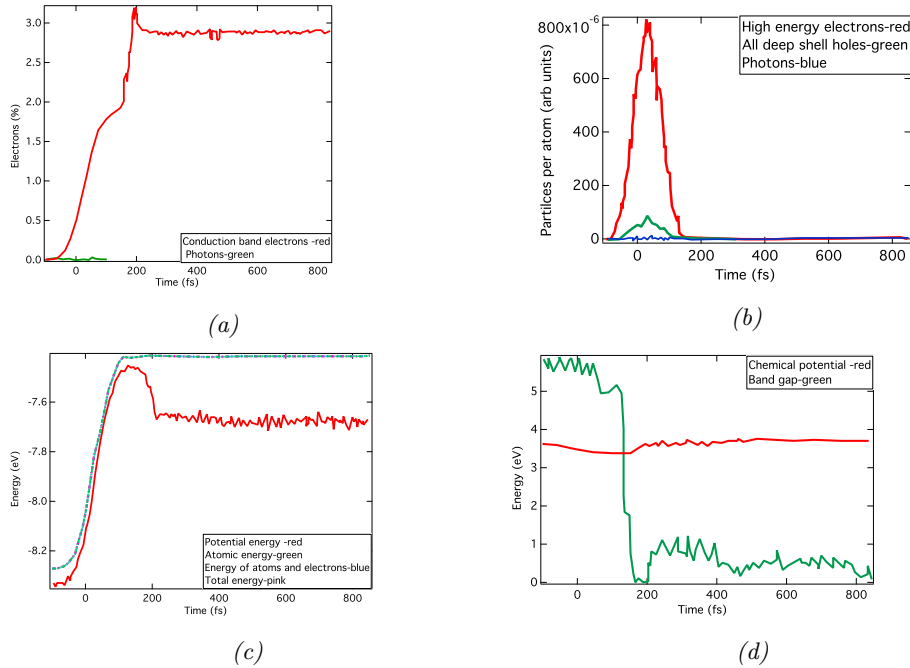


Fig. 9.4.: (a): Simulated evolution of conduction band electron occupancy in CVD diamond with 830 eV photon energy with  $1.87 J/cm^2$  fluence. The pulse duration was taken as in experiment 100 fs. Data is simulated with a new hybrid code XTANT developed by Dr. N. Medvedev. (b): Simulated high energy electrons and core hole densities. (c): Simulated changes of potential, atomic, electrons and the total energy of the system. (d): Simulated changes of potential energy and the band gap during and after the pulse.



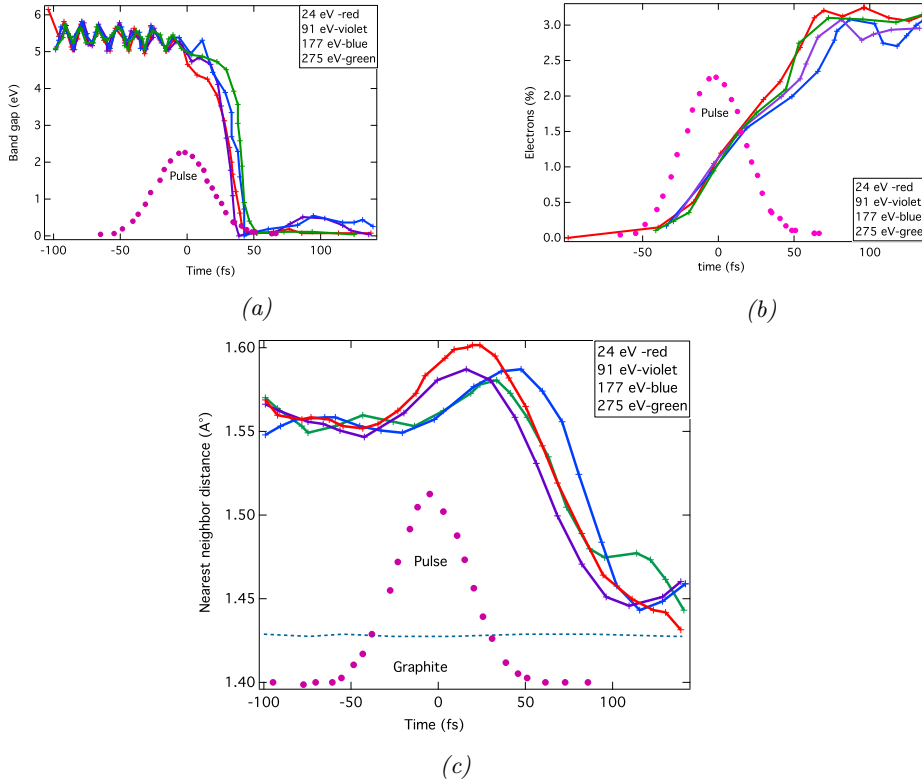


Fig. 9.5.: (a): Simulated changes of the band gap and chemical potential during and after the pulse with different photon energies (24, 91, 177, 275 eV) on CVD diamond sample. Pulse duration was taken to be 50 fs. These simulations result in average absorbed dose of 0.7 eV/atom for these photon energies. Data is simulated with a new Hybrid code XTANT developed by Dr.N.Medvedev [163]. (b): Simulated conduction electron density during and after the pulse. (c): Simulated nearest neighbor distance between the atoms in CVD diamond during and after the phase transition. Around 100 fs the electrons (free) population is at maximum at all examined photon energies.

except at energies around carbon K-edge, the absorbed dose is fluctuating around that value at most photon energies. Below the K-edge the attenuation length is simply longer and after K-edge, there is a drop (see Fig: 4.4). Hence, photons get absorbed in a larger volume (below K-edge) compared to other photon energies. As a result, the absorbed dose should decrease. As the number of free carriers increases, due to the screening effect more photons get reflected away, this causes the damage to occur at a higher absorbed dose. At low photon energies (20, 24 eV) the attenuation depth is very small. Hence, carriers escape from the surface, carrier diffusion and screening effect are more pronounced at these low photon energies.

The speed of sound in a crystal is defined as the speed of propagation of the acoustic mode (phonon vibration in long wavelength mode) and can be calculated with group velocity. The sound velocity is highest for diamond compared to all other solids, and its value is 1200 (m/s). This vibration starts to happen after some ps, after the irradiation. Where the phase transition has already taken place at the irradiated spot. This process and its timing generate the thought that no (Diamond) crystal structure in that time (after some ps)

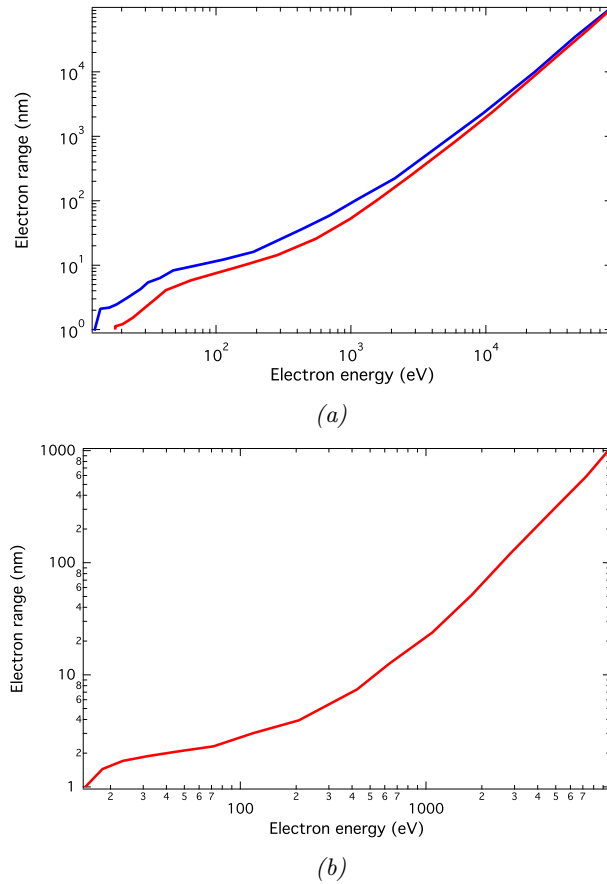


Fig. 9.6.: (a): Simulated the distance electrons with specific energy can travel to they have by Dr. N. Medvedev calculated with XCASCADE Monte Carlo code [163] in a-C (red) and Si (blue). (b): Simulated the distance electrons can travel to in CVD diamond.

exists after the irradiation. Hence, one can assume heat diffuses inside the phase transferred material (graphite) and distributes through phonon vibrations but with lower sound velocity (less than sound velocity in diamond) in the damage spot region.

Looking at the Fig 9.6, allows one to estimate the distance the free electrons cascade inside the a-C or Si as well as in CVD diamond. This is the distance they travel before their energy goes behind the threshold. One should consider the photon energy with which the sample has been ionized and subtract the energy of electrons at each shell and compare that value on the x-axis will hand in the distance the free electrons could travel. If the photon energy at the experiment is 830 eV and the sample is a-C coated Si. The 1S shell electrons with 291 eV will be ionized. The ionized electron will have 530 eV energy. Regarding the calculation in Fig 9.6, the free electron will have still enough energy to travel further 70 nm for a-C (in the case of Si they can travel further a distance of 90 nm) inside the sample. Coating (a-C) thickness is 50 nm and Si thickness is 60  $\mu m$ . This means that these electrons move from one material to the other and could cross their borders quickly. They have enough energy to ionize further atoms and produce more free carriers on their way.

Hence, through photo-ionization the first group of energetic free carriers will be released, these produce more free carriers via secondary processes like impact ionization, Auger processes, etc. (see Fig 9.7).

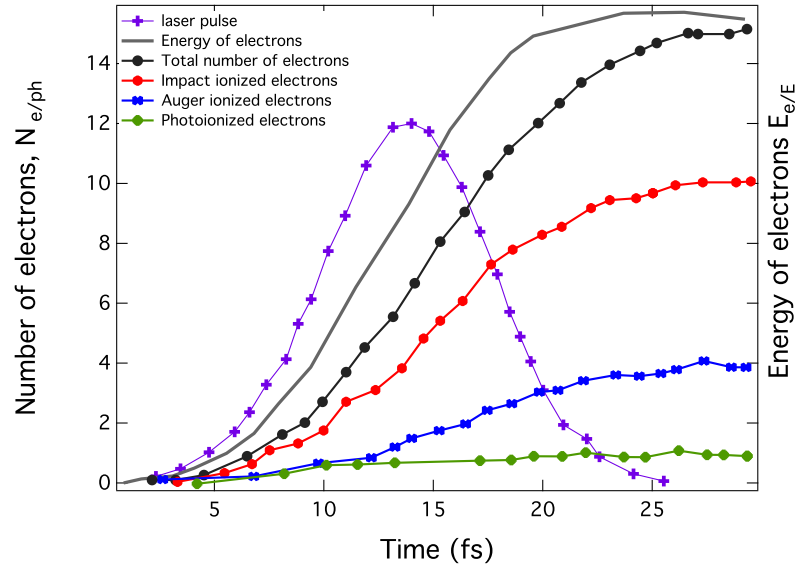


Fig. 9.7.: The total energy of free electrons in the conduction band normalized for the total absorbed energy (right ordinate). The number of free electrons created by different processes during the laser pulse irradiation and normalized per number of absorbed photons is also presented (left ordinate). The intensity envelope of the laser pulse is added as a dashed line in arbitrary units [36].

## 9.2 Heat diffusion simulation

In the early stages of damage process (very first  $100fs$  after the irradiation), phase transition through ionization processes (see section 9.1) takes place. Hence, the density of a-C or CVD diamond, both changes to graphite (Gr). This part of the process is recognized as non-thermal. Later on, after some  $100's$  of  $ps$  due to a direct increase in the kinetic energy (temperature) of atoms, heat diffusion process takes place and the melting temperature might be reached on the coating, the substrate or both. In the non-thermal section of the damage process, the area of each damage spot is on the logarithmic axes linearly dependent on the pulse energy. This is under the assumption that the beam has a Gaussian shape. If the beam shape changes or any other process like melting (heat diffusion) plays a role in the damage process, some changes regarding this dependency will be detectable from the experimental results (see Figs 9.26, 9.27 and 9.28).

Heat diffusion in this Ph.D. project is simulated via COMSOL. It is a software package based on advanced numerical methods, for modeling and simulating physics-based problems.

Benefits of use include COMSOL's graphical user interface and its options for different predefined interfaces and corresponding modeling tools. Based on the COMSOL simulation one can estimate if the melting temperature could be reached on the surface, in the volume, at the boundary between the coating and the substrate or the substrate alone.

As a first approach, the heat is simulated inside the a-C or CVD diamond after being illuminated by the pulse and without considering the phase transition. One can check if the melting temperature is achieved on the sample. The area (on the surface) up to which the melting temperature is reached, is then extracted and compared with the measured damaged areas on Nomarski images of each damaged spot at different pulse energies for various photon energies. In the more advanced approach, one can consider that phase transition has already taken place and simulate the diffusion of the heat from the center of the phase transferred material (graphite instead of a-C or CVD) inside the primary material (a-C or CVD diamond) further away.

Different cases are studied here

- Phase transition has happened in the area as large as the beam size
- Phase transition has happened in the area smaller or larger than the beam size
- The case where the created graphite is thinner in depth than the coating thickness
- Considering different length (partial formation or grating shape like structure) of created graphite on the surface with a thin or thick thickness

Fig 9.11 shows different studied models in this section. The last model is more of a realistic option. Based on Raman spectroscopy measurements

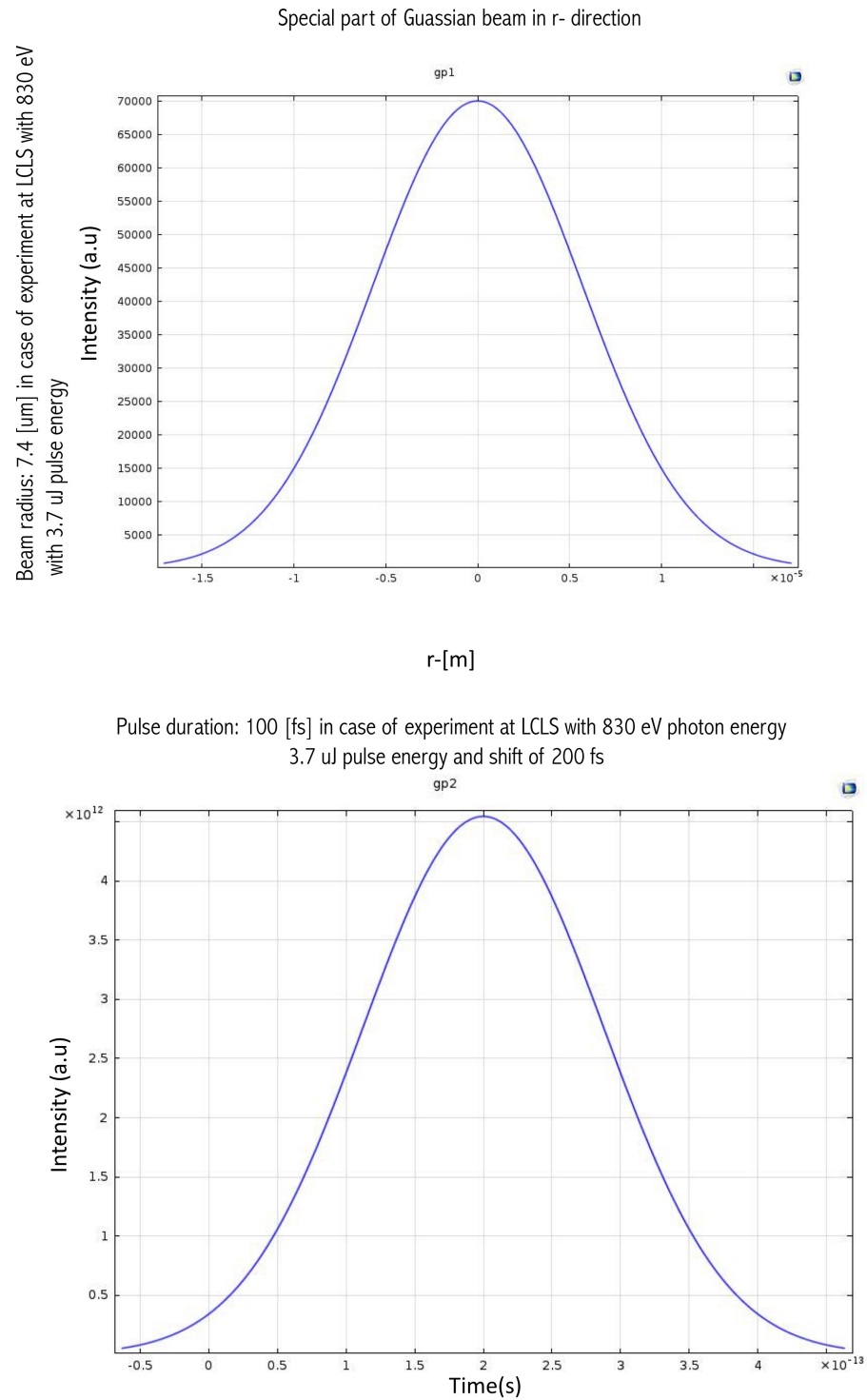


Fig. 9.8.: Spatial and temporal part of Gaussian pulse defined in COMSOL for the simulation.

(1-R) and  $A_c$  are not included in model

$$Q(x, y, z) = Q_0 (1 - R_c) \frac{A_c}{\pi \sigma_x \sigma_y} e^{-\left[ \frac{(x-x_0)^2}{2\sigma_x^2} + \frac{(y-y_0)^2}{2\sigma_y^2} \right]} \cdot e^{-A_c z}$$

2D Gaussian distribution in xy-plane

Input pulse energy  $\uparrow$   $Q_0$

Reflection coefficient  $\uparrow$   $(1 - R_c)$

Exponential decay due to absorption  $\uparrow$   $e^{-A_c z}$

Fig. 9.9.: Defined energy of the pulse.

one knows that the created graphite does not have a perfect long sheet and has defects. This means that graphite has been created in small areas in the range of few  $nm$  in length at the surface (see section 8.5 and the Equations of 8.10, 8.11). Therefore, considering the partial formation of graphite in the heat diffusion makes sense. Finally, comparing all these results and seeing when heat diffusion plays a strong role in the damage process and its consequences, leads to a better understanding of the damage process and its thermal and non-thermal parts.

Density ( $Kg/m^3$ )	Heat capacity ( $J/KgK$ )	Thermal conductivity ( $W/mK$ )	Relative permeability ( $\mu_r$ )	Electrical conductivity ( $\sigma$ )	coefficient of thermal expansion ( $\alpha$ )	Refractive index ( $n$ )
2329	700	130	1	$1e^{-12}$	$2.6e^{-6}$	3.48

Table 9.1.: Defined properties of Si in the simulated model via COMSOL

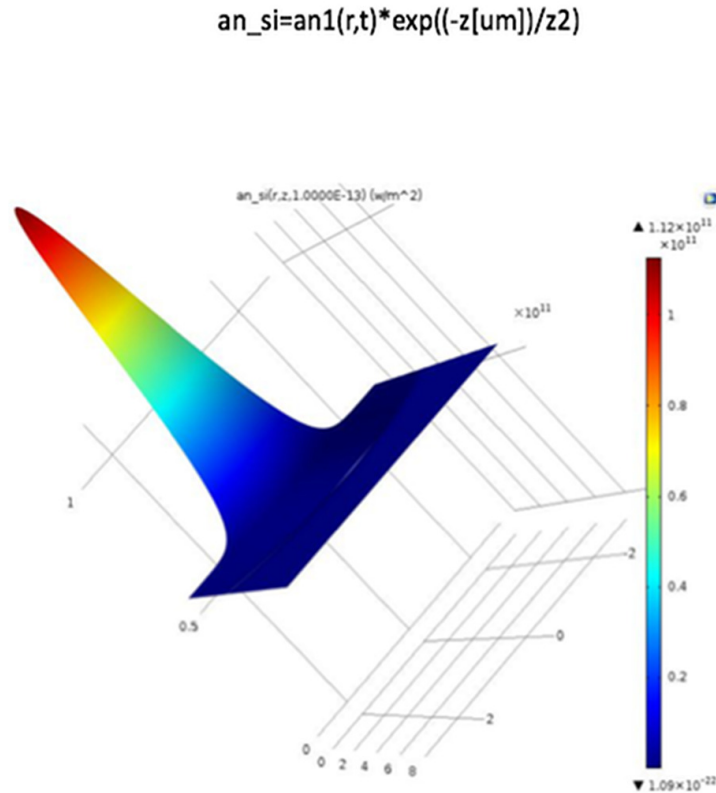


Fig. 9.10.: Defined coming FEL pulse on Si.

To simulate each case, one first finds the correct module in COMSOL and defines the parameters and the framework that mimics the actual process. In the case of this project, the basic physics module was chosen. The first step is to define the parameters which characterize the FEL beam. This includes beam shape, its size, energy of the pulse, the pulse duration, etc (see Fig 9.8, 9.9). The shape of the pulse should be defined as it was in the experiment (Gaussian) with its temporal and spatial parameters. The size of the pulse is taken as the beam size. The temporal size of the pulse corresponds to the pulse duration during the experiment. The simulated pulse going through the Si (as an example) is depicted in Fig 9.10. The attenuation depth is different in each case depending on the photon energy with which the experiment was performed.

The next step is to define sample dimensions (size of the sample which is the surface area and thickness of a-C, Si or CVD diamond) and its material

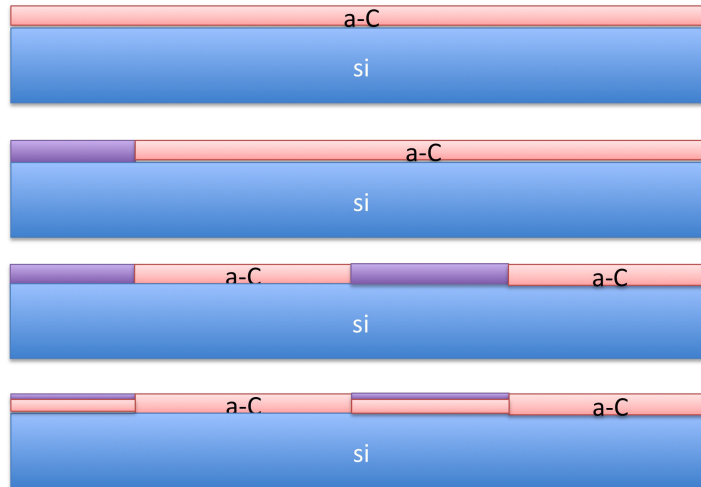


Fig. 9.11.: Different structured models studied to find out the closest possible effect during heat diffusion process. It is interesting to check if by changing the radius or depth of phase transferred material or its thermal conductivity any changes will be observed in the simulation results. The first image from the top shows a model which considers the heat gets distributed inside the a-C coating as pulse illuminates the surface. The next model is the case where the phase transition had happened, and the radius size of the graphite (violet section) is the same as the beam radius (or smaller/ larger in different studied cases), and the depth is the same as the attenuation depth of radiation at 830 eV. The next image shows the case where graphitization has happened in a grating-like structure (partially). The radius of graphite in the first part is the same as the beam size or different, and after that area there is a-C, and the next is a graphitized area. The radius of a-C or graphite is changing. The depth is taken to be the same as the attenuation depth. The fourth image represents the case where the graphitized area has a smaller depth than the attenuation depth. It is still partially structured. Different models are considered and examined to find out the closest possible effect to the real case observed from the areas of the damage spots and check if any changes can be detected by changing the radius or depth of graphitized region or even its thermal conductivity.

characteristics e.g. Optical and thermal properties, etc. (see Figs 9.12, 9.13, and Table 9.1). There is a fine mesh defined in the case of each material as well as the corresponding critical boundary conditions for heat conduction and convection. The simulation starts at the point where the pulse hits the sample (see Figs 9.14) and runs for few microseconds (see Figs 9.15). This is the average time during which the sample's temperature returns to the room temperature. There is some *ps* needed for the samples to reach their melting threshold. That is the required time to transfer the energy from electrons to atoms via electron-phonon



## Block components—axial symmetric geometry

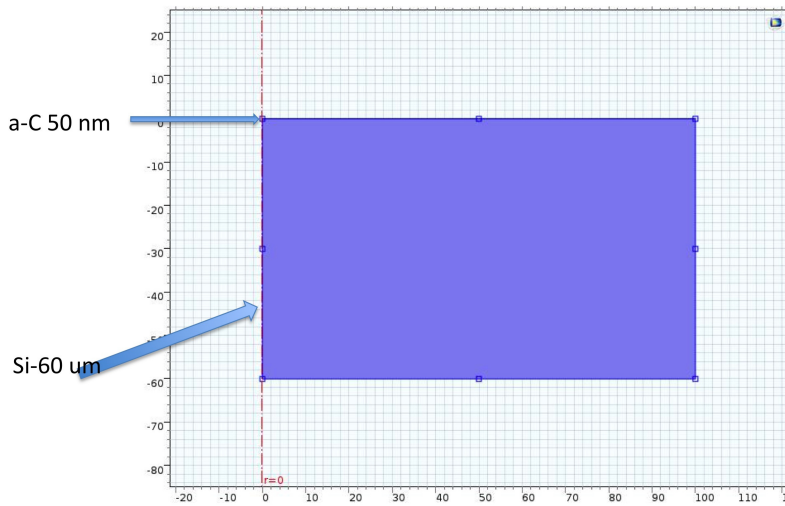


Fig. 9.12.: Defined components. a-C coating on top of Si substrate.

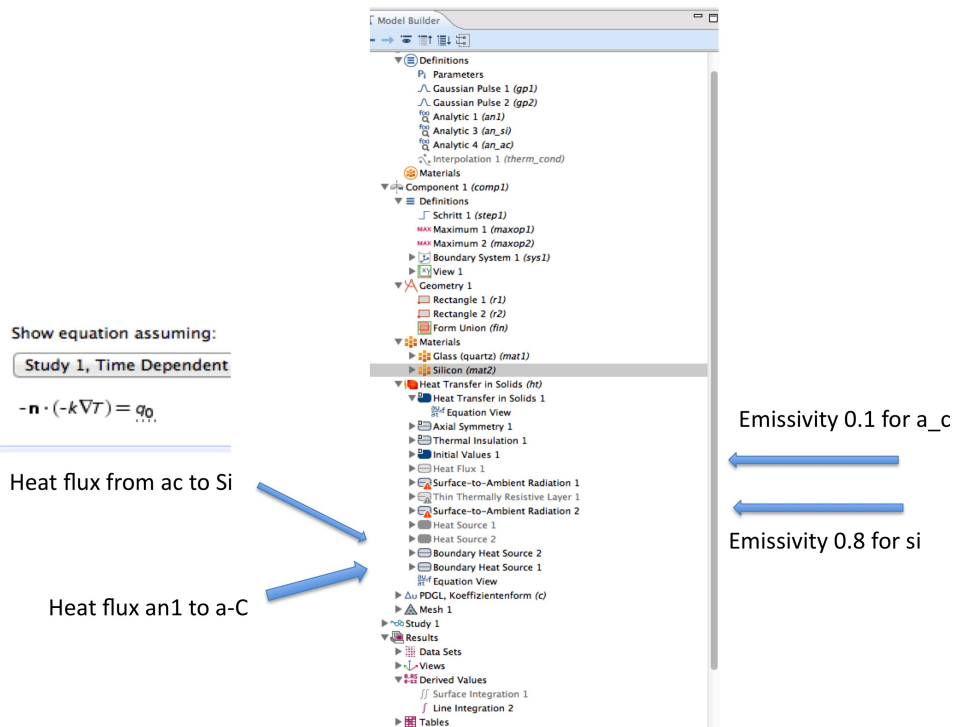


Fig. 9.13.: Defined boundary conditions.

coupling [8], [157]. This indicates that before this time the damage process is mainly governed by photo-ionization, and one can name it non-thermal. This was also proven by the Hybrid XTANT theoretical simulation in section 9.1. After some hundred's of *ps* both non/thermal processes are involved in the damage.

As an example are the pulses with 3.7 and 17.5  $\mu J$  depicted in Figs 9.15; as well as the temperature achieved on and in the sample. The corresponding radius up to which this temperature was reached is depicted in Fig 9.16. One can see how far the heat diffuses on the surface of a-C as well as in Si.

Simulations show that melting plays a role in the damage process starting with pulse energies around 10  $\mu J$  (2.7 *eV/atom*) at 830 *eV* without considering the phase transition (see Fig 9.19). In the case of phase transition this values changes to 5  $\mu J$  (1.38 *eV/atom*)(see Fig 9.20).

As mentioned earlier different designed models are studied in this project, even the value of the thermal conductivity at 830 *eV* photon energy was changed to lower values for comparison reasons. The thermal conductivity of the graphite was changed from 5.7 *W/mK* to 3 *W/mK* (see Fig: 9.21). Also the damage structure was changed to grating like (partial formed graphite areas). Some of the results are depicted in Figures 9.22, 9.23 and some are depicted in Appendix 12.6.e.g in Fig 12.30.

Silicon has higher thermal conductivity than amorphous carbon and graphite (see Table 9.1). It's (Si) heat capacity is almost the same as graphite but higher than amorphous carbon. Therefore, it can reach melting threshold on lower pulse energies compared to amorphous carbon and graphite. From the theoretical simulation, it can be seen that free electrons after photo-ionization process have still enough energy to travel and escape from a-C to Si, which could generate secondary processes. Figure 9.6 shows that one can estimate at a specific energy how far electrons can travel inside the a-C, Si or CVD diamond and generate free carriers.

In Figures 9.17 - 9.19 simulated heat diffusion at different photon energies of 20 *eV*, 177 *eV*, 296 *eV* and 830 *eV* on a-C sample at room temperature are depicted.

At 20 *eV*, compared to the higher photon energies, the heating starts at very low pulse energies and mainly is the a-C which reaches melting temperature. The attenuation depth of X-ray-FEL pulse at 20 *eV* is very small, and the photo-ionization mostly takes place in an area very close to the surface. Hence, lots of free carriers can escape from the surface, or the screening effect creates a hot plasma of electrons on the surface of the sample. The generated high pressure could cause shock waves and distribute the carriers out of the beam region (in size). All these processes lead to a high damage threshold value being obtained which is presented in chapter 8.

Considering the theoretical calculation in Fig 9.4, sample reaches 2000 *K* temperature after the phase transition. Starting with the 2000 *K* base temperature in heat diffusion simulations shows that Si reaches the melting threshold much faster and even before the a-C coating reaches its melting temperature. This means, after some few *ns* the Si melts.

Looking at the Figures 9.17- 9.19 shows that at very first low pulse energies

damage spot size increases linearly vs. the pulse energies on the logarithmic axis (this indicates that this part of the damage is mainly governed non-thermal and through photo-ionization). This dependency changes at higher pulse energies. The area of the damage spots observed under the microscope is shaped after all the processes have taken place (including melting of the Si, a-C or CVD diamond). Therefore there exists a high rate of error in determining the area of the damage spots in general. This doesn't have a huge impact on the energy threshold values but could have an impact on the evaluated absorbed dose (non/thermal effects both generate the damage). Hence, in most cases, one could use the initially given beam size to obtain the absorbed dose values instead of the beam imprint area, or at least these values (areas) should be cross-checked if they are too far from each other or almost the same (at the threshold).

Heat gets transferred inside graphite faster towards the substrate, compared to the case inside a-C (no phase transition). This is due to the different thermal conductivity of these two materials. Hence, a larger volume of the material can get heated up to the melting temperature when considering phase transition into graphite in the simulated models. Heat diffusion simulations on the already phase transferred material shows that in this case a larger area of the surface gets heated up and this could explain the non-linearly increasing damage areas especially in the case of a-C sample (see Figures 9.20).

The simulation studies went on by considering the partial formation of graphite planes. Different models, as depicted in Fig 9.11, are considered. Following Figures 9.20 - 9.23 and Figs 12.30, 12.31 illustrate the heat diffusion inside the phase-changed material with different possible sizes of graphite grains, different thickness or radius (length). Graphite with the  $1930 \text{ W/mK}$  thermal conductivity (graphite planes laying perpendicular to the surface) reaches melting temperature at higher pulse energies compared to the graphite with  $5.7 \text{ W/mK}$ . The Si reaches its melting temperature at lower pulse energies in comparison to graphite. It should be mentioned that these simulations are done all at  $830 \text{ eV}$  photon energy for a-C sample.

By changing the radius of the phase transferred material (into graphite) in the simulations, the result of heat diffusion process change. After testing different models, it became apparent that in the grating-like structure model, reducing the length or depth of the graphite sheet reduces the distance the heat should diffuse into; until it arrives at the next neighboring region (material). Therefore from a  $20 \text{ nm}$  layer of graphite, heat can diffuse into the a-C (neighboring area) in a shorter time and heats this layer up. If the initial incoming pulse has enough energy the a-C (laying below graphite layer) can reach its melting temperature as well. Looking at the Figure 9.23, shows that in the case of a small size graphitized volume with  $3 \mu\text{m}$  radius and  $50 \text{ nm}$  depth (depicted in Panel 1 from the top) the a-C (neighboring area) can still reach the melting temperature. In the case of graphitized volume with  $3 \mu\text{m}$  radius and  $20 \text{ nm}$  (Panel 2) the heat diffusion process runs differently and starts at a different pulse energy. In the case of the  $20 \text{ nm}$  graphitized volume, the heat transfers from graphite to a-C and the underlying a-C layer also reaches its melting temperature. Si reaches the melting temperature at different pulse energies (compared to a-C or graphite) in all these cases (depending on the

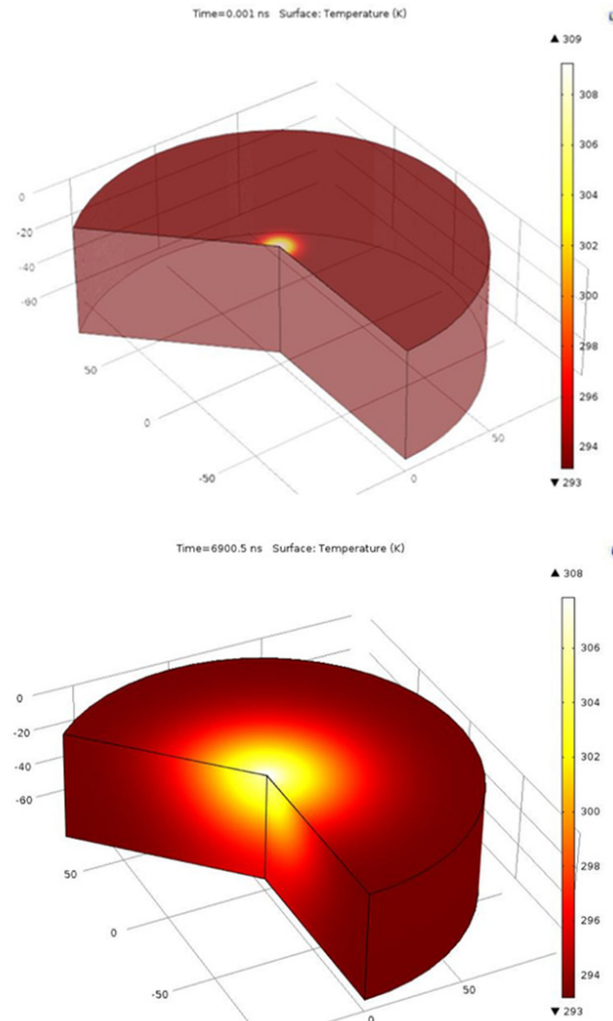


Fig. 9.14.: Simulated heat diffusion in the sample after a few 100's of  $ps$  after the FEL pulse in top figure and after few  $ns$  in lower figure at  $830 eV$  with  $3.7 \mu J$  pulse energy.

studied model).

The Figures in 9.25 illustrate the heat diffusion in the case of CVD diamond at  $830 eV$  for different pulse energies. The first plot represents the heat diffusion at room temperature without considering the phase transition. This shows that in this case, melting threshold lies at high pulse energies (almost around  $50 \mu J$ ). The second plot illustrates the heat diffusion in the CVD diamond with the phase transition (as large as beam size) and the thermal conductivity of  $5.7 W/mK$ . This is a possible explanation for the areas larger than the beam size which is measured as damage spot footprints size. The third graph (in the case of CVD diamond) shows that heat diffusion wouldn't play a significant role in the damage process when the thermal conductivity is taken to be  $1930 W/mK$ .

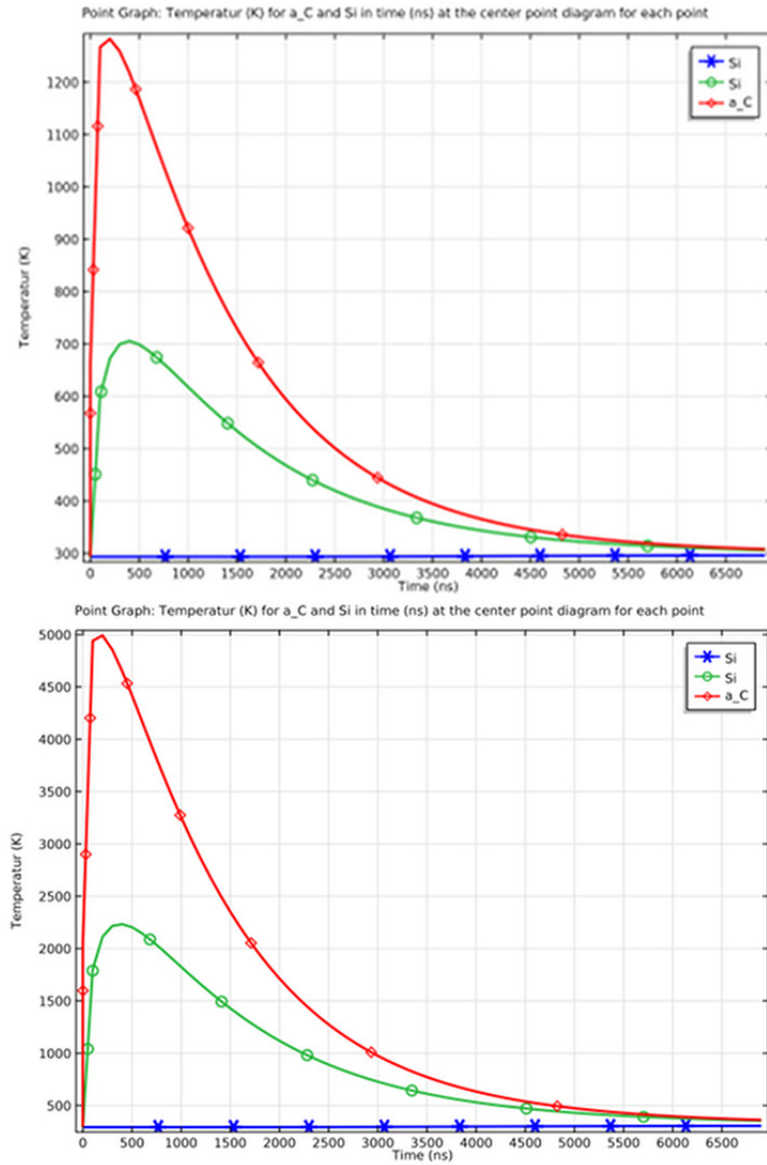


Fig. 9.15.: The temperature reached at the surface of a-C is depicted in red and Si at the boundary is depicted in green and Si at bottom of the sample in blue. There are two pulse energies examined here in top figure the pulse energy is taken  $3.7 \mu J$  and in the the bottom figure it's  $17.5 \mu J$  both at  $830 eV$ .

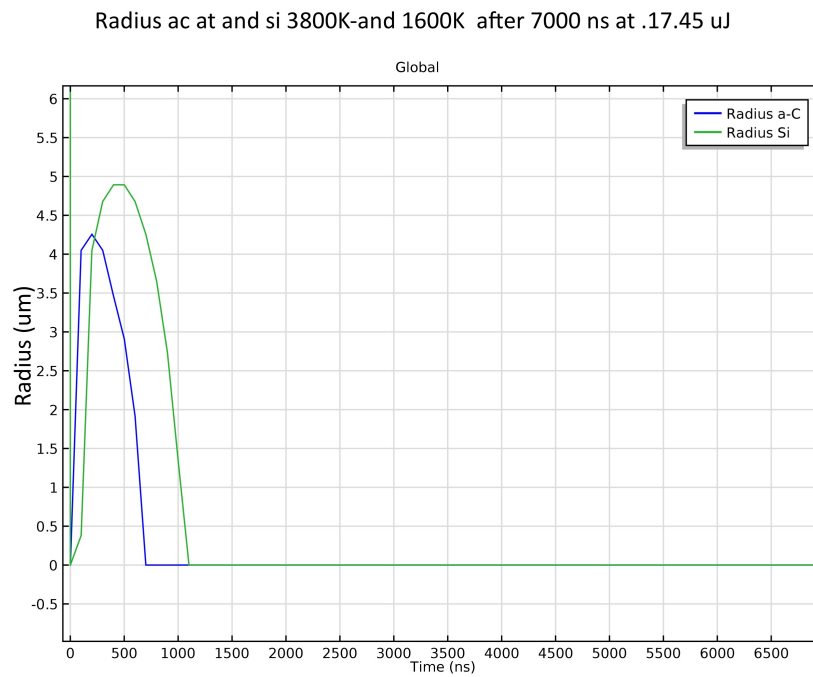
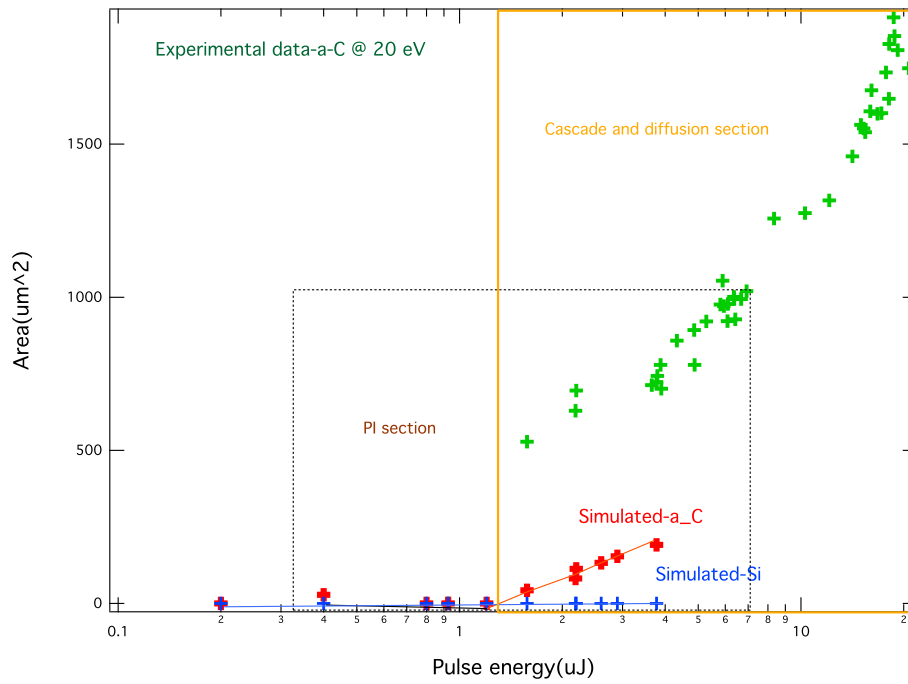
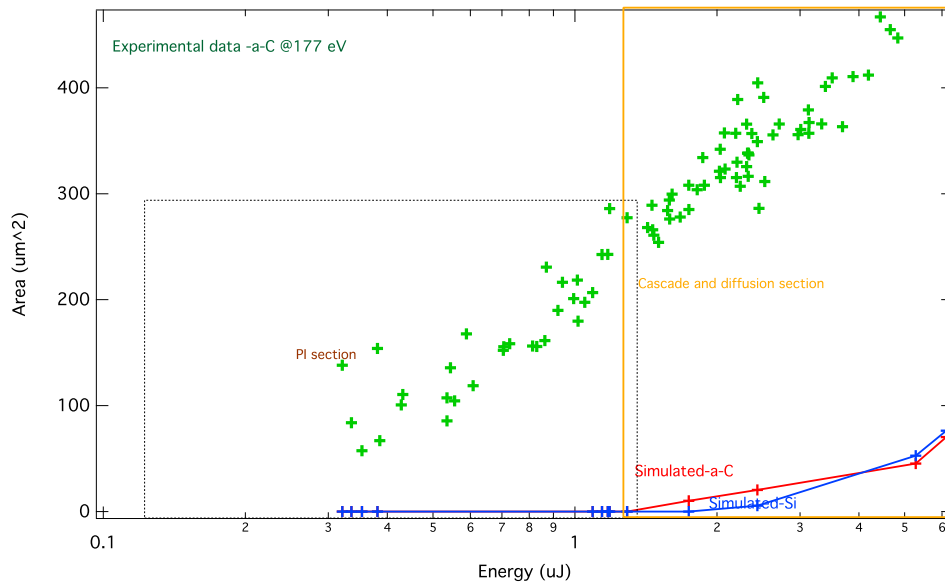


Fig. 9.16.: At 830 eV photon energy with 17.5  $\mu\text{J}$  pulse energy the maximum radius at which the sample reaches the melting temperature on a-C or Si is simulated via COMSOL and plotted here.



(a) Heat diffusion simulation at 20 eV. The beam radius is taken as in the experiment. The pulse duration was also matched to the experimental data; this was 100 fs. The a-C thickness was 50 nm. There are two sections pronounced in the plot. The first one is cited as PI (photo-ionization section), where all the ionization processes take place. Which results in phase transition of the material and initiating damage due to these processes. The second section corresponds to the mixture of the secondary processes, carrier and heat diffusion.



(b) Represents the simulation with 91 eV and the pulse duration was taken to be 30 fs.

Fig. 9.17.: In these calculations one has simulated if the a-C or Si reach their melting temperatures and the area up to which this temperature is reached is plotted vs the pulse energies. The experimental data also representing the area of each damaged spot vs the corresponding pulse energies on the logarithmic axis.

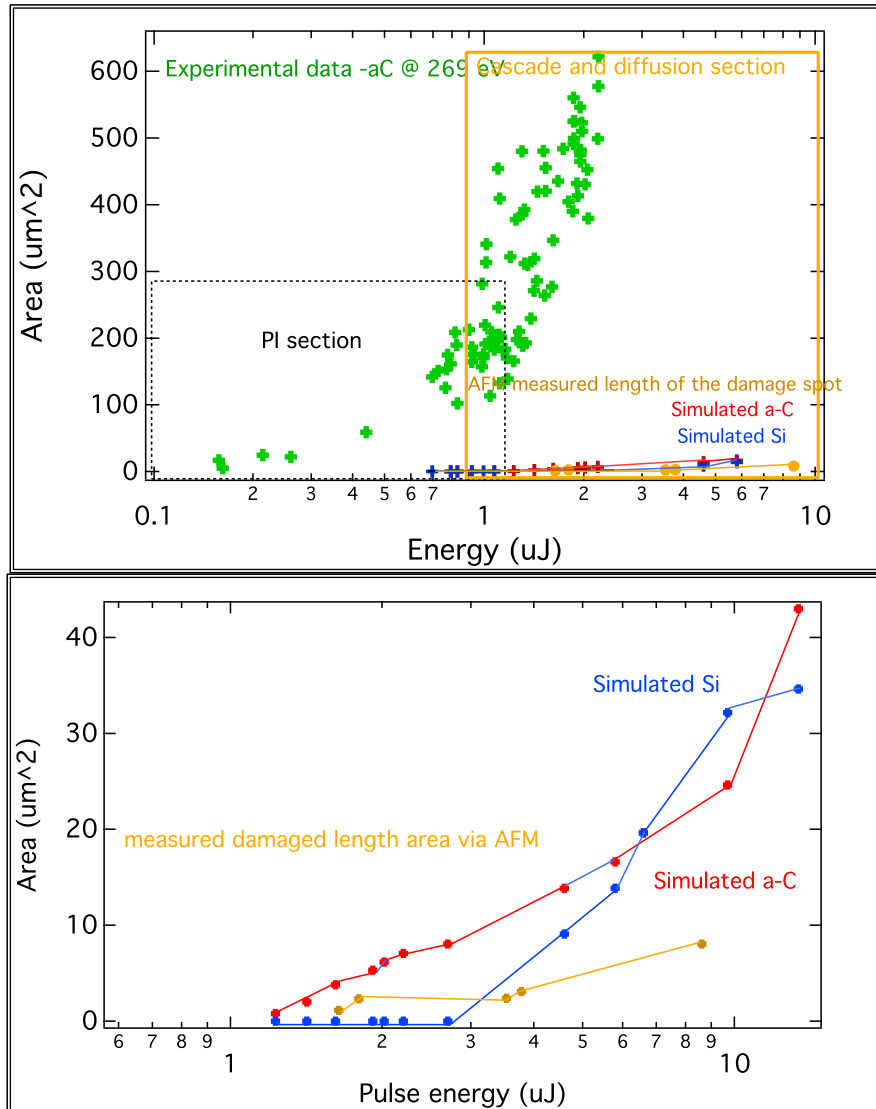


Fig. 9.18.: Heat diffusion simulation at 269 eV on a-C sample. Simulation ran over  $7 \mu\text{s}$  with the pulse duration of  $125 \text{ fs}$ . The beam radius is taken as in the experiment. a-C thickness was  $50 \text{ nm}$ . There is also an extra part which represents the measured length of the damaged spots via AFM (yellow) vs. their corresponding pulse energy to compare the localized and nonlocalized damage effect due to the heat on the damaged spots.



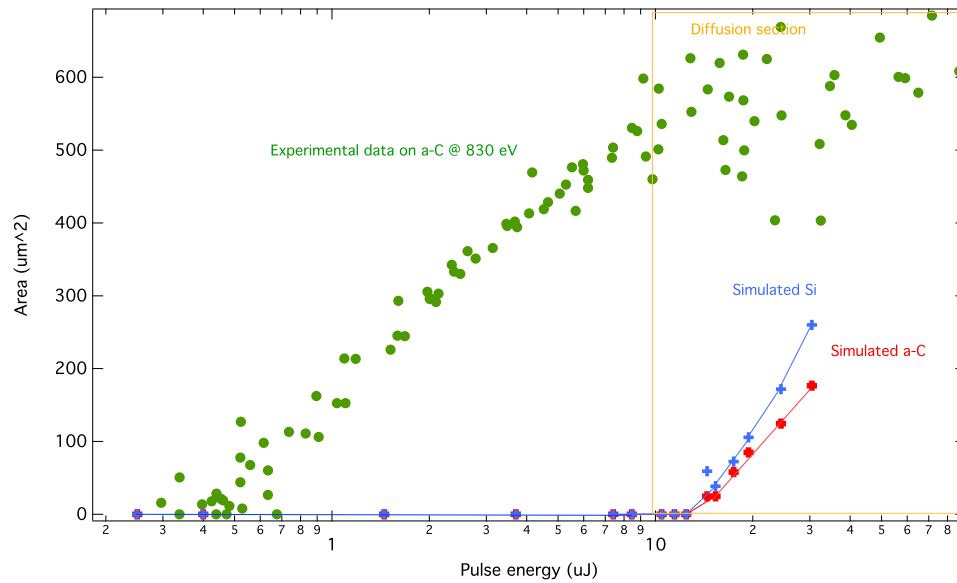
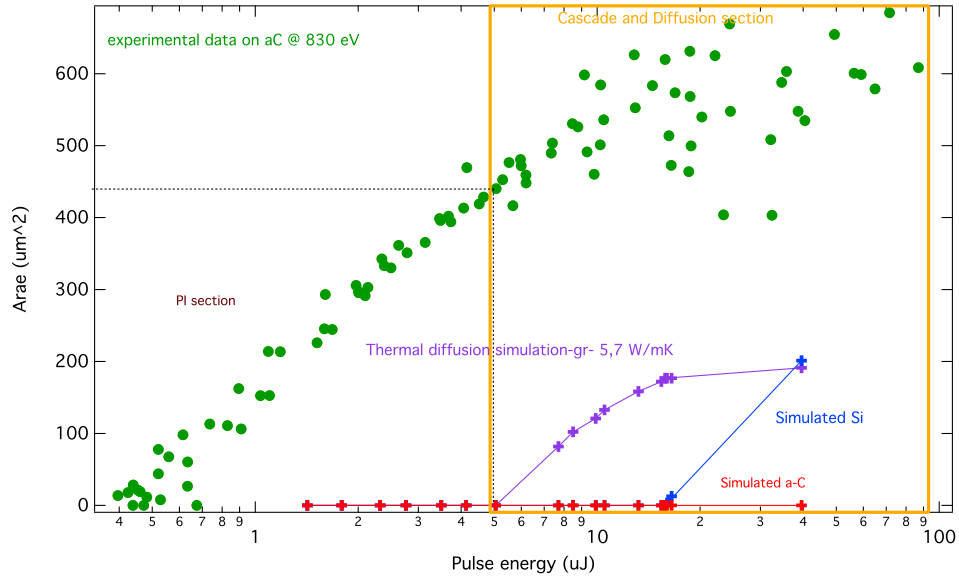
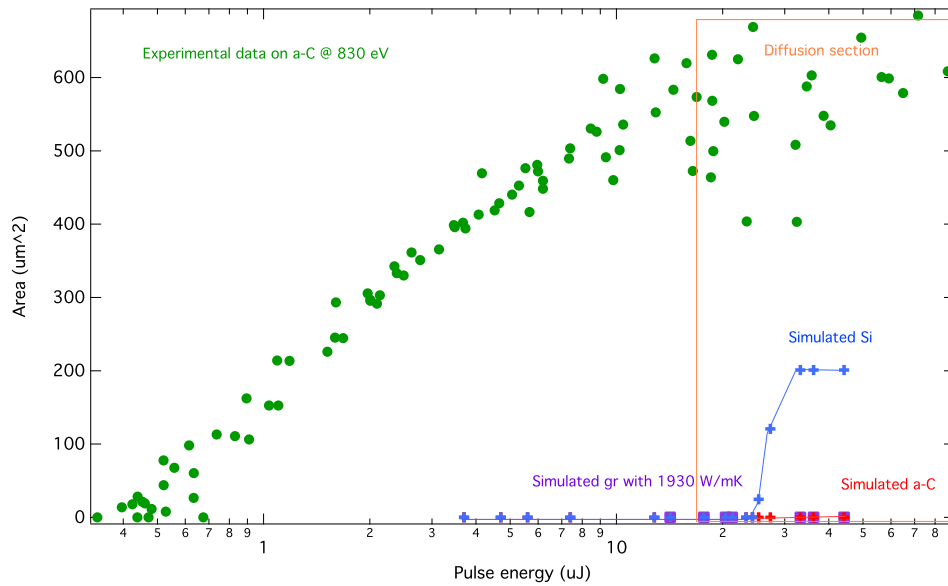


Fig. 9.19.: Heat diffusion simulation at 830 eV on a-C sample. Simulation ran over 7  $\mu$ s. The phase transition to graphite is not considered. One can see at which pulse energy Si / a-C reach their melting temperature and how deep in length on the surface this is distributed and where the melting can make changes in the size of the damaged spots.



(a) Illustrates the phase transition to graphite has already taken place and the thermal conductivity is taken to be  $5.7 \text{ W/mK}$  for graphite sheets parallel to the surface.



(b) In this case the thermal conductivity of graphite is taken to be  $1930 \text{ W/mK}$ .

Fig. 9.20.: Heat diffusion simulation at  $830 \text{ eV}$  on a-C sample. Simulation ran over  $7 \mu\text{s}$ . The simulation is done on the a-C sample with  $100 \text{ fs}$  pulse duration. The beam radius is taken as in the experiment ( $7.22 \mu\text{m}$ ). The a-C thickness was  $50 \text{ nm}$ .

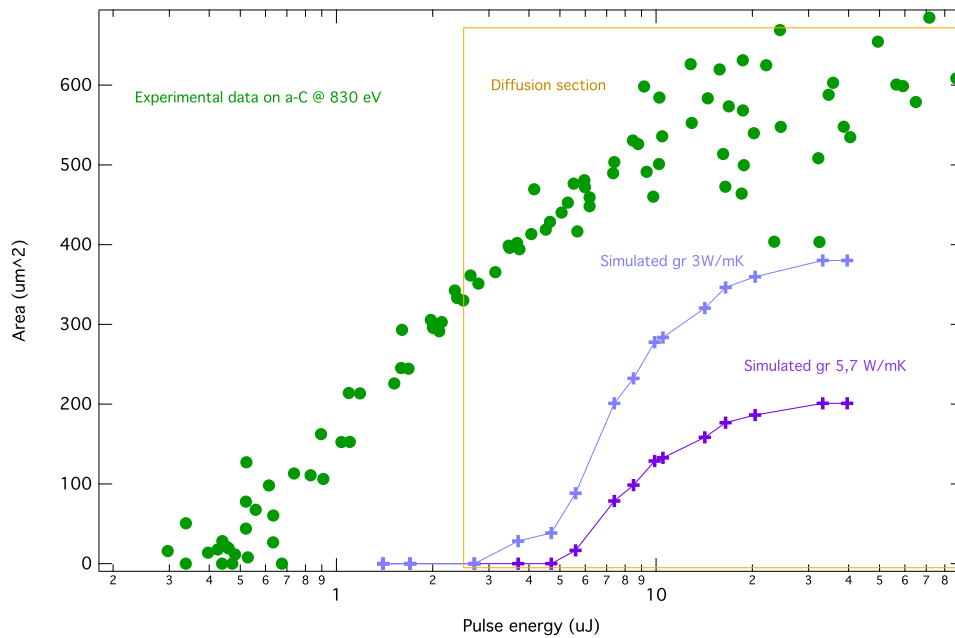


Fig. 9.21.: Heat diffusion simulation at 830 eV on a-C sample. Simulation ran over 7  $\mu$ s. The simulation is done on the a-C sample with 100 fs pulse duration. The beam radius is taken as in the experiment (7.22  $\mu$ m). The a-C thickness was 50 nm. The phase transition into graphite is considered. Heat diffusion is compared between two cases of low thermal conductivity (3 W/mK) and thermal conductivity of 5.7 W/mK. Larger radius is heated up in the case of low thermal conductivity.

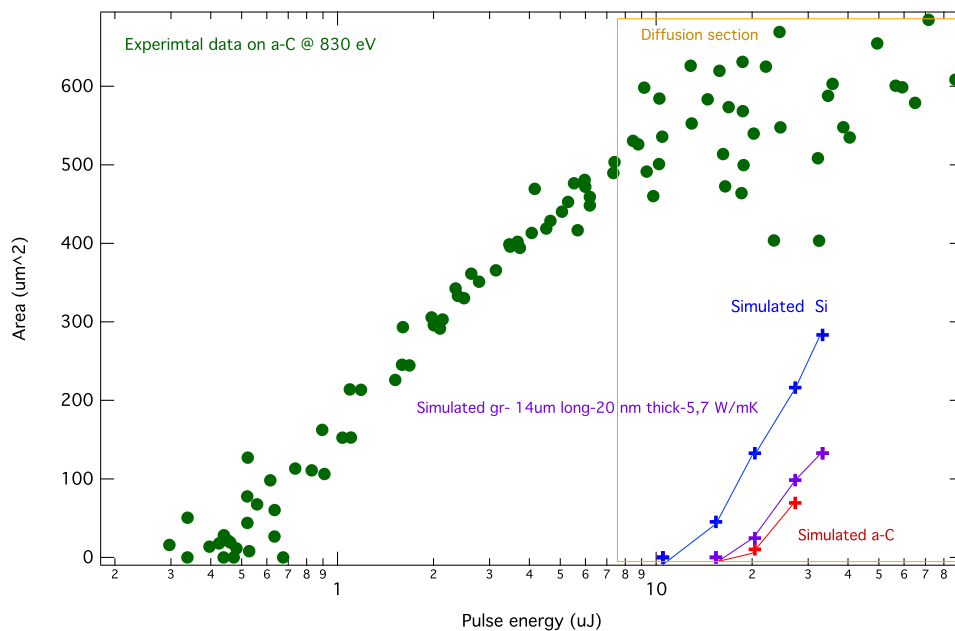


Fig. 9.22.: Heat diffusion simulation at 830 eV on a-C sample. The phase transition into graphite had already taken place. Simulation ran over 7  $\mu$ s. The graphite layer has 14  $\mu$ m radius. The thickness of graphite was 20 nm and underneath is a-C with thickness of 30 nm.

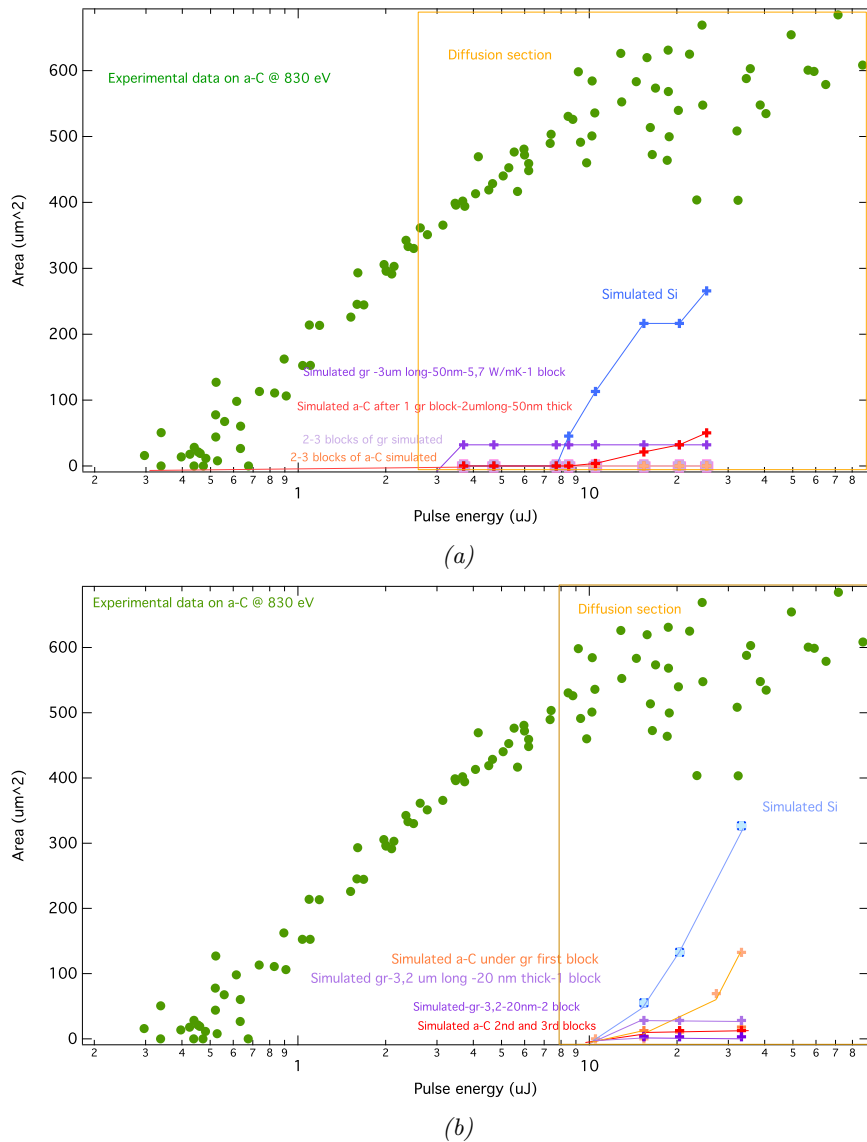


Fig. 9.23.: Heat diffusion simulation at 830 eV on a-C sample considering phase transition into graphite had already taken place. Simulation ran over 7  $\mu$ s. (a): Grating structured damaged region with graphite radius of 3.2, 2 and 3,2  $\mu$ m and thickness of 50 nm. (b): Same structure as in (a) but with 3.2, 2,3  $\mu$ m length and 20 nm thickness.

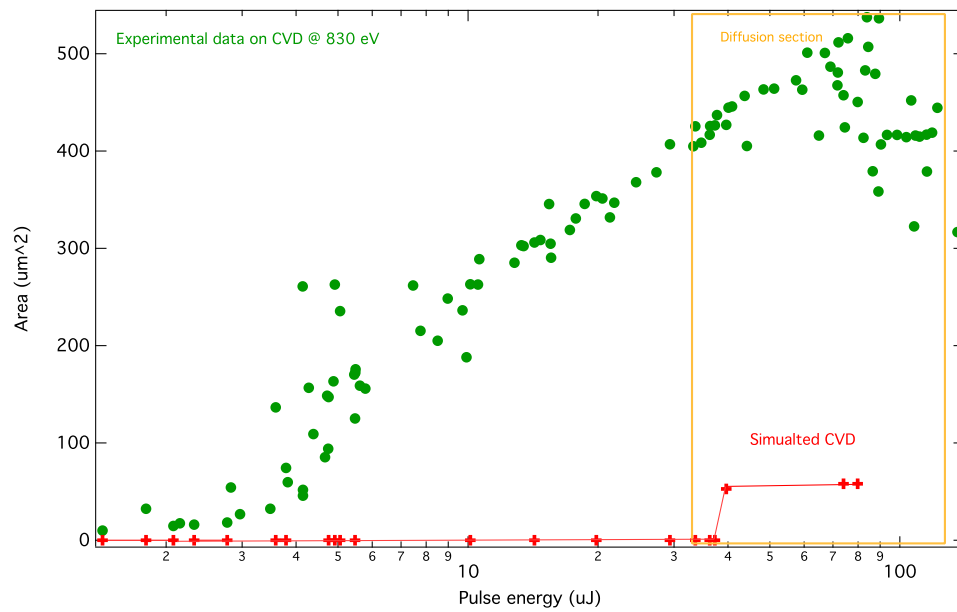
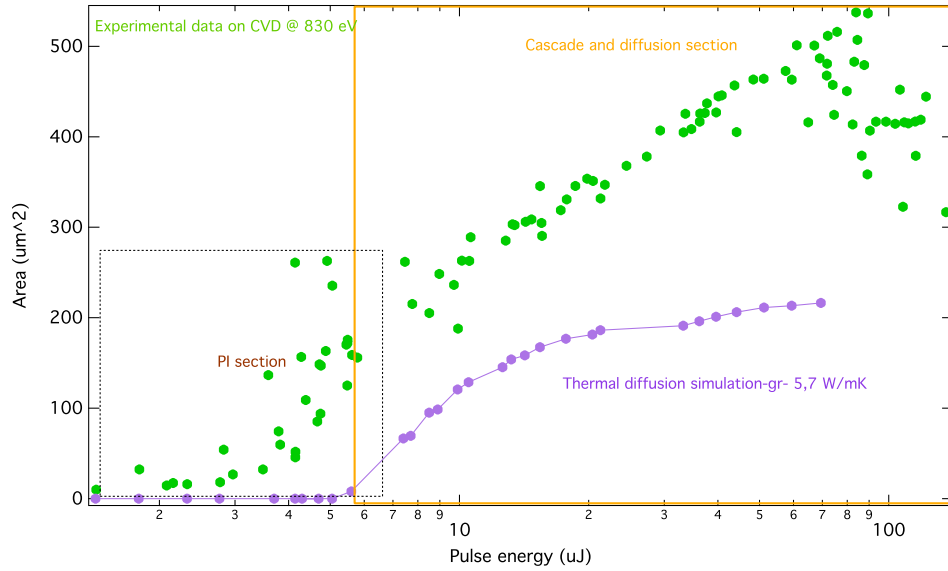
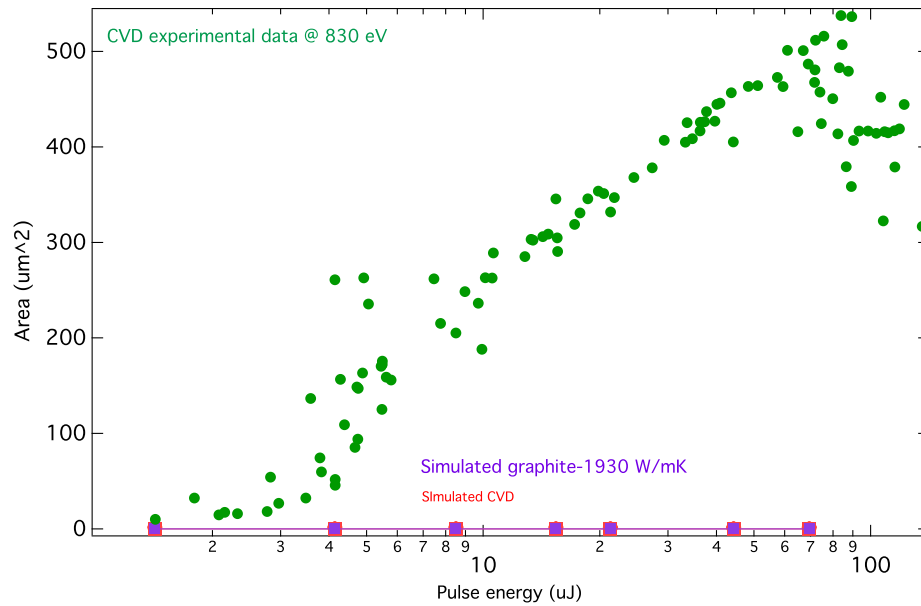


Fig. 9.24.: Heat diffusion simulation at 830 eV on CVD sample. Simulation ran over 7  $\mu s$ . The beam parameter are as in experiment. Estimating if the CVD reaches melting temperature and up to which radius it could have been heated up.



(a) Heat diffusion simulation at 830 eV on CVD sample. Considering phase transition into graphite had already taken place. The thermal conductivity of graphite is  $5.7\text{W}/\text{mK}$  and its size was taken as the beam radius.



(b) Same structure as in (a) but with  $1930\text{W}/\text{mK}$  thermal conductivity.

Fig. 9.25.

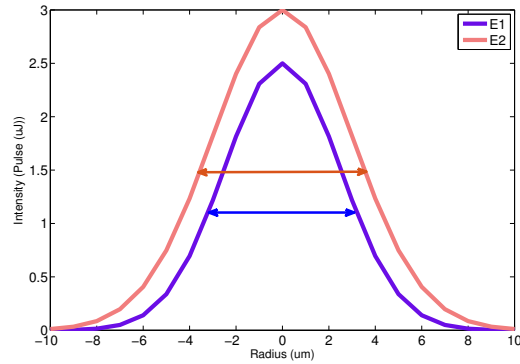
### 9.2.1 Discussions

The theoretical calculations via Hybrid XTANT code on damage process due to the X-ray FEL pulses give an estimation on the time regime during which different processes such as photo-ionization take place (within  $fs$ ). With which one can sort the thermal and nonthermal processes out. It is evident that the band gap (in the case of CVD diamond) shrinks from  $5.5 eV$  to  $1 eV$  in the early  $100fs$  of the damage process after the pulse. Through these simulations its approved that phase transition takes place.

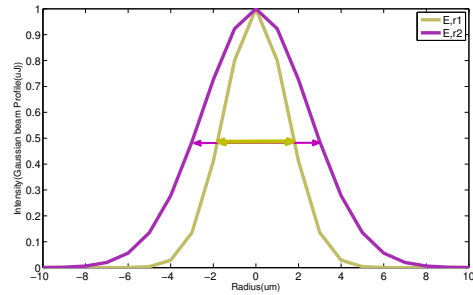
The experimental data set showed that the damage imprint spot size especially at high pulse energies doesn't always follow a linear path on the logarithmic scale vs. pulse energy. This has suggested that at this point carrier/heat diffusion processes cause this nonlinear effect (see Fig 9.26). Hence, heat diffusion is simulated for this project at different photon and pulse energies as mention in this chapter. The damage spot size from the experimental data set is then compared to simulated ones.

During the photo-ionization damage processes, the temperature starts to increase, and in some cases, the melting threshold will be reached after some  $ps$ . Hence, after some  $ps$  heat diffusion will cause more damage. Therefore one should consider two models combined to be able to describe the damage process. One model consists of irradiated matter undergoing the phase transition and heat diffusion. The second is the heat and carrier diffusion model inside the original state of the material (see Fig: 9.27– 9.28).

The Damage threshold due to non-thermal damage is compared to the melting damage threshold values obtained from simulations and are presented in Fig 9.29. One can see that at lower pulse energies of  $20 eV$  carrier escape, Coulomb explosion, screening effect (non-thermal processes) are the governing processes in the damage. Considering the partial formation of graphite sheets and estimating the heat diffusion effect shows an agreement with experimental data concerning the enlargement observed in the damaged spots specially at higher pulse energies.



(a)



(b)

Fig. 9.26.: It is expected that the damage spot areas and their corresponding pulse energies on the logarithmic scale show a linear dependency (Gaussian beam profile). From the experimental result, it can be seen that after the P-I (photo-ionized) section this dependency is no longer linear. Comparing the areas of the footprints with the given initial beam area at the experiment shows a different enlargement in the areas of the damage spots (see Fig 9.25). This can be explained at higher pulse energies with heat diffusion effect. Between the P-I section and very high pulse energies, there is another section. In this section, one can assume a series of complex processes, such as photo-ionization and secondary processes and heat diffusion taking place. (a): Shows changes of the FWHM of the imprints with the pulse energy linearly. (b): Shows that damage footprints areas expanding nonlinearly due to the heat diffusion and carrier distribution (see also Figs 9.27 and 9.28).



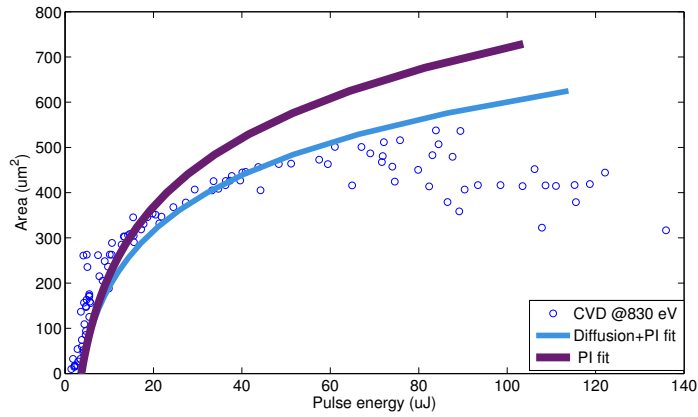


Fig. 9.27.: The model based on the fact that the Gaussian pulse exposing the sample cause a photo-ionization (PI) effect, as well as heat and carrier diffusion. The FEL Gaussian function and the distribution function are modeled in the form of convoluted Gaussian defining the damage spot size changes; going from low pulse energies to higher pulse energies. The Gaussian pulse in PI section describes the linear dependency of the spot size of the damage spots on the pulse energy (on the logarithmic scale). This dependency changes due to the carrier and heat distribution to a nonlinear dependency. The experimental data are represented with the empty blue circles, performed at 830 eV at LCLS on CVD diamond sample.

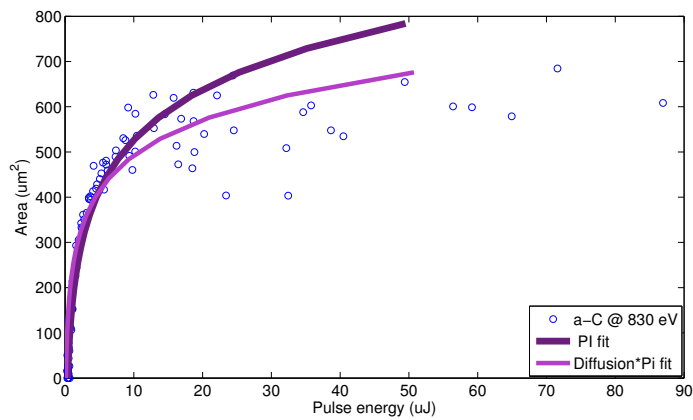
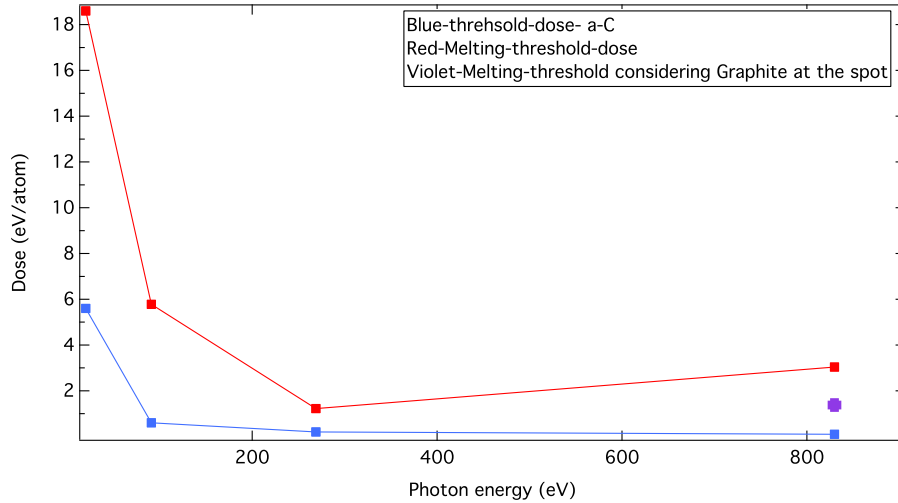
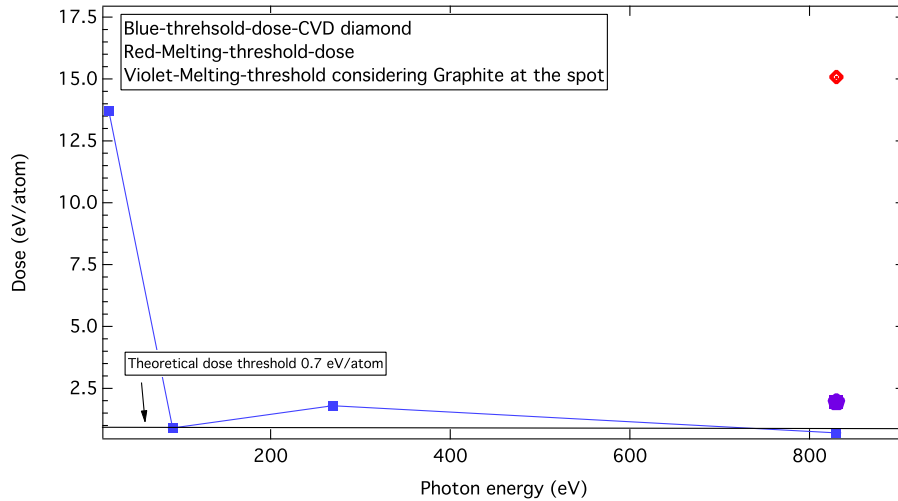


Fig. 9.28.: The model above tested on a-C (50 nm thick a-C coating on Si substrate) sample.



(a) The damage and melting threshold values on a-C are compared. Around 269 eV the melting threshold dose and non-thermal damage threshold are very close to each other. This could also be due to possibility of phase change because of the heat diffusion. Around 20 eV, there is a big gap between damage threshold value and the one obtained due to the melting. This can be interpreted as a sign of free carrier escape, plasma formation, etc. effects causing a high dose threshold values.



(b) Represents the same data set as above but on CVD diamond. The simulations were done at 830 eV. The melting threshold dose in this case is close to the photoionization section (considering the phase transition to graphite; violet point) and higher in the case of CVD diamond itself.

Fig. 9.29.: The damage threshold dose values calculated with Equation 5.12 and compared with the melting threshold dose values obtained from COMSOL simulation in chapter 9.

## Chapter 10

# Damage on gratings

A diffraction grating is an optical component with a periodic structure which splits and diffracts the light into several different directions. Based on the Huygens' principle, each point on the wavefront can be taken as a new source of light traveling in a particular direction which constructively or destructively interferes. This depends on the spacing and design of the grating, as well as on the wavelength of the light in general. The concept of grating discovered by James Gregory after Newtons discovery of prisms provides the monochromatized light for experiments in soft X-ray regime is realized by the use of grating-based monochromator. Damage on the grating is a major concern for designing the beamlines at FEL/ XFEL facilities.

Since the grating has a periodically structured surface, it causes a non-homogeneous electric field distribution on its surfaces which increases the degree of damage to some extent compared to the flat surfaces [164]. The reason is the changes in the incidence angle of the incoming beam, at the grazing and normal incidence angle and the reflected beam that hits the edges (causing a higher level of damage). The different types of gratings of particular concern are Variable Lines Spacing (VLS), Blazed and Lamellar grating. In this work, the experiment was done on a Lamellar grating. A diffraction Lamellar grating [165], [166] consists of a series of equally spaced parallel grooves. The substrate was made of silicon. To construct the grating structure, the substrate was etched, and grooves made. The structured substrate was coated with amorphous carbon (see Fig: 10.1). If the spacing between the grooves changes, instead of a Lamellar grating, one has a VLS grating. In Blazed grating as depicted in Fig 10.2 the grooves are done under a grazing angle and not normal to the surface. The waysee in which the grooves are formed separates gratings into two basic types, holographic and ruled. In general, ruled gratings have a higher efficiency than holographic gratings [167].

The distance between adjacent grooves and the angle with which the grooves are formed (with respect to the substrate) influence both the dispersion and efficiency of a grating. If the wavelength of the incident radiation is much larger than the groove spacing, diffraction will not occur. If the wavelength is much smaller than the groove spacing, the facets of the groove act as mirrors and again, no diffraction takes place. The relationship between the grating spacing and the angles of the incident and diffracted beams of light is known

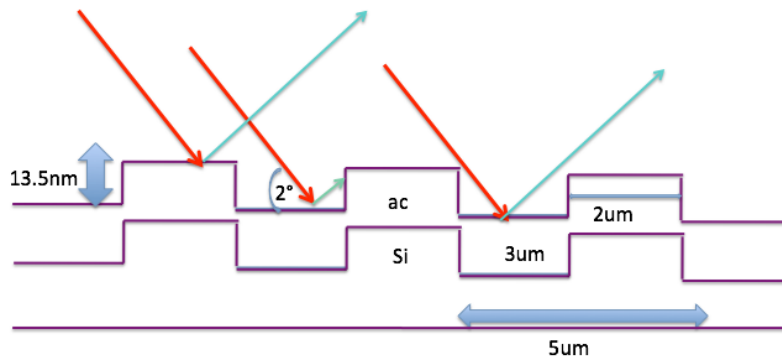


Fig. 10.1.: The Lamellar grating used in the damage experiment at FLASH 2011 had a Si substrate coated with a-C (45 nm). The groove density was 200 grooves / mm and the groove depth was 13.5 +/- 3 nm. The duty ratio was 0.41 +/- 0.1.

as the grating equation.

$$d(\sin \theta_i + \sin \theta_m) = m\lambda \quad (10.1)$$

$\lambda$  is the diffracted wavelength,  $d$  the grating constant (the distance between successive grooves),  $\theta_i$  the angle of incidence measured from the normal and  $\theta_m$  the angle of diffraction measured from the normal.

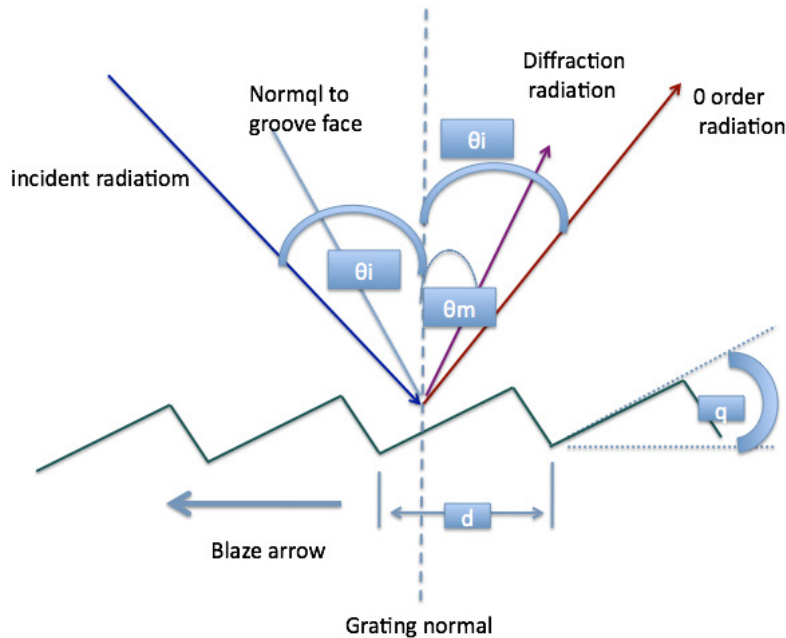


Fig. 10.2.: Image of grating, where  $n$  is the order of diffraction,  $\lambda$  is the diffracted wavelength,  $d$  the grating constant.  $\theta_i$  the angle of incidence measured from the normal and  $\theta_m$  the angle of diffraction measured from the normal [167].

The light that corresponds to direct transmission (or specular reflection in the case of a reflection grating) is called the zero order, and is denoted  $m = 0$ . The other maxima occur at angles which are represented by non-zero

integers  $m$ . Note that  $m$  can be positive or negative, resulting in diffracted orders on both sides of the zero order beam. This derivation of the grating equation is based on an idealized grating. However, the relationship between the angles of the diffracted beams, the grating spacing and the wavelength of the light apply to any regular structure of the same spacing, because the phase relationship between light scattered from adjacent elements of the grating remains the same. The detailed distribution of the diffracted light depends on the detailed structure of the grating elements as well as on the number of elements in the grating, but it will always give maxima in the directions given by the grating equation. The length of X-ray grating designed for European XFEL (in the frame of this project) is  $500\text{ mm}$  with  $150\text{--}200\text{ lines/mm}$ . This, in turn, results in a high amount of fluence hitting the surface of the grating, which can cause damage.

## 10.1 Grating's parameters

The grating sample is manufactured with parameters which reproduce the one currently in use in soft X-ray beamline at LCLS [168] with a length of  $200\text{ mm}$  and  $5\text{ }\mu\text{m}$  periods. Based on a  $1\text{ mm}$  thick ion etched Si wafer, with a duty ratio of 0.4. The duty ratio is the ratio of groove width and the period length. Since a-C is a typical coating candidate for optical elements at XFEL, a  $45\text{ nm}$  thick layer of a-C was used to coat the etch wafer. It was proved by means of AFM that the coating exactly reproduces the ion etched area [169]. The grating groove depth was  $13.5\text{ nm}$  (see Fig 10.3).

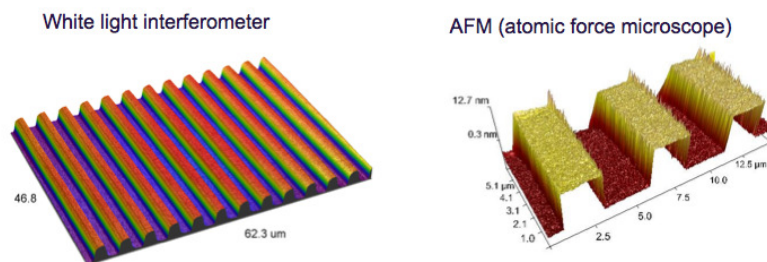


Fig. 10.3.: Image of grating before the damage taken via White Light Interferometer (WLI) and the AFM. Si substrate coated with a-C ( $45\text{ nm}$ ) The groove density was  $200\text{ grooves/mm}$  and the groove depth was  $13.5\text{ +/- }3\text{ nm}$ . The duty ratio was  $0.41\text{ +/- }0.1$ .

## 10.2 Results of damage experiment on gratings

The damage experiment was performed at FLASH in Hamburg in 2011 with  $4.6\text{ nm}$  wavelength (the wavelength varied between  $4.5\text{ nm}$  and  $4.7\text{ nm}$ ). In this wavelength domain, the beamline transmission is evaluated, taking into account the mirror's setting, to range from 0.20 (at  $4.50\text{ nm}$ ) to 0.46 (at  $4.70$

$nm$ ). The experimental results that are presented below are based on the beamline transmission of 0.39 corresponding to 4.6  $nm$ . The single shot damage experiment was done at a grazing angle, which was  $\alpha = 2^\circ \pm 0.1^\circ$  and each shot was made with a different pulse energy. Afterward, the experiment's sample was analyzed ex-situ with the same procedure as described in Chapter 8. With the difference that the damage areas were measured in this case for both flat mirror-like sample and grating sample to determine the damage threshold.

The energy threshold for grating was  $E_{G_{th}} = 0.40 \pm 0.04 \mu J$  and for the flat sample was determined to be  $E_{M_{th}} = 1.17 \pm 0.16 \mu J$ . The error bars correspond to the confidence on the fit, at the  $4.60 \pm 0.1 nm$  wavelength. The ratio  $E_{M_{th}}/E_{G_{th}} = 2.92 \pm 0.69$  is independent of the beamline transmission value and can be compared to the results of the suggested damage model on gratings (Beam Propagation Method (BPM)) in [170]. Considering effective beam area value (using imprints on the PMMA sample) to be  $A_{eff} = 22 \pm 2 \mu m^2$ , the fluence threshold was determined to be  $F_{G_{th}} = 63.7 \pm 8.7 mJ / cm^2$  and  $F_{M_{th}} = 186.6 \pm 29.9 mJ / cm^2$  [169].

Observing the grating under DIC microscope shows that damage mainly occurs at the edge of the grating structure. This was confirmed by taking AFM images (see Fig 10.7). Since at the edges of the grooves the reflected beam from the sides and from the flat surface between the grooves hits the surface at the edges and also at the sides the incidence beam interact with the surface at (close to) normal incidence, one can imagine that the damage and especially at the top of the edges should be stronger than the flat parts.

Increasing the fluence of the shot causes different degrees of damage. The damage at low fluence starts from the top corner of the grooves (which face the beam), and at very high fluences the bottom part of the grating (the lower flat area) gets damaged as well. This behavior can be explained by the interplay of reflectivity and extinction depth under total reflection conditions and heat diffusion.

Melting of the substrate (Si) or the removal of the a-C coating happens at extremely high fluence. Figures 10.6 to 10.8 show the increasing damage degree with increasing fluence of the impinging shot on the grating. In Fig 10.4 the amount of absorbed dose for different grazing angles was estimated. This shows that the best angles are grazing angles below 10 degrees and above 2 degrees.

With help of the Helmholtz equation in a paraxial approximation (see Equation 10.2) Dr. Krzywinski had simulated the model behind the grating damage (see Fig 10.5). This model is called the Beam Propagation Method (BPM). The refractive index of the medium is nearly equal to 1 (for the photon energy considered here). Basically, the Paraxial approximation of the Helmholtz equation in inhomogeneous media is the Schrödinger equation (see Eq 10.4). Propagation of the scalar field  $\psi$  can be expressed as [170]

$$\partial\psi_{(\vec{r},\vec{z})}/\partial\vec{z} = i/2[\partial^2\psi_{(\vec{r},\vec{z})}/\partial\vec{r}^2 + \delta\varepsilon(\vec{r},\vec{z})\psi(\vec{r},\vec{z})] \quad (10.2)$$

where paraxial approximation is given by

$$(k_x)^2 + (k_y)^2 \ll (k_z)^2 \quad (10.3)$$

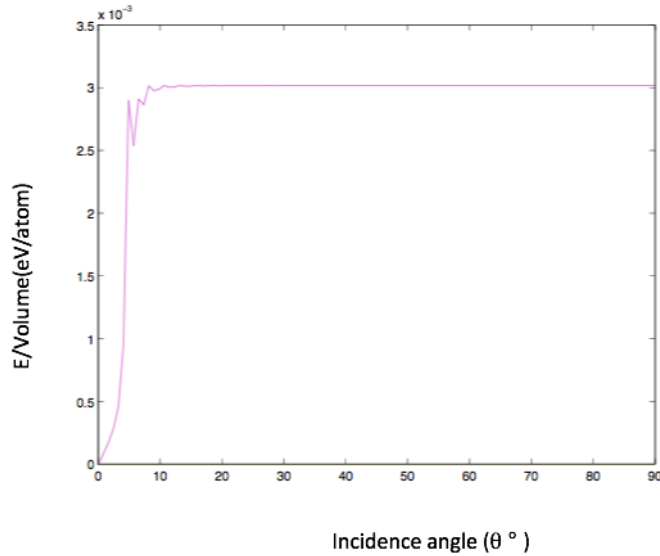


Fig.10.4.: Simulated dose absorbed distribution corresponding to the grazing angle. The amorphous carbon coating on the grating was 50 nm on Si.

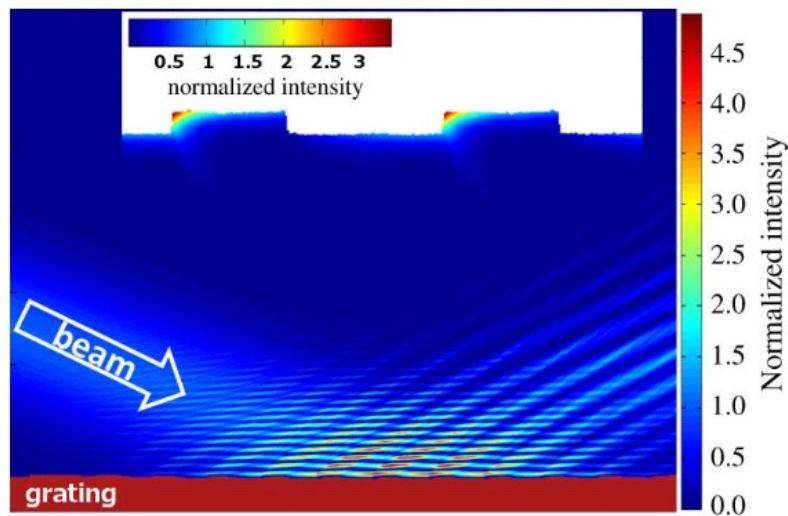


Fig. 10.5.: Simulated field distribution in the grating [170], [169]. X-ray intensity distribution is given by  $|\psi(r, z)|^2$  close to the grating surface. The beam comes from the left. Both color scales are normalized intensity to the impinging beam. The amorphous Carbon coating on the grating was 50 nm on Si and was exposed to the beam at  $2^\circ$  incidence angle. The absorbed power density is the reddish part and happens on the edge of the lamina grating structure which is 3 times higher than the flat surface. Interestingly, micro-roughness does not increase the maximum of absorbed energy by more than few percent.

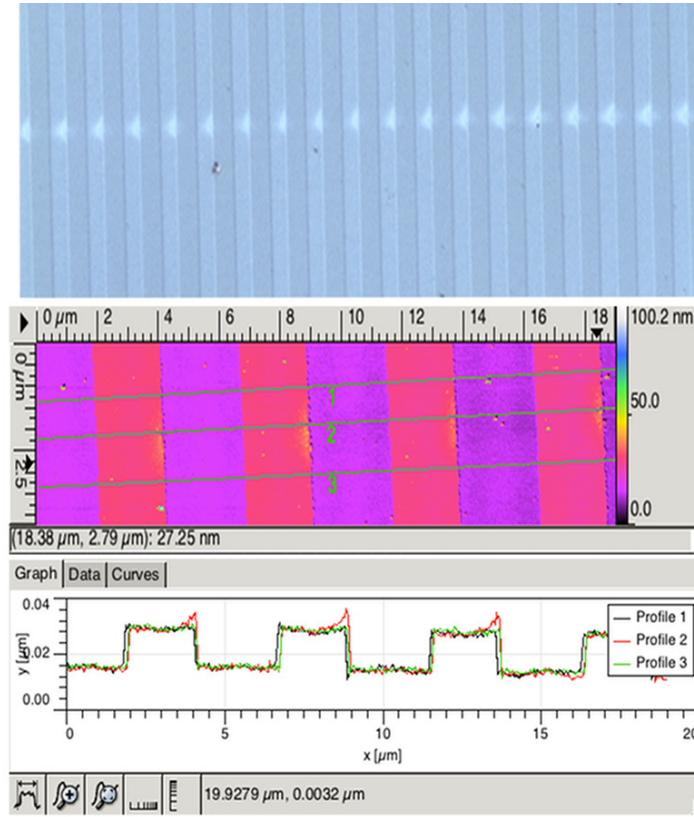


Fig. 10.6.: AFM and DIC image of grating after it being exposed to FEL shot. Pulse energy of  $1.64 \mu J$ . The lines represent the measured AFM lines on the spot. The the height of the damage spot is  $7 \text{ nm}$ .

the Schrödinger equation is given by

$$\partial\psi(\vec{r},\vec{z})/\partial\vec{z} = iH\psi \quad (10.4)$$

$$\psi(\vec{z}) = \psi(\vec{0})e^{iHz} \quad (10.5)$$

Where  $\lambda$  is the wavelength and  $\delta(r, z)$  describes the difference between the dielectric constant of vacuum and the medium. The mathematical form of Equation 10.2 is identical to the time-dependent, two-dimensional Schrödinger Equation 10.4 which can be solved by different methods. Here the beam propagation method that, applies a split operator technique, was chosen to solve this equation. The solution of Equation 10.2 would be of the kind of the Equation 10.5. The grating profile used in the simulations as a boundary is a real profile measured with AFM. As a result, the model also includes possible effects of the micro-roughness. A Gaussian beam profile was used as the initial condition. The incident angle and the photon energy were the same as in the experiment.

Since the damage occurs on the top of grooves (see Figs 10.5 and Figures 10.6 to 10.8) and at high fluence it reaches the bottom part (flat area) of the grating, a new design is considered (compared to the LCLS grating shown



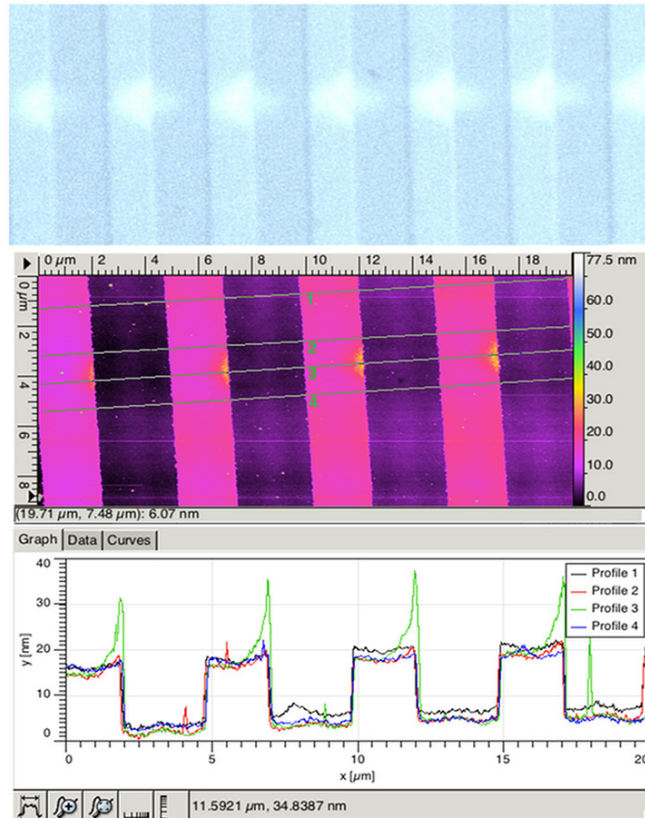


Fig. 10.7.: AFM and DIC image of grating after it being exposed to FEL shot. Pulse energy of  $1.8 \mu J$  was used here to create damage. The lines represent the measured AFM lines on the spot. The the height of the damage spot measured to be  $10 \text{ nm}$ .

in Figure 10.3), which is a Blazed grating (see Fig 10.2) [171], [172], [170], [169]. In general, one observes that damage is done mainly at the edges. Since the beam exposes the surface at the grazing angle except at the edges (at (around) normal incidence) the damage is much stronger at edges compared to the flat surface. Due to the fact that the reflected beam from the distance between the grooves also hit the edges, there is a much higher amount of beam which exposes the grating at this part. Therefore a high amount of dose will be absorbed in the edges. This was estimated to be three times higher than other parts of the grating. From the above threshold calculations this assumption is confirmed ( $E_{M_{th}}/E_{G_{th}} = 2.92 \pm 0.69$ ). From the AFM experiment results, the height of few damage spots is compared (with increasing pulse energies) to each other, which is depicted in Fig 10.11. Also, few damage spots were measured in length (the length of the damaged spot (diameter)). The length of the damaged spot is compared with the full length of each groove (grating constant) (see Fig: 10.9). The length of damaged spots is depicted vs the corresponding pulse energy with which they were made in Figure 10.10.

It is clear that when more than 50% of the groove is damaged, the damage height correspondingly increases. The growth is almost exponential. Heat diffusion plays a significant role in the damage process as well. looking at

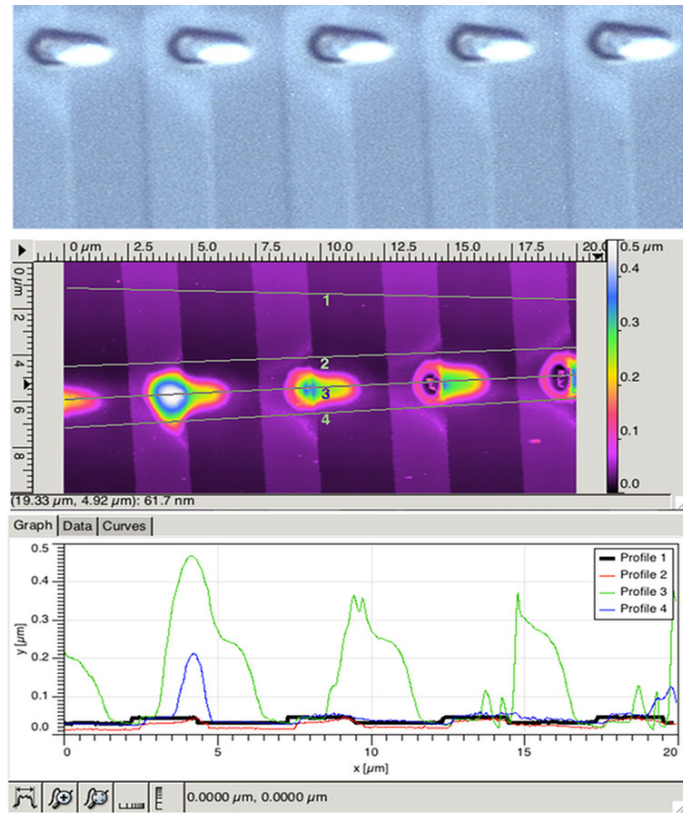


Fig. 10.8.: AFM and DIC image of grating after it being exposed to FEL shot. Pulse energy of  $8.64 \mu J$ . The lines represent the measured AFM lines on the spot. The the height of the damage spot measured is  $0.4 \mu m$ . Beam direction is from right to left in the profile pic.

Fig 9.19 for the case of the heat diffusion simulation on a flat a-C sample at  $269 eV$  shows that Si at normal incidence simulation reaches the melting temperature. Since the beam exposed the grating at the grazing incidence angle, the kinetics of free carriers and heat diffusion would differ slightly and decrease in intensity but this will not cancel the effect of heat diffusion out. The attenuation length at  $269 eV$  at  $2^\circ$  is  $6.35e^{-3} \mu m$  and at normal incidence this turns to be  $2.09 \mu m$ , which is a huge difference. Hence, one can not expect much melting of the substrate here compared to the flat sample at normal incidence. By looking at that figure it's also clear that a-C has already reached melting temperature even before silicon and that's an indication to the fact that, there is still a strong effect due to heat diffusion and melting of a-C in this damage process. As mentioned before through the reflection of the beam on the sides of each groove there is also a great part of the beam hitting the flat parts from the sides. Hence, there is still a strong probability of melting of Si. Comparing the length of damaged part to the radius up to which the melting temperature reached shows that these two lengths are comparable. Hence, heat diffusion is a good explanation of the length up to which the sample is damaged on the surface and the non-localized damage procedure.

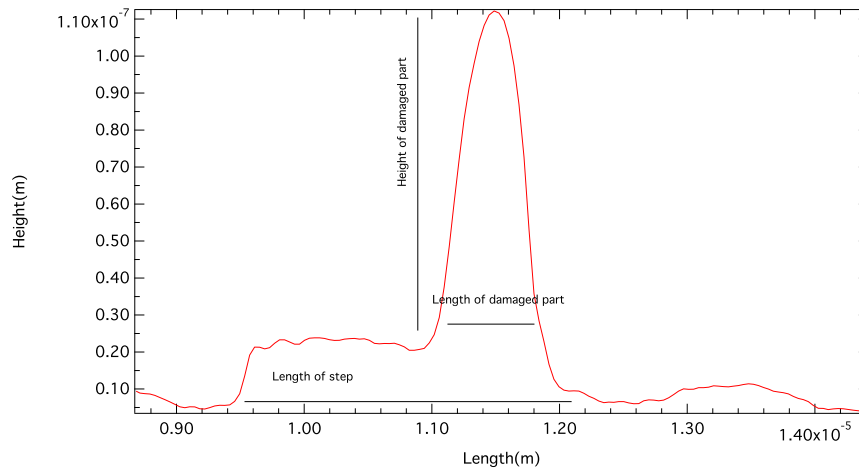


Fig. 10.9.: Illustrating the length up to which the damage is observable on the sample and the height of the spot. Damage is done mainly where its mostly absorbed (edges). The length and height of the spot was measured via AFM. Data are from the experiment at FLASH with 269 eV photon energy.

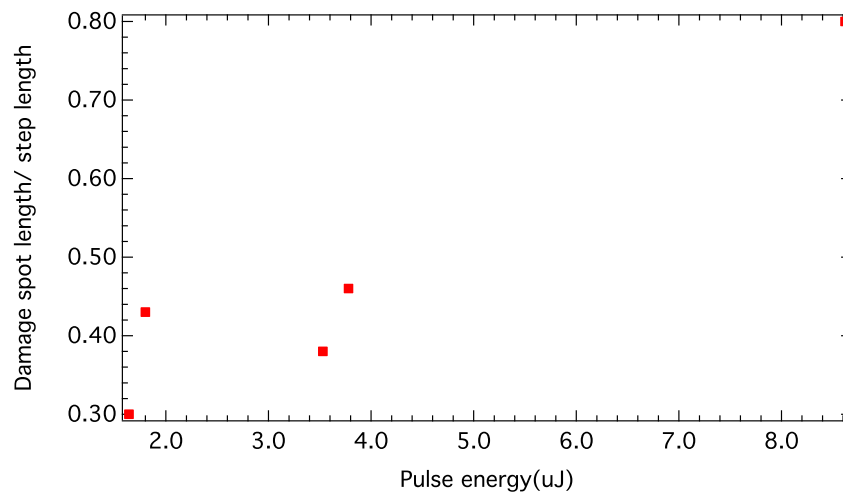


Fig. 10.10.: Illustrating the length of each damage spot vs the pulse energy which was used to generate that damage spot on the grating. The length and area of each spot was measured via AFM. Experiment performed with 269 eV photon energy at FLASH.

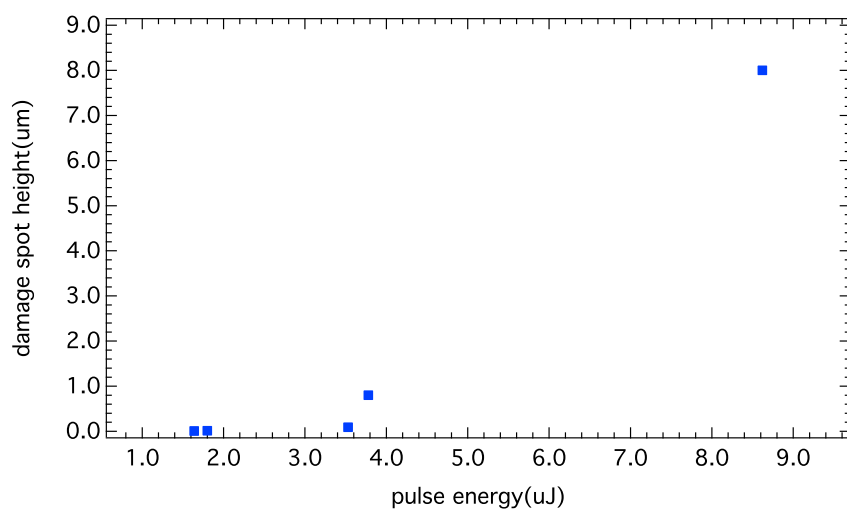


Fig. 10.11.: Illustrating the height of each damage spot vs the pulse energy which used to generate that damage spot on grating. The length and area of each spot was measured via AFM. Experiment performed with 269 eV photon energy at FLASH.

## Chapter 11

# Discussions and summary

### 11.1 Discussions

This project was concerned with the study of fundamental and application aspects of the damage caused by the femtosecond (30-130 *fs*) X-ray Free Electron Laser (XFEL) beam (see Fig: 11.1). The focus was on the damage process, the induced amount of absorbed energy and the fluence threshold for each photon energy at normal and grazing incidence angles. This includes processes such as photo-ionization, heat diffusion, secondary processes, and cascades. The fundamental processes are divided into thermal (an increase of the kinetic energy of atoms) as well as non-thermal (change of the potential energy of atoms). The potential phase changes that the material undergoes from the moment of the sample surface exposure with the XFEL pulse to when the sample cools down are essential in understanding the process of damage by the FEL beam. The temperature induced by the FEL beam is sufficient to cause damage to the substrate or the coating.

The subjected samples are amorphous carbon (a-C), CVD diamond, Ni, and MoB<sub>4</sub>C. The primary focus was on a-C and CVD diamond. Both a-C and CVD diamond undergo sequences of processes after being irradiated by an X-ray FEL pulse. The photon energies examined here are in the range of 20–830 eV. The a-C is a mixture of different types of bindings ( $sp^3/sp^2=2.2$ ). The CVD diamond, meanwhile, only has  $sp^3$  bonding and a crystal structure.

During the time that XFEL pulse illuminates the sample, electrons of deep shell state (K-shell in the case of a-C or CVD diamond) and valence band become ionized, and the conduction band electron density increases through photo-ionization (see Fig: 11.2, 11.3). The induced Auger electrons may carry enough energy so as to excite other atoms/electrons. Depending on the energy of ionized carriers, several secondary processes such as impact ionization, tunnel ionization, free carrier diffusion, free carrier scattering on atoms or phonons as well as the escape of free electrons from the surface with different degrees of strength take place. Among these secondary processes, the impact ionization occurs within a *fs* time scale and terminates when the energy of the electrons is lower than the threshold energy for the impact ionization ( $E < E_{bandgap}$ ). The phonon scattering takes a longer time, within a *ps* time scale (see chapter 5

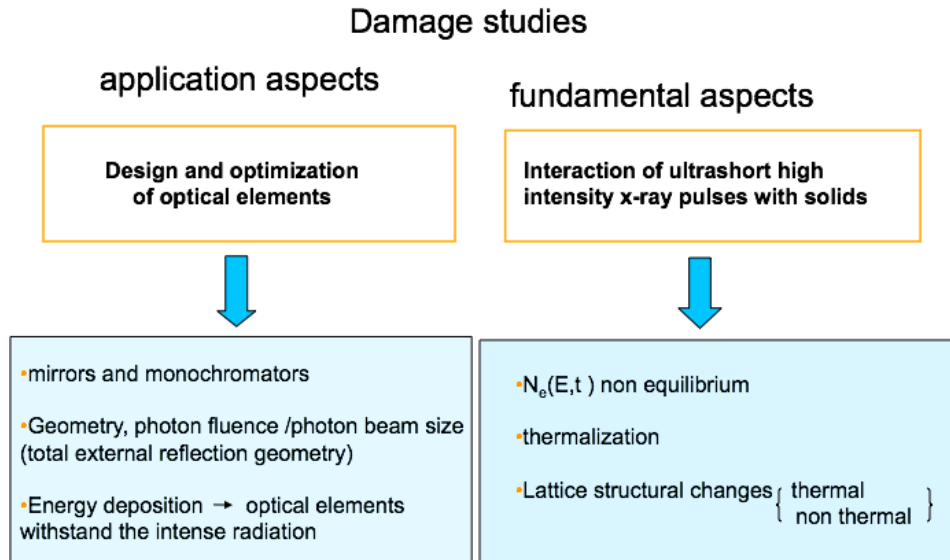


Fig. 11.1.: Damage studies

for more details). During these interactions, electrons (free carriers) lose their energy with rapid changes in the electronic state of the system. In covalently bonded materials, the electronic state of the system has a significant influence on the interatomic bonds. Rapid changes in the electronic state of the system induce rapid changes in the interatomic bonds, rearranging atoms and minimizing the system's potential energy (see Fig: 11.3).

In the case of a-C or CVD diamond, changes in  $sp^3$  bonds to  $sp^2$  bonds (see Fig: 11.4) reduce the potential energy of the system. Since  $\pi$  orbitals interact with  $\pi$  states of more than one atom, these bonds are more dominant and energetically reduce the potential energy of the system. Hence, the phase transition occurs which is confirmed through Raman and photoemission studies (see chapter 8). This phase transition is extremely fast ( $\sim 100s$  fs) and ought to be considered as non-thermal. The ionic phase transition, however, is not the only mechanism during the damage process. Carrier diffusion, heat diffusion, plasma expansion (shock waves) and Coulomb explosion are among the active processes which contribute to the damage (see Fig: 11.5).

The beam footprint size from the experimental data, in the case of the damage with fs XFEL pulses, do not always linearly depend on the incoming pulse energy on the logarithmic scale (assuming that the beam has a real Gaussian shape). At higher pulse energies this dependency changes to a nonlinear one. Hence, heat diffusion process has been simulated via COMSOL (see chapter 9) and it became apparent that it has an effect on the damage process. Heat diffusion takes place over a much longer time scale compared to the photo-ionization or other secondary processes, impact ionization for instance, etc. The melting threshold is found (through simulation) to be higher than the threshold calculated for the phase transition (through ionization) from the experimental

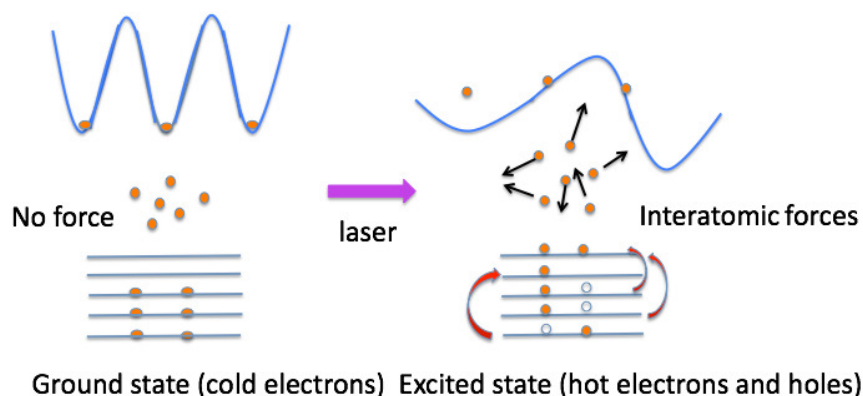


Fig. 11.2.: Very simple schematic of the matter and laser beam interaction [17]. The left side shows the system in its ground state, the electrons cold state. The potential landscape shows minima at the crystal lattice sites. Therefore, no (external) forces are acting on them except tight binding Coulomb potential induced by the lattice. On the right, the laser light has affected the system and transported it to an excited state. Hot electrons and holes are created here. The potential landscape undergoes qualitative and quantitative changes, resulting in disappearance or shifting of the minima. This happens in very short time scale (shorter than reaction time) as a result, forces act on the carriers/atoms and move them.

data (see e.g. Figs 9.17, 9.19). During the 100 *fs-ps* time scale the material undergoes a phase transition, and within the same time scale or rather after the photo-ionized phase change, the thermal process starts to take place and continues.

If the energy of a secondary electron is high, the system remains in an excited state for a longer period which takes the system longer to cool down. Since the system already has undergone a phase transition in very early stages of the damage process, one should consider that heat diffusion occurs in two different types of material. Starting from the part of the material which underwent phase transition, and continues within the original material (following Figures 9.17, 9.19 and 9.20, represent melting and the phase transition (through photo-ionization) threshold for a-C and in the case of CVD this is pictured in Fig 9.25).

The difference is that during the photo-ionization damage processes, the temperature starts to increase and the melting threshold will be reached after some *ps*. Hence, after some *ps* heat diffusion will cause more damage. Therefore

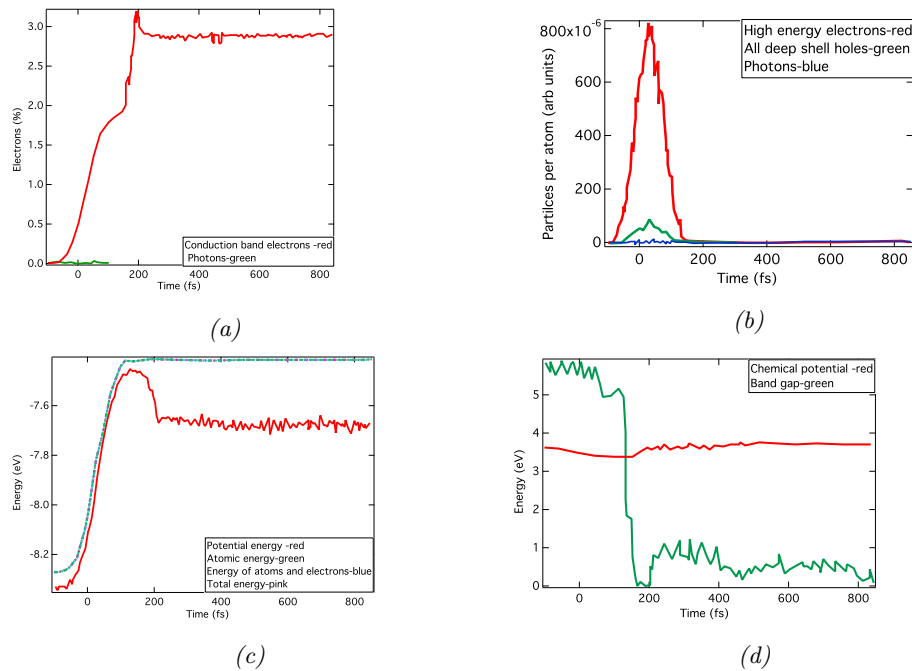


Fig. 11.3.: (a): Simulated evolution of conduction band electron occupancy in CVD diamond with 830 eV photon energy with  $1.87 J/cm^2$  fluence. The pulse duration was taken as in experiment 100 fs. Data is simulated with a new hybrid code XTANT developed by Dr. N. Medvedev. (b): Simulated high energy electrons and core hole densities. (c): Simulated changes of potential, atomic, electrons and the total energy of the system. (d): Simulated changes of chemical potential and the band gap during and after the pulse.

one should consider two models combined to be able to describe the damage process. One model consists of irradiated matter undergoing a phase transition and heat diffusion. The second is the heat and carrier diffusion model inside the original state of the material.

From Raman studies, it has been calculated that the high degree graphitized part of the matter has a smaller radius than the beam, located in the center of the damage footprint (see Section 8.5). Based on Raman measurements, taking

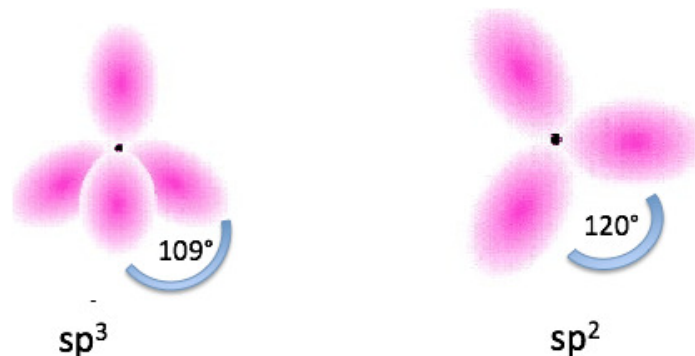


Fig. 11.4.: Orbital configuration of carbon  $Sp^3$  (mainly in Diamond),  $Sp^2$  (mainly in Graphite)



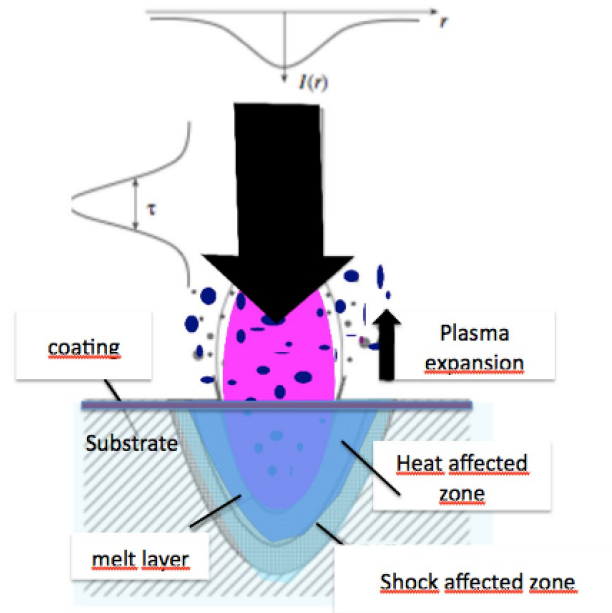


Fig. 11.5.: Very simple schematic of the matter and X-ray FEL beam interaction [39]. Where the heat affected zone shows the region where heat gets diffused into and the shock affected zone describes the region where high pressure starts to induce shock waves. There is a thin layer right behind the heat-affected zone, which shows the melted layer.

distance from the center of the damaged spot reveals; that the graphitization degree reduces. Taking these facts into account in connection with the heat diffusion simulation, small graphitized areas, partially phase transformed areas; which somehow look like grating structure, were considered in the simulations (see Fig 9.11).

It became evident that considering smaller graphitized regions enables neighboring areas (which are Si and a-C) to reach their respective melting temperatures. Accordingly, the large graphitized areas prevent a-C or Si from reaching their melting temperature. Hence, if the graphitization happens in small areas, a-C/Si could still reach their melting temperatures which may affect the damage imprint spot size. There is also a change in size due to the graphitization itself. As the density of material changes (with no mass loss), the volume at the spot should change.

The obtained damage dose threshold is concerned with the non-thermal melting (phase transition) state of the damage; keeping in mind that thermal melting threshold is reached at higher pulse energies (see Table 11.1). Since heat diffusion in the early stage of the damage process in the atomic system is very low, it can be neglected in the timeframe of  $fs$  to  $ps$ , whereas carrier diffusion must be taken into consideration. As an example, in the case of the experiment with  $830\text{ eV}$  photon energy, photons have enough energy to ionize the electrons of the atoms' K-shell. The ionized electron is then released with an energy

around  $530\text{ eV}$ , which is enough to ionize the other atoms' electrons of the K-shell. In the first case, the Auger process or fluorescence process take place. As a consequence, the Auger electron might create a free electron with enough energy to excite another atom. These secondary processes occur consecutively. Focusing on the first ionized electron in Figures 9.6, an estimate of the electron range is possible. The electron range is the distance the electron travels until it loses its energy below the threshold to ionize other atoms. Fig 9.6 shows that the free electron could travel up to  $70\text{ nm}$  inside the material for the considered case here. Considering the attenuation length at that photon energy, in the case of a-C as an example, shows that the beam had traveled up to  $1.26\text{ }\mu\text{m}$  inside the sample and the thickness of the a-C coating in that experiment was approximately  $1.4\text{ }\mu\text{m}$ . Considering the electron range, reveals that this free electron has already traveled into the Si substrate inducing additional damage (as there are lots of these types of electrons activated). The heating up of the substrate to its melting temperature, for instance, and then generating the extra pressure to push the graphitized matter outwards and towards the surface are among the results of this effect (see Fig 11.6, 11.7 and Figs in section 8.4).

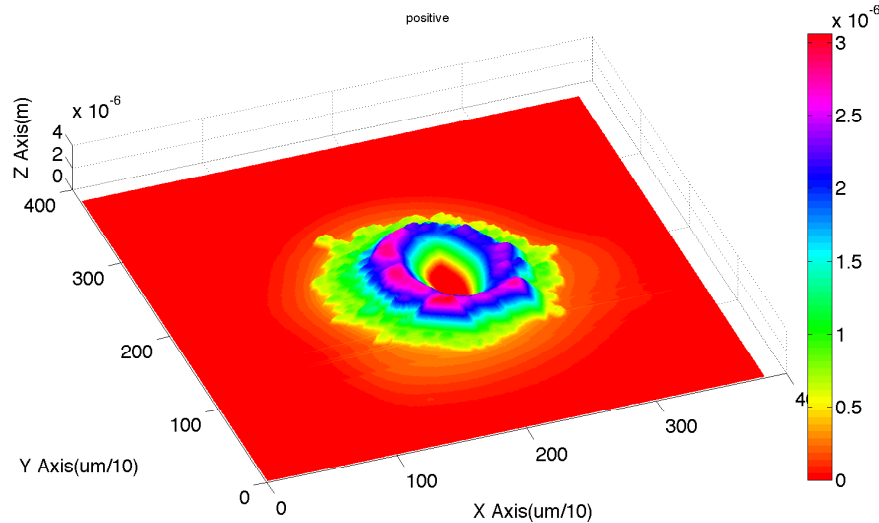
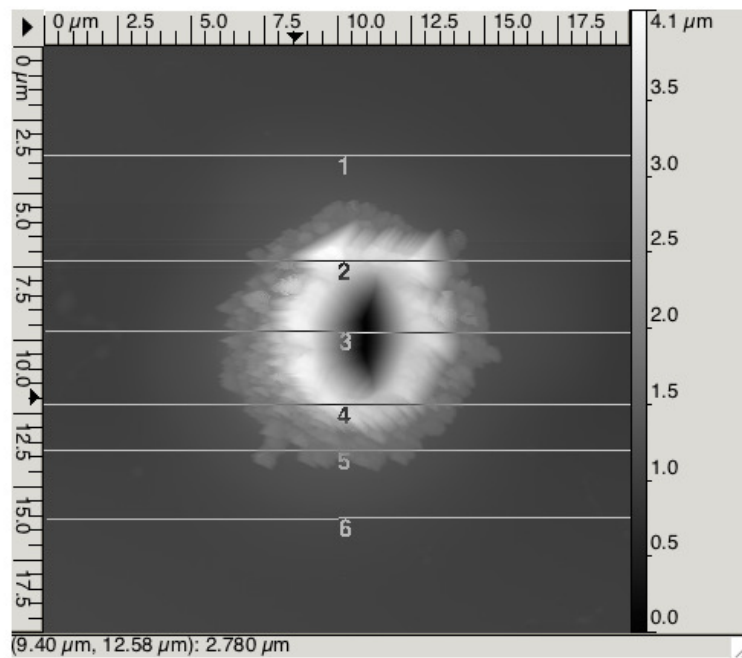
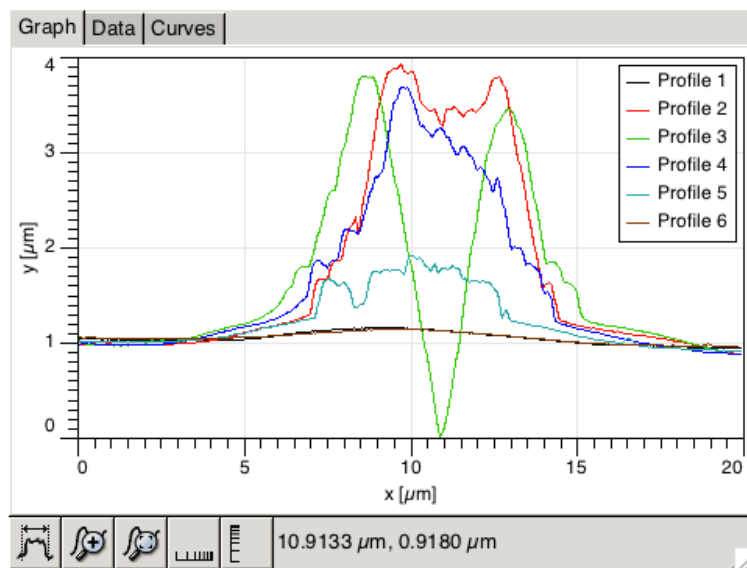


Fig. 11.6.: AFM topography volume profile of an irradiated area on a-C with a  $4,8\text{ }\mu\text{J}$  FEL pulse at  $177\text{ eV}$  at FLASH. Volume of the spot is calculated via the AFM image with help from the MATLAB Code.

In the case of lower photon energies ( $20\text{--}24\text{ eV}$ ), compared to higher photon energies (between  $90\text{--}830\text{ eV}$ ) there are other damage mechanisms governing the damage process (Figure 11.8 shows the amount of absorbed dose in each case of a-C and CVD at different photon energies). At low photon energies ( $20\text{--}24\text{ eV}$ ) the attenuation length is very short, ionization occurs in a very small volume close to the surface layer of the coating. The number of free carriers increases rapidly in a very short time; which results in the Inverse-Bremstrahlung, Coulomb explosion, reflection of the beam off the coating, a screening effect, and shock waves. This implies that the Hybrid XTANT model is not comparable to the measured experimental results at these lower photon energies.



(a) AFM topography depth profile of an irradiated area on a-C with a  $4,8 \mu\text{J}$  FEL pulse at  $177\text{eV}$ . Lines represent the taken profiles in (b).



(b) AFM topography depth profile.

Fig. 11.7.

As mentioned in chapter 9, in the case of constant volume, the system needed a longer time to stabilize in the XTANT simulations. In reality, one can not keep both volume and pressure constant. Considering that these two cases are valid at the same time, from simulation it is clear that the phase transition happens (non-thermal) between first 100-200 *fs* time after the irradiation (see Fig 11.10).

The Hybrid XTANT model in the case of CVD diamond predicts that temperature after the pulse goes up to 2000 *K*. This is still below the melting threshold temperature (3800 *K*) for carbon. A suggestion would be to start the heat simulation inside the graphite with a temperature of 2000 *K* after the irradiation and the surrounding original material (CVD /a-C ) with room temperature which gets heated up after a longer time during damage process. With that amount of energy, free carriers continue cascading and can travel up to few *nm* further and cause secondary effects.

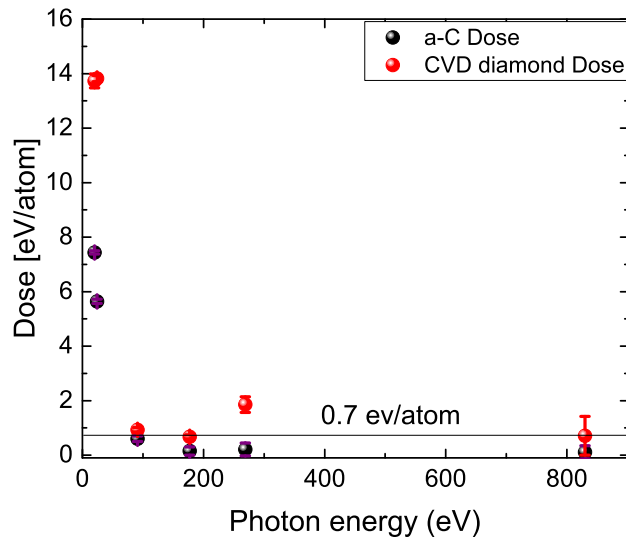


Fig. 11.8.: Comparing the damage dose threshold at different photon energies on CVD diamond and amorphous carbon. The line at 0.7 *eV* represents the calculated damage dose threshold theoretically via Hybrid XTANT model mentioned in chapter 9 [135].

With the help of other experimental techniques like AFM, Raman spectroscopy, and SPEM, one proves that both a-C and CVD have turned into graphite. The degree of graphitization changes from the middle part of the spot towards the edges of the damaged spot. Also, it becomes apparent that graphitization (in general and without considering its degree) happened over a longer distance compared to the beam size (see section: 8.5). In Figure 11.9 one can observe that the graphitization is detectable even outside the center of the damaged spot. This evidence indicates that the ionization process, as well as secondary processes, start in the center of the spot after irradiation. Secondary processes and heat diffusion are the reason for the increase in the radius of the damaged area and defects introduced in the transformed material. The beamline apertures could also induce some interference patterns as well as some defects in the beam focus. Hence, the sample will get exposed to the beam even outside of the focus. This in return causes phase transition not just in the center of the beam but also at some distances away from the center. Enlargement of the damaged area is more observable in the case of a-C sample than in CVD. This could be because a-C coating is a thin layer on a Si substrate which has a lower melting threshold.

With an increase in the photon energy, the degree of graphitization increases. From AFM studies it became clear that a negligible amount of mass disappeared or evaporated away (see chapter 8). Hence, with a very simple calculation, it is possible to estimate the depth which the beam influences the material and causes damage. Looking at the profile images, the height and radius of the parts transformed into graphite are easily read. The volume has a cone shape. Knowing the ratios of a-C to graphite density helps to estimate the volume of the material which could not be measured via AFM (the depth).

The density of graphite to a-C has a ratio of 1.02. The volume of graphite ( $V_{Gr}$ ) from the AFM measurements on the damage spot (at 177 eV with 4.8  $\mu J$  pulse energy; see Fig 11.7a) is 156.013  $\mu m^3$ . Hence, the depth of which the beam influenced the a-C could be estimated to be 6.07  $\mu m$ . This depth is higher than the attenuation depth at this photon energy (0.66  $\mu m$  at 177 eV photon energy). In the case of CVD diamond from the AFM profile, one can read the depth to which the damage has impinged inside the material in depth.

Taking stopping power (discussed in chapters 5 - 8) into account does not give the right answer to the question, how large is the volume which was influenced via irradiation during the whole damage process. One could speculate that it would be sufficient to take the attenuation length into account for the very first *fs* of the interaction where just photo-ionization, impact ionization, and the Auger process take place. The fact is that damage does not stop suddenly after that period and several other secondary processes, as well as carrier diffusion, scattering processes, and heat diffusion, carry on until the material reaches relaxed potential state. Hence, a larger volume is in fact involved in this process.

In the case of gratings, the significant part of the damage occurs at the edge of each groove (see chapter 10). The amount of absorbed dose was theoretically predicted to be 3 times higher than the remaining part of the step. This is confirmed through energy threshold calculations on flat and grating samples

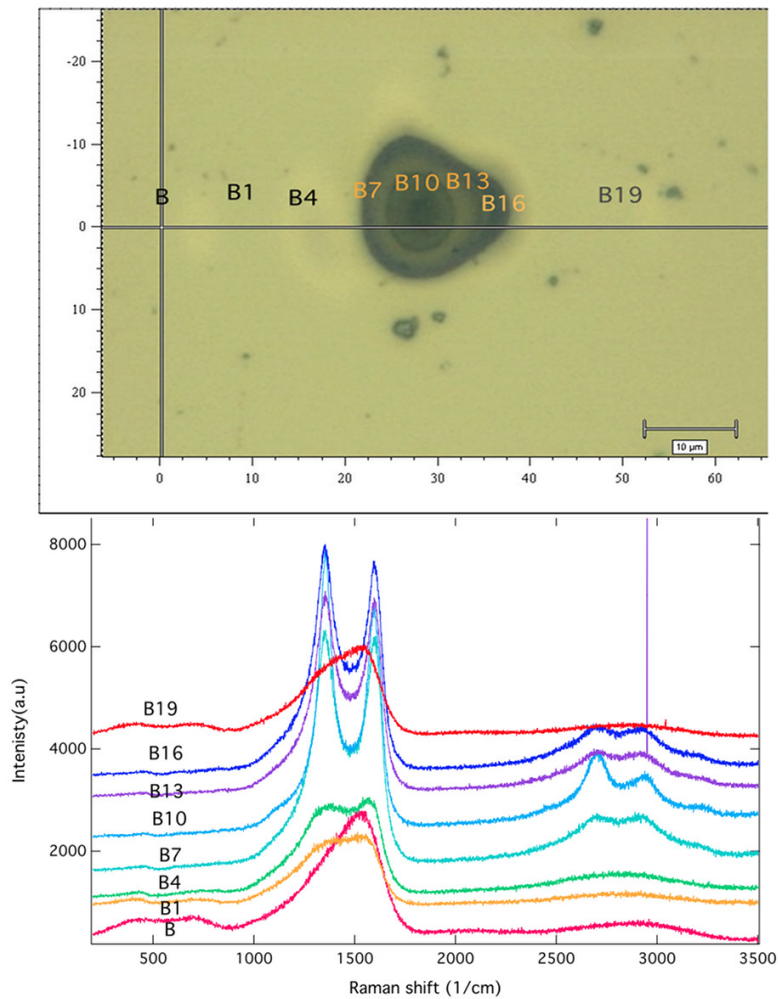


Fig. 11.9.: Amorphous carbon damage spot with  $4.83 \mu J$  and photon beam energy of  $91 eV$  single shots at FLASH. The  $\mu$ -Raman analysis evidence the ordering of the a-C structure to nano crystallites of graphite, in good agreement with the 3 step model of Ferrari et al [138], [109], [110], [139]. Looking at the heat simulation in chapter 9 shows that at this pulse energy a-C and Si have both reached melting temperature. This figure also shows that beam fringes are observable at this point. This could be due to the apertures in beamline and the beam focus which was causing interference patterns on the sample. This fact that graphitization is observable out of the main dark spot of the damage is clearly showing that a larger area of the sample at the damage spot compared to the beam radius at this experiment was effected and phase transformed.

and comparing those values. From the AFM experimental data, it is observed that the absorbed dose is significantly higher at the edges (see Fig 10.6).

As a matter of design, the blazed grating structure would be the better option. Less damage would take place on this type of grating. From AFM studies and heat diffusion simulations on grating one can see that a large area of the damage is due to the heat diffusion. In this particular case, one can see the difference between localized and non-localized damage in the material (see Fig 9.19). This means that the extended area of the damage on the grating is

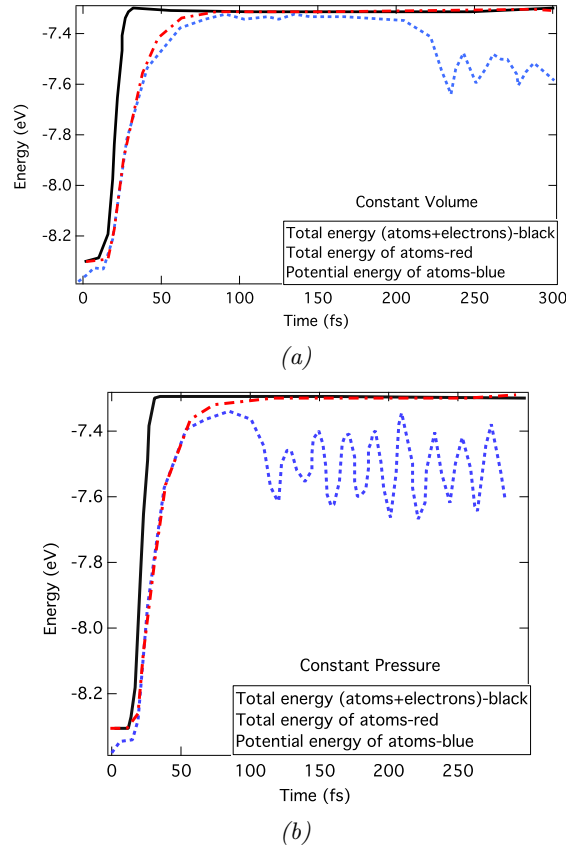


Fig. 11.10.: (a): Diamond irradiated at  $92\text{eV}$  photon energy with  $10\text{fs}$  laser pulse. The absorbed energy was  $1\text{ eV/atom}$ . The total energy of the system (electrons and atoms) is plotted in black and total energy of atoms is depicted in red dash line, the blue dashed line shows the potential energy of the system. Reference [158]. (b): The same simulation under the constant pressure.

due to the heat diffusion.

After all, it will be interesting to consider the following suggestions for future projects:

To measure the beam size more precisely and following the possible changes in the spot size or surface reflectivity, etc., it is suggested to plan an in-situ pump-probe experiment during the damage experiment inside the experimental chamber. Where it is possible to overlap FEL and laser pulses temporally and spatially. The shadowgraph technique was used at FLASH FEL in 2012 (see ref [173]). With the FEL intensity, a plasma effect on the surface of the sample is secured through ultra-fast ionization effect. This plasma can be exposed to the laser light (probe). The laser light after will be reflected at the critical density of plasma and less light will be transmitted through the area where the free electron density is above the critical density. This shadow can be observed by imaging the surface onto a CCD camera, which can be done in single shot basis. If the laser light arrives before, after or during the pulse at certain time steps (e.g. each  $50\text{ fs}$ ) one can obtain images of the development of the damage spot on the sample. All the complex processes such as photo-ionization, Auger

Photon energy (eV)	angle (°)	melting threshold ( $\mu J$ )	Beam area (imprint) ( $um^2$ )	Fluence threshold ( $J/cm2$ )	Dose ( $eV/atom$ )	Attenuation depth (Henke's tables) ( $\mu m$ )
830-CVD	90	$38.8 \pm 0.00$	114.04	$34.03 \pm 0.3$	$15.1 \pm 0.00$	$0.78 \pm 0.00$
830- a-C	90	$10 \pm 0.00$	163.15	$6.74 \pm 0.00$	$3.04 \pm 0.00$	$1.43 \pm 0.00$
269-a-C	90	$1 \pm 0.03$	22	$4.55 \pm 0.77$	$1.22 \pm 0.00$	$1.32 \pm 0.00$
91-a-C	90	$1.4 \pm 0.02$	106.68	$1.53 \pm 0.12$	$5.78 \pm 0.00$	$0.09 \pm 0.00$
24-a-C	90	$1.3 \pm 0.06$	302.71	$0.33 \pm 0.09$	$18.6 \pm 0.00$	$0.00593 \pm 0.01$

Table 11.1.: Results of the melting simulations on CVD diamond and a-C material at different photon energies. Sample thickness is  $0.5mm$  in the case of CVD diamond.

process, multiphoton-ionization, etc., could be studied by using photon, ion or electron spectrometers during the experiment. The X-ray diffraction could provide information on the order of crystallization of the samples.

To choose a coating, as mentioned before, many factors such as the reflectivity, damage threshold, etc. of the materials should be considered. According to the studies on a-C and partly on Ni in this project and other studies on B4C, become clear that two stripes of Ni and one out of B4C would be a great combination for coating on one mirror but due to cost reason it was decided to use  $50\text{ nm}$  B4C for mirrors with  $20\text{ mm}$  wide reflecting area at XFEL beamline; which was more of practical use. In the case of gratings, a combination of grating on multi-layers, where one can benefit from multi-layer structure, would be an attractive candidate which could be studied in future.



## 11.2 Summary

X-ray Free Electron Lasers (XFEL) contribute to several different scientific applications reaching from physics, over chemistry, material and earth sciences to biology. They deliver high peak brilliance, high power, femtosecond focused laser pulses. Optical elements in these facilities are of crucial importance as they need to survive those severe conditions (high peak power, etc.) during the distribution of a high-quality beam to the experimental stations.

The optical element such as the mirror or grating need to withstand the high peak power of the intense, focused *fs* pulses over a full spectral range of photon energies at FEL beamlines. Besides, the wavefront needs to stay undistorted during the transport along the beamline until the experimental station. Choosing a suitable substrate and coating for mirrors or gratings (as optical elements) in the beamline depends on many factors including high reflectivity, low roughness, high mechanical and thermal stability.

Many investigations have been done up to now on low and high *Z* materials to find out the suitable coating for soft/ hard X-ray beamlines. Among all these, one can mention  $B_4C$ , B, SiC, C, SiN, Al,  $Al_2O_3$ ,  $SiO_2$ , Li, Cu, InSb, Mo, etc [174], [132], [175], [176].

This Ph.D. project is concerned with the structural modification of solids under ultra-short X-ray FEL laser pulses. These materials are chosen from the group of low *Z* materials (amorphous carbon (a-C), CVD diamond). Additionally, a-C is tested as a potential coating on mirrors and CVD diamond to be used in monochromators for the soft X-ray beamline at the European XFEL facility. These two materials were studied at normal (to study the structural modification processes) and grazing incidence angles for the total external reflection. At normal incidence, the exposed material via FEL X-ray beam experiences a high peak power and exhibit non-linear effects. Among those, are photo-ionization, secondary processes (e.g. Auger, impact ionization, carrier diffusion, etc. (see Chapters 5, 9)) and high amount of heat induced, which influence the damage process.

The time scale of events happening during the interaction of the XFEL pulse with the material can be grouped in three different time zones. In early *fs* time, the photo-ionization is the ruling process; taking place. After some 100 *fs*, events like Auger, impact ionization, tunnel ionization, carrier diffusion start to take place. These are followed by free carriers interaction with the lattice (e.g. electron-phonon coupling, etc.), and heat diffusion is grouped in the third time zone, which starts after some 100 *ps* and continue till the system gets back to room temperature after some  $\mu s$ . Depending on the pulse energy at each photon energy, heat diffusion could play a substantial role in these interactions and cause effects like melting (see this in Figure 11.11). The consequence of crossing the threshold values of structural modifications of materials is causing damage to those coatings, gratings or monochromators used at the beamlines; which is not desirable.

One of the interesting points observed from the experimental results is that the damage footprint area on the logarithmic scale was not growing linearly with pulse energy as expected. The results of the experiments show that the

footprint area on the logarithmic scale at very low pulse energy increases linearly with the pulse energy. This behavior changes by increasing the pulse energy. Fig 11.11 shows, after the linearly increasing part, a second region starts which grows with a shallower slope. This is an indication of secondary processes and heat diffusion or heat diffusion mainly governing the damage process (depending on the pulse intensity). The heat distribution and secondary processes cause a non-linear increase in the size of the damage spots depending on the pulse energy on the logarithmic axis (see Fig 9.26). The conclusion is that the FEL pulse effects (after illuminating the sample) get limited by diffusion processes carried out by carrier diffusion and their kinetics which cause the heat diffusion. This is examined in a simple model which is presented in Figs 9.27 and 9.28. Here an FEL Gaussian beam is combined with a distribution function (as a convoluted Gaussian function) to model the photo-ionization (PI) and diffusion processes in one model.

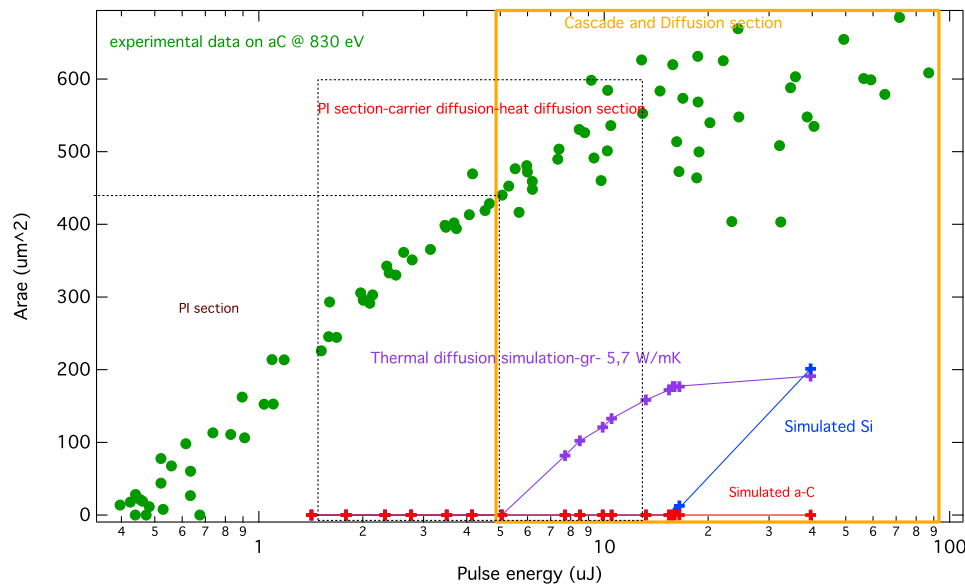


Fig. 11.11.: Figure illustrates experimental data at 830 eV on a-C in green dots. The violet data set shows the area up to which the sample was heated up considering phase transition into graphite in the case of a-C. Which is done via COMSOL simulations. One can see at which pulse energy Si/a-C reach their melting temperature and how far (on the surface) this temperature spread. The experimental size of the damage spot can then be compared to this value. Here, three sections could be defined in damage process: PI (photo-ionization) section, carrier diffusion and cascade section and the heat diffusion section. Where carrier diffusion starts during PI and could continue in heat diffusion section.

From heat diffusion simulation via COMSOL, one can extract the melting energy threshold for each material at different photon energies. Simulations show that melting plays a role in the damage process. As an example, at 830 eV, around  $10 \mu\text{J}$  ( $2.7 \text{ eV/atom}$ ) (see Fig: 9.19) one can see that Si or a-C reach their melting temperatures (graphite reaches this value around  $5 \mu\text{J}$  ( $1.38 \text{ eV/atom}$ )) (see Fig: 11.11).

Comparing the damage processes shows that at different photon energies in the case of a-C or CVD diamond, the damage due to the heat diffusion

(melting) in the system happens at high pulse energies compared to the non-thermal process. The next observation is that around K-edge these two values (non/thermal damage absorbed dose) get close to each other and at lower photon energies (20 eV) melting has a much weaker effect in the damage compared to non-thermal processes. Which is a hint to the point that at lower photon energies, effects like free carriers escape from the surface, secondary processes, plasma formation, Coulomb explosion, etc. are mainly the processes inducing the damage on the material. In the case of CVD diamond at 830 eV (considering the phase transition) the COMSOL simulation shows that the induced graphite can reach the melting temperature around 5  $\mu J$  which cause a thermal damage (see Figs: 9.25 and 9.29).

The CVD diamond is a suitable material to be used in monochromators [177], [4] and [178].

Based on the performed studies from other groups, the B4C seems to be a better candidate to be used on mirrors (optical elements) [174], [132], [175], [176]. Among multilayers, the MoB4C is an interesting candidate, and from the group of high Z material, Ni shows promising values and is interesting to be studied with more details with different photon energies. Results of the experiment on Ni at different grazing angles at 269 eV are presented in Table 12.5.

The result of the damage studies on MoB4C are presented in Table 12.6 and Figs 12.18a – 12.25. Looking at those results shows that the threshold fluence in the case of annealed MoB4C samples is higher than in the case of a-C (which is not annealed). This is due to the more stable structure of annealed samples. Hence, further studies on annealed multi layers are interesting to be continued.



## Chapter 12

# Appendix A

### 12.1 Damage threshold values summarized in Tables at different photon energies for a-C and CVD diamond

Photon energy (eV)	angle (°)	energy threshold ( $\mu J$ )	Beam area (imprint) ( $\mu m^2$ )	Fluence threshold ( $J/cm^2$ )	Dose ( $eV/atom$ )	Attenuation depth (Henke's tables) ( $\mu m$ )
830.0	90	$1.8 \pm 0.36$	114.04	$1.6 \pm 0.44$	$0.70 \pm 0.61$	$0.78 \pm 0.00$
269.0	90	$1.52 \pm 0.03$	22	$6.9 \pm 0.21$	$1.86 \pm 0.28$	$1.32 \pm 0.00$
177.0	90	$0.63 \pm 0.03$	78.53	$0.8 \pm 0.05$	$0.67 \pm 0.07$	$0.42 \pm 0.00$
91.0	90	$0.27 \pm 0.02$	106.68	$0.25 \pm 0.04$	$0.92 \pm 0.08$	$0.09 \pm 0.00$
24.0	90	$0.87 \pm 0.06$	302.71	$0.27 \pm 0.04$	$13.8 \pm 0.1$	$0.00593 \pm 0.01$
20.0	90	$0.54 \pm 0.08$	201.46	$0.26 \pm 0.02$	$13.7 \pm 0.1$	$0.00450 \pm 0.00$

Table 12.1.: Results of the damage experiment on CVD diamond material at different photon energies. Sample thickness is 0.5 mm

Photon energy (eV)	angle (°)	energy threshold ( $\mu J$ )	Beam area (imprint) ( $um^2$ )	Fluence threshold ( $J/cm^2$ )	Dose ( $d_e + d_z$ ) ( $eV/atom$ )	$d=d_e + d_z$ ( $\mu m$ )
830.0	90	$1.8 \pm 0.36$	114.04	$1.6 \pm 0.44$	$0.70 \pm 0.61$	$0.78 \pm 0.00$
269.0	90	$1.52 \pm 0.03$	22	$6.9 \pm 0.21$	$1.86 \pm 0.28$	$1.32 \pm 0.00$
177.0	90	$0.63 \pm 0.03$	78.53	$0.8 \pm 0.05$	$0.67 \pm 0.07$	$0.42 \pm 0.00$
91.0	90	$0.27 \pm 0.02$	106.68	$0.25 \pm 0.04$	$0.92 \pm 0.08$	$0.09 \pm 0.00$
24.0	90	$0.87 \pm 0.06$	302.71	$0.27 \pm 0.09$	$13.7 \pm 0.20$	$0.00590 \pm 0.01$
20.0	90	$0.54 \pm 0.08$	201.46	$0.26 \pm 0.08$	$13.6 \pm 0.25$	$0.00453 \pm 0.00$

Table 12.2.: Results of the damage experiment on CVD diamond material at different photon energies. The stopping power is considered here.

Photon energy (eV)	angle (°)	energy threshold ( $uJ$ )	Beam area (imprint) ( $um^2$ )	Fluence threshold ( $J/cm^2$ )	Dose ( $eV/atom$ )	Attenuation depth (Henke's tables) ( $\mu m$ )	Thickness of sample (coating) ( $\mu m$ )
830.0	90	$0.38 \pm 0.75$	163.15	$0.23 \pm 0.00$	$0.10 \pm 0.24$	1.26	1.4
269.0	90	$0.17 \pm 0.04$	22	$0.77 \pm 0.21$	$0.20 \pm 0.23$	2.11	1.4
177.0	90	$0.14 \pm 0.12$	78.53	$0.18 \pm 0.17$	$0.15 \pm 0.13$	0.66	0.89
91.0	90	$0.13 \pm 0.09$	78.53	$0.16 \pm 0.09$	$0.60 \pm 0.10$	0.15	0.89
24.0	90	$0.32 \pm 0.03$	328.57	$0.09 \pm 0.03$	$5.64 \pm 0.08$	0.0094	0.045
20.0	90	$0.33 \pm 0.05$	317.23	$0.1 \pm 0.05$	$7.44 \pm 0.06$	0.0070	0.045

Table 12.3.: Results of the damage experiment on amorphous carbon material at different photon energies

Photon energy (eV)	angle (°)	energy threshold ( $uJ$ )	Beam area (imprint) ( $um^2$ )	Fluence threshold ( $J/cm^2$ )	Dose ( $d_e + d_z$ ) ( $eV/atom$ )	$d=d_e + d_z$ ( $\mu m$ )	Thickness of sample (coating) ( $\mu m$ )
830.0	90	$0.38 \pm 0.75$	163.15	$0.23 \pm 0.00$	$0.04 \pm 0.01$	$0.04 \pm 0.00$	1.4
269.0	90	$0.17 \pm 0.04$	22	$0.77 \pm 0.23$	$0.20 \pm 0.22$	$2.11 \pm 0.00$	1.4
177.0	90	$0.14 \pm 0.12$	78.53	$0.18 \pm 0.17$	$0.15 \pm 0.13$	$0.66 \pm 0.00$	0.89
91.0	90	$0.13 \pm 0.09$	78.53	$0.16 \pm 0.09$	$0.6 \pm 0.10$	$0.15 \pm 0.00$	0.89
24.0	90	$0.32 \pm 0.03$	328.57	$0.09 \pm 0.03$	$5.61 \pm 0.08$	$0.009 \pm 0.00$	0.045
20.0	90	$0.33 \pm 0.05$	317.23	$0.1 \pm 0.05$	$7.36 \pm 0.06$	$0.0073 \pm 0.00$	0.045

Table 12.4.: Results of the damage experiment on amorphous carbon material at different photon energies. The stopping power has been taken into account here.

## 12.2 Damage energy threshold and effective beam area at different photon energies on a-C and CVD diamond

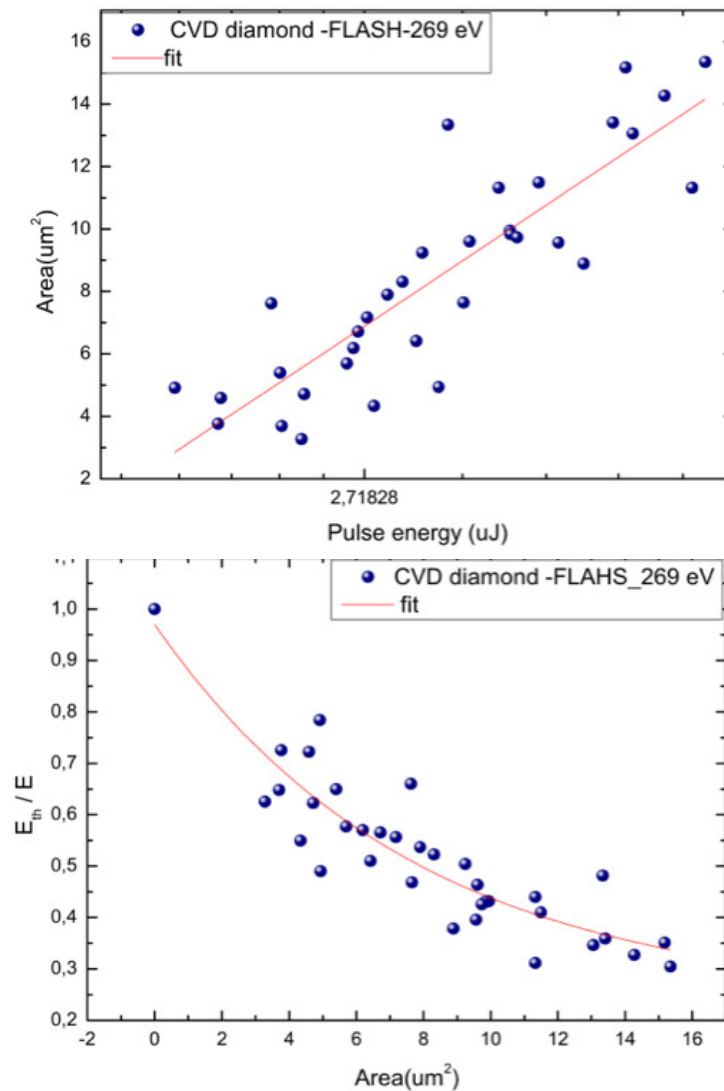


Fig. 12.1.: CVD diamond sample exposed to the 269 eV beam with single shots at FLASH at normal incidence angle. Top Fig shows the plotted pulse energy ( $\ln(E)$ ) vs the damage footprint area. Bottom Fig represents the F-scan method, where the footprint areas are plotted vs the corresponding normalized pulse energies for each shot. The Integral of the area underneath the curve (fit line) gives the effective area of the beam.

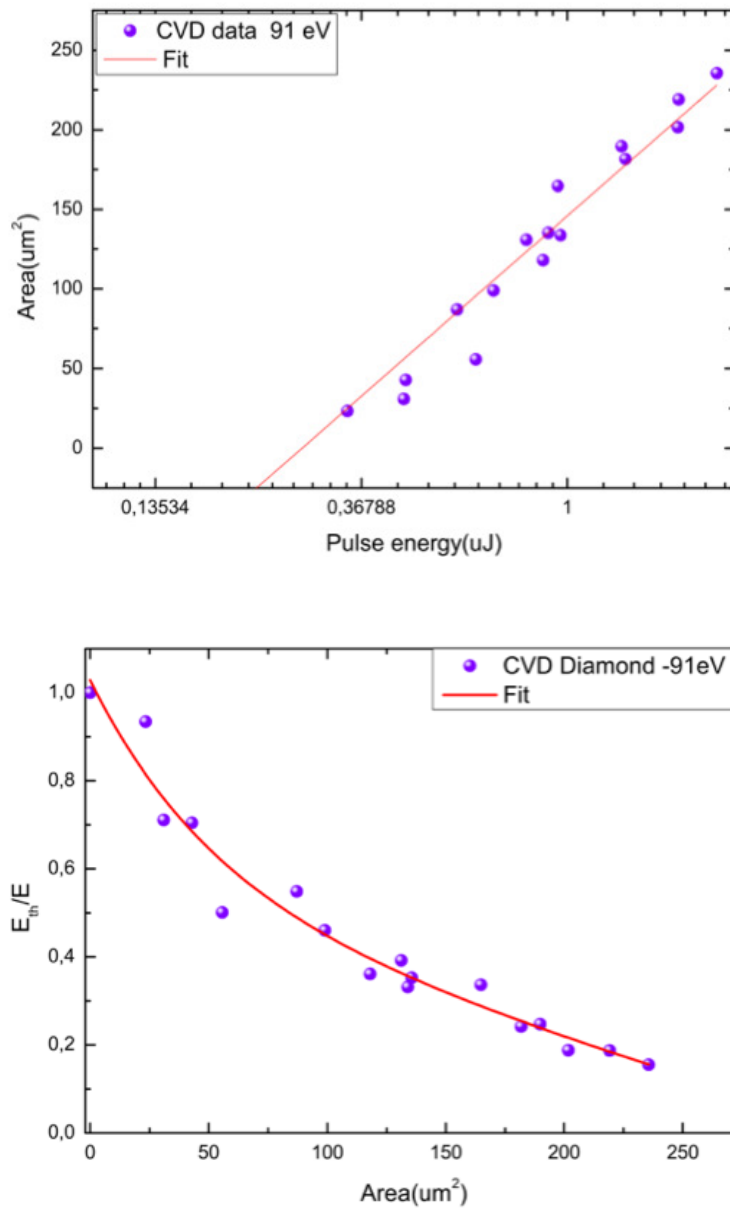


Fig. 12.2.: CVD diamond sample exposed to the 91 eV beam with single shots at FLASH. Top plot shows the damage threshold graph and the bottom Figure shows the fit for the effective beam area.



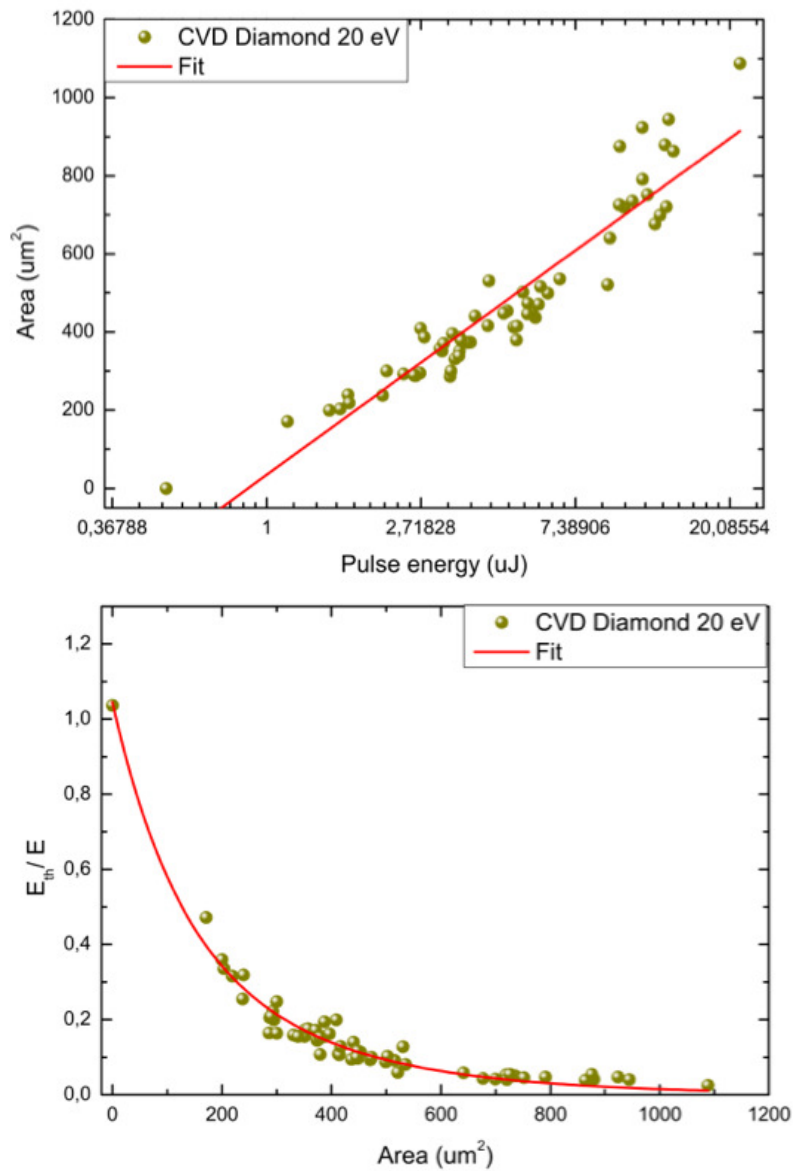


Fig. 12.3.: CVD diamond sample exposed to the 20 eV beam with single shots at SCSS. Top plot shows the damage threshold graph and the bottom Figure shows the fit for the effective beam area.

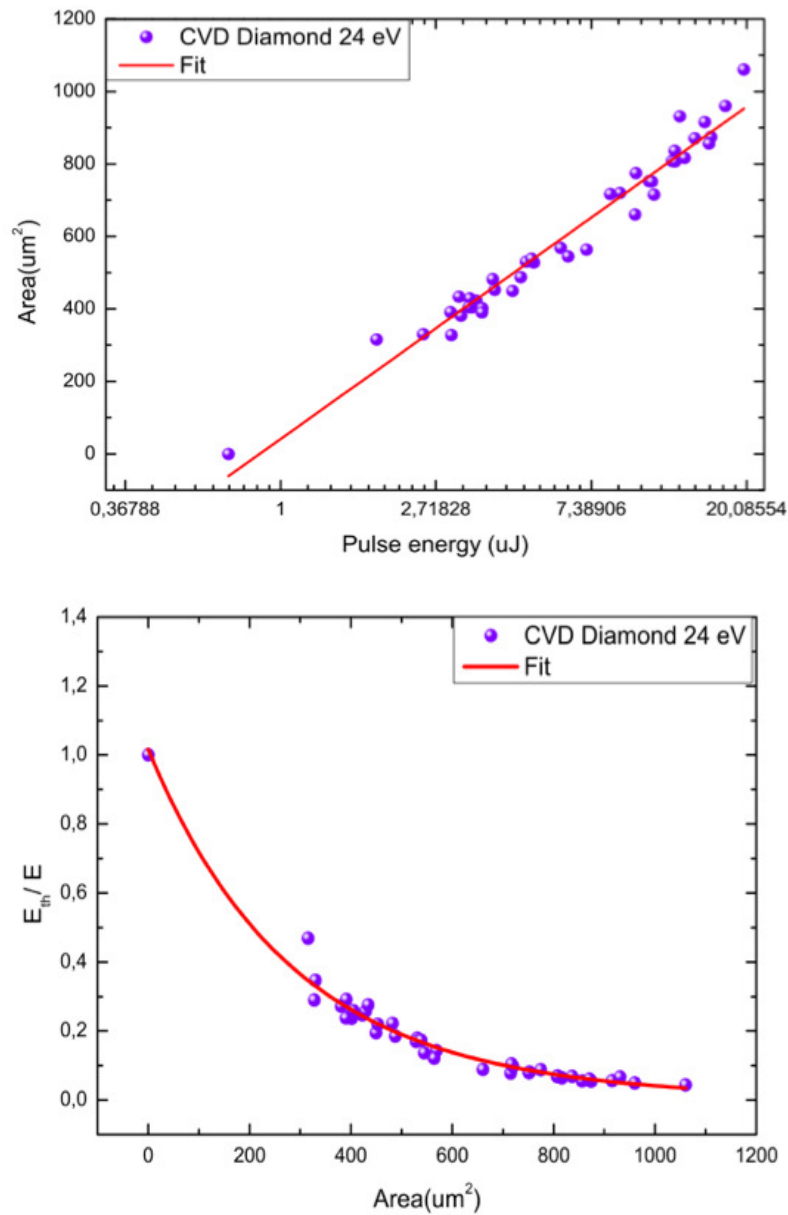


Fig. 12.4.: CVD diamond sample exposed to the 24 eV beam with single shots at SCSS. Top plot shows the damage threshold graph and the bottom Figure shows the fit for the effective beam area.

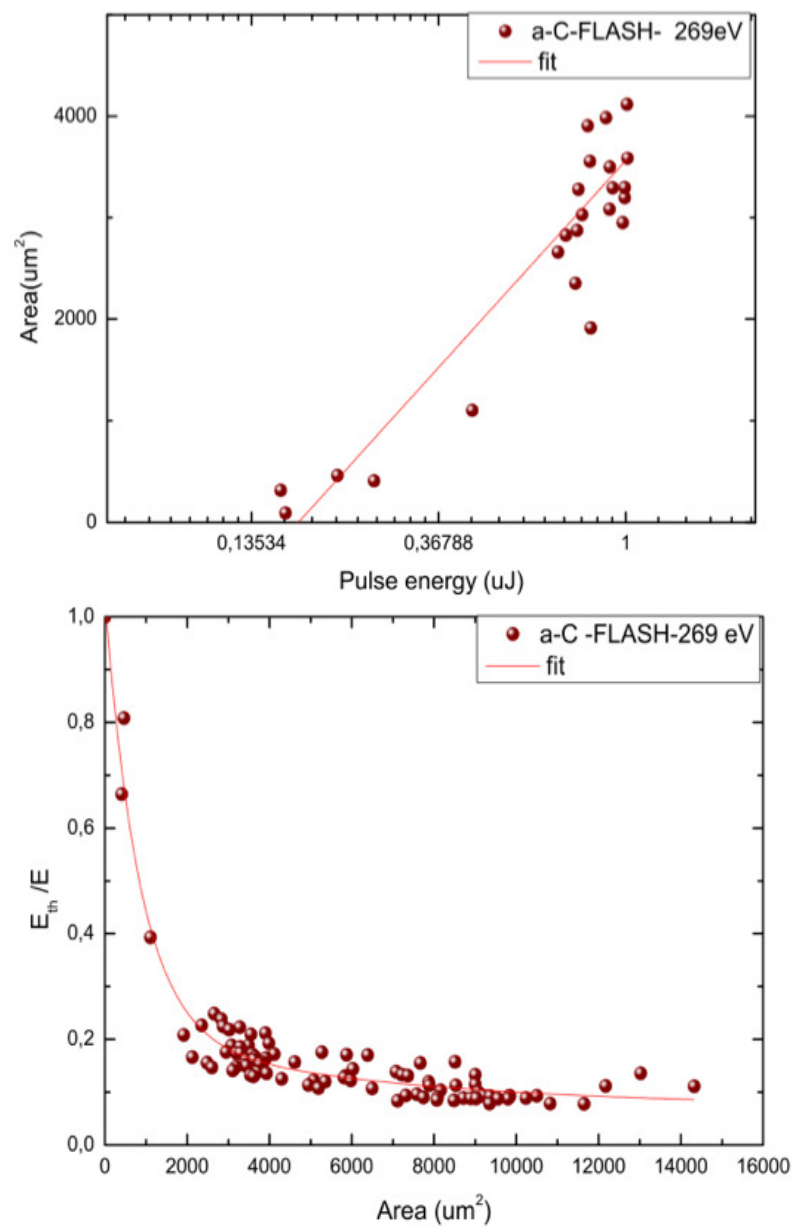


Fig. 12.5.: Amorphous carbon exposed to the 269 eV beam with single shots at FLASH. Top plot shows the damage threshold graph and the bottom Figure shows the fit for the effective beam area.

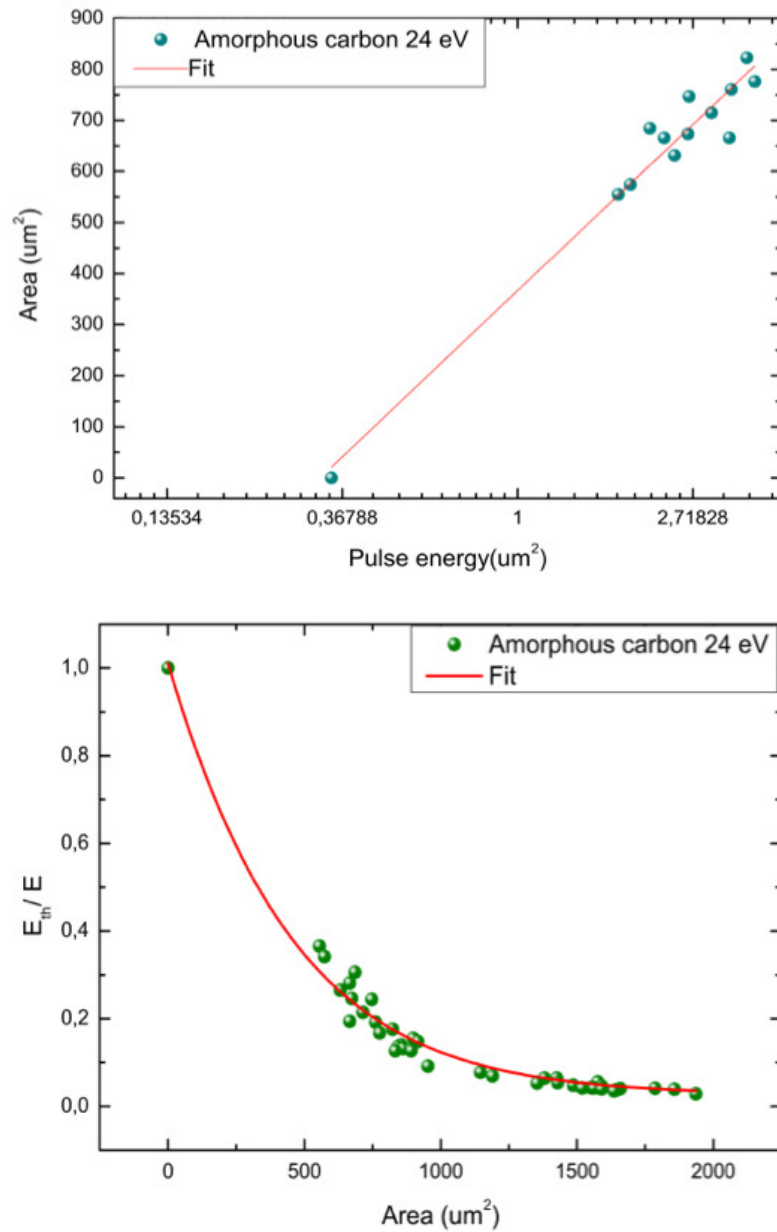


Fig. 12.6.: Amorphous carbon exposed to the 24 eV beam with single shots at SCSS. Top plot shows the damage threshold graph and the bottom Figure shows the fit for the effective beam area.

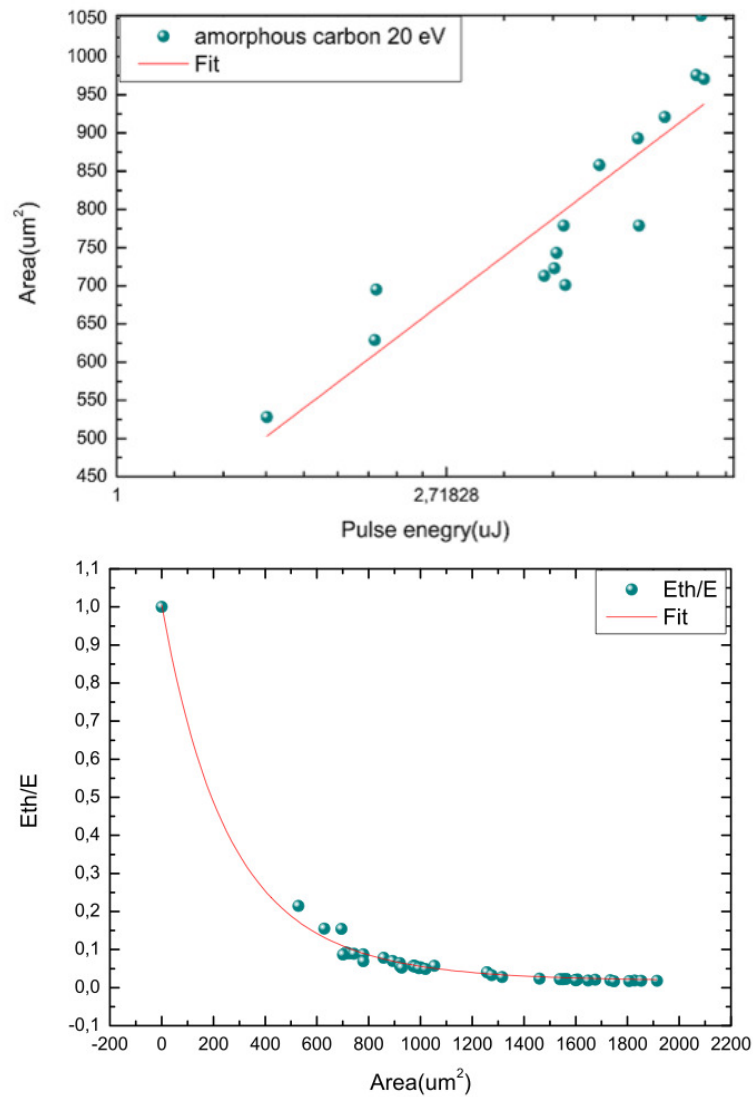


Fig. 12.7.: Amorphous carbon exposed to the 20 eV beam with single shots at SCSS. Top plot shows the damage threshold graph and the bottom Figure shows the fit for the effective beam area.

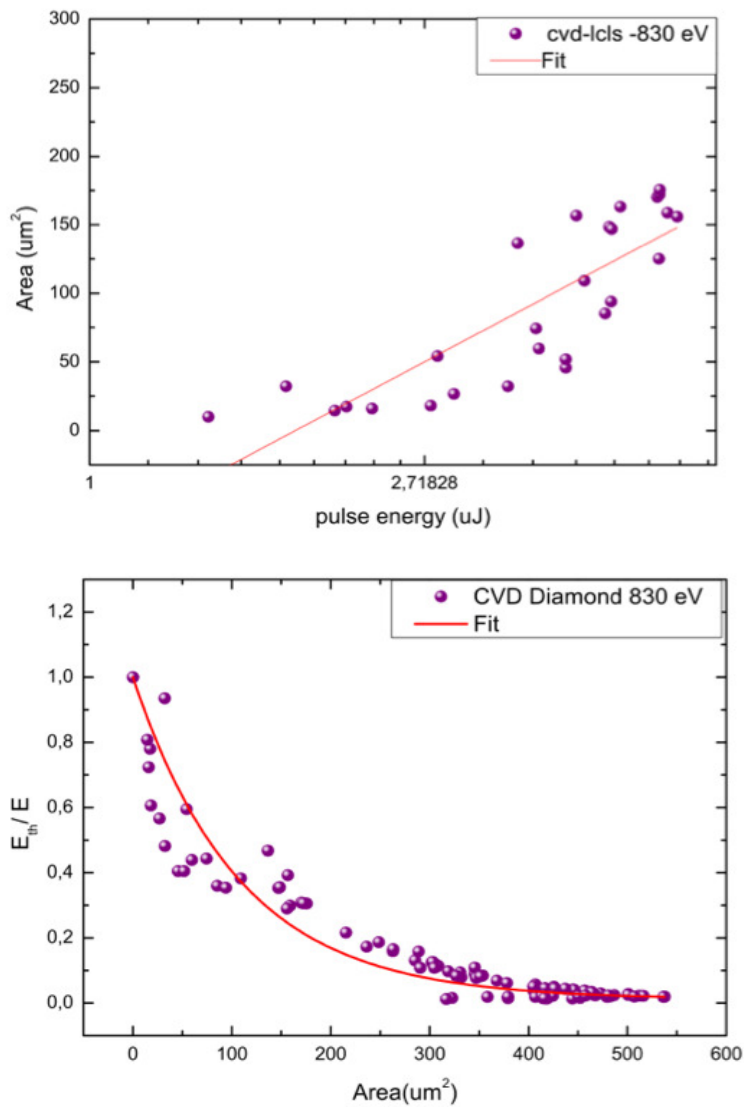


Fig. 12.8.: CVD diamond sample exposed to the 830 eV beam with single shots at LCLS. Top plot shows the damage threshold graph and the bottom Figure shows the fit for the effective beam area.

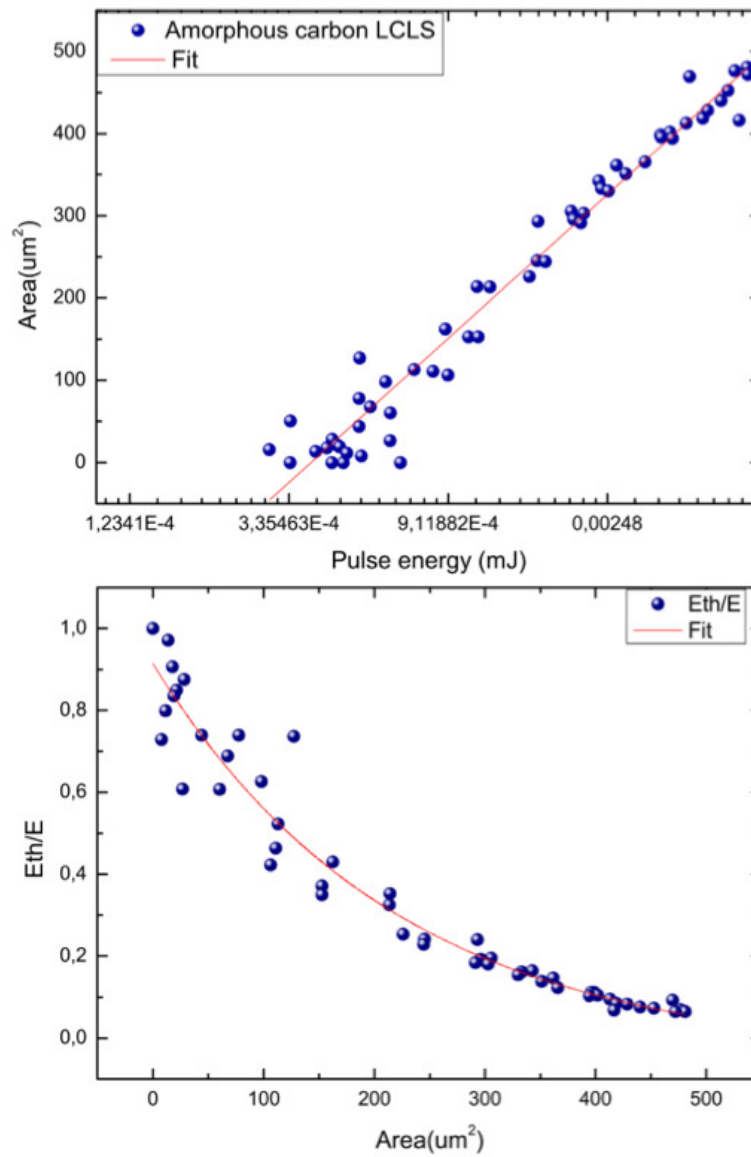


Fig. 12.9.: Amorphous carbon exposed to the 830 eV beam with single shots at LCLS. Top plot shows the damage threshold graph and the bottom figure shows the fit for the effective beam area.





### 12.3 Damage energy threshold and effective beam area at different grazing angles on Nickel at 269 eV

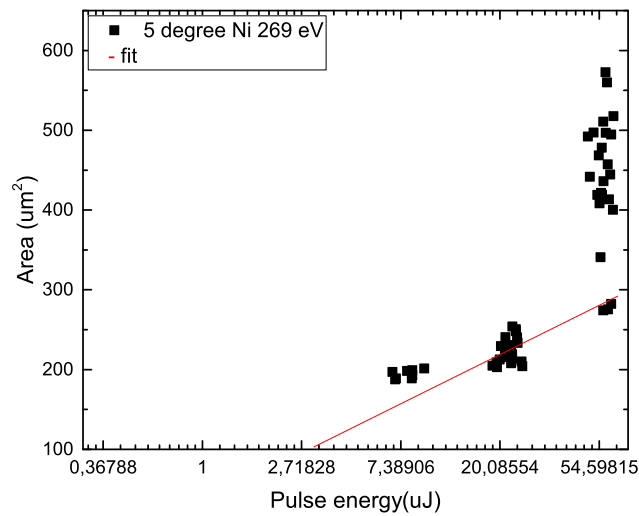


Fig. 12.10.: nickel sample irradiated at 5 degree grazing incidence angle at 4.6 nm wave length.

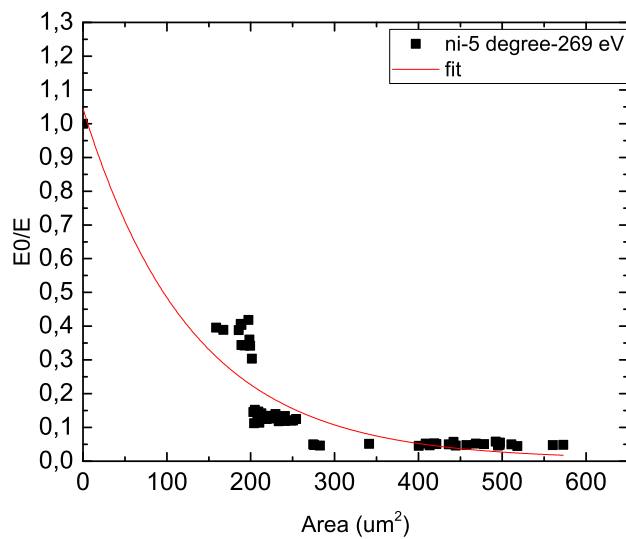


Fig. 12.11.: Nickel sample irradiated at 5 degree grazing incidence angle at 4.6 nm wave length. The integral under the fitted curve represents the effective area of the beam.

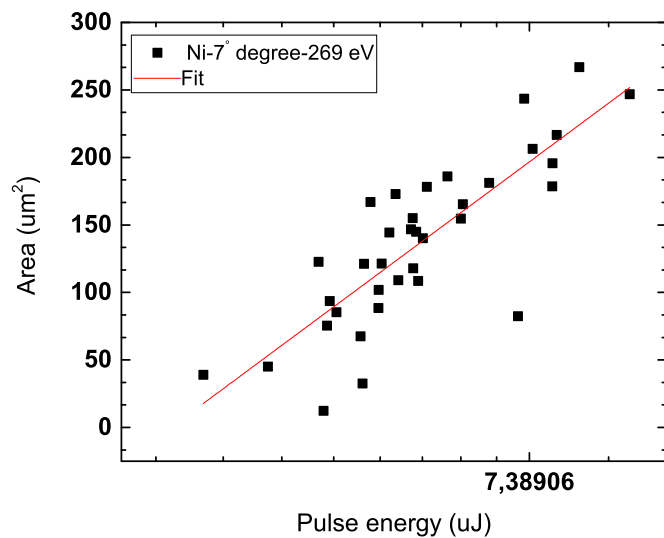


Fig. 12.12.: Nickel sample irradiated at 7 degree grazing incidence angle at 4.6 nm wave length.

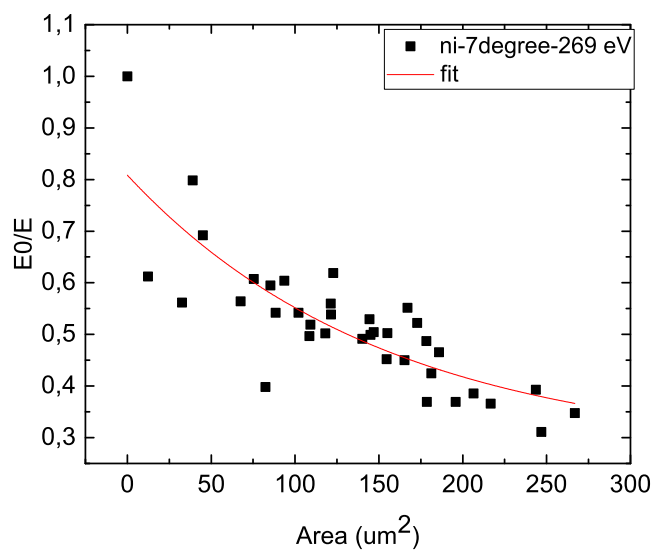


Fig. 12.13.: Nickel sample irradiated at 7 degree grazing incidence angle at 4.6 nm wave length. The integral under the fitted curve represents the effective area of the beam.

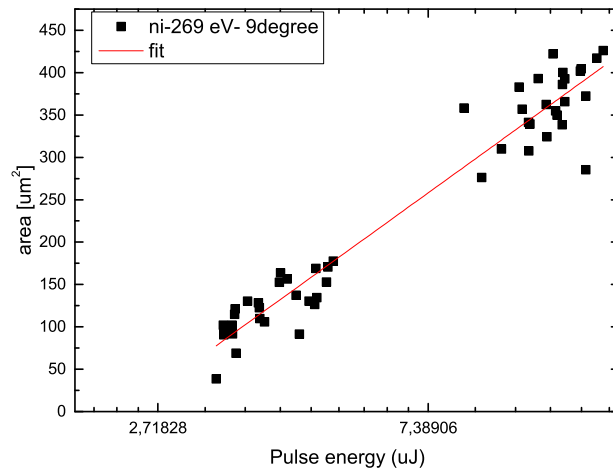


Fig. 12.14.: Nickel sample irradiated at 9 degree grazing incidence angle at 4.6 nm wave length.

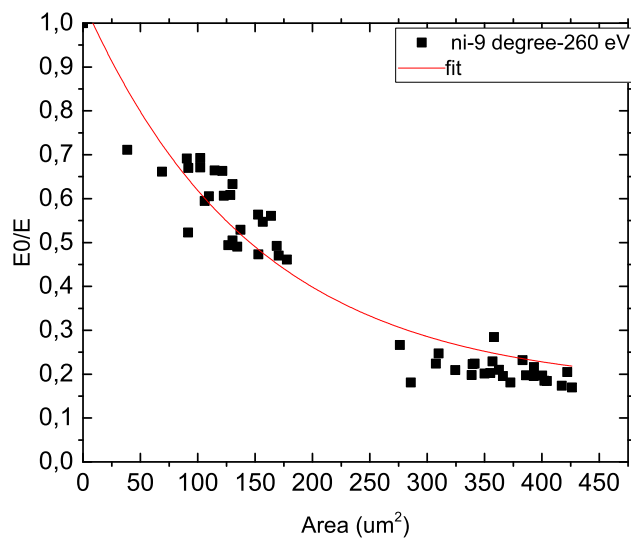


Fig. 12.15.: Nickel sample irradiated at 9 degree grazing incidence angle at 4.6 nm wave length. The integral under the fitted curve represents the effective area of the beam.

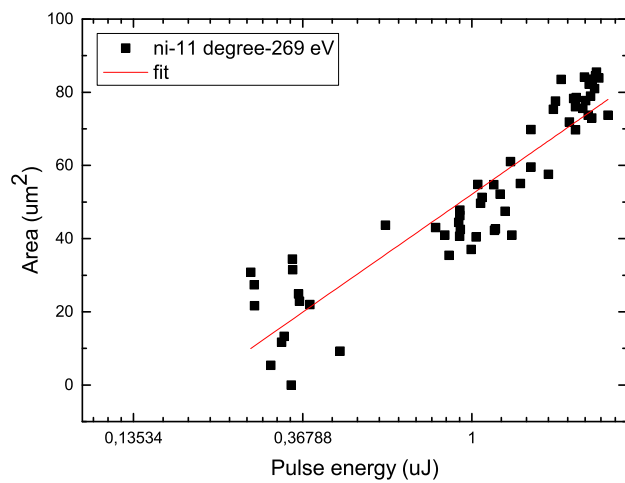


Fig. 12.16.: Nickel sample irradiated at 11 degree grazing incidence angle at 4.6 nm wave length.

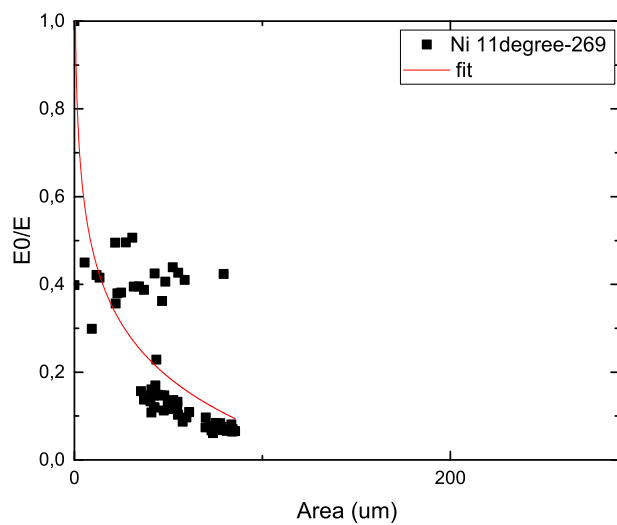


Fig. 12.17.: Nickel sample irradiated at 11 degree grazing incidence angle at 4.6 nm wave length. The integral under the fitted curve represents the effective area of the beam.

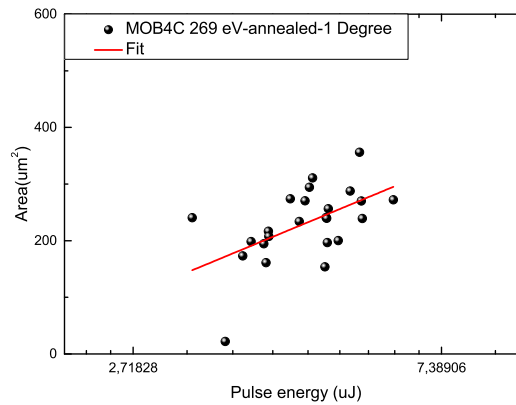
Photon energy (eV)	angle (°)	energy threshold ( $\mu J$ )	Beam area(imprint) ( $\mu m^2$ )	Fluence threshold ( $J/cm^2$ )	Dose ( $eV/atom$ )	Attenuation depth (Henkel table ) ( $\mu m$ )
269.0	5	$2.82 \pm 0.36$	135.28	$2.1 \pm 0.44$	$5.01 \pm 0.4$	$2.4E(-3) \pm 0.00$
269.0	7	$2.94 \pm 0.03$	150.48	$1.95 \pm 0.2$	$6.49 \pm 0.5$	$2.7E(-3) \pm 0.00$
269.0	9	$2.4 \pm 0.02$	192.15	$1.24 \pm 0.13$	$3.64 \pm 0.1$	$3.99E(-3) \pm 0.00$
269.0	11	$0.16 \pm 0.02$	48.43	$0.33 \pm 0.05$	$0.77 \pm .0.2$	$6.05E(-3) \pm 0.00$

Table 12.5.: results of the damage experiment on Nickel at different grazing incidence angle and with 269 eV photon energy.

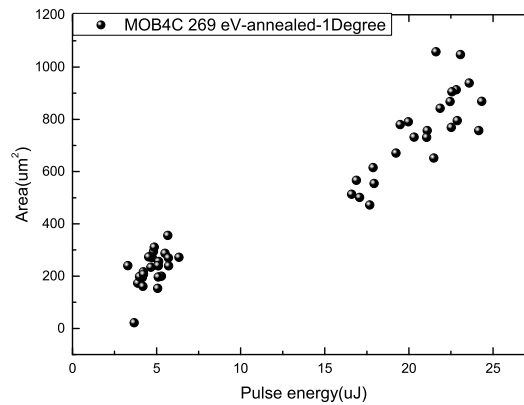


## 12.4 Damage energy threshold and effective beam area at different grazing angles on MoB4C at 269 eV

Comparing the threshold fluence with a-C's at the same photon energy shows that at 269 eV the a-C fluence threshold is higher than for the MoB4C which is not annealed. In the case where the MoB4C sample was annealed these two values are close to each other. This means that annealing helps the structure to get more resistance against the damage. The details (damage threshold graphs) at different incidence angles are presented here. The test were performed at 1, 2 degrees as well as on 90 degrees on normal and annealed multilayers of MoB4C.



(a) MoB4C sample irradiated at 1 degree grazing incidence angle at 4.6 nm wave length. The lower pulse energy section is used to determined the damage threshold. The whole section is plotted in Fig b.



(b) MoB4C sample irradiated at 1 degree grazing incidence angle at 4.6 nm wave length.

Fig. 12.18.

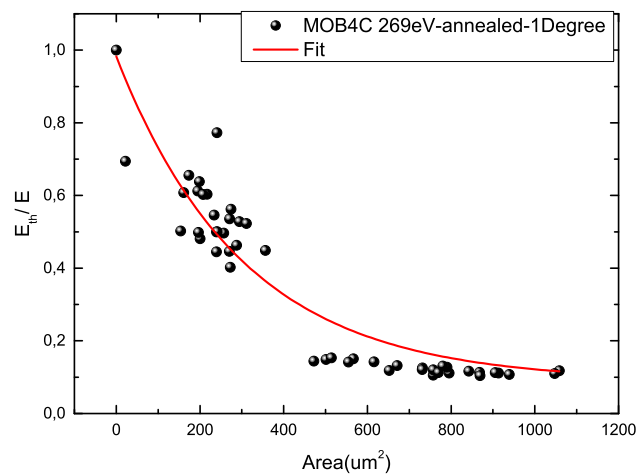


Fig. 12.19.: MoB4C sample irradiated at 1 degree grazing incidence angle at 4.6  $nm$  wave length. The plot shows the F-Scan method to gain information about the effective area of damage spot. The integral under the fitted curve represents the effective area of the beam.

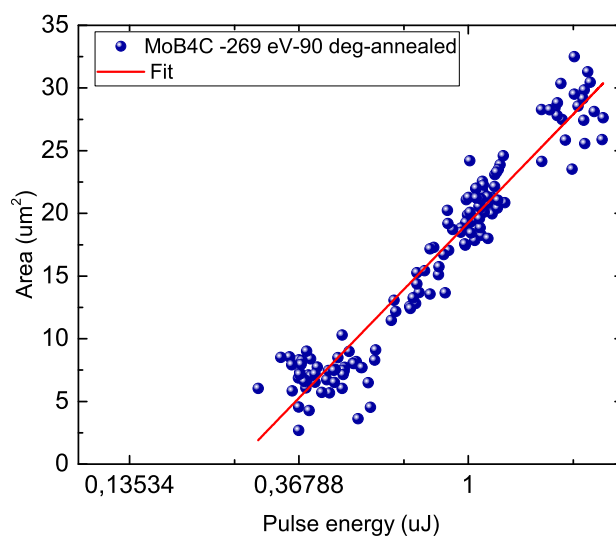


Fig. 12.20.: MoB4C sample irradiated at 90 degree grazing incidence angle at 4.6  $nm$  wave length.



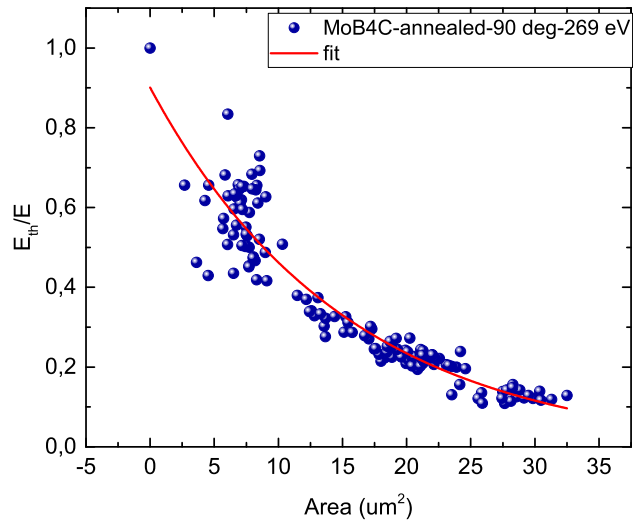


Fig.12.21.: MoB4C sample irradiated at 90 degree grazing incidence angle at 4.6 nm wave length. The integral under the fitted curve represents the effective area of the beam.

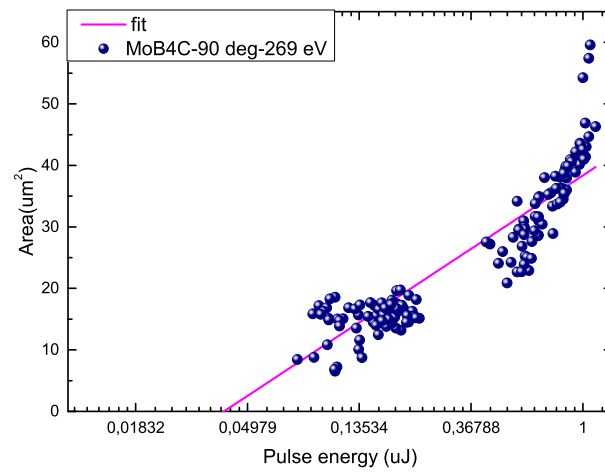


Fig.12.22.: MoB4C sample irradiated at 90 degree grazing incidence angle at 4.6 nm wave length.

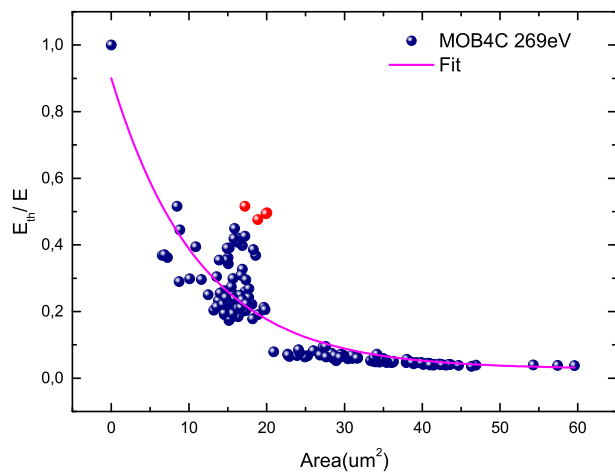


Fig. 12.23.: MoB4C sample irradiated at 90 degree grazing incidence angle at 4.6 nm wave length. The integral under the fitted curve represents the effective area of the beam.

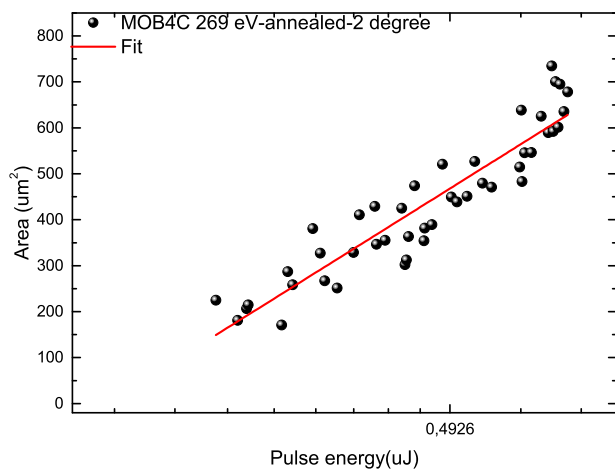


Fig. 12.24.: MoB4C sample irradiated at 2 degree grazing incidence angle at 4.7 nm wave length.

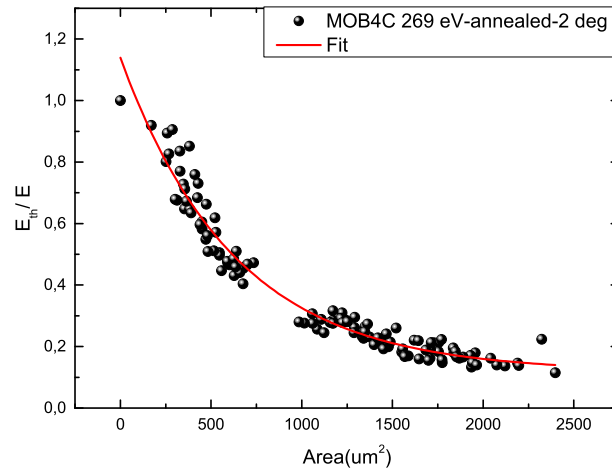


Fig.12.25.: MoB4C sample irradiated at 2 degree grazing incidence angle at 4.6 nm wave length. The integral under the fitted curve represents the effective area of the beam.

Photon energy (eV)	angle (°)	energy threshold ( $\mu J$ )	Beam area (imprint) ( $um^2$ )	Fluence threshold ( $J/cm^2$ )
269.0	2-annealed sample	$3.49 \pm 0.36$	643.98	$0.54 \pm 0.44$
269.0	1	$1.71 \pm 0.03$	251.31	$0.68 \pm 0.2$
269.0	2	$3.56 \pm 0.02$	643.98	$0.55 \pm 0.13$
269.0	90-annealed sample	$0.18 \pm 0.02$	22	$0.82 \pm 0.05$
269.0	90	$0.002 \pm 0.003$	22	$0.01 \pm 0.05$

Table 12.6.: results of the damage experiment on MoB4C (some were annealed) at different grazing/ incidence angle and with 269 eV photon energy.



## 12.5 Raman plots

The rest of Raman spectra taken at a-C damage spot made at  $4.83 \mu J$  pulse energy and with  $91 eV$  presented in Fig 8.29 are depicted here

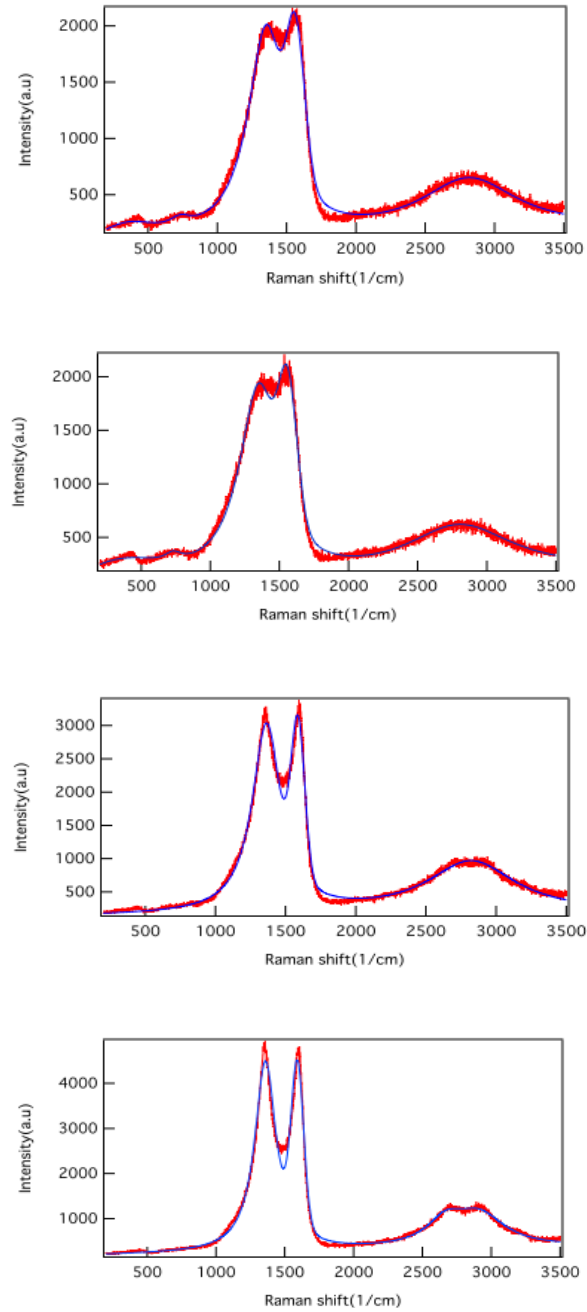


Fig. 12.26.: a-C exposed to the  $91 eV$  beam with single shots at FLASH with  $4.83 \mu J$  pulse energy (from up to down B4 - B7).

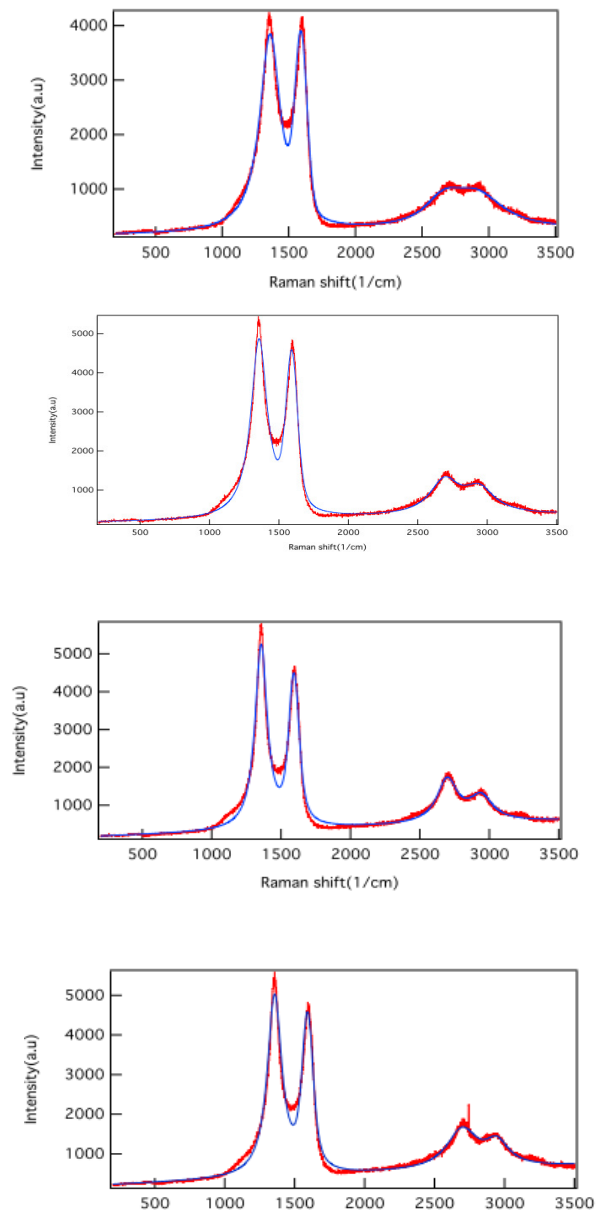


Fig. 12.27.: a-C exposed to the 91 eV beam with single shots at FLASH with  $4.83 \mu J$  pulse energy (from up to down B8 - B11).

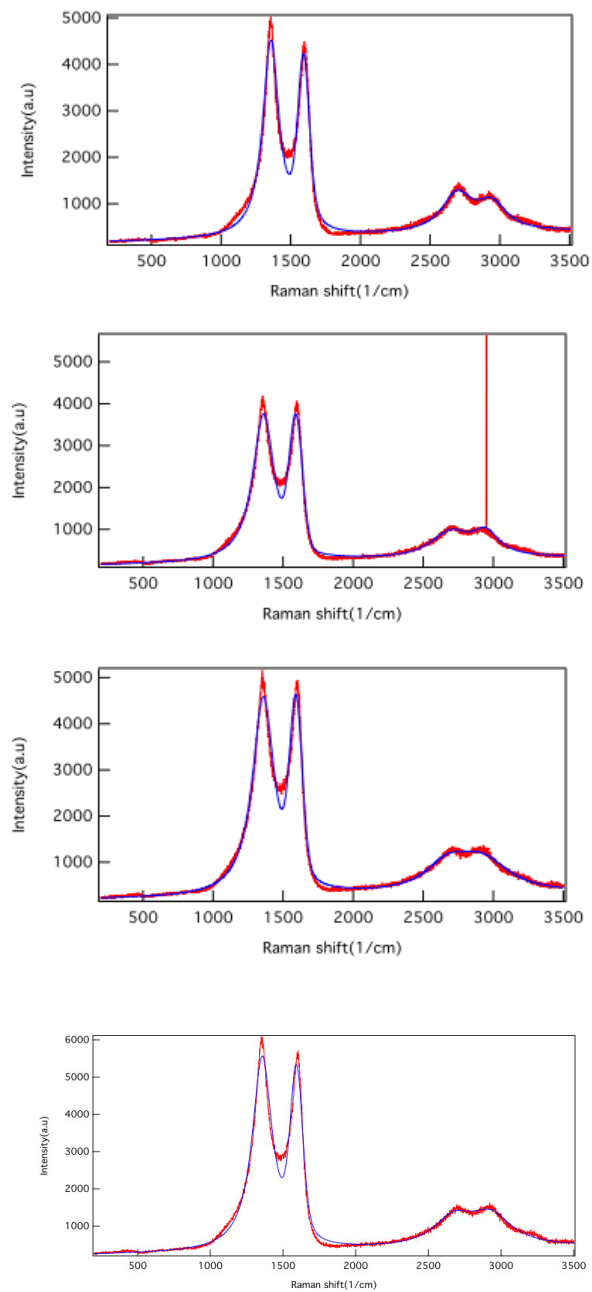


Fig. 12.28.: a-C exposed to the 91 eV beam with single shots at FLASH with 4.83  $\mu\text{J}$  pulse energy (from up to down B12 - B15).

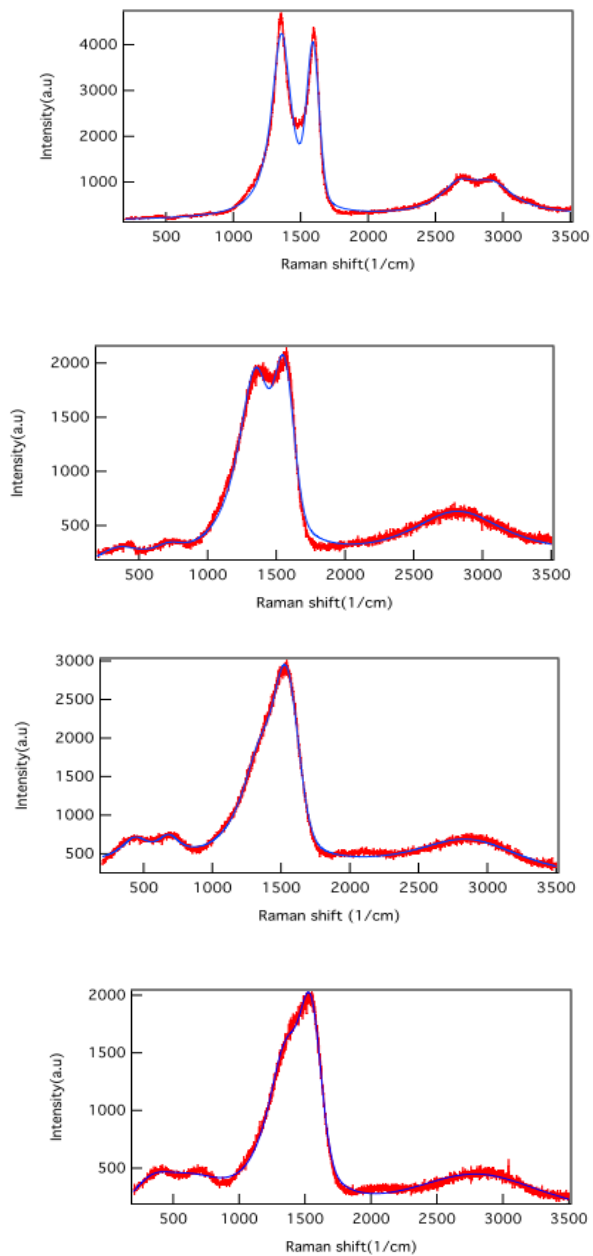
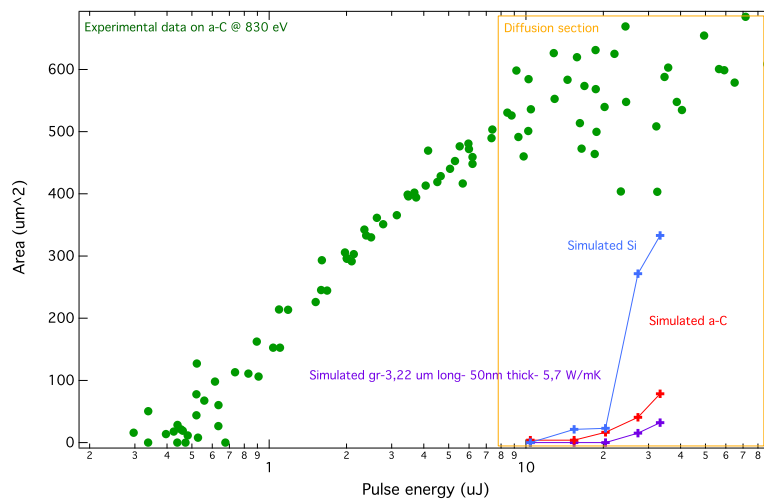


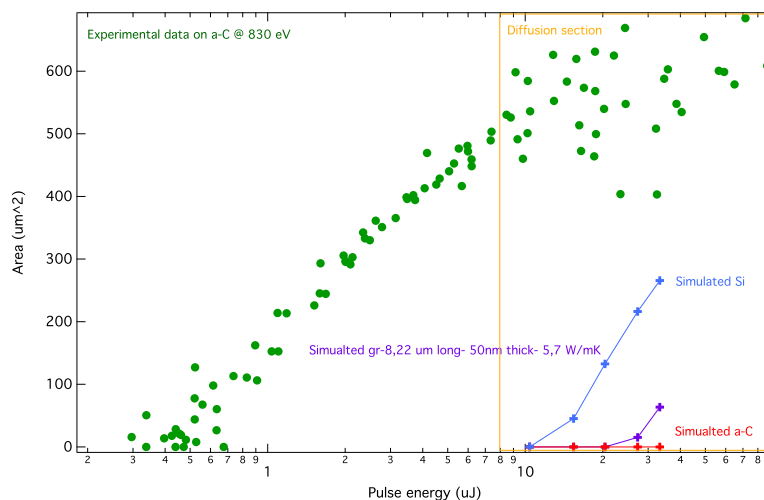
Fig. 12.29.: a-C exposed to the 91 eV beam with single shots at FLASH with 4.83  $\mu J$  pulse energy (from up to down B16 - B19).



## 12.6 Heat diffusion plots

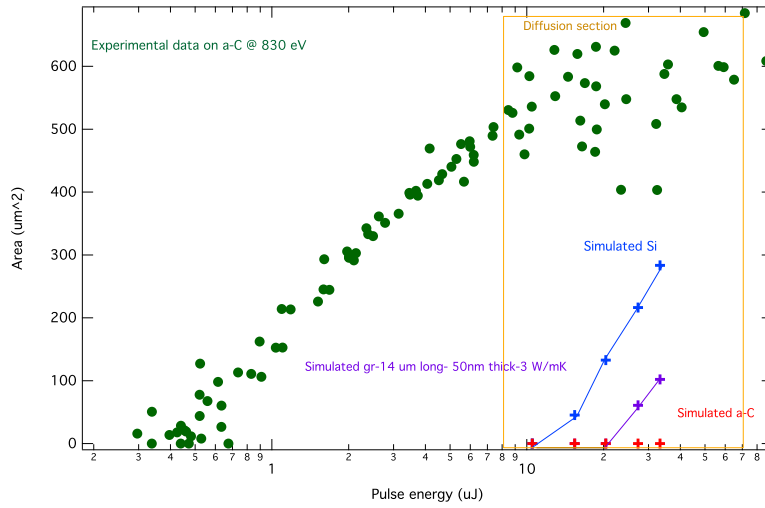


(a)

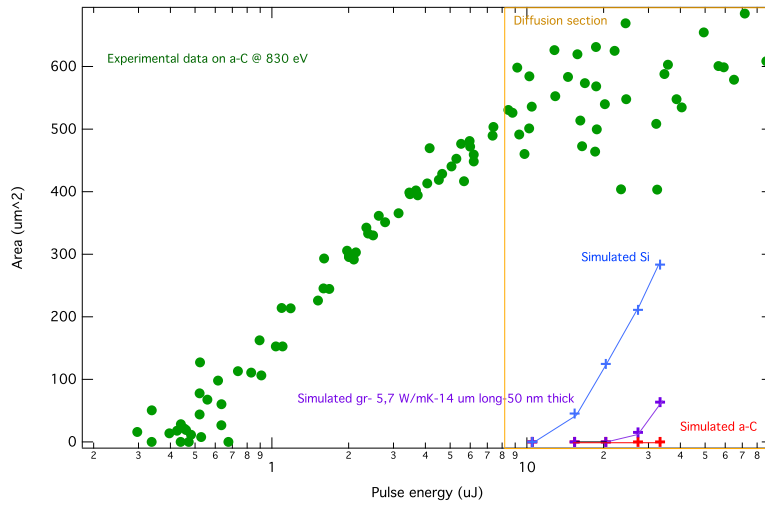


(b)

Fig. 12.30.: Heat diffusion simulation at 830 eV on a-C sample considering phase transition into graphite. Simulation ran over 7  $\mu$ s. (a): The graphite size is considered to be 3,2  $\mu$ m and 50 nm thickness. (b): The graphite has a larger size as the photon beam radius (8.22  $\mu$ m) and 50 nm thickness. The thermal conductivity is taken to be 5.7 W/mK. The interesting point is the changes of the radius of the graphite and if heat diffuses differently in each case. In the smaller area (a) the a-C can still reach the melting temperature, whereas at larger areas this effect can not be seen ((b) or in fig 9.11). Si reaches the melting temperature at the same pulse energy in all these cases. The melting threshold for graphite is not changing.



(a)



(b)

Fig. 12.31.: Heat diffusion simulation at 830 eV on a-C sample considering phase transition into graphite had already taken place. (a): The graphite size is taken to be (14.22  $\mu\text{m}$ ) and 50 nm thickness. The thermal conductivity is taken 3 W/mK. (b): The graphite has the same size at the beam radius (14.22  $\mu\text{m}$ ) and 50nm thickness. The thermal conductivity is taken to be 5.7 W/mK.

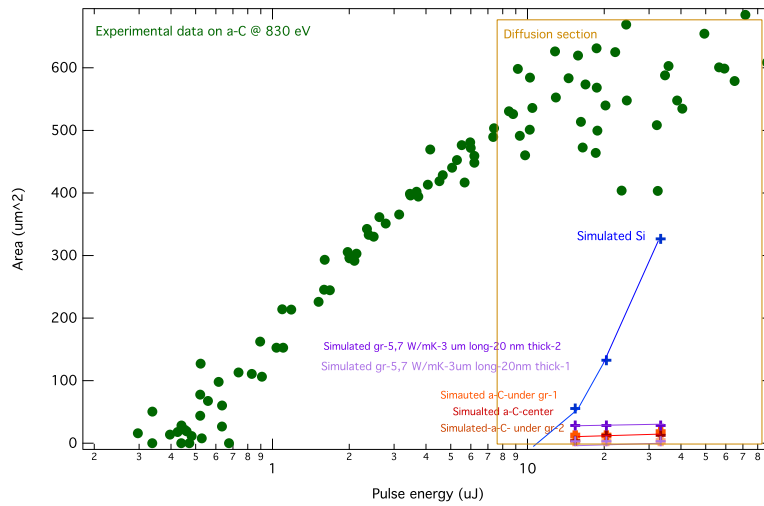


Fig. 12.32.: Grating structure (partially graphitized areas) on a-C sample with first block of graphite with  $1 \mu\text{m}$  radius and  $20 \text{ nm}$  thickness and the second block with  $3 \mu\text{m}$  and  $20 \text{ nm}$  thickness. Underneath the graphite layer there is considered a  $30 \text{ nm}$  thick layer of a-C and below that there is the substrate and between the both graphite layers there is a layer of a-C as well with  $50 \text{ nm}$  thickness and  $4 \mu\text{m}$  radius.



## List of Figures

3.1	An example of beamline components like mirror configuration at SASE 3 beamline at European XFEL [7]. . . . .	13
3.2	Damage studies. . . . .	14
4.1	(a): The refractive index $1 - \delta$ as a function of frequency. In case of X-ray the refractive index for all materials is less than 1 which means the total external refraction would take place in case of X-rays which is not the case in other regime with frequencies below X-rays. The edges are the resonance frequencies at which the radiation will be absorbed [13]. (b): This plot represents the simulated refractive index (see Equation 4.24) for X-ray on a-C. . . . .	21
4.2	. . . . .	24
4.3	A comparison of the real ( $1 - \delta$ ) (a) and imaginary part (b) of the refractive index of X-ray radiation inside a wide energy range for a-C (red), Si (violet) and Ni (green) is shown in this plot. Raw data has been taken from [15]. Ni has density $8.9 \text{ gr/cm}^3$ and Si $2.33 \text{ gr/cm}^3$ and a-C has the density of $2.2 \text{ gr/cm}^3$ . Plots show that at very low energy basically the absorption and phase velocity of the X-ray light is high and going towards higher photon energies both of these parameters decrease. . . . .	25
4.4	(a): Attenuation length at different photon energies are compared for different materials. a-C (red), CVD (pink), Si (violet) and Ni (green). (b): Reflectivity of a-C (red), CVD (pink), Si (Violet), Ni (green) vs photon energies are compared here. . . . .	26
5.1	Very simple schematic of the matter and laser beam interaction [17]. The left side shows the system in its ground state; the electrons cold state. The potential landscape shows minima at the crystal lattice sites. Therefore, no external forces are acting on them except tight binding Coulomb potential induced by the lattice. On the right side, the laser light has affected the system and transported it to an excited state. Hot electrons and holes are created here. The potential landscape undergoes qualitative and quantitative changes, resulting in disappearance or shifting of the minima. This happens in very short time scale (shorter than reaction time); as a result, forces act on the carriers/atoms and move them. . . . .	28

5.2	Very simple schematic of the matter and X-ray FEL beam interaction [39]. The incoming beam has its temporal and spatial dimensions depicted in the picture with the Gaussian profiles on the top and the side. The material is undergone photo-ionization processes. Some free carriers escaped from the surface, and hot plasma of free carriers is created inside the material at the beam affected zone. The heat affected zone shows the region where the heat gets diffused into and the shock affected zone describe the area where the high pressure starts to induce shock waves. There is a thin layer right behind the heat-affected zone, which is showing the melted layer. . . . .	33
5.3	Attenuation length of X-ray radiation with different energies inside a thin layer of amorphous carbon with 2.2 ratio of $SP^3/SP^2$ [15]. The drop is at the cutting edge at 284 eV. . . . .	37
6.1	Maps of CVD diamond and amorphous carbon samples exposed with single shots at LCLS. . . . .	39
6.2	Snapshot of the 64 atom ta-C network. The heavy lines show the network of bonds; the 22 dark spheres depict threefold coordinated atoms ( $sp^2$ hybridized) and the 42 light spheres show the fourfold coordinated atoms ( $sp^3$ hybridized). The simulations were performed by N. Marks, (Dept of Applied Physics, University of Sydney) at the Max Planck Institute, Stuttgart [79].	40
6.3	Electron configuration of carbon in ground state(a), excited hybridized state $SP^1$ (b), $Sp^2$ (c), $Sp^3$ (d). . . . .	41
6.4	Orbital configuration of carbon $Sp^3$ (mainly in Diamond), $Sp^2$ (mainly in Graphite). . . . .	41
6.5	Measured surface roughness with AFM on (a) 40 nm thick aC coating and on (b) 900 nm aC coating on Si substrate. The 900 nm sample has an rms roughness of 1.28 nm, the peak to valley value is 35.24 nm and maximum peak height is 50.6 nm and the 40 nm samples roughness is 0.4 nm rms, the peak to valley value for this sample is 72.14 nm and maximum peak height is 80.5 nm [16]. . . . .	43
6.6	Sketch of diamond crystal [92]. . . . .	43
7.1	Schematic view of developed GMD at FLASH [85]. A Faraday cup counts the electrons and ions that are produced as the FEL pulse passes through the ionization chamber containing nitrogen or rare gases at very low pressure. After the faraday cup there are the two split electrodes to determine the horizontal position of the beam. . . . .	48
7.2	(a): Draft of the FELIS experimental chamber at FLASH in Hamburg in 2005 [94], [100]. (b): The FELIS experimental chamber modified for the damage experiment in 2011 at FLASH in Hamburg . . . . .	49

7.3	View of the inside of the chamber from the sample holder with mounted samples on it. . . . .	50
7.4	Schematic view of the inside of the chamber, illustrating the sample positioning. . . . .	50
7.5	Schematic view of the inside the chamber with the sample rotation axis. . . . .	51
7.6	Correlation of the pulse energy measured by the GMD with the amplitude of the MCP signal when sample was exposed to 500 pulses attenuated below the multi shot damage threshold of Si sample [97]. . . . .	52
7.7	Schematic view of the sample's position on the sample holder, they were given an x and y position regarding their position on the sample holder. . . . .	54
7.8	PMMA 5 $\mu m$ was shot at 13.5 $nm$ at FLASH (11-08-2008) to find the beam size and focus point, the highlighted area is taken to be the beam area and it was measured to be 101.4 $\mu m^2$ . . . .	55
7.9	Schematic view of the inside of the chamber showing the angle determination . . . . .	55
7.10	Maps of amorphous carbon sample with 1.4 $\mu m$ thickness, exposed to single shots at LCLS 2009 with 830 $eV$ . On the left side, one can see the picture taken from the sample after the shots. The numbers (names) of the lines are marked and the shot direction as well. The right pic is the image of the sample itself after the shots are made. The pictures are taken via Nomarski microscope. . . . .	56
7.11	Marker on the map of amorphous carbon sample with 890 $nm$ thickness, exposed to single shots at FLASH 2008 with 177 $eV$ . Scale size on the bottom right side is 20 $\mu m$ . . . . .	56
7.12	Scanning pinhole structure designed for the SCSS in Japan in 2010 [101]. . . . .	58
7.13	Gas attenuator and Photon intensity monitor at SCSS in Japan in 2010 [102], [103], [101]. . . . .	58
7.14	(a): Design of the experimental beamline at SCSS in Japan [101]. (b): The experimental beamline and chamber. (c): The experimental chamber. . . . .	59
7.15	(a): The structure of the AMO beam-line at LCLS [104]. (b): The Gas Monitor at AMO beam-line at LCLS based on the photoluminescence process [106]. . . . .	61
7.16	(a): Idealized schematic diagram of the major components and light pathways through a typical DIC microscope optical train [107]. (b): A DIC microscope image taken from a damage spot on a-C (890 $nm$ thick on Si substrate) sample. The sample was exposed to a single pulse with 4.83 $\mu J$ energy at FLASH. The experiment was performed at 91 $eV$ photon energy. The scale is 20 $\mu m$ . . . . .	63
7.17	Simple schematic of Atomic Force Microscopy spectroscopy. . . .	64
7.18	. . . . .	65

7.19	.....	66
7.20	Simple schematic of Micro-Raman spectroscope. ....	67
7.21	Top: Raman spectrum taken on the point marked as "A" on the amorphous carbon coated sample (890 nm thick on Si substrate) exposed to the 177 eV beam with single shot of 4.8 $\mu J$ at FLASH. Marked points show the coordinates on which Raman data were taken. Bottom: Raman profile spectra showing the position and width of D, G, G' and T peaks (see section 8.5). ....	68
7.22	White Light Interferometer image of the a-C damaged at SCSS. The single shot with 4.8 $\mu J$ with photon beam energy of 24 eV. .	69
7.23	Simple image of an Scanning Electron Microscope (SEM). ....	70
7.24	SEM, AFM, Nomarski microscope images taken at the damaged spot on amorphous carbon sample (890 nm thick on Si substrate) exposed to the 91 eV beam with single shot pulse energy of 4.83 $\mu J$ at FLASH. The three SEM images step by step zoom inside the damaged spot and show more details. From the top, the first image has 10 $\mu m$ scale and the second taken with 5 $\mu m$ and the third with 2 $\mu m$ . The rough surface is completely obvious that smooth surface of a-C has turned into a rough graphite surface. There is a swollen observable area around the damaged spot which might have been created due to shock waves as the pressure goes high inside the hot plasma of free carriers. Since the material can't expand easily towards the rest of the volume, it causes a shock wave to reduce the pressure inside the damaged region. This also causes the material not to be easily removed from the surface [113]. The other reason might be due to beam-line aperture which causes some other parts be illuminated by the beam at the time of exposure. This defect could be also created at the boundary between Si and a-C. From the heat diffusion simulation in chapter 9 it can be seen that material (a-C and Si) has reached melting temperature at this pulse energy which causes the larger damage area and explains the deformations observed on the surface. ....	72
7.25	Nomarski microscope, AFM and SEM images taken of the damage spot on amorphous carbon sample (890 nm thick on Si substrate) exposed to the 91 eV beam with single shot pulse energy of 2.97 $\mu J$ at FLASH. From the heat diffusion simulation in chapter 9 it can be seen that material (a-C and Si) was melted at this pulse energy. ....	73



- 8.1 Damage spots on CVD diamond and amorphous carbon samples. These are exposed to single shots at LCLS with 830 eV photon energy. From left to right the pulse energy increases and one can see that the damage is more intense. These images are taken ex situ, via Nomarski microscope. With increasing the pulse energy, the shock waves appear in CVD diamond. Through heat diffusion part of sample get melted (including the Si substrate) in the case of a-C (amorphous carbon). The scale is 20  $\mu m$  in all these pictures. . . . . 77
- 8.2 The schematic view of the damaged spot on the amorphous carbon sample in the experiment at FLASH May 2011 with 269 eV. The sample thickness was small (1.4  $\mu m$ ) for this photon energy and the beam has penetrated into the substrate, and one of the following effects may be responsible for what one observes on the surface. It may be that the coating is peeled from the substrate, from the AFM image taken one could estimate about 0.5 nm to be the height of the swollen surface. The second possibility for this effect is that the substrate was melted at higher fluence and pushed the coating to the top, towards the outside. It is possible that the coating had a defect at that region of the sample (attenuation length at 269 eV is approximately 2.2  $\mu m$ ). . . . . 78
- 8.3 Comparison between beam profile in the case of a Gaussian (lui's method) and Non-Gaussian beam (F-scan method) . . . . . 79
- 8.4 View of the damage spot on the CVD Diamond sample at the experiment at FLASH may 2011 with 269 eV. . . . . 79
- 8.5 (a): The damage spots on PMMA (green dots measured via Nomarski microscope) and PbWO4 (black dots measured via Nomarski microscope) to measure the beam size at FLASH May 2011 with 269 eV. The red dots are the extrapolated data points and the red dotted line is the linear fit function defined in reference [117]. (b): An F-scan derived from PbWO4 and PMMA ablation imprints. The PbWO4 data were fitted by a sum of two exponential functions applicable as a model for a Gaussian beam surrounded by an extended background. Determined parameters are :  $f_{01} = 0.79 \pm 0.015$  ,  $S_{01} = 8.90 \pm 0.32$  ,  $f_{02} = 0.209 \pm 0.012$  and  $S_{02} = 62.3 \pm 2.9$ . These are samples examined at FLASH in May 2011 with 269 eV photon energy [119]. . . . . 81
- 8.6 CVD diamond sample exposed to the 177 eV beam with single shots at FLASH at normal incidence angle. Top panel shows the plotted pulse energy ( $\ln(E)$ ) vs the damage footprint area. Bottom panel represents the F-scan method, where the footprint areas are plotted vs the corresponding normalized pulse energies for each shot. The Integral of the area underneath the curve (fit line) gives the effective area of the beam. This method is explained in Section 8.1. . . . . 83

- 8.7 Amorphous carbon exposed to the 830  $eV$  beam with single shots at LCLS. The Top panel shows the pulse energy in logarithmic scale vs the measured footprint area. The fit gives the energy threshold. The Bottom panel represents the plotted areas vs normalized pulse energies (for each shot) with the energy threshold evaluated in the top plot. The integral of the curve under the fit gives the effective beam area (see Section 8.1). . . . . 84
- 8.8 (a): Damage on amorphous carbon at grazing angles of  $4.3^\circ$  and  $7.7^\circ$  at 177 $eV$  at FLASH. (b): Comparing changes of the attenuation length and reflectivity on the thin (40  $nm$ ) and bulk (900  $nm$ ) a-C sample at 177  $eV$  on a-C. The attenuation length doesn't change but the reflectivity slightly changes and on a thicker sample the drop happens at a slightly lower angle. . . . 85
- 8.9 (a): Damage shots at the grazing incidence angle of  $7^\circ$  at 269  $eV$  on a-C with a thickness of 50  $nm$ . The above panel shows the damaged spot at 14.4  $\mu J$  and the lower panel shows the damaged spot at 20.08  $\mu J$ . (b): Reflectivity and attenuation depth plotted as a function of grazing angle. The changes are shown here around critical angle ( $3.6^\circ$ ) at 269  $eV$  for a 50  $nm$  thick a-C layer on a Si substrate. At very low grazing angle the reflectivity is at the maximum of its range, this is plotted in red. Attenuation depth is plotted in blue. The solid lines are taken from CXRO data set [15]. . . . . 86
- 8.10 Top panel: Damage area versus the pulse energy of the grazing angle of  $4.31^\circ$  for 40  $nm$  thick sample and at the grazing angle of  $7.71^\circ$ . The energy threshold of damage is found with the logarithmic fit. Bottom panel: Damage on amorphous carbon at grazing angle of  $7^\circ$  at 269  $eV$  at FLASH on the left side and on the right side is the effective area obtained using the F-scan method (integral underneath the fit gives the effective damage area). . . . . 88
- 8.11 Comparing the damage energy threshold at different photon energy on CVD diamond and amorphous carbon. . . . . 93
- 8.12 Comparing the damage Fluence threshold at different photon energy on CVD diamond/a-C. . . . . 94
- 8.13 Comparing the damage dose threshold at different photon energies on CVD diamond and amorphous carbon. The line at 0.7  $eV$  represents the calculated damage dose threshold theoretically via Hybrid XTANT model mentioned in chapter 9 [135]. . . . 94
- 8.14 . . . . . 96
- 8.15 a-C Photoemission spectra from SPEM measurements obtained from averaging over two 10 X 10 pixel areas. Black curve: Non-irradiated sample. Gray curve: Center of the irradiated sample corresponding to 1.4  $J/cm^2$  with 830  $eV$  photon energy [80]. . . 99

8.16	A: AFM topography of an irradiated area on a-C sample with a 2.5 $\mu J$ FEL pulse with 830 eV photon energy. B: Fluence map deduced from the AFM measurement. The color scale is in $J/cm^2$ [80]. The material is expanded in volume. . . . .	100
8.17	AFM topography volume profile of an irradiated area on a-C with a 0.56 $\mu J$ FEL pulse at 269eV at FLASH. Volume of the spot is calculated via the AFM image with the self derived MATLAB Code. The color scale is in $J/cm^2$ [80]. . . . .	101
8.18	. . . . .	102
8.19	AFM topography volume profile of an irradiated area on a-C with a 4,8 $\mu J$ FEL pulse at 177eV at FLASH. Volume of the spot is calculated via the AFM image with the self derived MATLAB Code. The color scale is in $J/cm^2$ . . . . .	103
8.20	. . . . .	104
8.21	AFM topography volume profile of an irradiated area on CVD diamond sample damaged at LCLS at 830 eV photon energy, with 0.49 mJ pulse energy. Volume of the spot is calculated via the AFM image with the self derived MATLAB Code. The color scale is in $J/cm^2$ . . . . .	105
8.22	. . . . .	106
8.23	Amorphous carbon damaged with 2.97 $\mu J$ pulse energy and photon beam energy of 91 eV at FLASH. The height and length are measured and through the Equation 8.8 the depth to which the damage could have been created is calculated. In region one the depth is calculated to be 0.4 $\mu m$ , region 2 it is 0.1 $\mu m$ , region 3 it is 0.35 $\mu m$ and region 4 it is 0.61 $\mu m$ . The attenuation depth at this photon energy is 0.15 $\mu m$ . In all these regions the depth to which damage might be reached is deeper than the attenuation depth. This is evidence that taking the attenuation depth for calculating the dose is not necessary the most accurate. . . . .	107
8.24	. . . . .	108
8.25	Amorphous carbon damage spot with 4.83 $\mu J$ and photon beam energy of 91 eV single shots at FLASH. The $\mu$ -Raman analysis evidence the ordering of the a-C structure to nanocrystallites of graphite, in good agreement with the 3 step model of Ferrari et al [138], [109], [110], [139]. Looking at the heat simulation in chapter 9 shows that at this pulse energy a-C and Si both have reached melting temperature. This figure also shows that beam fringes are observable at this point. This could be due to the apertures in beamline and the beam focus which was causing interference patterns on the sample. This fact that graphitization is observable outside of the main dark spot of the damage is clearly showing that a larger area of the sample at the damaged spot compared to the beam radius at this experiment was effected, and phase transformed. The rest of Profiles which are not shown here are presented in the Appendix. The profiles are enumerated from B-B20 (see Fig 8.29 and in Appendix 12.5). . . . .	110

8.26	structural changes from amorphous to graphite. . . . .	111
8.27	Raman spectrum of CVD diamond sample damaged at LCLS with 830eV photon energy and 5.11 $\mu J$ pulse energy. Raman spectra were taken from two different spots on the sample, marked as 1 and 2. The red line shows the Raman spectrum taken on the spot and the blue line shows the fit. Spectrum on point 1 is plotted first and underneath is the spectrum on point 2, which is on the damaged spot directly. Point 1 lies at the edge where no graphitization is observed and it shows a CVD diamond characteristic peak. . . . .	111
8.28	Sketch of Graphite structure [140]. . . . .	112
8.29	a-C exposed to the 91 eV beam with single shots at FLASH with 4.83 $\mu J$ pulse energy. The positions on which spectrum has been taken are marked in Fig 8.25 respectively from top to bottom (B-B3).The rest of spectra on the pointed spots are depicted in the appendix A. . . . .	114
8.30	Raman spectrum on CVD sample at different photon energies with the same pulse energy (5 $\mu J$ ) are compared. Graphitization process has been seen in all of these experiments and the degree of this process changes. Depending on the photon energy and experimental conditions these differences in peak width, position etc. have happened. Samples have had the same quality in all of these experiments. . . . .	117
8.31	Raman spectrum of pure Graphite sample to compare with the damaged a-C and CVD diamond samples. Raman spectra were taken from the white spots and black spots on both the samples. The results were the same. . . . .	118
9.1	Schematic picture of the algorithm of the developed combined model consisting of the interconnected modules responsible for different calculations: MC, Temperature equation for electrons, tight binding model and MD [158]. . . . .	122
9.2	(a): Diamond irradiated at 92 eV photon energy with 10 fs laser pulse. The absorbed energy was 1 eV/atom. The total energy of the system (electrons and atoms) is plotted in black and total energy of atoms is depicted in red dash line, the blue dashed line shows the potential energy of the system [158]. (b): The same simulation under the constant pressure. . . . .	123
9.3	Simulated fluence energy threshold for the graphitization of diamond as a function of photon energy during and after the pulse at different photon energies on CVD diamond sample vs experimental values. Data is simulated with a Hybrid code XTANT developed by Dr.N.Medvedev [158]. . . . .	124

- 9.4 (a): Simulated evolution of conduction band electron occupancy in CVD diamond with 830  $eV$  photon energy with  $1.87 J/cm^2$  fluence. The pulse duration was taken as in experiment 100  $fs$ . Data is simulated with a new hybrid code XTANT developed by Dr. N. Medvedev. (b): Simulated high energy electrons and core hole densities. (c): Simulated changes of potential, atomic, electrons and the total energy of the system. (d): Simulated changes of potential energy and the band gap during and after the pulse. . . . . 124
- 9.5 (a): Simulated changes of the band gap and chemical potential during and after the pulse with different photon energies (24, 91, 177, 275  $eV$ ) on CVD diamond sample. Pulse duration was taken to be 50  $fs$ . These simulations result in average absorbed dose of 0.7  $eV/atom$  for these photon energies. Data is simulated with a new Hybrid code XTANT developed by Dr.N.Medvedev [163]. (b): Simulated conduction electron density during and after the pulse. (c): Simulated nearest neighbor distance between the atoms in CVD diamond during and after the phase transition. Around 100  $fs$  the electrons (free) population is at maximum at all examined photon energies. . . . . 125
- 9.6 (a): Simulated the distance electrons with specific energy can travel to hey have by Dr. N. Medvedev calculated with XCASCADE Monte Carlo code [163] in a-C (red) and Si (blue). (b): Simulated the distance electrons can travel to in CVD diamond. 126
- 9.7 The total energy of free electrons in the conduction band normalized for the total absorbed energy (right ordinate). The number of free electrons created by different processes during the laser pulse irradiation and normalized per number of absorbed photons is also presented (left ordinate). The intensity envelope of the laser pulse is added as a dashed line in arbitrary units [36]. . 127
- 9.8 Spatial and temporal part of Gaussian pulse defined in COMSOL for the simulation. . . . . 129
- 9.9 Defined energy of the pulse. . . . . 130
- 9.10 Defined coming FEL pulse on Si. . . . . 131

- 9.11 Different structured models studied to find out the closest possible effect during heat diffusion process. It is interesting to check if by changing the radius or depth of phase transferred material or its thermal conductivity any changes will be observed in the simulation results. The first image from the top shows a model which considers the heat gets distributed inside the a-C coating as pulse illuminates the surface. The next model is the case where the phase transition had happened, and the radius size of the graphite (violet section) is the same as the beam radius (or smaller/ larger in different studied cases), and the depth is the same as the attenuation depth of radiation at 830 eV. The next image shows the case where graphitization has happened in a grating-like structure (partially). The radius of graphite in the first part is the same as the beam size or different, and after that area there is a-C, and the next is a graphitized area. The radius of a-C or graphite is changing. The depth is taken to be the same as the attenuation depth. The fourth image represents the case where the graphitized area has a smaller depth than the attenuation depth. It is still partially structured. Different models are considered and examined to find out the closest possible effect to the real case observed from the areas of the damage spots and check if any changes can be detected by changing the radius or depth of graphitized region or even its thermal conductivity. . . . 132
- 9.12 Defined components. a-C coating on top of Si substrate. . . . . 133
- 9.13 Defined boundary conditions. . . . . 133
- 9.14 Simulated heat diffusion in the sample after a few 100's of *ps* after the FEL pulse in top figure and after few *ns* in lower figure at 830 eV with 3.7  $\mu J$  pulse energy. . . . . 136
- 9.15 The temperature reached at the surface of a-C is depicted in red and Si at the boundary is depicted in green and Si at bottom of the sample in blue. There are two pulse energies examined here in top figure the pulse energy is taken 3.7  $\mu J$  and in the the bottom figure it's 17.5  $\mu J$  both at 830 eV. . . . . 137
- 9.16 At 830 eV photon energy with 17.5  $\mu J$  pulse energy the maximum radius at which the sample reaches the melting temperature on a-C or Si is simulated via COMSOL and plotted here. . . . . 138
- 9.17 In these calculations one has simulated if the a-C or Si reach their melting temperatures and the area up to which this temperature is reached is plotted vs the pulse energies. The experimental data also representing the area of each damaged spot vs the corresponding pulse energies on the logarithmic axis. . . . . 139

- 9.18 Heat diffusion simulation at 269 eV on a-C sample. Simulation ran over 7  $\mu s$  with the pulse duration of 125 fs . The beam radius is taken as in the experiment. a-C thickness was 50 nm. There is also an extra part which represents the measured length of the damaged spots via AFM (yellow) vs. their corresponding pulse energy to compare the localized and nonlocalized damage effect due to the heat on the damaged spots. . . . . 140
- 9.19 Heat diffusion simulation at 830 eV on a-C sample. Simulation ran over 7  $\mu s$ . The phase transition to graphite is not considered. One can see at which pulse energy Si / a-C reach their melting temperature and how deep in length on the surface this is distributed and where the melting can make changes in the size of the damaged spots. . . . . 141
- 9.20 Heat diffusion simulation at 830 eV on a-C sample. Simulation ran over 7  $\mu s$ . The simulation is done on the a-C sample with 100 fs pulse duration. The beam radius is taken as in the experiment (7.22  $\mu m$ ). The a-C thickness was 50 nm. . . . . 142
- 9.21 Heat diffusion simulation at 830 eV on a-C sample. Simulation ran over 7  $\mu s$ . The simulation is done on the a-C sample with 100 fs pulse duration. The beam radius is taken as in the experiment (7.22  $\mu m$ ). The a-C thickness was 50 nm. The phase transition into graphite is considered. Heat diffusion is compared between two cases of low thermal conductivity (3 W/mK) and thermal conductivity of 5.7 W/mK. Larger radius is heated up in the case of low thermal conductivity. . . . . 143
- 9.22 Heat diffusion simulation at 830 eV on a-C sample. The phase transition into graphite had already taken place. Simulation ran over 7  $\mu s$ . The graphite layer has 14  $\mu m$  radius. The thickness of graphite was 20 nm and underneath is a-C with thickness of 30 nm. . . . . 143
- 9.23 Heat diffusion simulation at 830 eV on a-C sample considering phase transition into graphite had already taken place. Simulation ran over 7  $\mu s$ . (a): Grating structured damaged region with graphite radius of 3.2, 2 and 3,2  $\mu m$  and thickness of 50 nm. (b): Same structure as in (a) but with 3.2, 2,3  $\mu m$  length and 20 nm thickness. . . . . 144
- 9.24 Heat diffusion simulation at 830 eV on CVD sample . Simulation ran over 7  $\mu s$ . The beam parameter are as in experiment. Estimating if the CVD reaches melting temperature and up to which radius it could have been heated up. . . . . 145
- 9.25 . . . . . 146

- 9.26 It is expected that the damage spot areas and their corresponding pulse energies on the logarithmic scale show a linear dependency (Gaussian beam profile). From the experimental result, it can be seen that after the P-I (photo-ionized) section this dependency is no longer linear. Comparing the areas of the footprints with the given initial beam area at the experiment shows a different enlargement in the areas of the damage spots (see Fig 9.25). This can be explained at higher pulse energies with heat diffusion effect. Between the P-I section and very high pulse energies, there is another section. In this section, one can assume a series of complex processes, such as photo-ionization and secondary processes and heat diffusion taking place. (a): Shows changes of the FWHM of the imprints with the pulse energy linearly. (b): Shows that damage footprints areas expanding nonlinearly due to the heat diffusion and carrier distribution (see also Figs 9.27 and 9.28). . . . . 148
- 9.27 The model based on the fact that the Gaussian pulse exposing the sample cause a photo-ionization (PI) effect, as well as heat and carrier diffusion. The FEL Gaussian function and the distribution function are modeled in the form of convoluted Gaussian defining the damage spot size changes; going from low pulse energies to higher pulse energies. The Gaussian pulse in PI section describes the linear dependency of the spot size of the damage spots on the pulse energy (on the logarithmic scale). This dependency changes due to the carrier and heat distribution to a nonlinear dependency. The experimental data are represented with the empty blue circles, performed at 830 eV at LCLS on CVD diamond sample. . . . . 149
- 9.28 The model above tested on a-C (50 nm thick a-C coating on Si substrate) sample. . . . . 149
- 9.29 The damage threshold dose values calculated with Equation 5.12 and compared with the melting threshold dose values obtained from COMSOL simulation in chapter 9. . . . . 150
- 10.1 The Lamellar grating used in the damage experiment at FLASH 2011 had a Si substrate coated with a-C (45 nm). The groove density was 200 grooves / mm and the groove depth was 13.5 +/- 3 nm. The duty ratio was 0.41 +/- 0.1. . . . . 152
- 10.2 Image of grating, where n is the order of diffraction,  $\lambda$  is the diffracted wavelength, d the grating constant.  $\theta_i$  the angle of incidence measured from the normal and  $\theta_m$  the angle of diffraction measured from the normal [167]. . . . . 152
- 10.3 Image of grating before the damage taken via White Light Interferometer (WLI) and the AFM. Si substrate coated with a-C (45 nm) The groove density was 200 grooves / mm and the groove depth was 13.5 +/- 3 nm. The duty ratio was 0.41 +/- 0.1. . . . 153



10.4	Simulated dose absorbed distribution corresponding to the grazing angle. The amorphous carbon coating on the grating was 50 nm on Si. . . . .	155
10.5	Simulated field distribution in the grating [170], [169]. X-ray intensity distribution is given by $ \psi(r, z)^2 $ close to the grating surface. The beam comes from the left. Both color scales are normalized intensity to the impinging beam. The amorphous Carbon coating on the grating was 50 nm on Si and was exposed to the beam at $2^\circ$ incidence angle. The absorbed power density is the reddish part and happens on the edge of the laminar grating structure which is 3 times higher than the flat surface. Interestingly, micro-roughness does not increase the maximum of absorbed energy by more than few percent. . . . .	155
10.6	AFM and DIC image of grating after it being exposed to FEL shot. Pulse energy of $1.64 \mu J$ . The lines represent the measured AFM lines on the spot. The the height of the damage spot is 7 nm. . . . .	156
10.7	AFM and DIC image of grating after it being exposed to FEL shot. Pulse energy of $1.8 \mu J$ was used here to create damage. The lines represent the measured AFM lines on the spot. The the height of the damage spot measured to be 10 nm. . . . .	157
10.8	AFM and DIC image of grating after it being exposed to FEL shot. Pulse energy of $8.64 \mu J$ . The lines represent the measured AFM lines on the spot. The the height of the damage spot measured is $0.4 \mu m$ . Beam direction is from right to left in the profile pic. . . . .	158
10.9	Illustrating the length up to which the damage is observable on the sample and the height of the spot. Damage is done mainly where its mostly absorbed (edges). The length and height of the spot was measured via AFM. Data are from the experiment at FLASH with 269 eV photon energy. . . . .	159
10.10	Illustrating the length of each damage spot vs the pulse energy which was used to generate that damage spot on the grating. The length and area of each spot was measured via AFM. Experiment performed with 269 eV photon energy at FLASH. . . . .	159
10.11	Illustrating the height of each damage spot vs the pulse energy which used to generate that damage spot on grating. The length and area of each spot was measured via AFM. Experiment performed with 269 eV photon energy at FLASH. . . . .	160
11.1	Damage studies . . . . .	162

- 11.2 Very simple schematic of the matter and laser beam interaction [17]. The left side shows the system in its ground state, the electrons cold state. The potential landscape shows minima at the crystal lattice sites. Therefore, no (external) forces are acting on them except tight binding Coulomb potential induced by the lattice. On the right, the laser light has affected the system and transported it to an excited state. Hot electrons and holes are created here. The potential landscape undergoes qualitative and quantitative changes, resulting in disappearance or shifting of the minima. This happens in very short time scale (shorter than reaction time) as a result, forces act on the carriers/atoms and move them. . . . . 163
- 11.3 (a): Simulated evolution of conduction band electron occupancy in CVD diamond with 830 eV photon energy with 1.87J/cm<sup>2</sup> fluence. The pulse duration was taken as in experiment 100 fs. Data is simulated with a new hybrid code XTANT developed by Dr. N. Medvedev. (b): Simulated high energy electrons and core hole densities. (c): Simulated changes of potential, atomic, electrons and the total energy of the system. (d): Simulated changes of chemical potential and the band gap during and after the pulse. . . . . 164
- 11.4 Orbital configuration of carbon  $Sp^3$ (mainly in Diamond),  $Sp^2$ (mainly in Graphite) . . . . . 164
- 11.5 Very simple schematic of the matter and X-ray FEL beam interaction [39]. Where the heat affected zone shows the region where heat gets diffused into and the shock affected zone describes the region where high pressure starts to induce shock waves. There is a thin layer right behind the heat-affected zone, which shows the melted layer. . . . . 165
- 11.6 AFM topography volume profile of an irradiated area on a-C with a 4,8 μJ FEL pulse at 177eV at FLASH. Volume of the spot is calculated via the AFM image with help from the MATLAB Code.166
- 11.7 . . . . . 167
- 11.8 Comparing the damage dose threshold at different photon energies on CVD diamond and amorphous carbon. The line at 0.7 eV represents the calculated damage dose threshold theoretically via Hybrid XTANT model mentioned in chapter 9 [135]. . . . . 168

- 11.9 Amorphous carbon damage spot with  $4.83 \mu J$  and photon beam energy of  $91 eV$  single shots at FLASH. The  $\mu$ -Raman analysis evidence the ordering of the a-C structure to nano crystallites of graphite, in good agreement with the 3 step model of Ferrari et al [138], [109], [110], [139]. Looking at the heat simulation in chapter 9 shows that at this pulse energy a-C and Si have both reached melting temperature. This figure also shows that beam fringes are observable at this point. This could be due to the apertures in beamline and the beam focus which was causing interference patterns on the sample. This fact that graphitization is observable out of the main dark spot of the damage is clearly showing that a larger area of the sample at the damage spot compared to the beam radius at this experiment was effected and phase transformed. . . . . 170
- 11.10(a): Diamond irradiated at  $92eV$  photon energy with  $10fs$  laser pulse. The absorbed energy was  $1 eV/atom$ . The total energy of the system (electrons and atoms) is plotted in black and total energy of atoms is depicted in red dash line, the blue dashed line shows the potential energy of the system. Reference [158]. (b): The same simulation under the constant pressure. . . . . 171
- 11.11 Figure illustrates experimental data at  $830 eV$  on a-C in green dots. The violet data set shows the area up to which the sample was heated up considering phase transition into graphite in the case of a-C. Which is done via COMSOL simulations. One can see at which pulse energy Si/a-C reach their melting temperature and how far (on the surface) this temperature spread. The experimental size of the damage spot can then be compared to this value. Here, three sections could be defined in damage process: PI (photo-ionization) section, carrier diffusion and cascade section and the heat diffusion section. Where carrier diffusion starts during PI and could continue in heat diffusion section. . . 174
- 12.1 CVD diamond sample exposed to the  $269 eV$  beam with single shots at FLASH at normal incidence angle. Top Fig shows the plotted pulse energy ( $\ln(E)$ ) vs the damage footprint area. Bottom Fig represents the F-scan method, where the footprint areas are plotted vs the corresponding normalized pulse energies for each shot. The Integral of the area underneath the curve (fit line) gives the effective area of the beam. . . . . 179
- 12.2 CVD diamond sample exposed to the  $91 eV$  beam with single shots at FLASH. Top plot shows the damage threshold graph and the bottom Figure shows the fit for the effective beam area. 180
- 12.3 CVD diamond sample exposed to the  $20 eV$  beam with single shots at SCSS. Top plot shows the damage threshold graph and the bottom Figure shows the fit for the effective beam area. . . 181

12.4	CVD diamond sample exposed to the 24 eV beam with single shots at SCSS. Top plot shows the damage threshold graph and the bottom Figure shows the fit for the effective beam area. . . .	182
12.5	Amorphous carbon exposed to the 269 eV beam with single shots at FLASH. Top plot shows the damage threshold graph and the bottom Figure shows the fit for the effective beam area. . . . .	183
12.6	Amorphous carbon exposed to the 24 eV beam with single shots at SCSS. Top plot shows the damage threshold graph and the bottom Figure shows the fit for the effective beam area. . . . .	184
12.7	Amorphous carbon exposed to the 20 eV beam with single shots at SCSS. Top plot shows the damage threshold graph and the bottom Figure shows the fit for the effective beam area. . . . .	185
12.8	CVD diamond sample exposed to the 830 eV beam with single shots at LCLS. Top plot shows the damage threshold graph and the bottom Figure shows the fit for the effective beam area. . . .	186
12.9	Amorphous carbon exposed to the 830 eV beam with single shots at LCLS. Top plot shows the damage threshold graph and the bottom figure shows the fit for the effective beam area. . . . .	187
12.10	nickel sample irradiated at 5 degree grazing incidence angle at 4.6 nm wave length. . . . .	189
12.11	Nickel sample irradiated at 5 degree grazing incidence angle at 4.6 nm wave length. The integral under the fitted curve represents the effective area of the beam. . . . .	189
12.12	Nickel sample irradiated at 7 degree grazing incidence angle at 4.6 nm wave length. . . . .	190
12.13	Nickel sample irradiated at 7 degree grazing incidence angle at 4.6 nm wave length. The integral under the fitted curve represents the effective area of the beam. . . . .	190
12.14	Nickel sample irradiated at 9 degree grazing incidence angle at 4.6 nm wave length. . . . .	191
12.15	Nickel sample irradiated at 9 degree grazing incidence angle at 4.6 nm wave length. The integral under the fitted curve represents the effective area of the beam. . . . .	191
12.16	Nickel sample irradiated at 11 degree grazing incidence angle at 4.6 nm wave length. . . . .	192
12.17	Nickel sample irradiated at 11 degree grazing incidence angle at 4.6 nm wave length. The integral under the fitted curve represents the effective area of the beam. . . . .	192
12.18	. . . . .	195
12.19	MoB4C sample irradiated at 1 degree grazing incidence angle at 4.6 nm wave length. The plot shows the F-Scan method to gain information about the effective area of damage spot. The integral under the fitted curve represents the effective area of the beam. . . . .	196
12.20	MoB4C sample irradiated at 90 degree grazing incidence angle at 4.6 nm wave length. . . . .	196

12.21	MoB4C sample irradiated at 90 degree grazing incidence angle at 4.6 <i>nm</i> wave length. The integral under the fitted curve represents the effective area of the beam. . . . .	197
12.22	MoB4C sample irradiated at 90 degree grazing incidence angle at 4.6 <i>nm</i> wave length. . . . .	197
12.23	MoB4C sample irradiated at 90 degree grazing incidence angle at 4.6 <i>nm</i> wave length. The integral under the fitted curve represents the effective area of the beam. . . . .	198
12.24	MoB4C sample irradiated at 2 degree grazing incidence angle at 4.7 <i>nm</i> wave length. . . . .	198
12.25	MoB4C sample irradiated at 2 degree grazing incidence angle at 4.6 <i>nm</i> wave length. The integral under the fitted curve represents the effective area of the beam. . . . .	199
12.26a-C	exposed to the 91 <i>eV</i> beam with single shots at FLASH with 4.83 $\mu J$ pulse energy (from up to down B4 - B7). . . . .	201
12.27a-C	exposed to the 91 <i>eV</i> beam with single shots at FLASH with 4.83 $\mu J$ pulse energy (from up to down B8 - B11). . . . .	202
12.28a-C	exposed to the 91 <i>eV</i> beam with single shots at FLASH with 4.83 $\mu J$ pulse energy (from up to down B12 - B15). . . . .	203
12.29a-C	exposed to the 91 <i>eV</i> beam with single shots at FLASH with 4.83 $\mu J$ pulse energy (from up to down B16 - B19). . . . .	204
12.30	Heat diffusion simulation at 830 <i>eV</i> on a-C sample considering phase transition into graphite. Simulation ran over 7 $\mu s$ . (a): The graphite size is considered to be 3, 2 $\mu m$ and 50 <i>nm</i> thickness. (b): The graphite has a larger size as the photon beam radius (8.22 $\mu m$ ) and 50 <i>nm</i> thickness. The thermal conductivity is taken to be 5.7 <i>W/mK</i> . The interesting point is the changes of the radius of the graphite and if heat diffuses differently in each case. In the smaller area (a) the a-C can still reach the melting temperature, whereas at larger areas this effect can not be seen ((b) or in fig 9.11). Si reaches the melting temperature at the same pulse energy in all these cases. The melting threshold for graphite is not changing. . . . .	205
12.31	Heat diffusion simulation at 830 <i>eV</i> on a-C sample considering phase transition into graphite had already taken place. (a): The graphite size is taken to be (14.22 $\mu m$ ) and 50 <i>nm</i> thickness. The thermal conductivity is taken 3 <i>W/mK</i> . (b): The graphite has the same size at the beam radius (14.22 $\mu m$ ) and 50 <i>nm</i> thickness. The thermal conductivity is taken to be 5.7 <i>W/mK</i> . . . . .	206
12.32	Grating structure (partially graphitized areas) on a-C sample with first block of graphite with 1 $\mu m$ radius and 20 <i>nm</i> thickness and the second block with 3 $\mu m$ and 20 <i>nm</i> thickness. Underneath the graphite layer there is considered a 30 <i>nm</i> thick layer of a-C and below that there is the substrate and between the both graphite layers there is a layer of a-C as well with 50 <i>nm</i> thickness and 4 $\mu m$ radius. . . . .	207



## List of Tables

7.1	Characteristic parameters at SCSS in Japan 2010. [101] . . . . .	57
7.2	Characteristic parameters at SCSS in Japan 2010 [101] . . . . .	69
8.1	Damage experiment parameter on CVD diamond/a-C at different photon energy levels. . . . .	76
8.2	Results of the damage experiment on amorphous carbon material at different photon energies at different grazing angles, comparing thin layer and bulk sample. The values in case of the bulk sample are from the experiment performed at FLASH in 2009 [73] and the results of grazing experiment at 7 degrees grazing angle on a-C at 269 eV in 2011 at FLASH. The attenuation length is taken from Henke's tables on CXRO website. . . . .	90
8.3	Results of the damage experiment on amorphous carbon material at different photon energies and different grazing angles, comparing thin layer and bulk sample. The values in case of the bulk sample are from the experiment performed at FLASH in 2009 with photon energy of 177 eV [73] and the results of grazing experiment at 7 degrees grazing angle on a-C at 269 eV in 2011 at FLASH. The attenuation length is calculated with the electron stopping power in each case. . . . .	91
8.4	Bonds and their pick position on a Raman spectra . . . . .	113
8.5	Result of the Raman experiment on a-C sample damaged with the photon beam of 91 eV and with pulse energy of 4.83 $\mu J$ . In the case of spot B the D peak is not detectable, instead the $sp^3$ peak. The amorphous carbon has combination of $sp^3, sp^2$ and $sp^1$ bonds. In the case of the samples for this project the ratio initially was $sp^3/sp^2=0.2$ . . . . .	113
8.6	Result of the Raman experiment on a-C sample damaged with the photon beam of 91 eV and with pulse energy of 4.83 $\mu J$ . The amorphous carbon has combination of $sp^3, sp^2$ and $sp^1$ bonds. Initially the ratio of $sp^3/sp^2$ was 0.2. . . . .	115
8.7	Result of the Raman experiment on CVD diamond at LCLS with 830 eV photon energy and the pulse energy of 5.11 $\mu J$ sample. . . . .	116
8.8	Result of the Raman experiment on the Graphite sample. . . . .	116
9.1	Defined properties of Si in the simulated model via COMSOL . . . . .	130

---

11.1	Results of the melting simulations on CVD diamond and a-C material at different photon energies. Sample thickness is $0.5\text{mm}$ in the case of CVD diamond. . . . .	172
12.1	Results of the damage experiment on CVD diamond material at different photon energies. Sample thickness is $0.5\text{ mm}$ . . . . .	177
12.2	Results of the damage experiment on CVD diamond material at different photon energies. The stopping power is considered here.	178
12.3	Results of the damage experiment on amorphous carbon material at different photon energies . . . . .	178
12.4	Results of the damage experiment on amorphous carbon material at different photon energies. The stopping power has been taken into account here. . . . .	178
12.5	results of the damage experiment on Nickel at different grazing incidence angle and with $269\text{ eV}$ photon energy. . . . .	193
12.6	results of the damage experiment on MoB4C (some were annealed) at different grazing/ incidence angle and with $269\text{ eV}$ photon energy. . . . .	199



## Bibliography

- [1] *Felbe free electron laser web page*, <http://www.hzdr.de/db/>, accessed April 2013.
- [2] *Fermi@elettra*, URL <https://www.elettra.trieste.it/FERMI/>.
- [3] W. Ackermann, G. Asova, V. Ayvazyan, A. Azima, N. Baboi, J. Baehr, V. Balandin, B. Beutner, A. Brandt, A. Bolzmann, R. Brinkmann, O. I. Brovko, *et al.*, *Nature Photonics* **1**, 336 (2007).
- [4] P. Emma, R. Akre, J. Arthur, R. Bionta, C. Bostedt, J. Bozek, A. Brachmann, P. Bucksbaum, R. Coffee, F.J. Decker, Y. Ding, *et al.*, *Nature Photonics* **4**, 641 (2010).
- [5] K. Tiedtke, A. Azima, N. von Bargen, L. Bittner, S. Bongt, S. Dsterer, B. Faatz, U. Frhling, M. Gensch, C. Gerth, N. Guerassimova, U. Hahn, *et al.*, *New Journal of Physics* **11**, 023029 (2009).
- [6] S. Moeller, J. Arthur, A. Brachmann, R. Coffee, F.-J. Decker, Y. Ding, D. Dowell, S. Edstroma, P. Emma, Y. Feng, A. Fisher, J. Frisch, *et al.*, *Nuclear Instrumental Methods* **A**, 56 (2011).
- [7] M. Altarelli, *Nuclear Instruments and Methods A* **269**, 2845 (2011).
- [8] N. Medvedev, A. E. Volkov, and B. Ziaja, *Nuclear Instruments and Methods in Physics Research B* **365**, 437 (2015).
- [9] J. Jackson, *Classical Electrodynamics* (John Wiley and sons, University of California Berkeley, 1962-1975).
- [10] G. Fowles, *Introduction to modern optics* (Dover publications, Newyork, 1968).
- [11] C. Kittel, *Introduction to solid state physics* (John wiley and sons, California Berkely, 2005).
- [12] S. H. Simon, *Lecture notes for solid state physics* (2012), URL <http://www-thphys.physics.ox.ac.uk/people/SteveSimon/condmat2012/LectureNotes2012.pdf>.
- [13] D. Attwood, *soft x ray and ultraviolet radiation* (University Press, Cambridge, 1999).

- 
- [14] X. Liu, D. Du, and G. Mourou, IEEE Applied Mechanics and Technical Physics **33**, 1706 (1997).
- [15] *X-ray interactions with matter*, URL <http://www.lbl.gov/security/>.
- [16] S. D. Farahani, J. Chalupsky, T. Burian, H. Chapman, A. J. Gleeson, V. Hajkoya, L. Juha, M. Jurek, D. Klinger, H. Sinn, R. Sobierajski, M. Stormer, *et al.*, Nuclear Instruments and Methods in Physics **39**, 635 (2011).
- [17] H. O. Jeschke, M. S. Diakhte, and M. E. Garcia, Applied Physics A Journal (2008).
- [18] A. Tien, S. Backus, H. Kapteyn, M. Murnane, and G. Mourou, Physical Review Letter **82**, 3883 (1999).
- [19] S. S. Li, *Semiconductor Physical Electronics* (Kluwer Academic / Plenum Publishers, 1993).
- [20] A. Kaiser, B. Rethfeld, M. Vicanek, and G. Simon .
- [21] P. S. Banks, M. D. Feit, A. M. Rubenchik, B. C. Stuart, and M. D. Perry, Applied Physics A **69**, 377 (1999).
- [22] D. Arnold and E. Cartier, Physical Review B **82**, 15102 (1992).
- [23] M. V. Ammosov, N. B. Delone, and V. P. Krainov, Soviet Physical Journal JETP **64**, 1191 (1986).
- [24] X. Mao, S. S. Mao, and R. E. Russo, Physical Review Letter **82**, 697 (2003).
- [25] M. D. Perry, B. C. Stuart, P. S. Banks, V. Y. M D Feit, and A. M. Rubenchik, Applied Physics **85**, 6803 (1999).
- [26] A. A. Manenkov, Laser Physics **6**, 501 (1996).
- [27] K. Wong, S. Vongehr, and V. V. Kresin, Physical Review B **67**, 035406 (2003).
- [28] B. C. Stuart, M. D. Feit, S. Herman, A. M. Rubenchik, B. W. Shore, and M. D. Perry, Physical Review B **53**, 1749 (1996).
- [29] S. K. sundaram and E. Mazur, Nature-Nature Materials **1**, 217 (2002).
- [30] B. Ziaja and N. Medvedev, High Energy Density Physics **8** (2012).
- [31] O. Klein and Y. lishina, Zeitschrift fuer Physik A Hadrons and Nuclei **52**, 853 (1928).
- [32] D. V. Rao, R. Cesareo, and G. E. Gigante, Physica Scripta **50**, 314 (1994).
- [33] D. V. Rao, R. Cesareo, and G. E. Gigante, Journal of Physics **74**, 10 (1996).

- [34] Y. Namito, S. Ban, H. Hirayama, N. Nariyama, H. Nakamshima, Y. Nakane, Y. Sakamoto, N. Sasamoto, Y. Asano, and S. Takana, *Physical Review A* **51**, 3036 (1995).
- [35] M. L. Garg, R. R. Garg, F. Hennrich, and D. Heimerman, *Nuclear Instruments and Methods B* **73**, 109 (1993).
- [36] N. Medvedev and B. Rethfeld, *New Journal of Physics* **12**, 073037 (2010).
- [37] J. F. Seely, H. J. Schwarz, and H. Hora, *Laser Interaction and Related Plasma Phenomena*, vol. 3B (New York, 1974).
- [38] L. Jiang and H. L. Tsai, *Proceeding of NSF Workshop on Research* pp. 1–13 (2003).
- [39] J. Krger and W. Kautek, *Laser Physics* **9 No 1** (1999).
- [40] N. Bloembergen, *IEEE QE* **10**, 375 (1974).
- [41] D. Du, X. Liu, J. Squier, and G. Mourou, *Applied Physics Letter* **64**, 3071 (1994).
- [42] R. Stoian, D. Ashkenasi, A. Rosenfeld, and E. E. B. Campbell, *Physical Review B* **62**, 13167 (2000).
- [43] B. Rethfeld, V. V. Temnov, K. S. Tinten, P. Tsu, D. von der Linde, S. I. Anisimov, S. I. Ashitkov, and M. B. Agranat, *Optical Technology* **71**, 348 (2004).
- [44] M. F. Koldunov, A. A. Manenkov, and I. L. Pokotilo, *Quantum Electronics* **32**, 335 (2002).
- [45] P. N. Saeta and B. I. Greene, *Physical Review Letters* **70**, 3588 (1993).
- [46] L. V. Keldysh, *Soviet Physics JETP* **20**, 1307 (1965).
- [47] D. von der Linde, K. S. Tinten, and J. Bialkowski, *Applied Surface Science* **109r110**, 1 (1996).
- [48] K. S. Tinten, J. Bialkowski, A. Cavalleri, and D. von der Linde, *Physical Review Letters* **81** (1998).
- [49] M. Bergh, *Interaction of Ultrashort X-ray Pulses with Material*, Ph.D. thesis, University Uppsala (2007).
- [50] E. G. Gamaly, A. V. Rode, B. L. Davies, V. T. Tikhonchuk, M. Jurek, D. Klinger, R. Nietubye, J. B. Pelka, H. Reniewicz, M. Sikora, and W. Sobala, *Physics of Plasmas* **9**, 949 (2002).
- [51] M. D. Perry, B. C. Stuart, P. S. Banks, M. D. Feit, V. Yanovsky, and A. M. Rubenchik, *Journal of Applied Physics* **85**, 6803 (1999).
- [52] E. G. Gamaly, A. V. Rode, B. L. Davies, and V. T. Tikhonchuk, *Physics of Plasmas* **9**, 949 (2002).

- [53] E. G. Gamaly, N. R. Madsen, M. Duering, A. V. Rode, V. Z. Kolev, and B. L. Davies, *Physical Review B* **71**, 174405 (2005).
- [54] C. Wang, L. Jiang, F. Wang, X. Li, Y. P. Yuan, and H. L. Tsai, *Physics Letters A* **375**, 32003204 (2011).
- [55] A. M. Malvezzi, N. Bloembergen, and C. Y. Huang, *International Journal of Thermo Physics* **13**, 131 (1992).
- [56] B. L. Davies, E. G. Gamaly, Y. Wang, A. V. Rode, and V. T. Tikhonchuk, *Soviet Journal of Quantum Electron* **22**, 289 (1992).
- [57] K. Eidmann, J. M. T. Vehn, T. Schlegel, and S. Huller, *Physical Review E* **62**, 1202 (2000).
- [58] W. Rozmus and V. T. Tikhonchuk, *Physical Review A* **42 number 12**, 7401 (1990).
- [59] B. L. Davies, E. G. G. and Y. Wang, A. V. Rode, and V. T. Tikhonchuk, *Soviet Journal of Quantum Electron* **22**, 289 (1992).
- [60] E. M. Lifshitz and L. P. Pitaevskii, *Physical kinetics* (Pergamon Press, Oxford, 1981).
- [61] Y. P. Raizer, *Laser Induced Discharge Phenomena* (Plenum Publishing, New York, 1997).
- [62] A. M. Molotvin, *Applied Mechanics and Technical Physics* **44**, 135 (2003).
- [63] D. Ashkenasi, A. Rosenfeld, H. Varel, M. Waehmer, and E. Campbell, *Applied Surface Science* **120**, 65 (1997).
- [64] A. C. Tam, H. K. Park, and C. P. Grigoropoulos, *Applied Surface Science* **127**, 721 (1998).
- [65] V. P. Krainov and A. S. Roshchupkin, *Physical Review A* **64**, 063204 (2001).
- [66] H. P. Cheng and J. D. Gillaspay, *Physical Review B* **55**, 2628 (1997).
- [67] C. Cornaggia, *Molecules and Clusters in Intense Laser Fields* (Cambridge, Cambridge University Press, 2001).
- [68] X. Wang and X. Xu, *Journal of Heat Transfer* **124**, 265 (2002).
- [69] A. Miotello and R. Kelly, *Physical Review A Supplemental* **69**, 67 (1999).
- [70] E. N. Glezer, Y. Siegal, L. Huang, and E. Mazur, *Physical Review B* **51**, 9589 (1995).
- [71] B. W. Rottke, J. Ihlemann, H. Schmidt, and A. Scholl, *Physical Review A Supplemental* **60**, 13 (1995).
- [72] H. A. Scott, *Journal of Quantum Spectroscopy Radiation* **71**, 689 (2001).

- [73] J. Chalupsky, V. H. Jkova, V. Altapova, T. Burian, A. J. Gleeson, L. Juha, M. Jurek, H. Sinn, M. Stoermer, R. Sobierajski, K. Tiedtke, S. Toleikis, *et al.*, Applied Physics letter **95**, 031111 (2009).
- [74] D. C. Joy, EM Facility University of Tennessee FAMS scanning **17**, 270 (1995).
- [75] E. J. kobetich, Physical Review Letter **170**, 391 (1968).
- [76] D. D. Ryutov, Review of Scientific Instruments **74**, 3722 (2003).
- [77] A. R. B. de Castro, A. R. Vasconcellos, and R. Luzzi, Review of Scientific Instruments **81**, 073102 (2010).
- [78] Y. Iwakaji, M. Kanasugi, S. Iguchi, O. Maida, and T. Ito, *Performance of CVD Diamond Photon Detectors in the Soft X-ray Region* (Graduate School of Engineering Osaka UniversityJapan, 2007).
- [79] *Amorphous carbon simulated structure*, <http://www.rcc.uq.edu.au/gallery/diamond/>, accessed Jan 2013.
- [80] J. Gaudin, a Peyrusse, J. Chalupsky, M. Toufarova, L. Vysn, V. Hajkov, R. Sobierajsk, T. Burian, S. D. Farahani, A. Graf, M. Amati, L. Gregoratti, *et al.*, Physical Review B **86**, 024103 (2012).
- [81] J. Robertson, Materials Science and Engineering R Reports **37**, 129 (2002).
- [82] J. Robertson, Material Science Engeeniering **R 37**, 129 (2002).
- [83] A. C. Ferrari, B. Kleinsorge, N. A. Morrison, A. Hart, V. Stolojan, and J. Robertson, Journal of Applied Physics **85**, 7191 (1999).
- [84] J. A. Robinson, M. LaBella, M. Zhu, M. Hollander, R. Kasarda, Z. Hughes, K. Trumbull, R. Cavalero, and D. Snyder, Applied Physics Letter **88**, 163106 (2006).
- [85] K. Takai, M. Oga, H. Sato, T. Enoki, Y. Ohki, A. Taomoto, K. Suenaga, and S. Iijima, Physical Review B **67**, 214202 (2003).
- [86] D. G. McCulloch, X. L. Xiao, J. L. Peng, P. C. T. Ha, D. R. McKenzie, M. M. M. Bilek, S. P. Lau, D. Sheeja, and B. K. Tay, Physical Review B **52**, 850 (1995).
- [87] Y. Linang, Y. Mera, and K. Maeda, Diamond Related Matter **17**, 137 (2008).
- [88] V. S. Kovivchak, T. V. Panova, O. V. Krivozubov, and N. A. Davletkildiev, Applied Physics A **79**, 543 (2004).
- [89] M. Stoermer, C. Horstmann, F. Siewert, F. Scholze, M. Krumrey, and F. Hertlein, Proceeding of SPIE p. 707705 1 (2008).

- [90] J. Robertson, *Materials Science and Engineering R* **37**, 129 (2002).
- [91] M. Stoermer, C. Horstmann, F. Siewert, F. Scholze, M. Krumrey, and F. Hertlein, 10th International Conference on Synchrotron Radiation Instrumentation (Melbourn, Australia) pp. 756–759 (2010).
- [92] *Image of diamond crystal structure*, <http://en.wikipedia.org/>, accessed Jan 2013.
- [93] *Cvd single crytsal dimond-element6*, URL <http://www.e6.com/>.
- [94] R. Sobierajski, J. Krzywinski, A. Andrejczuk, U. Hahn, R. Treusch, M. Jurek, D. Klinger, R. Nietubyc, J. B. Pelka, H. Reniewicz, M. Sikora, and W. Sobala, *Review Scientific Instruments* **76**, 013909 (2005).
- [95] A. A. Sorokin, S. V. Bobashev, T. Feigl, K. Tiedtke, H. Wabnitz, and M. Richter, *Physical Review Letter* **99**, 213002 (2008).
- [96] S. P. H. Riege, R. A. London, R. M. Bionta, M. A. McKernan, S. L. Baker, J. Krzywinski, R. Sobierajski, R. Nietubyc, J. B. Pelka, , M. Jurek, L. Juha, *et al.*, *Applied Physics Letter* **90**, 173128 (2008).
- [97] R. Sobierajski, M. Jurek, J. Chalupsky, J. Krzywinski, T. Burian, S. D. Farahani, V. Hajkova, M. Harmand, L. Juha, D. Klinger, R. A. Loch, C. Ozkan, *et al.*, *IOP* **8**, 02010 (2013).
- [98] K. Tiedtke, J. Feldhaus, U. Hahn, U. Jastrow, T. Nunez, T. Tschentscher, S. V. Bobashev, A. A. Sorokin, J. B. Hastings, S. Moeller, L. Cibik, A. Gottwald, *et al.*, *Applied Physics* **103**, 094511 (2008).
- [99] M. Richter, C. Blome, S. V. Bobashev, L. Cibic, J. B. Hastings, R. Ischebeck, U. Jastrow, U. Kroth, M. Krumrey, S. Moeller, J. Schneider, H. Schoeppe, *et al.*, *Applied Physics Letter* **83**, 2970 (2003).
- [100] J. B. Pelka, A. Andrejczuk, H. Reniewicz, N. Schell, J. Krzywinski, R. Sobierajskie, A. Wawro, Z. R. Zytkeiwicz, D. Klinger, and L. Juha, *Journal of Alloys and Compounds* **382**, 264 (2004).
- [101] M. Nagasono, RIKEN XFEL Project Head Office 3-site FEL meeting (2010).
- [102] N. Saito, P. N. Juranic, M. Kato, M. Richter, A. A. Sorokin, K. Tiedtke, U. Jastrow, U. Kroth, H. Schoppe, M. Nagasono, M. Yabashi, K. Tono, *et al.*, *IOP Publishing Metrologia* **47**, 21 (2010).
- [103] M. Kato, N. Saito, T. Tanaka, Y. Morishita, H. Kimura, H. Ohashi, M. Nagasono, M. Yabashi, K. Tono, T. Togashi, A. Higashiya, and T. Ishikawa, *Nuclear Instruments and Methods in Physics Research A* **612**, 209 (2009).
- [104] SLAC, *Lcls machine real time status* (2012), URL [https://portal.slac.stanford.edu/sites/lcls\\_public/Pages/status.aspx](https://portal.slac.stanford.edu/sites/lcls_public/Pages/status.aspx).

- [105] K. Tiedtke, A. A. Sorokin, U. Jastrow, P. Juranic, S. Kreis, N. Gerken, M. Richter, U. Arp, Y. Feng, D. Nordlund, R. Soufli, M. F. Perea, *et al.*, *Optics Express* **22**, 21214 (2014).
- [106] P. Heimann, A. Busse, Y. Feng, N. Kelez, J. Krzywinski, S. Moeller, M. Rowen, P. Stefan, and J. Welch, School of Chemistry of University of Bristol (2012).
- [107] *Nomarski microscope (olympus)*, URL <http://http://www.olympusmicro.com/primer/techniques/dic/dicintro.html>.
- [108] A. Vilalta-Clemente and K. Gloystein, *Physics of Advanced Materials Winter School* pp. 1–10 (2008).
- [109] A. C. Ferrari and J. Robertson, *Physical Review B* **61**, 14095 (2000).
- [110] A. C. Ferrari and J. Robertson, *Philosophical Transactions of the Royal Society London A* **362**, 14095 (2004).
- [111] R. H. and E. Riedo, A. Pasquarello, and A. Baldereschi, *Physical Review B* **65**, 045101 (2001).
- [112] J. Diaz, G. Paolicelli, S. Ferrer, and F. Comin, *Physical Review B* **54**, 8064 (1996).
- [113] H. S. Niehoff and F. Vollersten, *MJOM Journal of Metallurgy* p. 183 (2012).
- [114] R. Mitzner, *Physical Review Letter* **A80**, 025402 (2009).
- [115] M. K. Abyaneh, L. Gregoratti, M. Amati, M. Dalmiglio, and M. Kiskinova, *Surface Science Nanotechnology* **9**, 158 (2011).
- [116] W. Wierzchowski, K. Wieteska, T. Balcer, D. Klinger, R. Sobierajski, D. ymierska, J. Chalupsky, V. Hajkova, T. Burian, A. J. Gleeson, L. Juha, K. Tiedtke, *et al.*, *Radiation Physics and Chemistry* **80**, 1036 (2011).
- [117] J. M. Liu, *Optical physics letter* **7**, 196 (1982).
- [118] J. Chalupsky, J. Krzywinski, L. Juha, V. H. jkova, J. Cihelka, T. Burian, L. Vysan, J. Gaudin, A. Gleeson, M. Jurek, A. R. Khorsand, D. Klinger, *et al.*, *Optical Express* (2011).
- [119] J. Chalupsky and V. Hajkova, *IOP* (2011).
- [120] V. Hajkova, L. Juha, P. Bohacek, T. Burian, J. Chalupsky, L. Vysin, J. Gaudin, P. A. Heimann, S. P. H. Riege, M. Jurek, D. Klinger, J. Pelka, *et al.*, *Proceeding SPIE* **8077**, 807718 (2011).
- [121] T. Burian, V. Hajkova, J. Chalupsky, L. Vysin, P. Bohacek, M. Precek, J. Wild, C. Ozkan, N. Coppola, S. D. Farahani, J. Schulz, H. Sinn, *et al.*, *Optical Materials Express* **254** **5**, 224407 (2015).

- [122] T. Burian, V. Hajkova, J. Chalupsky, L. Juha, M. Toufarova, and V. Vorlicek, WDS 11 Proceedings of Contributed Papers **2**, 247 (2011).
- [123] K. S. Tinten, W. Ziegler, D. von der Linde, M. P. Siegal, and D. L. Overmyer, Applied Physics Letter **86**, 121911 (2005).
- [124] E. Spillers, Advances in X-ray Analysis **42**, 297 (2011).
- [125] A. F. Jankowski and P. L. Perry, Thin Solid Films **206**, 365 (1991).
- [126] S. S. Andreev, M. M. Barysheva, N. I. Chkhalo, S. A. Gusev, A. E. Pestov, V. N. Polkovnikov, D. N. Rogachev, N. N. Salashchenko, Y. A. Vainer, and S. Y. Zuev, Technical Physics **55**, 1168 (2010).
- [127] A. Thompson, D. Attwood, E. Gullikson, M. Howells, K. J. Kim, J. Kirz, J. Kortright, I. Lindau, Y. Liu, P. Pianetta, A. Robinson, J. Scofield, *et al.*, Lawrence Berkeley National Laboratory **55**, 1168 (2009).
- [128] P. A. Kearney, J. M. Slaughter, and C. M. Falco, Optical Engineering **30**, 1076 (1991).
- [129] I. A. Kopilets, V. V. Kondratenko, and A. I. Fedorenko, Metal Physics and Advanced Technology **17**, 717 (1998).
- [130] A. Kopilets, V. V. Kondratenko, A. I. Fedorenko, E. N. Zubarev, O. V. Poltseva, A. G. Ponomarenko, and I. I. Lyakhovskaya, X-ray Science Technology **6**, 141 (1996).
- [131] M. Niibe, H. Nii, and Y. Sugie, Journal of Applied Physics **41**, 3069 (2002).
- [132] M. Stoermer, F. Siewert, and H. Sinn, Journal of Synchrotron radiation **23**, 50 (2015).
- [133] M. Barthelmess and S. Bajt, Applied Optics **50**, 1610 (2011).
- [134] D. L. Civita, N. Gerasimova, H. Sinn, and M. Vannoni, Proceeding SPIE **9210**, 921002 (2014).
- [135] N. Medvedev, H. O. Jeschke, and B. Ziaja, SPIE proceeding **8777-877709-1** (2013).
- [136] M. A. Kazemian, L. G. M. Amati, M. Dalmiglio, and M. Kiskinova, eJournal of Surface Science and Nanotechnology **9**, 13 (2011).
- [137] J. Daz, G. Paolicelli, S. Ferrer, and F. Comin, Physical Review B **54**, 8064 (1996).
- [138] J. Robertson and E. P. O. Reilly, Advance Physics **35**, 317 (1986).
- [139] A. C. Ferrari and J. Robertson, Physical Review B **64**, 075414 (2001).
- [140] *Image of graphite structure*, <http://image.tutorvista.com/content/chemical-bonding/>, accessed Jan 2013.



- [141] J. Schwan, S. Ulrich, V. Batori, H. Ehrhardt, and S. R. P. Silva, *Journal of Applied Physics* **80**, 440 (1996).
- [142] C. A. Coulson and H. C. L. Higgins, *Proceeding of Royal Society of London Series A* **39**, 191 (1996).
- [143] F. Tuinstra and J. L. Koenig, *Journal of Chemical Physics* **539**, 1126 (1970).
- [144] M. J. Matthews, M. A. Pimenta, G. Dresselhaus, M. S. Dresselhaus, and M. Endo, *Physical Review B* **59**, R6585 (1999).
- [145] D. S. Knight and W. B. White, *Journal of Material Research* **4**, 385 (1989).
- [146] W. A. Harrison, *Physical Review B* **8**, 4487 (1973).
- [147] Q. Wu, L. Yu, Y. Ma, Y. Liao, L. Zhang, X. Chen, and K. Wang, *Journal of Applied Physics* **93**, 94 (1994).
- [148] M. A. Tamor and W. C. Vassell, *Journal of Applied Physics* **76**, 3823 (1994).
- [149] A. C. Ferrari and J. Robertson, *Philosophical Transactions of the Royal Society London A* **362**, 14095 (2004).
- [150] C. Casiraghi, A. C. Ferrari, and J. Robertson, *Physical Review B* **72**, 085401 (2005).
- [151] D. G. McCulloch and S. Prawer, *Applied Physics* **78**, 3040 (1995).
- [152] S. Prawer, K. W. Nugent, Y. Lifshitz, G. D. Lempert, E. Grossman, J. Kulik, I. Avigal, and R. Kalish, *Diamond Related Mater* **5**, 433 (1996).
- [153] D. G. McCulloch, S. Prawer, and A. Hoffman, *Physical Review B* **50**, 5905 (1994).
- [154] B. Ziaja, N. Medvedev, V. Tkachenko, T. Maltezopoulos, and W. Wurth, *Nature Scientific Reports* **5**, 18068 (2015).
- [155] B. Ziaja, , H. Wabnitz, E. Weckert, and T. Moller, *New Journal of Physics (IOP)* **10**, 043003 (24 pages) (2008).
- [156] V. Strelakov (2012), URL <http://arxiv.org/pdf/1208.1535.pdf>.MoscowStateUniversityofTechnology.
- [157] N. Medvedev, *Applied Physics B journal* **Volume 118**, 417 (2015).
- [158] N. Medvedev, H. O. Jeschke, and B. Ziaja, *Physical Review B* **88** (2013).
- [159] N. Medvedev, U. Zastrau, E. Forster, D. O. Gericke, and B. Rethfeld, *Physical Review Letter* **107** (2011).

- [160] O. Osmani, N. Medvedev, and B. Rethfeld, *Physical review B* **84**, 214105 (2010).
- [161] M. Parrinello and A. Rahman, *Physical Review Letter* **45**, 1196 (1980).
- [162] J. F. Lutsko, D. Wolf, S. Yip, S. R. phillpot, and T. Nguyen, *Physical review B* **38 Nr 16**, 11572 (1988).
- [163] J. Gaudin, N. Medvedev, J. Chalupsky, T. Burian, S. D. Farahani, V. Hajkova, M. H. H. O. Jeschke, L. Juha, D. Klinger, J. Krzywinski, R. A. Loch, S. Moeller, *et al.*, *Physical Review B* **88**, 060191 (2013).
- [164] S. Hocquet, J. Neauport, and N. Bonod, *Applied Physics Letter* **99**, 061101 (2011).
- [165] J. Strong and G. A. Vanasse, *Journal of the Optical Society of America* **50**, 113 (1960).
- [166] G. Naumenko, B. Kalinin, G. Saruev, D. Karlovets, Y. Popov, A. Potylitsyn, L. Sukhikh, and V. Cha p. 481 (2009).
- [167] *Diffraction grating*, URL [http://www.optometrics.com/diffraction\\_grating.html#GRATINGEQUATION](http://www.optometrics.com/diffraction_grating.html#GRATINGEQUATION).
- [168] P. Heimann, O. Krupin, W. F. Schlotter, J. Turner, J. Krzywinski, F. Sorgenfrei, M. Messerschmidt, D. Bernstein, J. Chalupsky, V. Hajkova, S. H. Riege, M. Holmes, *et al.*, *Review Scientific Instruments* **82**, 093104 (2011).
- [169] J. Gaudin, C. Ozkan, J. Chalupsky, S. Bajt, T. Burian, L. Vyein, N. Coppola, S. D. Farahani, H. N. Chapman, G. Galasso, V. Hajkova, M. Harmand, *et al.*, *Optic Letters* **37**, 3033 (2012).
- [170] J. Krzywinski, J. Gaudin, and A. Andrejczuk, *SLAC Talk* (2012).
- [171] H. J. W. M. Hoekstra, *Optical Quantum Electron* **29**, 157 (1997).
- [172] O. K. Ersoy, *Diffraction, Fourier Optics and Imaging* (WILEY, University College London, 2007).
- [173] M. Harmand, C. D. Murphy, C. R. D. Brown, M. Cammarata, T. Doppner, S. Dusterer, D. Fritz, E. Forster, E. Galtier, J. Gaudin, S. H. Glenzer, S. Gode, *et al.*, *IOP PUBLISHING FOR SISSA MEDIALAB* **7**, 1 (2012).
- [174] SLAC, *Lcls conceptual design report-x-ray beam transport and diagnostics* (2016), URL <http://www.slac.stanford.edu/cgi-wrap/getdoc/slac-r-978.pdf>.
- [175] A. Aquila, R. Sobierajski, C. Ozkan, V. Hajkova, T. Burian, J. Chalupsky, L. J. ad M Stoermer, S. Bajt, M. T. K. abd P Dluzwski, K. Morawiec, H. Ohashi, T. Koyama, *et al.*, *Applied physics letter* **106**, 241905 (2015).

- 
- [176] L. Patthey, U. Flechsig, R. Follath, P. Juranic, B. Pedrini, B. Patterson, C. Milne, G. Ingold, M. Radovic, and R. Abela pp. 1–96 (2013), URL [https://www.psi.ch/swissfel/CurrentSwissFELPublicationsEN/CDR\\_ARAMIS\\_Beamline\\_V2\\_2013-06-21\\_VM16-S.pdf](https://www.psi.ch/swissfel/CurrentSwissFELPublicationsEN/CDR_ARAMIS_Beamline_V2_2013-06-21_VM16-S.pdf).
- [177] M. Yabashi and T. Tanaka, *Nature Photonics* **6**, 648 (2012).
- [178] G. Gelonia, V. Kocharyanb, and E. Saldinb, *Journal of Modern Optics* **6**, 1391 (2011).



## Chapter 13

# Acknowledgement

To my life-coach, forever interested, encouraging and always concerned lovely mother Farah (Zeinab) Sotoudeh: because I owe it all to you. Many Thanks! To my supportive and encouraging Dad: Massoud Dastjani Farahani. Who is always keen to know what I am doing and how I am proceeding. Supportive to the very last moment and who helped me stand on my feet when I couldn't do so.

Dear Prof. Nader Shah Angha, I would have never decided to study physics as I was eight without you in my life. Thank you for inspiring me and teaching me so many life lessons.

I would like to express my sincere gratitude to my advisors Prof. Dr. Henry Chapman and Prof. Dr. Michael Alexander Rübhausen for the continuous support of my Ph.D. study and related research, for their patience, motivation, and immense knowledge. Their guidance helped me in all the time of research and writing of this thesis. I could not have imagined having better advisors and mentors for my Ph.D. study. Besides my advisors, I would like to thank the rest of my thesis committee: Prof. Arwen Pearson, Prof. Nils Huse, and Dr. Harald Sinn, for their insightful comments and encouragement, but also for questions which incensed me to widen my research from various perspectives.

My sincere thanks also go to Dr. Nikita Medvedev for the stimulating discussions in the theory section and his collaboration to this thesis through his simulations with XTANT Code. Many thanks to Dr.S. Bajt who provided me an opportunity and gave me access to her laboratory and research facilities for AFM measurements at CFEL Hamburg and Dr.G.Hoffman for the using their AFM facility at the University of Hamburg. I Would to thank Prof. Dr. Juha for allowing me using their Raman Spectroscope at Prague university.

In particular, I am grateful to Prof. Dr. L. Juha, Dr. J. Chalupsky, Dr. T. Burian, V. Hajkoya, Dr. R. Sobierajskie, Dr.M. Störmer, Dr. K. Tiedtkeg, Dr. S. Toleikisg for their collaboration during the experiments at different FEL facilities. I would like to thank Prof.Dr. H. O. Jeschke at Frankfurt University, Dr. S. Boutet, Dr. J. Bozek, Dr. C. Borstedt, Dr. J. Krzywinski at LCLS, also Dr. S. Hau-Riege, Dr. R. London, Dr. R. Bionta at Lawrence Livermore National Lab. I also thank my friend Dr.B.Dicke at CFEL for his support.

Special thanks to Prof. Dr. M. Altarelli, Dr. Th. Tschentscher Dr. J Gaudin and European XFEL for offering me the chance to start my Ph.D. at

European XFEL in Hamburg and coaching me on my way.

Thank you so much for being in my life; Eddie Palmieri, Luques Curtis, and Raul Valdez. Without you three I wouldn't learn many different valuable life lessons.

# Curriculum vitae – Lebenslauf

## PERSÖNLICHE ANGABEN

- Name: Shafagh Dastjani Farahani
- Date of Birth: 27.03.1980
- Place of Birth: Iran/Tehran
- Nationality: German

## EDUCATION

- Jan.2003-Dec.2003  
High school Diploma at the students college of Hamburg In Mathematics and Physics. Grade: satisfactory
- Aug.1994- Jul.1998  
High school diploma at the BU ALI SINA High school in Tehran, Iran. Grade: excellent

## MAJOR SUBJECT

- Oct.2009-Sep.2017  
PhD Project at Hamburg University; physics department co-operation with European XFEL
- 2008 Sept.2009  
PhD Project at Gutenberg University of Mainz in inorganic chemistry and Physics
- 1.Feb.2008  
Diploma degree from Hamburg University in Physics
- 2006-Aug.2007  
Diploma Project at the institute of Applied Physics at the University of Hamburg. Topic: Studying thin magnetic Ni<sub>2</sub>MnIn Heusler alloys films
- Oct.2003-Feb.2008  
Major in Physics at the University of Hamburg Nuclear Physics, Neutrino Physics, High energy Physics, Atom and Molecular Physics, Bio Physics, Solid states Physics and others

- Aug.1998-Jul.2002

Studies in Physics at the Governmental University of ALZAHRA in Tehran, Iran

#### WORK EXPERIENCE

- 2013-present

Freelance

- Oct.2009-2013

Research fellow at European XFEL Hamburg, Optic department

- Oct.2008-2009

Research fellow at Gutenberg University of Mainz in Organic chemistry department AK Felser

- Jun.2004-Feb.2008

Students assistant at the national library in Hamburg customer service

- Jan.2005-Jan.2006

Students assistant at the Optic and Nano structure, Department at the University of Hamburg Simulation With ZEMAX and SHADOW

#### TEACHING ACTIVITIES

- Dez.2004-May.2016

Private lessons in Physics, Mathematics and Persian and English in Hamburg

#### COMPUTER SKILLS

- MS Office
- LATEX
- ORIGIN
- CASA XPS
- ZEMAX
- MATLAB
- IGOR
- COMSOL simulation
- Python (basic knowledge)

#### LANGUAGES

- Farsi: mother tongue
- English: fluent
- German: fluent



- Arabic: basic knowledge
- French: basic knowledge

## EXPERIMENTAL EXPERIENCES

- FLASH at DESY in Hamburg (damage experiment)
- Petra at DESY in Hamburg (White light and Nomarski spectroscopy)
- BESSY in Berlin (Photoemission spectroscopy)
- ESRF in Grenoble in France (Time resolved x-ray reflectometry)
- Prague University (Raman spectroscopy)
- CFEL at DESY in Hamburg (AFM)
- Hamburg University (AFM, Etching, Coating, Molecular beam epitaxy, Auger spectroscopy, cleanroom sample preparation)
- Gutenberg university of Mainz (Arc-melting, rare earth superconductor compounds preparation, X-ray diffraction, SQUID measurement, Annealing, Glovebox sample preparation, annealing under vacuum conditions, vacuum ampules preparation)



## List of Publications

1. **Damage threshold of amorphous carbon mirror for 177 eV FEL radiation**

**Sh. Dastjani Farahani**, J. Chalupsky , T. Burian , H. Chapman , A.J. Gleeson, V. Hajkova, L. Juha, M. Jurek, D. Klinger, H. Sinn, R. Sobierajski, M. Stormer, K. Tiedtke, S. Toleikis, Th. Tschentscher, H. Wabnitz, J. Gaudin, Nuclear Instruments and Methods in physics research. 635, 39 (2011)

2. **Soft x-ray free-electron laser induced damage to inorganic scintillators**

T. Burian, V Hajkov, J. Chalupsky, L. Vysin, P. Bohacek, M. Precek, J. Wild, C. Ozkan, N. Coppola, **Sh. Dastjani Faharani**, J. Schulz, H. Sinn, Th. Tschentscher, J. Gaudin, S. Bajt, K. Tiedtke, S. Toleikis, H. N. Chapman, R. A. Loch, M. Jurek, R. Sobierajski, J. Krzywinski, S. Moeller, M. Harmand, G. Galasso, M. Nagasono, K. Saskl, P. Sovak, L. Juha , OSA. (2015). Optical Materials Express. 254

3. **Photon energy dependence of graphitization threshold for diamond irradiated with an intense XUV FEL pulse**

J. Gaudin, **Sh. Dastjani Farahani**, J. Chalupsky, T. Burian, L. Vysin, H. Wabnitz, V. Hajkova, M. Harmand, L. Juha, M. Jurek, R. A. Loch, S. Moeller, M. Nagasono, M. Stormer, H. Sinn, K. Saksl, R. Sobierajski, P. Sovak, S. Toleikis, K. Tiedtke, Th. Tschentscher, J. Krzywinski, B. Ziaja, M. Nagasono, K. Saksl, K. Tiedtke, M. Harmand, N. Medvedev, D. Klinger, J. Krzywinski, H. O. Jeschke, M. Toufarova, P. Sovak, C. Ozkan, V. Vorlcek, Physical Review. B 88, 060101(R) (2013)

4. **Experimental set-up and procedures for the investigation of XUV free electron laser interactions with solids**

R. Sobierajski, M. Jurek, J. Chalupsky, J. Krzywinski, T. Burian, **Sh. Dastjani Faharani**, V. Hajkova, M. Harmand, L. Juha, D. Klinger, R. A. Loch, C. Ozkan, J. B. Pelka, K. Sokolowski-Tinten , H. Sinn, S. Toleikis, K. Tiedtke, Th. Tschentscher, H. Wabnitz, J. Gaudin. Journal of Instrumentation. 8(2) February 2013

5. **Investigating the interaction of X-ray free electron laser radiation with grating structure**

- J. Gaudin, C. Ozkan, J. Chalupsky, S. Bajt, T. Burian, L. Vysin, N. Coppola, **Sh. Dastjani Farahani**, H. N. Chapman, G. Galasso, V. Hajkova, M. Harmand, L. Juha, M. Jurek, R. A. Loch, S. Moeller, M. Nagasono, M. Stormer, H. Sinn, K. Saksl, R. Sobierajski, J. Schulz, P. Sovak, S. Toleikis, K. Tiedtke, Th. Tschentscher, J. Krzywinski, *Optics Letters*. 37, Issue 15- 3033(2012)
6. **Amorphous to crystalline phase transition in carbon induced by intense femtosecond X-ray free-electron laser pulses**  
J. Gaudin, O. Peyrusse, J. Chalupsky, M. Toufarova, L. Vysn, V. Hajkova, R. Sobierajski, T. Burian, **Sh. Dastjani Farahani**, A. Graf, M. Amati, L. Gregoratti, S. P. Hau-Riege, G. Hoffmann, L. Juha, J. Krzywinski, R. A. London, S. Moeller, H. Sinn, S. Schorb, M. Stormer, Th. Tschentscher, V. Vorlcek, H. Vu, J. Bozek, C. Bostedt, *Physical Review*. B, 86-2, 024103 (2012)
7. **Solid-to-solid phase transition from amorphous carbon to graphite nanocrystal induced by intense femtosecond X-ray pulses**  
J. Gaudin, J. Chalupsky, M. Toufarova, L. Vysin, V. Hajkova, R. Sobierajski, T. Burian, **Sh. Dastjani Farahani**, A. Graf, M. Amati, L. Gregoratti, S. P. Hau-Riege, G. Hoffmann, L. Juha, J. Krzywinski, R. A. London, S. Moeller, H. Sinn, S. Schorb, M. Stoermer, Th. Tschentscher, V. Vorliceck, H. Vu, J. Bozek, C. Bostedt, *Physical Review*. B 86, 0241103 (2012)
8. **Picosecond time-resolved X-ray reflectivity of a laser-heated amorphous carbon film**  
R. Nueske, A. Jurgilaitis, H. Enquist, **Sh. Dastjani Farahani**, J. Gaudin, L. Guerin, M. Harb, C. v. Korff Schmising, M. Stoermer, M. Wulff, and J. Larsson, *Applied Physics Letter*. 98, 101909 (2011)
9. **Ternary rare earth compounds**  
**Sh. Dastjani Farahani**, F. Casper, C. Felser, Research Report AK Felser. Moment Group, Material for Optical, Magnetic and Energy technology (2008/2009)
10. **Electronic structure studies of BaFe<sub>2</sub>As<sub>2</sub> by angle-resolved photoemission spectroscopy**  
J. Fink, S. Thirupathaiah, R. Ovsyannikov, H. A. Duerr, R. Follath, Y. Huang, S. de Jong, M.S. Golden, Yu-Zhong Zhang, H. O. Jeschke, R. Valenti, C. Felser, **Sh. Dastjani Farahani**, M. Rotter, D. Johrendt, *Physical Review Research*. B 79, 155118 (2009)
11. **Giant Magneto-resistance in Rare Earth Compounds**  
F. Casper, **Sh. Dastjani Farahani**, C. Felser *et al*, *Zeitschrift fuer anorganische und allgemeine Chemie* 634, 2033, September 2008

- 
12. **Dielectric properties of TbMnO<sub>3</sub> and La(Sr,Ca)<sub>0.3</sub>MnO<sub>3</sub> evidence for spectral weight changes up to 20 eV** S. Mueller, M. Ruebhausen, R. Rauer, A. Rusydi, M. Bastjan, G. Neuber, **Sh. Dastjani Foharani**, B. Schulz, S. Singer, A. Lichtenstein, D. Argyriou, and K. Doerr, American Physical Society (2006)

**Talks:**

1. Results of damage experiments at FLASH and LCLS, Frankfurt, 2011. University of Frankfurt
2. Results of damage experiments at FLASH, Hamburg, 2011. XFEL
3. First results of damage experiment done at LCLS, Hamburg, 2010. XFEL  
Damage investigation on a-C and CVD, Hamburg, 2010. XFEL
4. Damage investigation on a-C and CVD, Hamburg, 2010. CFEL

**List of Posters:**

1. Damage investigations caused by femtosecond X-ray pulses, Hamburg 2011
2. Ultrafast phase transition in Carbon based coatings. User meeting 2011
3. Damage of amorphous carbon induced by X-ray femtosecond Free Electron Laser pulses, Prague, 2011
4. Investigation of damage induced on X-ray optics by femtosecond X-ray FEL pulses, Hamburg, 2010
5. Investigation of damage caused by femtosecond X-ray laser pulses. User meeting, Hamburg, 2010.



